

國立臺灣大學 理學院物理學研究所

博士學位論文

Graduate Institute of Physics

College of Science

National Taiwan University

Doctoral Dissertation



尋找 $D^0 \rightarrow \nu\bar{\nu}$ 以及 $B^0 \rightarrow p\bar{\Lambda}\pi^-\gamma$ 衰變與
Belle II 中央飄移室觸發系統之韌體設計

Search for $D^0 \rightarrow \nu\bar{\nu}$ and $B^0 \rightarrow p\bar{\Lambda}\pi^-\gamma$ decay at
Belle, and Belle II CDCTRG system firmware
design.

賴昶樅

Yun-Tsung Lai

指導教授：王名儒 博士

Advisors : Min-Zu Wang, Ph.D.

中華民國105年9月

September, 2016








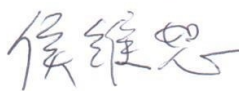


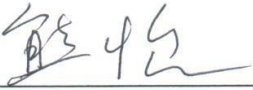


國立臺灣大學博士學位論文
口試委員會審定書

尋找 $D^0 \rightarrow \nu\bar{\nu}$ 以及 $B^0 \rightarrow p\bar{\Lambda}\pi^-\gamma$ 衰變與
Belle II 中央飄移室觸發系統之韌體設計

Search for $D^0 \rightarrow \nu\bar{\nu}$ and $B^0 \rightarrow p\bar{\Lambda}\pi^-\gamma$ decay at
Belle, and Belle II CDCTRIG system firmware
design.

本論文係賴昀樅君 (D00222037) 在國立臺灣大學物理學系、所
完成之博士學位論文，於民國 105 年 7 月 13 日承下列考試委員審查
通過及口試及格，特此證明

口試委員：

	 (簽名)
(指導教授)  張元勳	 張寶棟
 侯維恩	 徐靜
 李己中	 謝怡
 柳世民	 謝怡





Acknowledgment

First of all, I would like to express my sincere gratitude to my advisors, Prof. Min-Zu Wang, Prof. Paoti Chang, and Dr. Jing-Ge Shiu. With their guidance, I am able to solve problems I encountered and to enjoy the happiness during my research. The most important thing I learn from them is how to think and work like a physicist. I also appreciate Dr. Yoshihito Iwasaki, who gives me lots of help and leads my work in CDCTRG group when I was working in KEK. I would like to thank Prof. Yee Hsiung, Prof. Wei-Shu Hou, Prof. Kei-Feng Chen, Prof. Cheng-Hsiang Wang, Prof. Shiu-Min Liu, Prof. Yuan-Hann Chang, and Prof. Koji Ueno. Without their professional suggestions, I cannot complete this thesis.

The data analysis works are completed with the technical direction and efforts from many Belle members. I appreciate the continuous help from Belle analysis referees: Hitoshi Ozaki (Chair), Bipul Bhuyan, Tetsuro Kumita, Yoshihide Sakai (Chair), and Shoji Uno; EWP convener: Shohei Nishida; Charm group conveners: Chengping Shen and Vishal Bhardwaj; Physics coordinators: Mikihiro Nakao and Youngjoon Kwon, and all the experts who give me useful suggestions about writing of the journal article: Jim Libby, Simon I. Eidelman, Leo Piilonen, etc.

During my Ph.D., I spent about half the time staying in KEK for Belle II TRG work. KEK is just like my second home, and all the colleagues I work with in KEK are just like families. I would like to thank all the people I meet in KEK and TRG group: Prof. Eunil Won, Prof. Byung-Gu Cheon, Prof. Ming-Chuan Chang, Dr. Yuuji Unno, Dr. Hideyuki Nazakawa, Dr. Taniguchi Nanae, Jae-Bak Kim, Kyungtae Kim, Hyunki Moon, Donghyun Lee, Insoo Lee, Yang Chen, Sara Neuhaus, Steffen Bähr, Zheng-Xian Chen, Kai-Yu Chen, and Hui-Ching Lin. Besides the technical skills and knowledge regarding hardware system, I also learn the importance of teamwork during collaborating with them.

About six years ago, when I just became a member of NTUHEP and started my

work here, I also got lots of help from the senior members here and I would like to express my sincere thanks to them: Bean Huang, Yen-Yung Chang, Chien-Wei Chiou, Po-Yuan Chen, You-Hao Chang, Kai-Jen Tein, Chia-Ling Hsu, Yi-Ting Duh, Ruei-Jhu Li, Yuan-Pao Yang, Pei-Cheng Lu, Yeng-Ming Tzeng, Yu-Chen Tung, Yu-Wei Chang, John Chao, Chou Tat Hoi, and Alan Teng. I would also like to all the colleagues in NTUHEP: Chun-Hung Chen, Yu-Tan Chen, Kuan-Bo Lin, Tzu-An Shen, Jia-Hao Tu, Bo-Yuan Yang, Yu-Chieh Ku, Pinchun Chou, Bo-Ting Wang, Yu-Chieh Ku, Po-Hsun Chen, Alpha Tsai, Chiao-Yu Tao, Shih-Hsuan Chen, Yu-Cheng Lin, Dr. Suman Koirala, Chien-Hung Chou, Jenny Huang, and Link Liu. I will never forget all the happiness and laughter we have shared together in this lab.

My special thanks to my best friends since university days: Fa-Hui Lin, Guo-Jun Liao, Wei-Lin Duh, and Tzu-Chieh Kuo, and my best friend since junior high: Chen-En Yu. Although the chances for us to meet each other would be few in the future, I believe our friendship will live forever.

Finally, I would like to express my deepest thanks to my girl friend Pheobe Liao, all my families, and my pet guinea pig. Their kindly encouragement and spiritual support always inspire me to overcome all the difficulties and make me keep going on the road.

It has been a long way so far, and Ph.D. is just a beginning of my future career. I am so lucky to have help and support from so many people I met in this journey. Thank you!

Yun-Tsung Lai

July, 2016



摘要

本論文主要包含三個主題。第一、二部分為以KEKB對撞機於Belle偵測器累積的數據進行物理分析。第三部分為Belle II中央飄移室觸發系統的韌體設計。

第一個主題為尋找 D^0 至不可見末態粒子以及測量 $D^0 \rightarrow h^- \ell^+ \nu_\ell$ 衰變，數據來源是Belle偵測器收集於KEKB對撞機於接近 $\Upsilon(4S)$ 與 $\Upsilon(5S)$ 震盪態產生的事件，這些衰變模式的絕對分支比可藉由魅夸克味標籤法所得到，在 D^0 至不可見末態粒子的測量結果中沒有發現顯著性的訊號，因此我們以90%的信心水準，設定此衰變的分支比上限為 8.8×10^{-5} 。我們也用相同的分析方法測量了四個 $D^0 \rightarrow h^- \ell^+ \nu_\ell$ 的衰變分支比，其測量結果與PDG的世界平均值相合。

第二個主題為尋找 $B^0 \rightarrow p \bar{\Lambda} \pi^- \gamma$ 之衰變，在理論預測中，此模式主要透過 $b \rightarrow s \gamma$ 的途徑衰變，於末態包含一個高能量的光子，測量結果中沒有發現顯著性的訊號，因此我們以90%的信心水準，設定此衰變的分支比上限為 6.5×10^{-7} 。

第三個主題是台大高能實驗室參與Belle II第一階中央飄移室觸發系統的研究，在此系統中，Merger電路板負責簡化從前端讀出板的資料，再傳送到後段的帶電粒子軌跡重建模組，關於Merger電路板各方面的設計將在論文中詳細描述。台大團隊發展了自定義的光纖傳輸通訊協定，使用於在中央飄移室觸發系統的資料流之中，亦發展了整體系統的流量控制與資料同步的方式，論文中也會提到此通訊協定的發展與應用的細節。

關鍵詞：夸克味標籤、暗物質、輻射性 B 介子衰變、強子性 B 介子衰變、觸發系統、FPGA韌體、光纖傳輸





Abstract

The thesis includes three major topics. Two physics data analysis on D^0 and B^0 decays at Belle. The other is the firmware design for Belle II CDCTRГ system.

The first topic is a search for the $D^0 \rightarrow \nu\bar{\nu}$ decay at Belle. We study the D^0 decay to $\nu\bar{\nu}$ and $h^-\ell^+\nu_\ell$ ($h = K, \pi$, and $\ell = e, \mu$) using the data sample collected at or near the $\Upsilon(4S)$ and $\Upsilon(5S)$ with Belle detector at the KEKB asymmetric energy e^+e^- collider. Absolute branching fraction measurements of these decays are done with charm flavor tagging method. Since no significant signal is found, we set an upper limit of 8.8×10^{-5} for the branching fraction of $D^0 \rightarrow \nu\bar{\nu}$ at the 90% confidence level. We also perform the measurement of $D^0 \rightarrow h^-\ell^+\nu_\ell$, and the measured branching fractions are consistent with the PDG world average.

The second topic is the search for the charmless B^0 decay with final state particles $p\bar{\Lambda}\pi^-\gamma$. This decay is predicted to proceed predominantly via the $b \rightarrow s\gamma$ radiative penguin process with a high energy photon. No significant signal is found. We set an upper limit of 6.5×10^{-7} for the branching fraction of $B^0 \rightarrow p\bar{\Lambda}\pi^-\gamma$ at the 90% confidence level.

The third topic is NTUHEP group's work on Belle II Level-1 CDCTRГ system. In this system, the trigger Merger boards simplify the data flow from readout boards to the rear-end tracking modules. The development of Merger, including hardware and firmware, will be presented in this thesis. For the data flow in the CDCTRГ system, we developed an user-defined optical transmission protocol, and also the scheme of data flow control and synchronization for the whole trigger system. The design of user-defined protocol and its application will also be introduced.

Key words : "Quark flavor tagging", "Dark Matter", "Radiative B decay", "Baryonic B decay", "Trigger system", "FPGA firmware", "Optical transmission"



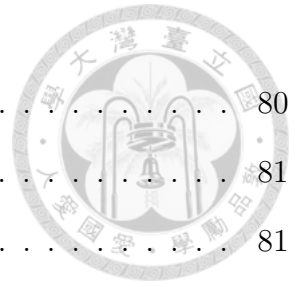


Contents

1	Introduction	1
1.1	Standard Model	1
1.2	CKM Matrix	2
1.3	CP Violation	4
1.4	B Physics	5
2	Belle Experiment	7
2.1	KEKB Accelerator	8
2.2	Belle Detector	9
2.2.1	Beam Pipe	12
2.2.2	Silicon Vertex Detector (SVD)	15
2.2.3	Extreme Forward Calorimeter (EFC)	16
2.2.4	Central Drift Chamber (CDC)	18
2.2.5	Aerogel Čerenkov Counter (ACC)	21
2.2.6	Time of Flight (TOF)	21
2.2.7	Electromagnetic Calorimeter (ECL)	24
2.2.8	K_L and Muon Detection System (KLM)	26
3	Search for $D^0 \rightarrow \nu\bar{\nu}$ Decay at Belle	27
3.1	Motivation	27
3.2	Data Sample	28

3.2.1	Blind Analysis and Monte Carlo Samples	29
3.3	Charm Tagger Method	29
3.3.1	Overview	29
3.3.2	D_{tag} Reconstruction	30
3.3.3	D_{tag}^* Reconstruction	33
3.3.4	X_{frag} Reconstruction	36
3.3.5	Recoil Spectrum $\bar{D}_{sig}^{*-} \rightarrow \bar{D}_{sig}^0 \pi_s^-$ (Inclusive D^0 Sample)	36
3.4	MC Study and Signal Extraction	40
3.4.1	Selection Criterion	40
3.4.2	Signal Extraction and Fitting Strategy	40
3.5	Ensemble Test	45
3.5.1	Gsim Test	45
3.5.2	ToyMC Test	49
3.6	Control Sample Study: $D^0 \rightarrow K^- \pi^+$, and $D^0 \rightarrow h^- \ell^+ \nu_\ell$	51
3.6.1	$D^0 \rightarrow K^- \pi^+$	51
3.6.2	$D^0 \rightarrow K^- \mu^+ \nu_\mu$	54
3.6.3	$D^0 \rightarrow K^- e^+ \nu_e$	56
3.6.4	$D^0 \rightarrow \pi^- \mu^+ \nu_\mu$	59
3.6.5	$D^0 \rightarrow \pi^- e^+ \nu_e$	61
3.7	Systematic Uncertainties	64
3.8	Physics Results	73
3.8.1	$D^0 \rightarrow h^- \ell^+ \nu_\ell$	73
3.8.2	$D^0 \rightarrow \nu \bar{\nu}$	73
3.9	Summary	76
4	Search for $B^0 \rightarrow p \bar{\Lambda} \pi^- \gamma$ Decay at Belle	79
4.1	Motivation	79

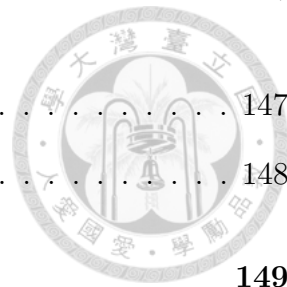
4.2	Data Sample	80
4.2.1	Blind Analysis and Monte Carlo Samples	81
4.3	Signal MC Generation	81
4.4	Event Selection and B Reconstruction	82
4.5	Background Suppression	85
4.5.1	Continuum Background	85
4.5.2	Continuum Background Suppression	86
4.5.3	Likelihood Ratio	88
4.5.4	Generic B Background	92
4.5.5	Peaking Background in Rare B MC	92
4.5.6	Self-crossfeed Background	93
4.6	Signal Extraction	95
4.6.1	Fitting Strategy	95
4.6.2	Probability Density Function	96
4.6.3	Measurements for the Branching Fraction	100
4.6.4	Ensemble Test	101
4.7	Control Sample Study: $B^+ \rightarrow K^{*+}\gamma$	105
4.7.1	Event selection and MC Study	105
4.7.2	Signal Extraction	105
4.7.3	Result	108
4.8	Physics Result	110
4.8.1	Fit Results	110
4.8.2	Systematic Uncertainties	110
4.8.3	Upper Limit Estimation	113
4.9	Summary	114
5	Belle II Experiment and CDC Trigger System	117



5.1	Super KEK- <i>B</i> Factory (SuperKEKB)	117
5.2	Belle II Detector	117
5.3	Belle II Central Drift Chamber (CDC)	121
5.3.1	Wire Configuration	121
5.4	Belle II Level-1 Trigger (TRG) System	122
5.5	Belle II Central Drift Chamber Trigger (CDCTRG)	125
6	CDCTRG Merger Board	129
6.1	Introduction	129
6.2	Merger Firmware	130
6.2.1	Normal Operation Mode	130
6.2.2	Optical Transmission Module and First-In-First-Out (FIFO)	133
6.2.3	VME Interface	133
6.2.4	Data Exchange Module between U1 and U2	134
6.2.5	Data Player Mode	134
6.2.6	Transmission Test Mode	134
6.2.7	Usage of LED on Front-Panel	134
6.3	Core Logic of CDCFE and Merger	135
6.3.1	SL0 Inside CDCFE	135
6.3.2	SL0 Outside CDCFE	137
6.3.3	Outer SL Inside CDCFE	139
6.3.4	Outer SL Outside CDCFE	140
6.3.5	SL0 Merger	141
6.3.6	Outer SL Merger	142
6.4	Operation Test	144
6.4.1	Setup	144
6.4.2	Test Result of Normal Operation Mode	146



6.4.3	Test Result of Data Player Mode	147
6.5	Summary	148
7	Data Transmission in CDCTRG	149
7.1	Introduction	149
7.2	Introduction to Hardware Components	149
7.2.1	Embedded Optical Module (AVAGO connector)	149
7.2.2	FPGA Chips and Transceivers in CDCTRG	151
7.3	Aurora Protocols	153
7.3.1	Firmware Structure	153
7.3.2	Firmware Test Results	156
7.3.3	Long-Term BERT on Aurora 8B/10B Protocol	156
7.4	Raw-Level Protocols	158
7.4.1	Design of the Protocols	158
7.4.2	Test Mode	162
7.4.3	Test Result on Raw-Level Protocols	162
7.4.4	Long-Term BERT on Raw-Level Protocols	165
7.4.5	Summary of Functionalities	166
7.5	CDCTRG Data Flow	167
7.5.1	CDCTRG Data Flow	167
7.5.2	Balance between Sections by First-In-First-Out (FIFO)	171
7.5.3	TRG Data Flow Control and Synchronization	173
7.5.4	Operation Test	179
7.6	Summary	180
8	Conclusions	183
A	Merger VME Functions	185



B Inclusive D^0 under Different $D_{tag}^{(*)}/X_{frag}$ modes	191
B.1 Inclusive D^0 under Different $D_{tag}^{(*)}$ Modes	191
B.2 Inclusive D^0 under Different X_{frag} cases	199
Bibliography	201





List of Figures

1.1	Summary of elementary particles in SM.	2
1.2	Summary of interactions between elementary particles in SM.	3
1.3	Total e^+e^- cross section measured by CLEO and CUSB showing the masses of Υ resonances.	5
1.4	$e^+e^- \rightarrow \Upsilon(4S) \rightarrow B\bar{B}$ process.	6
2.1	Bird's eye view of the KEKB accelerator at KEK.	7
2.2	Illustration of beam bunches rotation by crab cavity.	9
2.3	Configuration of the KEKB accelerator. The Belle detector is located in the interaction point in Tsukuba hall.	10
2.4	Configuration of the Belle detector.	13
2.5	Cross-section of the beryllium beam pipe near the IP.	15
2.6	Arrangement of the beam pipe and horizontal masks.	15
2.7	Configuration of SVD.	16
2.8	Graphical illustration of sub-detector SVD1 and SVD2.	17
2.9	Isometric view of the BGO crystals in EFC of the forward and backward parts.	18
2.10	Overview of the CDC structure.	19
2.11	Cell structure and the cathode sector configuration of CDC.	20
2.12	Scatter plot for dE/dx versus momentum.	20
2.13	Arrangement of ACC at the central part of the Belle detector.	22

2.14	Schematic drawing of a typical ACC counter module: (a) barrel and (b) end-cap ACC.	22
2.15	Illustration of a TOF/TSC module.	23
2.16	Mass distribution from TOF measurements for particle momenta below 1.2 GeV/c.	24
2.17	Overall configuration of ECL.	25
2.18	Schematic diagrams of the internal spacer arrangement of RPC.	26
3.1	The decay diagrams of $D^0 \rightarrow \nu\bar{\nu}$	28
3.2	π^0 mass demonstration plot with direct π^0 reconstruction.	32
3.3	p^* demonstration plots with direct D_{tag} reconstruction for some cases.	34
3.4	The variables used in best candidate selection.	38
3.5	Multiple candidates number distribution.	38
3.6	Inclusive D^0 fit result on six times data size generic MC.	39
3.7	Inclusive D^0 fit result on data.	39
3.8	PDF modeling in $D^0 \rightarrow \nu\bar{\nu}$ study with $E_{ECL} < 2.1$ GeV. Green solid line is flat background PDF. Blue solid line is peaking background PDF.	42
3.9	Scattering plot of MC samples in $D^0 \rightarrow \nu\bar{\nu}$ study with $E_{ECL} < 2.1$ GeV.	43
3.10	E_{ECL} distribution of $D^0 \rightarrow \nu\bar{\nu}$ MC samples with projecting to different recoil M_{D^0} region.	44
3.11	Comparison on sideband between data and MC. The histograms are normalized.	44
3.12	Gsim linearity test with different E_{ECL} range. ($N_{flatbck}^{input}$ and $N_{peakbck}^{input}$ are scaled by sideband data.)	46
3.13	ToyMC linearity test with $E_{ECL} < 2.1$ GeV. ($N_{flatbck}^{input}$ and $N_{peakbck}^{input}$ are scaled by sideband data.)	50
3.14	Recoil M_{D^0} and E_{ECL} distribution of six times data size of signal and all generic background MC in $D^0 \rightarrow K^-\pi^+$ study.	52

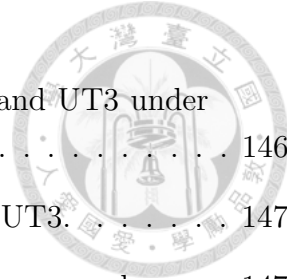
3.15	PDF modeling in $D^0 \rightarrow K^- \pi^+$ study.	53
3.16	Data fit result of $D^0 \rightarrow K^- \pi^+$. Red solid line is signal PDF. Blue solid line is peak background PDF. Green solid line is flat background PDF.	54
3.17	M_{miss}^2 distribution of six times data size of signal and all generic background MC in $D^0 \rightarrow K^- \mu^+ \nu_\mu$ study.	55
3.18	PDF modeling in $D^0 \rightarrow K^- \mu^+ \nu_\mu$ study.	55
3.19	Data fit result of $D^0 \rightarrow K^- \mu^+ \nu_\mu$. Red solid line is signal PDF. Blue solid line is flat background PDF. Cyan solid line is peaking background PDF.	56
3.20	M_{miss}^2 distribution of six times data size of signal and all generic background MC in $D^0 \rightarrow K^- e^+ \nu_e$ study.	57
3.21	PDF modeling in $D^0 \rightarrow K^- e^+ \nu_e$ study.	58
3.22	Data fit result of $D^0 \rightarrow K^- e^+ \nu_e$. Red solid line is signal PDF. Blue solid line is background PDF.	58
3.23	M_{miss}^2 distribution of six times data size of signal and all generic background MC in $D^0 \rightarrow \pi^- \mu^+ \nu_\mu$ study.	60
3.24	PDF modeling in $D^0 \rightarrow \pi^- \mu^+ \nu_\mu$ study.	60
3.25	Data fit result of $D^0 \rightarrow \pi^- \mu^+ \nu_\mu$. Red solid line is signal PDF. Green solid line is $D^0 \rightarrow K^- \mu^+ \nu_\mu$ background PDF. Blue solid line is flat background PDF. Cyan solid line is peaking background PDF.	61
3.26	M_{miss}^2 distribution of six times data size of signal and all generic background MC in $D^0 \rightarrow \pi^- e^+ \nu_e$ study.	62
3.27	PDF modeling in $D^0 \rightarrow \pi^- e^+ \nu_e$ study.	63
3.28	Data fit result of $D^0 \rightarrow \pi^- e^+ \nu_e$. Red solid line is signal PDF. Green solid line is $D^0 \rightarrow K^- e^+ \nu_e$ background PDF. Blue solid line is background PDF.	63
3.29	$D^0 \rightarrow K^- \pi^+$ data distribution of E_{ECL} and recoil M_{D^0}	66
3.30	$D^0 \rightarrow K^- \pi^+$ data and signal MC distribution of E_{ECL} and recoil M_{D^0}	66
3.31	The original and calibrated signal PDF of E_{ECL}	66

3.32	The original and calibrated flat background PDF of E_{ECL}	67
3.33	Data fit result of $D^0 \rightarrow \nu\bar{\nu}$ measurement.	77
3.34	Likelihood distributions obtained by $D^0 \rightarrow \nu\bar{\nu}$ data fits.	78
4.1	Decay diagram of $B^0 \rightarrow p\bar{\Lambda}\pi^-\gamma$	80
4.2	$p\bar{\Lambda}$ invariant mass distribution obtained by signal MC.	82
4.3	X_s mass distribution obtained by signal MC.	82
4.4	Λ mass ($M_{p\pi^-}$) distribution of signal MC.	83
4.5	The γ energy distribution in CM frame of signal MC and the selected region.	84
4.6	The ΔE and M_{bc} distribution of the continuum background MC.	85
4.7	The normalized $\cos\theta_B$ distributions. Red: signal MC. Blue: continuum background.	88
4.8	The KSFW moments distributions of the in seven missing mass regions. Red: signal MC. Blue: continuum background.	89
4.9	The normalized \mathcal{LR} distributions. Red: signal MC. Blue: continuum background.	89
4.10	The F.O.M. distributions with different \mathcal{LR} selections, estimated by total number of signal (in red) and true signal (in blue).	90
4.11	The ΔE and M_{bc} distribution of the generic B MC.	92
4.12	The ΔE and M_{bc} distributions of signal MC events with the selection criteria (left), true events (middle), and self-cross feed (right).	94
4.13	The comparison between background MC and data in the sideband region. Black error bar: data. Red: the combination of all background MC ($q\bar{q}$ MC, generic B MC, $B^+ \rightarrow p\bar{\Lambda}\pi^0$, and $B^+ \rightarrow p\bar{\Lambda}\gamma$). Blue: generic B MC. Green: $B^+ \rightarrow p\bar{\Lambda}\pi^0$. Yellow: $B^+ \rightarrow p\bar{\Lambda}\gamma$	95
4.14	Scattering plot of M_{bc} and ΔE distribution of the true signal MC.	97
4.15	The ΔE and M_{bc} distribution of the rare B^0 peaking modes with all selection criteria.	98



4.16	The ΔE and M_{bc} distribution of the rare B^+ peaking modes all selection criteria.	99
4.17	Ensemble test results (yield, fitting error and pull distribution) with $N_{sig} = 4$	103
4.18	Ensemble test results (yield, fitting error and pull distribution) with considering $B^0 \rightarrow p\bar{\Lambda}\gamma$, $B^0 \rightarrow p\bar{\Lambda}\pi^0$ components, and $N_{sig} = 25$	104
4.19	Ensemble test result (yield, fitting error and pull distribution) by using data fit result as input.	104
4.20	The ΔE and M_{bc} distributions of signal MC with all selection criteria (left), true signal (middle), and self-crossfeed (right) in $B^+ \rightarrow K^{*+}\gamma$ study.	106
4.21	The ΔE and M_{bc} distribution of the continuum background in $B^+ \rightarrow K^{*+}\gamma$ study.	106
4.22	ΔE and M_{bc} distribution of rare B MC in $B^+ \rightarrow K^{*+}\gamma$ study.	107
4.23	Scattering plot of M_{bc} and ΔE distribution of the true signal MC in $B^+ \rightarrow K^{*+}\gamma$ study.	107
4.24	Illustration of smoothed histogram with additional shape parameters.	108
4.25	$B^+ \rightarrow K^{*+}\gamma$ data fit result. Black error bar: data. Blue: total PDF. Red: signal PDF. Green: self-crossfeed PDF. Yellow: continuum background PDF. Magenta: rare B PDF.	109
4.26	Data fit result of $B^0 \rightarrow p\bar{\Lambda}\pi^-\gamma$. The points with error bars are data; the solid line is the fit result; the green dotted line is continuum background; the blue dash-dotted line is the combination of $B^+ \rightarrow p\bar{\Lambda}\pi^0$ and $B^+ \rightarrow p\bar{\Lambda}\gamma$, and the red area is the combination of signal and self-crossfeed.	114
4.27	The likelihood function obtained by $B^0 \rightarrow p\bar{\Lambda}\pi^-\gamma$ data fit.	115
5.1	A schematic view of SuperKEKB.	118
5.2	Cut view of BelleII detector.	120
5.3	Side view of Belle and Belle II detector.	120
5.4	Overall structure of Belle II CDC.	121

5.5	Sense wire configuration comparison between Belle and Belle II CDC.	122
5.6	Photos taken during wire stringing work.	123
5.7	Signal flow of BelleII Level-1 trigger system.	124
5.8	Belle II CDCTRG system.	126
5.9	An example of PTS of sense wire cell. Each square corresponds to a wire cell in CDC.	126
5.10	An example of TS of sense wire cell. Inner TSF is at SL0, and outer TSF are st SL 1~8. Each square corresponds to a wire cell in CDC. .	127
5.11	Schematic view of the conformal transformation: (a) in CDC transverse plane, (b) in the conformal plane.	127
6.1	Merger board v3.02 production type.	130
6.2	Schematic view of Merger firmware under normal operation mode. . .	131
6.3	Schematic view of Merger firmware under data player mode.	132
6.4	Merger's LED on front-panel.	136
6.5	Part of CDC SL0 inside wire cell configuration.	136
6.6	Bit map of CDC SL0 inside function output.	137
6.7	Part of CDC SL0 outside wire cell configuration.	137
6.8	Bit map of CDC SL0 outside function output.	138
6.9	Part of CDC outer SL inside wire cell configuration.	139
6.10	Bit map of CDC outer SL inside function output.	139
6.11	Part of CDC outer SL outside wire cell configuration.	140
6.12	Bit map of CDC outer SL outside function output.	140
6.13	Part of CDC SL0 wire cell configuration.	141
6.14	Bit map of Merger SL0 function output.	142
6.15	Part of CDC outer SL wire cell configuration.	143
6.16	Bit map of Merger outer SL function output.	143
6.17	Setup of the testbench for Merger operation test.	145



6.18 Clock counters synchronization at two Merger units and UT3 under normal operation mode. 146

6.19 Wire hit patterns from two Merger units received by UT3. 147

6.20 Clock counters synchronization at UT3 under data player mode. . . . 147

6.21 Merger data player result after pseudo data is inserted. 148

7.1 AVAGO HFBR-7934WZ connector. 150

7.2 AVAGO AFBR-79Q4Z connector. 150

7.3 CDCFE board. 151

7.4 Merger board. 152

7.5 Universal Trigger board (UT3). 152

7.6 Schematic view of Aurora firmware structure. 153

7.7 Test result of firmware with Aurora 8B/10B protocol for UT3. 156

7.8 Test result of firmware with Aurora 8B/10B protocol for Merger. . . . 156

7.9 Long-term BERT on Aurora 8B/10B protocol with UT3 and Merger. 157

7.10 Schematic view of raw-level protocols firmware structure. 158

7.11 The lane_up signal provided by the lane connection module. 160

7.12 Work flow chart of reset logic module. 161

7.13 K character with 8B/10B encoding. 162

7.14 Work flow chart of the raw-level 8B/10B protocol core logic. 163

7.15 Work flow chart of the raw-level 64B/66B protocol core logic. 164

7.16 Test result of raw-level 8B/10B protocol core module. 165

7.17 Test result of raw-level 8B/10B protocol at user side. 165

7.18 Test result of raw-level 64B/66B protocol core module. 165

7.19 Test result of raw-level 64B/66B protocol at user side. 166

7.20 Hardware setup for BERT on raw-level 64B/66B protocol. 166

7.21 CDCTRG data flow. 168

7.22	Illustration of a regular type 1 - 4 FIFO's operation.	172
7.23	Test result of a regular type 1 - 4 FIFO.	172
7.24	Design of the 3 - 16/16 - 3 FIFO.	173
7.25	Test results of the 3 - 16/16 - 3 FIFO.	173
7.26	A simplified CDCTRG data flow.	174
7.27	Overview work flow of the flow control and synchronization scheme.	175
7.28	Illustration of error recovery function in flow control with a simplified data flow system.	176
7.29	Detailed flow control firmware design of CDCFE (the front-most module).	177
7.30	Detailed flow control firmware design of Merger (the middle module).	178
7.31	Detailed flow control firmware design of TSF (the rear-most module).	178
7.32	Schematic view of a simplified data flow system.	179
7.33	Clock counter synchronization at 2D of a simplified data flow system.	179
7.34	Schematic view of a simplified data flow system with additional 3D board and GRL board.	180
7.35	Clock counter synchronization at GRL of a simplified data flow system.	180
7.36	Status of CDCTRG data flow in KEK E-Hut.	181
A.1	Dip switch of Merger board.	185
A.2	VME_IF.	186
A.3	Read 32bits data by VME_IF.	187
A.4	Result of hit_count.	188
A.5	Result of hit_rate.	189



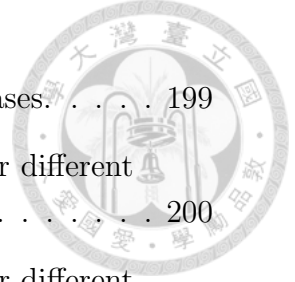
List of Tables

1.1	Properties of the four types of B mesons.	6
1.2	B -factories	6
2.1	Parameters of the KEKB accelerator design.	11
2.2	Performance parameters for the Belle detector.	14
2.3	Geometrical parameters of ECL.	25
3.1	List of D_{tag} decay modes included in the charm tagger and the corresponding branching fraction.	31
3.2	p^* and π^0 selection for D_{tag}	33
3.3	List of D_{tag}^{*+} decay modes included in the charm tagger and the corresponding branching fraction.	35
3.4	Mass window and ΔM selection of D_{tag}^*	36
3.5	List of X_{frag} cases with corresponding $D_{tag}^{(*)}$	37
3.6	Contribution on $E_{ECL} = 0$ peak from six times data size of background MC.	41
3.7	Gsim linearity test detailed result with $E_{ECL} < 2.1$ GeV. ($N_{flatbck}^{input}$ and $N_{peakbck}^{input}$ are scaled by sideband data.)	47
3.8	Gsim linearity test detailed result with $E_{ECL} < 2.4$ GeV. ($N_{flatbck}^{input}$ and $N_{peakbck}^{input}$ are scaled by sideband data.)	48
3.9	ToyMC linearity test detailed result with $E_{ECL} < 2.1$ GeV. ($N_{flatbck}^{input}$ and $N_{peakbck}^{input}$ are scaled by sideband data.)	49

3.10	PID calibration factors and uncertainties in $D^0 \rightarrow h^- \ell^+ \nu$ and $D^0 \rightarrow K^- \pi^+$ study.	64
3.11	Comparison between signal MC and data on recoil M_{D^0} PDF.	65
3.12	Summary of reconstruction efficiency uncertainties.	68
3.13	Comparison between MC and data under different vetoes.	69
3.14	Calibration factors and uncertainties due to vetoes.	69
3.15	MC and data veto eff. based on $D_{tag}^{(*)}$ modes.	71
3.16	MC and data veto eff. based on X_{frag} cases.	72
3.17	Summary of $D^0 \rightarrow h^- \ell^+ \nu_\ell$ measurement results. For the measured \mathcal{B} , the first uncertainties are statistical and the second are systematic. The calibration factors are obtained by Table 3.10 and Table 3.14.	73
3.18	Summary of systematic uncertainties for $D^0 \rightarrow h^- \ell^+ \nu_\ell$ study.	74
3.19	Fitting strategy for $D^0 \rightarrow \nu \bar{\nu}$ measurement.	75
3.20	Summary of systematic uncertainties for $D^0 \rightarrow \nu \bar{\nu}$ study.	75
3.21	Data fit result of $D^0 \rightarrow \nu \bar{\nu}$ measurement.	76
4.1	The regions of missing mass of KSFW.	87
4.2	Optimization of \mathcal{LR} selection with total number of signal (F.O.M _{tot}), and number of true signal (F.O.M _{true}). \mathcal{B} is assumed to be 10^{-5}	91
4.3	Summary of the selection criteria.	91
4.4	Number of remaining $q\bar{q}$ and generic B background MC events corresponding to one times data with all selection criteria.	93
4.5	Number of remaining rare B MC corresponding to one times data with all selection criteria. The red number is from the rare B MC result with assumed branching fraction, and the black number is scaled with measured branching fraction.	94
4.6	Efficiency of Signal MC with all selection criteria.	95
4.7	PDF and fitting parameters in $B^0 \rightarrow p\bar{\Lambda}\pi^-\gamma$ study. Note that P_{rare} is not included in the nominal fit for measurement.	97
4.8	PID correction factors.	100

4.9	Results of ensemble test.	102
4.10	Result of ensemble tests with considering $B^0 \rightarrow p\bar{\Lambda}\gamma$ and the $B^0 \rightarrow p\bar{\Lambda}\pi^0$ components.	103
4.11	Result of ensemble test by using data fit result as input.	103
4.12	Summary of the selection criteria for $B^+ \rightarrow K^{*+}\gamma$ study.	105
4.13	Fauge factors of signal PDF obtained by $B^+ \rightarrow K^{*+}\gamma$ data fit.	108
4.14	PID correction factors in $B^+ \rightarrow K^{*+}\gamma$ study.	109
4.15	Summary of the systematic uncertainties for $B^+ \rightarrow K^{*+}\gamma$ study.	110
4.16	Summary of the systematic uncertainties for $B^0 \rightarrow p\bar{\Lambda}\pi^-\gamma$ study.	113
5.1	Comparison on main parameters between Belle and Belle II CDC.	121
5.2	Belle II CDC sense wire configuration. ID of 9 SL in is used in later chapter about the CDCTRG system.	122
7.1	Summary of all hardware components used for CDCTRG optical transmission.	152
7.2	Latency comparison between raw-level protocols and Aurora.	167
7.3	Type of links with different raw-level protocols and hardware configurations used in CDCTRG data flow.	169
7.4	Summary of CDCFE→Merger links.	169
7.5	Summary of Merger→TSF links.	170
7.6	FIFO types used in CDCTRG data flow.	171
B.1	Inclusive D^0 data fit results (N_{D^0}) under different $D_{tag}^{(*)}$ modes.	193
B.2	Inclusive D^0 data fit results (N_{bck}) under different $D_{tag}^{(*)}$ modes.	194
B.3	Inclusive D^0 six times data size MC fit results (N_{D^0}) under different $D_{tag}^{(*)}$ modes.	196
B.4	Inclusive D^0 six times data size MC fit results (N_{bck}) under different $D_{tag}^{(*)}$ modes.	198
B.5	Inclusive D^0 data fit results (N_{D^0}) under different X_{frag} cases.	199

B.6	Inclusive D^0 data fit results (N_{bck}) under different X_{frag} cases.	199
B.7	Inclusive D^0 six times data size MC fit results (N_{D^0}) under different X_{frag} cases.	200
B.8	Inclusive D^0 six times data size MC fit results (N_{bck}) under different X_{frag} cases.	200





Chapter 1

Introduction

1.1 Standard Model

The Standard Model (SM) [1] is a quantum field theory which describes the properties and interactions of elementary particles in the universe. Basically, most of the experimental results of particle physics so far could be explained by SM. The basic elements of SM consists of four types of fundamental particles along with corresponding anti-particles, including quarks (q), lepton, gauge bosons, and Higgs boson, and also three types of interaction between the fundamental particles, including electromagnetic interaction, weak interaction, and strong interaction.

Quarks and leptons are spin-1/2 fermions with three generations. Each quark carries a fractional electric charge ($\pm\frac{2}{3}$ or $\pm\frac{1}{3}$) and each lepton carries integral electric charge. There are six flavors (types) of quarks, which includes up (u), down (d), charm (c), strange (s), top (t), and bottom (b). Based upon the quantum chromodynamics (QCD), there are three kinds of color charge denoted as r , g , and b , and a quark would carry one type of the color. Due to the color confinement principle in QCD, single quark can never be observed, but can be observed as a stable form of hadron, which includes baryon (qqq) and meson ($q\bar{q}$). With multiple quarks as a compound state, hadron is colorless and has integer electric charge. Leptons also includes six types: electron (e), muon (μ), tau (τ), and their corresponding neutrinos belonged to each generations (ν_e , ν_μ , and ν_τ).

The spin-1 gauge bosons are the force carriers of three types of interaction. The electromagnetic interaction takes place between charged leptons and quarks, where

γ is the electromagnetic force carrier. The weak interactions takes place between all leptons and quarks, where W^\pm and Z are the weak force carrier. The strong interaction only takes place between quarks, where the strong force carrier is gluon (g).

In Higgs mechanism of SM, the neutral, the spin-0 Higgs boson can explain the mass source of elementary particles. A Toroidal LHC ApparatuS (ATLAS) and Compact Muon Solenoid (CMS) experiment at Large Hadron Collider (LHC) in European Organization for Nuclear Research (CERN) have discovered a Higgs-like boson with mass around $126 \text{ GeV}/c$, and most of its properties are also proven to be consistent with the SM prediction.

The properties of all fundamental particles are summarized in Figure 1.1, and the summary of interactions between all elementary particles are shown in Figure 1.2.

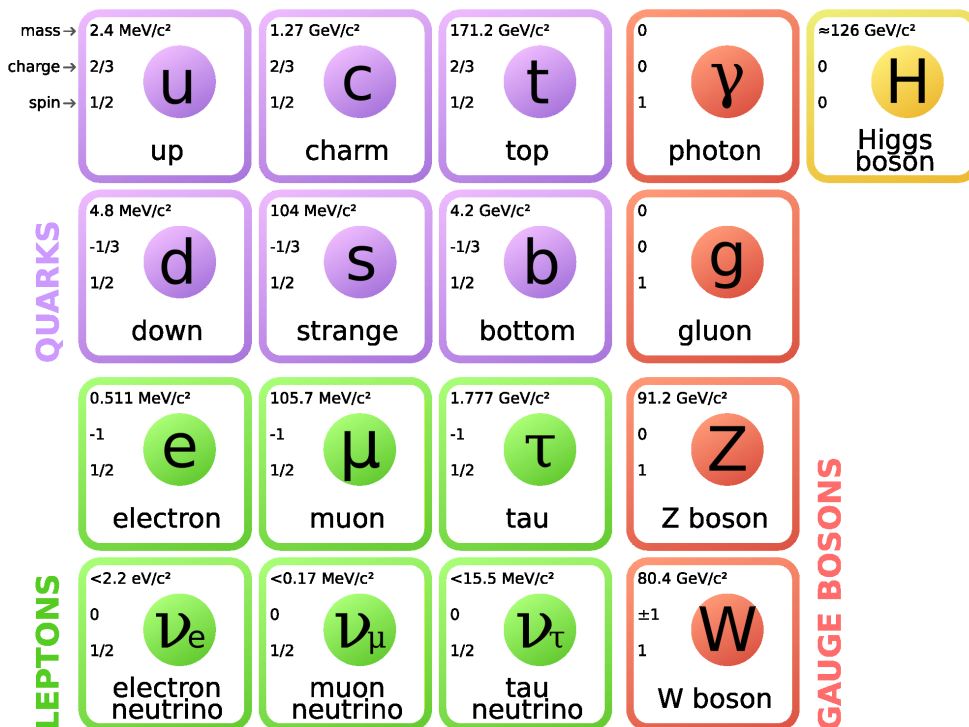


Figure 1.1: Summary of elementary particles in SM [2].

1.2 CKM Matrix

In the SM weak decays, the quark can change its flavor to another generation. A constant θ_c , which is called Cabibbo angle, is introduced by N. Cabibbo in order

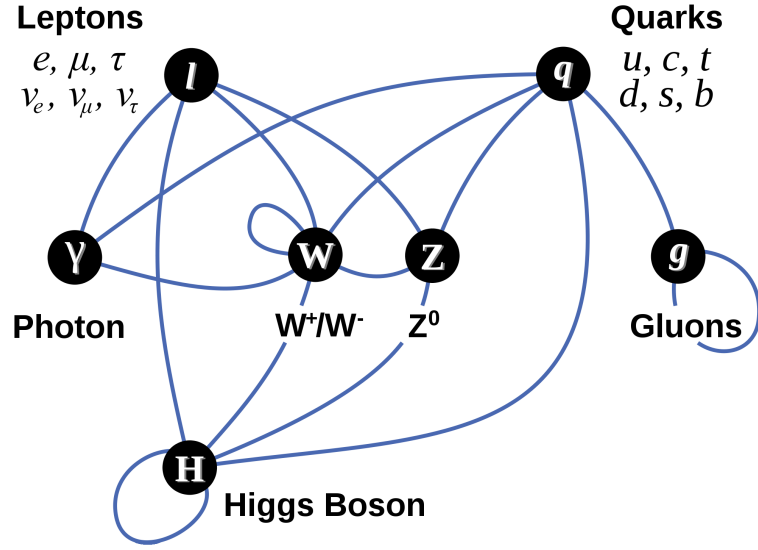


Figure 1.2: Summary of interaction between elementary particles in SM [3].

to transform the quark mass eigenstate into the weak interaction eigenstate [4]. For instance, the d and s are not pure but mixing states between them in the weak interaction,

$$\begin{cases} |d'\rangle = \cos \theta_c |d\rangle + \sin \theta_c |s\rangle, \\ |s'\rangle = -\sin \theta_c |d\rangle + \cos \theta_c |s\rangle, \end{cases} \quad (1.1)$$

M. Kobayashi and T. Maskawa extended the Cabibbo matrix into the 3×3 unitary Cabibbo-Kabayashi-Maskawa matrix (CKM matrix) with considering the third generation quarks (t, b) [5]. CP violation phase is introduced to make the matrix elements complex in order to explain CP violation. Each element in the CKM matrix is understood as the strength of quarks transformation under weak interaction. The form of CKM matrix can be represented as:

$$\begin{pmatrix} d' \\ s' \\ b' \end{pmatrix} = V_{\text{CKM}} \begin{pmatrix} d \\ s \\ b \end{pmatrix} = \begin{pmatrix} V_{ud} & V_{us} & V_{ub} \\ V_{cd} & V_{cs} & V_{cb} \\ V_{td} & V_{ts} & V_{tb} \end{pmatrix} \begin{pmatrix} d \\ s \\ b \end{pmatrix}. \quad (1.2)$$

The standard way to parameterize the CKM matrix [6] is by three mixing angles ($\theta_{12}, \theta_{13}, \theta_{23}$) and a CP -violating phase (δ):

$$V_{\text{CKM}} = \begin{pmatrix} c_{12}c_{13} & s_{12}c_{13} & s_{13}e^{-i\delta} \\ -s_{12}c_{23} - c_{12}s_{23}s_{13}e^{i\delta} & c_{12}c_{23} - s_{12}s_{23}s_{13}e^{i\delta} & s_{23}c_{13} \\ s_{12}s_{23} - c_{12}c_{23}s_{13}e^{i\delta} & -c_{12}s_{23} - s_{12}c_{23}s_{13}e^{i\delta} & c_{23}c_{13} \end{pmatrix}, \quad (1.3)$$



where $s_{ij} = \sin \theta_{ij}$, and $c_{ij} = \cos \theta_{ij}$ for $i, j = 1, 2, 3$.

An approximation on the parametrization introduced by Lincoln Wolfenstein [7] expresses the elements in powers of λ :

$$V_{\text{CKM}} \approx \begin{pmatrix} 1 - \frac{1}{2}\lambda^2 & \lambda & A\lambda^3(\rho - i\eta + \frac{i}{2}\eta\lambda^2) \\ -\lambda & 1 - \frac{1}{2}\lambda^2 - i\eta A^2\lambda^4 & A\lambda^2(1 + i\eta\lambda^2) \\ A\lambda^3(1 - \rho - i\eta) & -A\lambda^2 & 1 \end{pmatrix} + \mathcal{O}(\lambda^4), \quad (1.4)$$

where $\lambda = s_{12} = \sin \theta_c$, $A\lambda^2 = s_{23}$, and $A\lambda^3(\rho - i\eta) = s_{13}e^{-i\delta}$. This approximation implies the hierarchy

$$|V_{ub}|^2 \ll |V_{cb}|^2 \ll |V_{us}|^2 \ll 1, \quad (1.5)$$

which implies that the tendency of $b \rightarrow c$ is larger than $b \rightarrow u$.

The four real quantities in the Wolfenstein parametrization can be determined with experimental measurement results [8]:

$$\begin{aligned} \lambda &= 0.22535 \pm 0.00065, & A &= 0.811_{-0.012}^{+0.022}, \\ \rho &= 0.131_{-0.013}^{+0.026}, & \eta &= 0.345_{-0.014}^{+0.013}, \end{aligned} \quad (1.6)$$

$$V_{\text{CKM}} = \begin{pmatrix} 0.97427 \pm 0.00015 & 0.22534 \pm 0.00065 & 0.00351_{-0.00014}^{+0.00015} \\ 0.22520 \pm 0.00065 & 0.97344 \pm 0.00016 & 0.0412_{-0.0005}^{+0.0011} \\ 0.00867_{-0.00031}^{+0.00029} & 0.0404_{-0.0005}^{+0.0011} & 0.999146_{-0.000046}^{+0.000021} \end{pmatrix}. \quad (1.7)$$

1.3 CP Violation

There are three usual symmetries in particle physics: charge conjugation (C), parity (P), and time reversal (T). In the beginning, the three types of symmetry were believed to be invariant separately. However, the huge imbalance between matter and anti-matter in this universe indicates that C symmetry is absolutely broken. P violation was proposed by T. D. Lee and C. N. Yang in 1956 [9], and then it was confirmed by C. S. Wu in the β decay experiment in 1957 [10]. At that time, physicists believed the combination of C and P (CP) would be invariant.

In 1964, the first evidence of CP violation was observed in $K_L \rightarrow \pi^+\pi^-$ decay [11], which is forbidden under CP symmetry. In 1980, Carter and Sanda also suggested the potential of large CP violation in B meson decays [12]. The first

observation of large CP violation in the neutral B meson system [13] was found by the Belle experiment at the High Energy Accelerator Research Organization (KEK) in Japan.



1.4 *B* Physics

The third generation bottom quark (b) was observed in 1977 by the Columbia-Fermilab-Stony Brook collaboration (CFS) E288 experiment headed by Leon Lederman at Fermilab [14] by the newly discovered dimuon resonance at 9.5 GeV (recognized as $\Upsilon(1S)$ now). The flavorless Υ meson is formed by a b and a \bar{b} . Figure 1.3 shows the cross section of different Υ states particle production as a function of mass measured by Columbia University - Stony Brook (CUSB) and CLEO detector in Cornell Electron Storage Ring (CESR) at Cornell University [15].

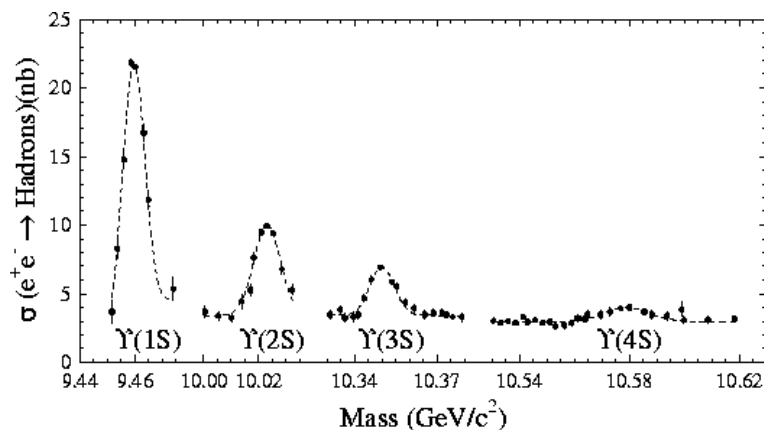


Figure 1.3: Total e^+e^- cross section measured by CLEO and CUSB showing the masses of Υ resonances [16].

B mesons are the bound states of a (\bar{b}) and either an u , d , s , or c , which are charged B meson (B^+), neutral B meson (B^0), strange B meson (B_s^0), or charmed B meson (B_c^+), respectively. The B mesons and their properties are summarized in Table 1.4.

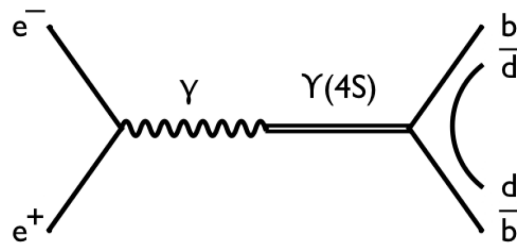
Regarding B decays, the majority is with $b \rightarrow c$ transition at the quark level with a charmed hadron or charmonium ($c\bar{c}$ mesons) in the final state. For the B decays which are through $b \rightarrow u$, d or s transition, the decay channels are called rare B decays. Rare B decay is basically suppressed by the CKM matrix element V_{ub} and it is sensitive to CP asymmetry and new physics.

Since $\Upsilon(4S)$ have a mass of (10.5794 ± 0.0012) GeV, which is only 20 MeV

Type	Quark content	$I(J^P)$	Rest mass (MeV/ c^2)	Mean lifetime(ps)
B^+	$u\bar{b}$	$\frac{1}{2}(0^-)$	5279.17 ± 0.29	1.641 ± 0.008
B^0	$d\bar{b}$	$\frac{1}{2}(0^-)$	5279.50 ± 0.30	1.519 ± 0.007
B_s^0	$s\bar{b}$	$0(0^-)$	5366.3 ± 0.6	1.425 ± 0.041
B_c^+	$c\bar{b}$	$0(0^-)$	6277 ± 6	0.453 ± 0.041

Table 1.1: Properties of the four types of B mesons [8].

above $B\bar{B}$ threshold, and $\mathcal{B}(\Upsilon(4S) \rightarrow B\bar{B})$ is larger than 96% [8], B mesons can be generated in abundance via $\Upsilon(4S)$ decay. Experimentally, we produce B mesons by the e^+e^- collisions at a center-of-mass energy on $\Upsilon(4S)$ resonance, and $\Upsilon(4S)$ almost immediately decays to $B\bar{B}$ pairs (including B^+B^- and $B^0\bar{B}^0$, the branching fractions are almost the same). Figure 1.4 shows the Feynman diagram of this decay process. This kind of experimental design which is dedicated to the $\Upsilon(4S)$ production is called B -factory, which is essential for the B physics study, e.g. rare B decay, CP violation in B decay. Table 1.2 lists the two B -factories in the world.

Figure 1.4: $e^+e^- \rightarrow \Upsilon(4S) \rightarrow B\bar{B}$ process.

Institute	Accelerator	Detector	Location
SLAC	PRP-II	BaBar	Stanford California, USA
KEK	KEKB	Belle	Tsukuba, Japan

Table 1.2: B -factories



Chapter 2

Belle Experiment

The main goal of the Belle experiment is to study the physics of CP violation, which holds the key to the baryogenesis (the matter-antimatter asymmetry). It is conducted by the Belle Collaboration, an international collaboration of physicists and engineers from 16 countries, located at the High Energy Accelerator Research Organization (KEK) in Tsukuba, Ibaraki Prefecture, Japan. There are two major facilities in the Belle experiment: the KEKB accelerator and the Belle detector. Figure 2.1 shows the bird's eye view of the organization and the KEKB accelerator.

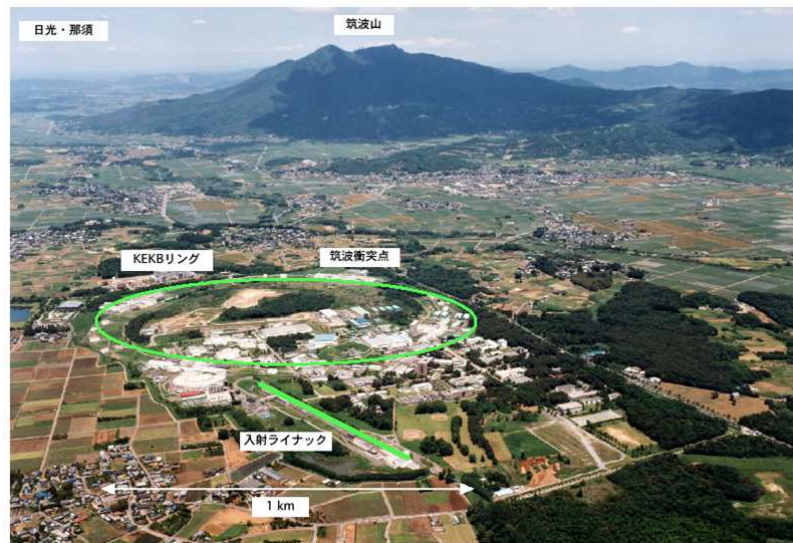


Figure 2.1: Bird's eye view of the KEKB accelerator at KEK [17].



2.1 KEKB Accelerator

KEK B -factory (KEKB) [18, 19] is an asymmetric energy electron-positron collider located at KEK. It has two storage rings: a low-energy ring (LER) for 3.5 GeV positron beam and a high-energy ring (HER) for 8 GeV electron beam, and both rings are constructed side by side in the TRISTAN tunnel with a circumference of 3 km. There are straight sections in the circular tunnel: Fuji, Nikko, Tsukuba and Oho. In Fuji area, there is a cross-over design used in order to ensure exactly the same circumference for the two rings. The two energy-asymmetry beams are designed to collide at the interaction point (IP) with a crossing angle of ± 11 mrad, and the Belle detector is also located at the IP in Tsukuba hall, which is on the northeast side of the rings.

The design of KEKB is known as a B factory with the center-of-mass energy of 10.580 GeV at the $\Upsilon(4S)$ resonance, which is just barely above the $B\bar{B}$ production threshold. With the center-of-mass energy, the cross section of $\Upsilon(4S) \rightarrow B\bar{B}$ process is about 1.05 nb while the cross section of the $e^+e^- \rightarrow q\bar{q}$ ($q = u, d, s, c$) continuum process is about 3.7 nb.

The crossing angle of ± 11 mrad is a notable feature of KEKB's design. It can provide advantages as following:

- Reducing the parasitic collisions near IP to reach higher luminosity.
- Eliminating the need for the separation-bend magnets, which reduces beam background in the detectors significantly.
- Making room to fill all RF buckets with the beam

\hat{z} is defined to be the inverse direction of LER, and \hat{x} is perpendicular to z -axis which let x - z plain containing both HER and LER. Crab cavities are placed near the IP in order to rotate the beam bunches to make head-on collision. An illustration of beam bunches rotation by crab cavity is shown in Figure 2.2. The KEKB accelerator configuration is illustrated in Figure 2.3, and the parameters for the KEKB accelerator design are summarized in Table 2.1.

KEKB is designed to operate with a peak luminosity at the order of $10^{34} \text{ cm}^{-2}\text{s}^{-1}$, which corresponds to about $10^8 B\bar{B}$ pairs per year. The operation from December, 1998 to 30 June, 2010 reaches the instantaneous luminosity record of 2.11×10^{34}

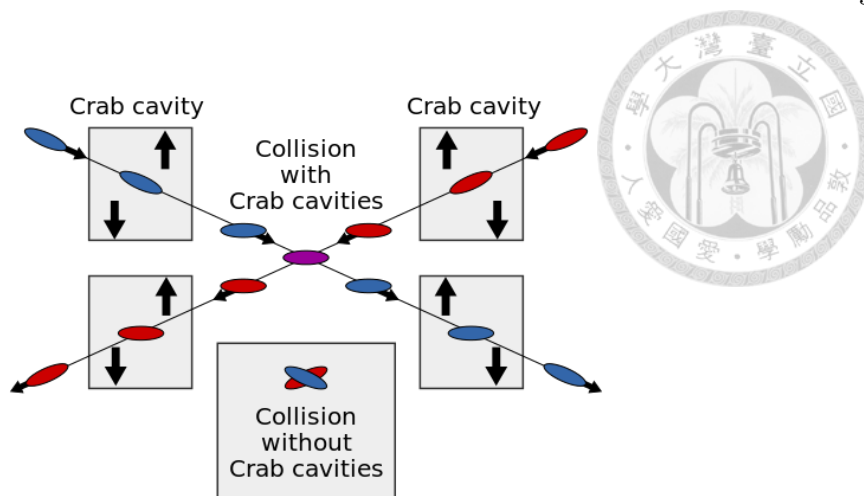


Figure 2.2: Illustration of beam bunches rotation by crab cavity [20].

$\text{cm}^{-2}\text{s}^{-1}$. Total integrated luminosity of 1052 fb^{-1} was accumulated by Belle detector.

In order to further probe the new physics e.g. physics in rare B decays, the KEKB accelerator and the Belle detector are now upgrading to SuperKEKB [21] and Belle II [22], to achieve the instantaneous luminosity by a factor of 40.

2.2 Belle Detector

The Belle detector [23, 24] is a multilayer detector with various sub-detectors in order to detect and reconstruct most of the final state particles from e^+e^- collision. It is configured around a 1.5 T superconductor solenoid and iron structure surrounding the KEKB beams at the Tsukuba interaction region. The main part of the detector has a polar angle (θ) coverage from 17° to 150° . In the Belle detector, there are various sub-detectors with different functionalities. Brief introductions to them are below:

- Silicon Vertex Detector (SVD): The inner-most detector which provides measurement of B decay vertices
- Central Drift Chamber (CDC): Located outside of SVD and beam pipe, and provides tracking information and dE/dx measurement of charged particles.
- Aerogel Čerenkov Counters (ACC): An array of silica aerogel threshold Čerenkov counters, which provides information for particle identification.

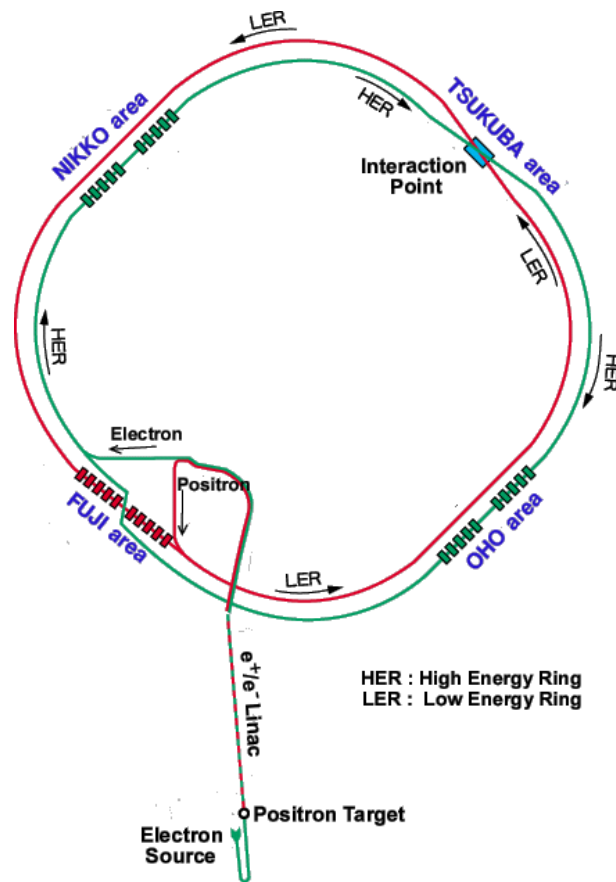


Figure 2.3: Configuration of the KEKB accelerator. The Belle detector is located in the interaction point in Tsukuba hall [17].



Ring		LER	HER	Unit
Energy	E	3.5	8.0	GeV
Circumference	C	3016.26		m
Luminosity	L	1×10^{34}		$\text{cm}^{-2}\text{s}^{-1}$
Crossing angle	θ_x	± 11		mrad
Tune shifts	ξ_x/ξ_y	0.039/0.052		
Beta function at IP	β_x^*/β_y^*	0.33/0.01		m
Beam current	I	2.6	1.1	A
Natural bunch length	σ_z	0.4		cm
Energy spread	σ_ε	7.1×10^{-4}	6.7×10^{-4}	
Bunch spacing	s_b	0.59		m
Particles/bunch	N	3.3×10^{10}	1.4×10^{10}	
Emittance	$\varepsilon_x/\varepsilon_y$	$1.8 \times 10^{-8}/3.6 \times 10^{-10}$		
Synchrotron	ν_s	0.01 ~ 0.02		
Betatron tune	ν_x/ν_y	45.52/45.08	47.52/43.08	
Momentum compaction factor	α_p	$1 \times 10^{-4} \sim 2 \times 10^{-4}$		
Energy loss/turn	U_0	0.81 [†] /1.5 ^{††}	3.5	MeV
RF voltage	V_c	5 ~ 10	10 ~ 20	MV
RF frequency	f_{RF}	508.887		MHz
Harmonic number	h	5120		
Longitudinal damping time	τ_ε	43 [†] /23 ^{††}	23	ms
Total beam power	P_b	2.7 [†] /4.5 ^{††}	4.0	MW
Radiation power	P_{SR}	2.1 [†] /4.0 ^{††}	3.8	MW
HOM power	P_{HOM}	0.57	0.15	MW
Bending radius	ρ	16.3	104.5	m
Length of bending magnet	l_B	0.915	5.86	m

†: without wigglers, ††: with wigglers

Table 2.1: Parameters of the KEKB accelerator design [18].

- Time of Flight (TOF): A barrel-like arrangement of time-of-flight scintillation counters, which provides information for particle identification.
- Electromagnetic Calorimeter (ECL): A CsI(Tl) crystal array, which is located outside of ACC and TOF, and inside the coil of solenoid magnet.
- K_L^0 and muon detection system (KLM): An iron flux-return located outside of the coil of solenoid magnet.
- Extreme Forward Calorimeter (EFC): A pair BGO crystal arrays which detects tracks from the extreme forward and backward directions, and extends the original angular coverage of ECL.

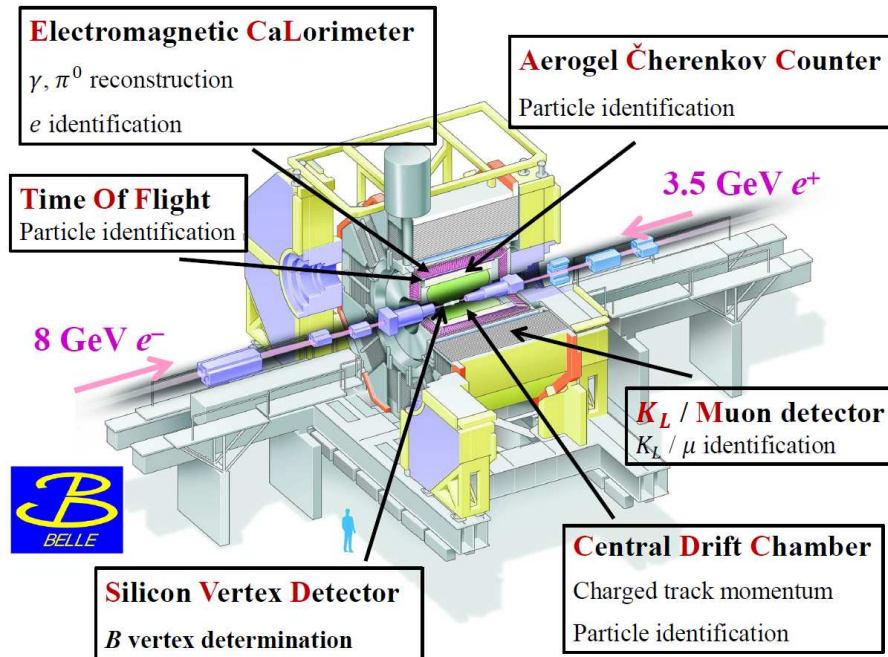
The configuration of the Belle detector is shown in cut view and side view in Figure 2.4. The performance of the Belle detector is summarized in Table 2.2. Descriptions of each sub-detector are included in following sections. More information about the Belle detector is detailed in Ref. [23].

2.2.1 Beam Pipe

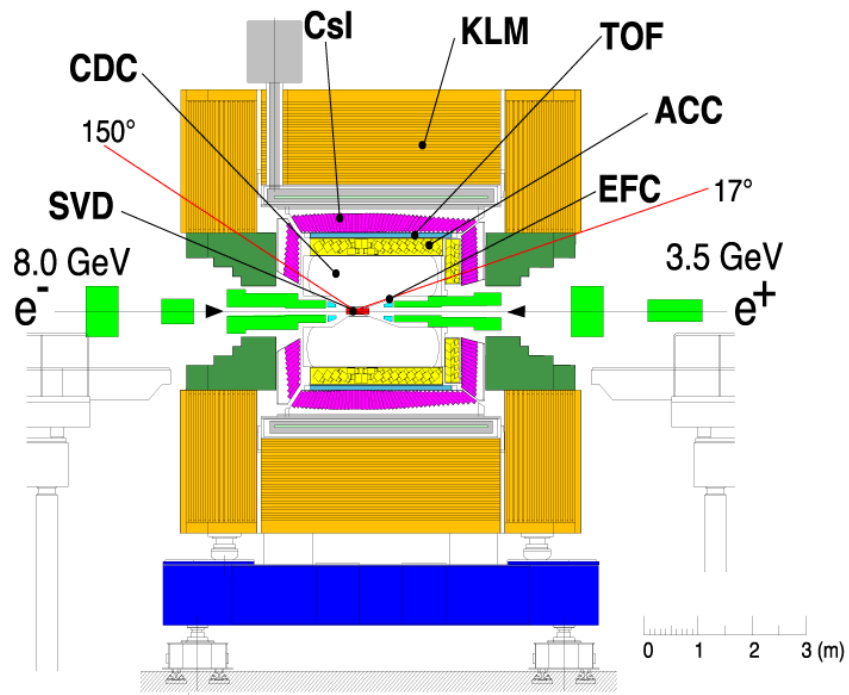
In the Belle experiment, precise measurement of decay vertices is essential to observe time-dependent CP asymmetries of B mesons. The first layer of the silicon vertex detector should be placed as close to the IP and beam pipe as possible in order to increase the vertex position resolution. However, multiple Coulomb scattering in the beam pipe wall and the first layer of the silicon detector are the limiting factors on the z -vertex resolution, a thin beam pipe is required.

The beam pipe is designed to have an inner radius of 2.0 cm, and an outer wall 2.3 cm in radius. The central part ($-4.6 \text{ cm} \leq z \leq 10.1 \text{ cm}$) of the beam pipe consists of double beryllium cylinders of 0.5 mm thickness. A 20 mm thick gold sheet is attached outside the outer beryllium cylinder in order to reduce the low-energy X-ray background ($\sim 0.5 \text{ keV}$). Due to the heat induced by the beam with a few hundred watt, the 2.5 mm gap between the inner and outer walls is filled with Helium gas for cooling. Figure 2.5 shows the cross-section of the beryllium beam pipe near the IP.

Figure 2.6 shows the arrangement of the beam pipes and masks. The beryllium central section is brazed to aluminum pipes that extend outside of the collision region. The apertures of the beam pipe and masks (SR Mask) near IP are designed to



(a) Cut view of the Belle detector.



(b) Side view of the Belle detector.

Figure 2.4: Configuration of the Belle detector [23].



Detector	Type	Configuration	Readout	Performance
Beam pipe for DS-I	Beryllium double wall	Cylindrical, $r = 20\text{mm}$, $0.5/2.5/0.5(\text{mm}) = \text{Be/He/Be}$ w/ He gas cooled		
Beam pipe for DS-II	Beryllium double wall	Cylindrical, $r = 15\text{mm}$, $0.5/2.5/0.5(\text{mm}) = \text{Be/PF200/Be}$		
EFC	BGO	Photodiode readout Segmentation : 32 in ϕ ; 5 in θ	160×2	Rms energy resolution: 7.3% at 8 GeV 5.8% at 2.5 GeV
SVD1	Double-sided Si strip	3-layers: 8/10/14 ladders Strip pitch: 25(p)/50(n) μm	ϕ : 40.96k z: 40.96k	$\sigma(z_{CP}) \sim 78.0\mu\text{m}$ for $B \rightarrow \phi K^0 2_s$
SVD2	Double-sided Si strip	4-layers: 6/12/18/18 ladders Strip pitch: 75(p)/50(n) μm (layer1-3) 73(p)/65(n) μm (layer4)	ϕ : 55.29k z: 55.296k	$\sigma(z_{CP}) \sim 78.9\mu\text{m}$ for $B \rightarrow \phi K_s^0$
CDC	Small cell drift chamber	Anode: 50 layers Cathode: 3 layers $r = 8.3 - 86.3 \text{ cm}$ $-77 \leq z \leq 160 \text{ cm}$	Anode: 8.4k Cathod: 1.8k	$\sigma_{r\phi} = 130\mu\text{m}$ $\sigma_z = 200 \sim 1400\mu\text{m}$ $\sigma_{Pt}/Pt = 0.3\% \sqrt{p_t^2 + 1}$ $\sigma_{dE}/dx = 0.6\%$
ACC	Silica aerogel	960 barrel/228 end-cap FM-PMT readout		$N_{p.e.} \geq 6$ K/π separation: $1.2 < p < 3.5\text{GeV}/c$
TOF	Scintillator	128 ϕ segmentation $r = 120 \text{ cm}$, 3-cm long	128×2	$\sigma_t = 100 \text{ ps}$ K/π separation: up to $1.2 \text{ GeV}/c$
TSC		64 ϕ segmentation	64	
ECL	CsI (Towered- structure)	Barrel: $r = 125 - 162 \text{ cm}$ End-cap: $z =$ -102 cm and $+196\text{cm}$	6624 1152(F) 960(B)	$\sigma_E/E = 1.3\%/\sqrt{E}$ $\sigma_{pos} = 0.5 \text{ cm}/\sqrt{E}$ (E in GeV)
KLM	Resistive plate counters	14 layers (5 cm Fe + 4cm gap) 2 RPCs in each gap	θ : 16k ϕ : 16k	$\Delta\phi = \Delta\theta = 30\text{mr}$ for K_L $\sim 1\%$ hadron fake
Magnet	Supercon.	Inner radius = 170 cm		B=1.5T

Table 2.2: Performance parameters for the Belle detector. There were two configurations of inner detectors used to collect two data sets, DS-I and DS-II, corresponding to a 3-layer SVD1 and a 4-layer SVD2 with a smaller beam pipe, respectively [23].

make synchrotron X-ray from QCS and QC1 magnets pass through without hitting the beam pipe inner wall. Photons from QC2 and QC3 with a critical energy less than 2 keV can also easily be absorbed in the material of the SR mask.

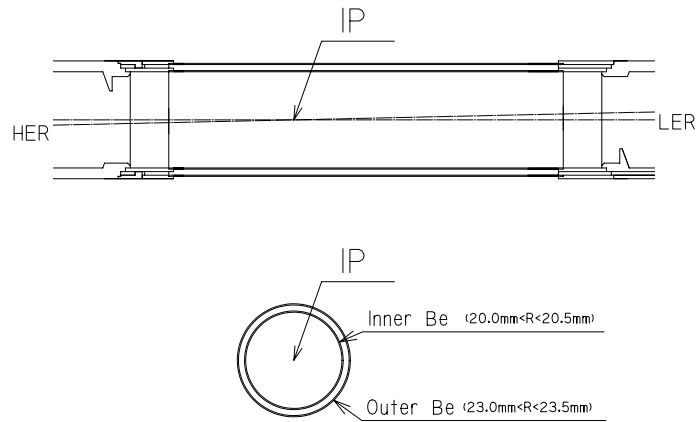


Figure 2.5: Cross-section of the beryllium beam pipe near the IP [23].

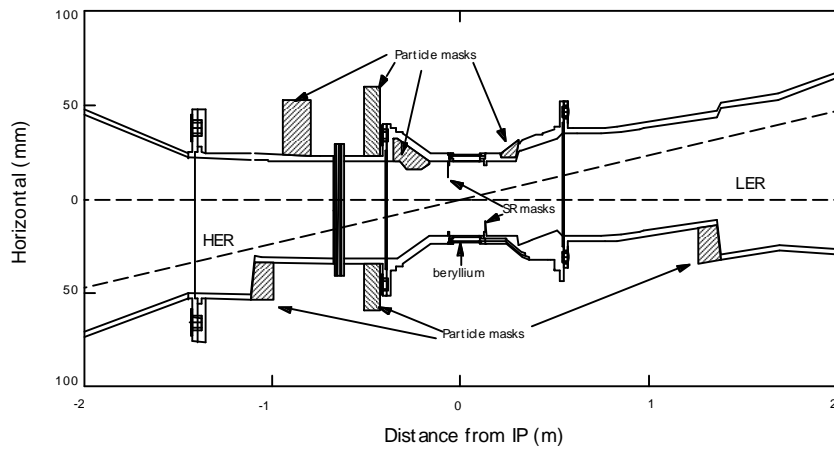


Figure 2.6: Arrangement of the beam pipe and horizontal masks [23].

2.2.2 Silicon Vertex Detector (SVD)

SVD is primarily for the B mesons decay vertices measurement, since a primary goal of Belle experiment is time-dependent CP violation, which requires a position resolution of $\sim 100 \mu\text{m}$ for the measurement of z -vertex position difference for B meson pairs. In addition, SVD is useful to determine the decay vertices of D meson and τ , and also contributes to the improvement of tracking.

The first version of SVD (SVD1) started to operate in 1999. It consists of three concentric cylindrical layers of double-sided silicon strip detector (DSSD) with 8, 10, and 14 ladders in each layer. The radii of three layers are 30 mm, 45.5 mm, and 60.5 mm. Its angular coverage is $23^\circ < \theta < 139^\circ$ where θ is the angle from the beam axis, corresponding to 86% of the solid angle. Each ladder is made of two joined half-ladders, and each half-ladder contains one or two DSSDs which are supported by boron-nitride (BN) ribs sandwiched with carbon-fiber reinforced plastic (CFRP). Each DSSD contains 1280 sense strips and 640 readout pads on both opposite sides. The z -strip (ϕ -strip) pitch is 42 (25) μm , and readout z -strip (ϕ -strip) is 84 (50) μm , respectively. The active region size in DSSD is $53.5 \times 32.0 \text{ mm}^2$ on the z -side and is $54.5 \times 32.0 \text{ mm}^2$ on the ϕ -side. Figure 2.7 shows the designed configuration of SVD.

SVD was upgraded to SVD2 in summer 2003 [25]. SVD2 is made of four detector layers, with 6, 12, 18 and 18 ladders, and a radius of 20 mm, 43.5 mm, 70 mm, and 80 mm in each layer, respectively. Two types of DSSD are used for different layers. It also has a larger polar angle coverage ($17^\circ < \theta < 150^\circ$), which is the same as CDC's coverage. The beam pipe is replaced by a smaller (1.5 cm in radius) one. SVD2 successfully improves the vertex resolution and also performs a higher radiation hardness than SVD1. The side view and the end view of SVD1 and SVD2 systems are illustrated and compared in Figure 2.8.

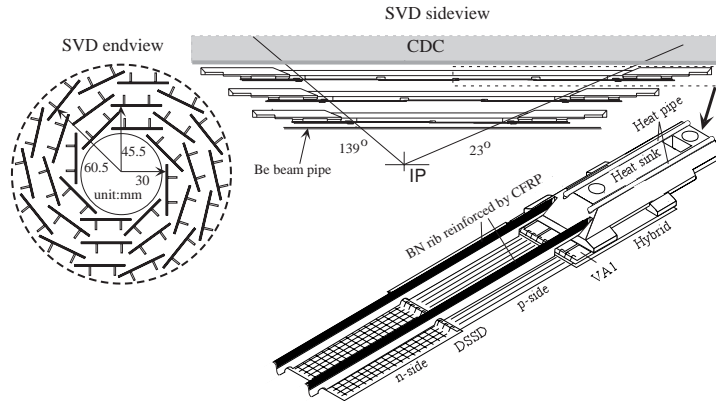


Figure 2.7: Configuration of SVD [23].

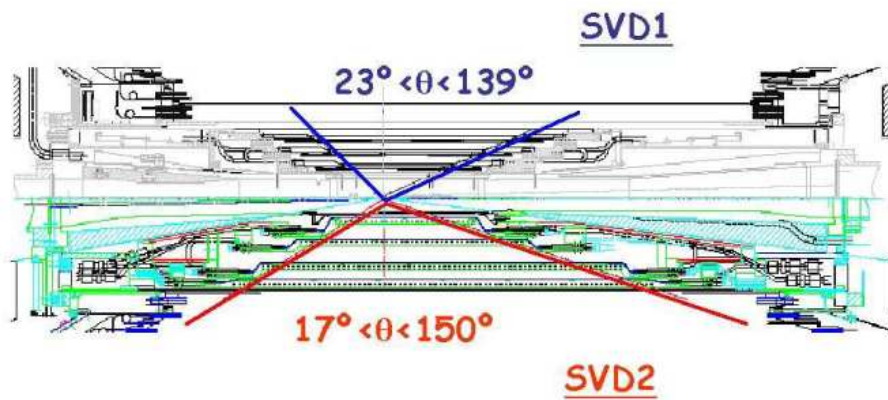
2.2.3 Extreme Forward Calorimeter (EFC)

EFC extends the polar angle coverage of ECL ($17^\circ < \theta < 150^\circ$) to the extreme region, which is useful to improve the experimental sensitivity to some physics processes, e.g. $B \rightarrow \tau\nu$ and two-photon physics. Its polar angle coverage is

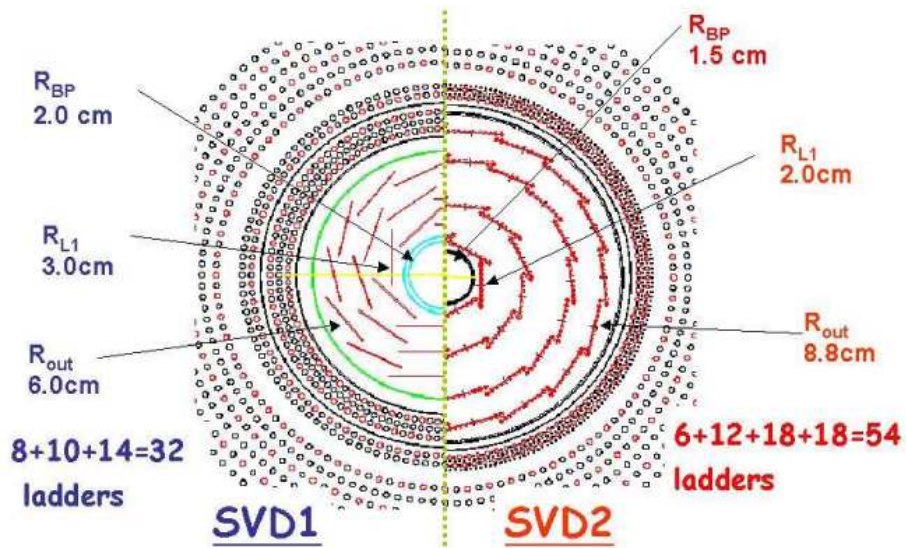


•Larger acceptance

Outermost ladder : $L=22\text{cm} \Rightarrow L=46\text{cm}$



(a) Side view comparison of SVD1 and SVD2.



(b) End view comparison of SVD1 and SVD2.

Figure 2.8: Graphical illustration of sub-detector SVD1 and SVD2 [23].

$6.4^\circ < \theta < 11.5^\circ$ in the forward direction (the e^- direction) and $163.3^\circ < \theta < 171.2^\circ$ in the backward direction (the e^+ direction). EFC is also used as a beam monitor for the KEKB control and a luminosity monitor for the Belle experiment.

Since EFC is placed around the beam pipe near the IP, it is under long-term exposure to high radiation level. The material of EFC is chosen to be radiation-hard BGO (Bismuth Germanate, $\text{Bi}_4\text{Ge}_3\text{O}_{12}$) crystal calorimeter, which can also provide better energy resolution [26]. Figure 2.9 shows an isometric view of the BGO crystals in EFC. EFC is attached to the front faces of the cryostats of the compensation solenoid magnets of the KEKB accelerator, surrounding the beam pipe. EFC is also required to function as a beam mask to reduce backgrounds for CDC. There are in total 320 photodiode readout channels. By the energy sum spectra for Bhabha events, an 8 GeV peak with RMS resolution of 7.3% is seen in the forward EFC, and a 3.5 GeV peak with an RMS resolution of 5.8% is seen for the backward EFC.

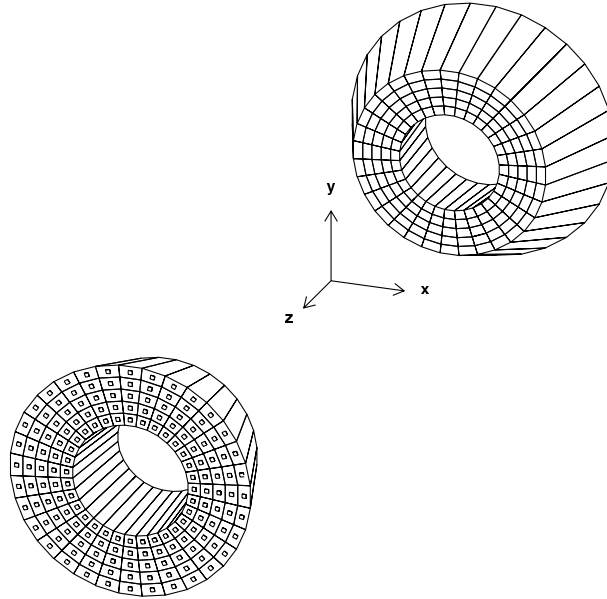


Figure 2.9: Isometric view of the BGO crystals in EFC of the forward and backward parts [23].

2.2.4 Central Drift Chamber (CDC)

CDC is designed to provide information of charged particles, including three dimensional tracking information, momentum measurement, and the energy loss dE/dx . It has a polar angle coverage of $17^\circ < \theta < 150^\circ$. The transverse momentum

(p_T) is obtained by the curvature of the track in transverse plane, and the longitudinal momentum is obtained by the measured p_T and helical information. The precise dE/dx information is also essential for particle identification. The goals of the Belle experiment require a momentum resolution of $\sigma_{p_T}/p_T \sim 0.5\% \sqrt{1 + p_T^2}$ for all charged particles with $p_T \geq 0.1 \text{ GeV}/c$

Figure 2.10 shows the structure of CDC. Its inner radius is 103.5 mm and its outer radius is 874 mm. CDC has 50 cylindrical layers and three cathode strip layers. Each cylindrical layer contains between three and six either axial layers or stereo layers with a small angle. The 50 wire layers are arranged in 12 superlayers (SLs), and each SL contains either axial or stereo layers. There are 8400 drift cells in CDC, and the individual cells are nearly square. Except for the inner three layers, the individual cells have a maximum drift distance between 8 mm and 10 mm and a radial thickness between 15.5 mm and 17 mm. The drift cells in the inner layers are smaller than the cells in other layers and the signals are read out by cathode stripes on the cylinder walls. Figure 2.11 shows the cell arrangement of drift cells and the structure near cathode part.

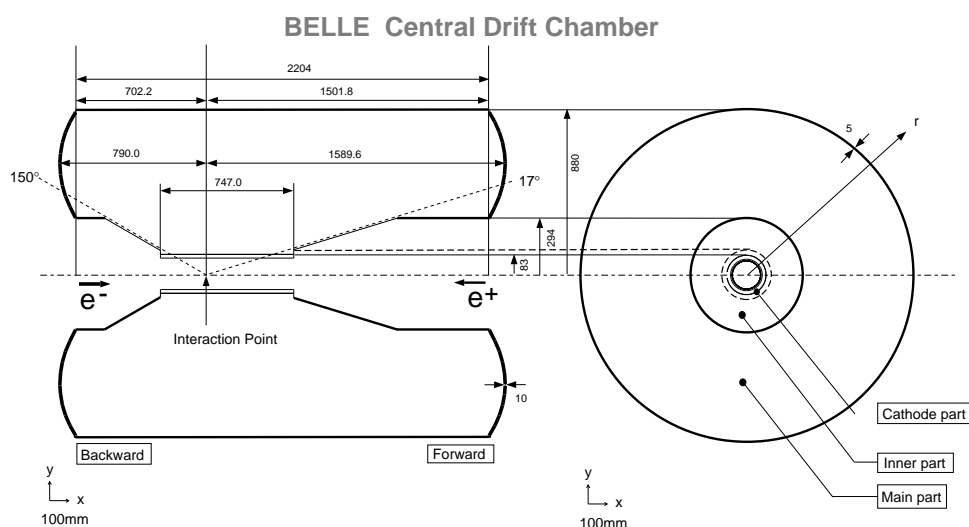


Figure 2.10: Overview of the CDC structure. The lengths in the figure are in units of mm [23].

Since the majority of decay particles from B meson have momenta lower than $1 \text{ GeV}/c$, the minimization of multiple scattering is important to improve the momentum resolution. Hence, the use of low- Z (atomic number) gas is desirable. In addition, the use of ethane can provide good dE/dx resolution. Therefore, we choose a 50% He and 50% C_2H_6 gas mixture with a radiation length of around 640 m and a drift velocity of around $4 \text{ cm}/\mu\text{s}$.

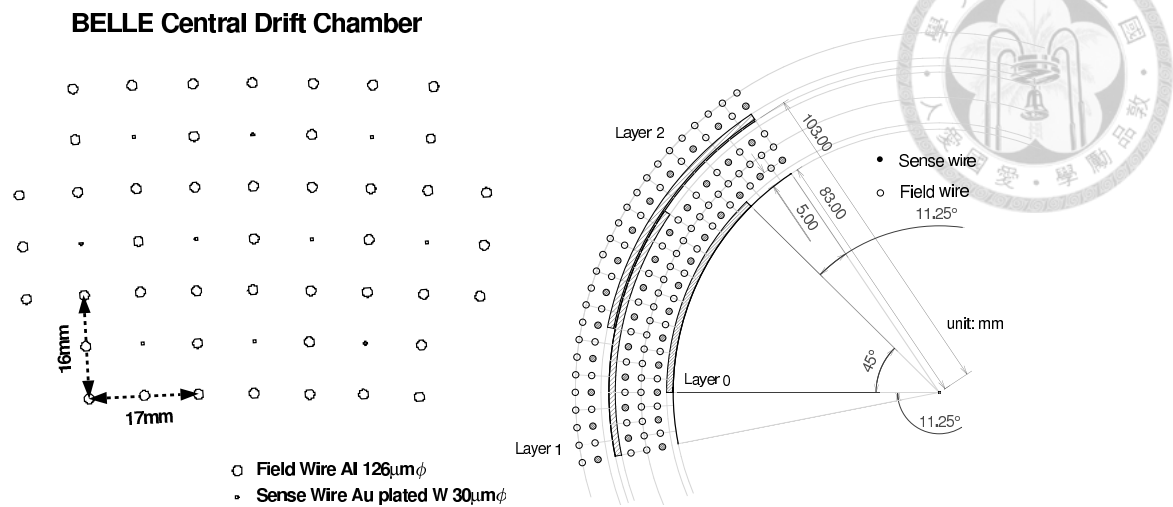


Figure 2.11: Cell structure and the cathode sector configuration of CDC [23].

The truncated-mean method was used to estimate the most probable energy loss. The largest 20% of measured dE/dx values for each track were ignored and the remaining data were averaged in order to minimize occasional large fluctuations in the Landau tail of the dE/dx distribution. The expected truncated-mean is a useful variable for particle identification, especially for the separation of K^\pm and π^\pm in the momentum region below 0.5 GeV/c. Figure 2.12 shows a plot of dE/dx and particle momentum, together with the expected truncated mean. Populations of π , K , p , and e can be clearly seen.

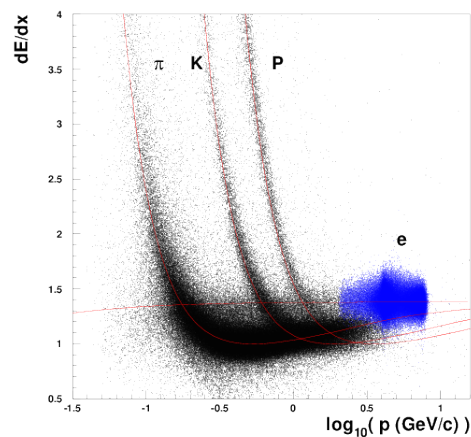


Figure 2.12: Scatter plot for dE/dx versus momentum. Expected results for π , K , p and e are shown by solid curves. The unit of the momentum is GeV/c [23].

2.2.5 Aerogel Čerenkov Counter (ACC)

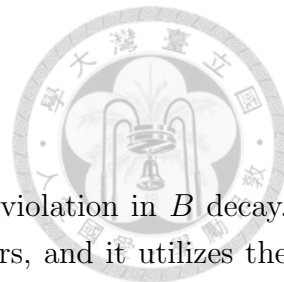
Separation between π^\pm and K^\pm is important for the CP violation in B decay. ACC is an array of silica aerogel threshold Čerenkov counters, and it utilizes the detection of Čerenkov light for particle identification, specifically to distinguish π^\pm from K^\pm in the further momentum coverage ($1.2 \text{ GeV}/c \sim 4.0 \text{ GeV}/c$) which is beyond the reach of dE/dx measurements by CDC and TOF. Čerenkov light is the emitted photons by the charged particles exceeding the speed of light in a medium, and it takes place if the velocity of particle(β) satisfies $n > 1/\beta = \sqrt{1 + (m/p)^2}$.

The configuration of ACC is shown in Figure 2.13. ACC contains two parts, including barrel and end-cap. The barrel part consists of 960 counter modules segmented into 60 cells in the ϕ direction covering $33.3^\circ < \theta < 127.9^\circ$, and the end-cap part consists of 228 modules arranged in five concentric layers for the forward end-cap part of the detector ($13.6^\circ < \theta < 33.4^\circ$). All of the counters are arranged in semi-tower geometry and are pointing to the IP. A typical ACC module comprises five aerogel tiles stacked in a thin aluminum box, which is approximately $12 \times 12 \times 12 \text{ cm}^3$. In order to detect Čerenkov radiation effectively, ACC use fine-mesh photomultipliers (FM-PMT) which are designed to operate in strong magnetic fields of 1.5 T. Two FM-PMTs are installed for the barrel ACC modules and one for the end-cap ACC modules. Two types of the unit modules are shown in Figure 2.14.

The performance of ACC modules has been tested at the π^2 beam line at KEK Proton Synchrotron (PS). In the pulse-height spectra, separation between π^\pm and p^\pm with more than three standard deviations can be clearly seen. By using Bhabha and hadronic events, a clear separation between e^\pm and K^\pm is also observed. Careful calibrations for the pulse height of each FM-PMT signal have been performed with μ -pair events. The light yields for the μ tracks depends on the index of refraction of aerogel radiators, the geometry of each ACC module, and also the size and number of FM-PMTs attached on the modules.

2.2.6 Time of Flight (TOF)

A time-of-flight (TOF) detector system using plastic scintillation counters is very powerful for particle identification in e^+e^- collider detectors. With a typical flight length of 1.2 m and a time resolution of 100 ps, TOF can identify charged particles with momenta below $1.2 \text{ GeV}/c$ effectively, which encompasses 90% of the particles produced in $\Upsilon(4S)$ meson decays. It also provides information for K/p separation,



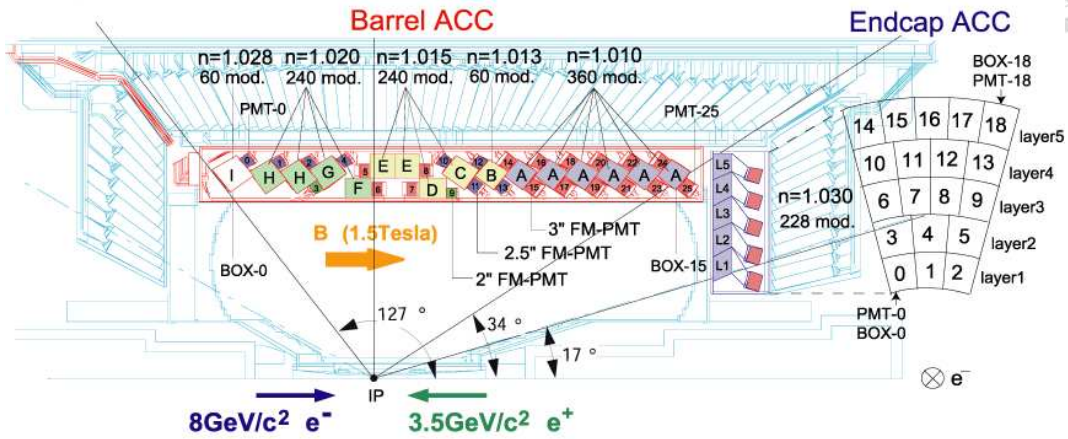


Figure 2.13: Arrangement of ACC at the central part of the Belle detector. The index of refraction(n) is for each ACC module [23].

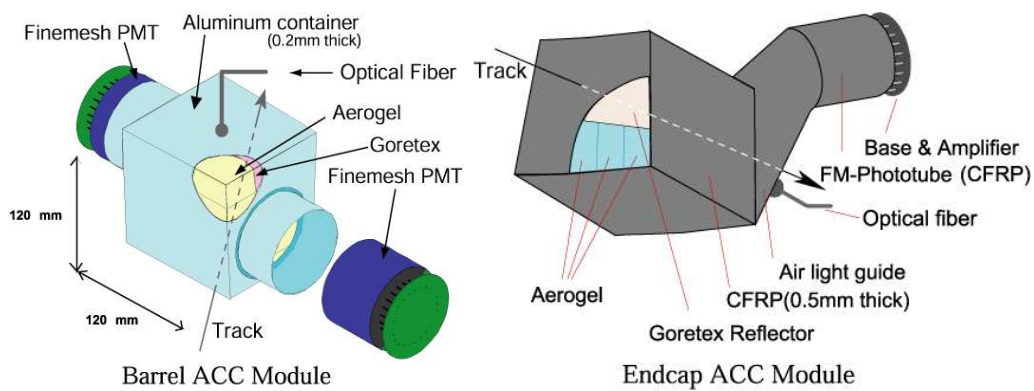


Figure 2.14: Schematic drawing of a typical ACC counter module: (a) barrel and (b) end-cap ACC [23].

which is not covered by the design of ACC system. The TOF counters is also used for the Belle trigger system by the capability of fast timing resolution. In order to keep the fast trigger rate below 70 kHz to avoid pile-up in trigger system, the TOF system is augmented with thin trigger scintillation counters (TSC).

TOF counters and TSCs are made of fast scintillators and FM-PMTs that are directly mounted on the scintillator. The whole TOF system consists of 128 TOF counters and 64 TSCs. A TOF/TSC module contains two trapezoidally shaped TOF counters and one TSC counter, with a 1.5-cm intervening radial gap. Structure of the module is shown in Figure 2.15. In total, 64 TOF/TSC modules are located in the barrel region outside the ACC and have a polar angle coverage of $34^\circ < \theta < 120^\circ$. For a charged particle, its p_T is required to be greater than about $0.28 \text{ GeV}/c$ to reach the TOF counters. Readout of each TOF counter and TSC is done by two FM-PMTs attached at both ends and a single FM-PMT at the backward end, respectively.

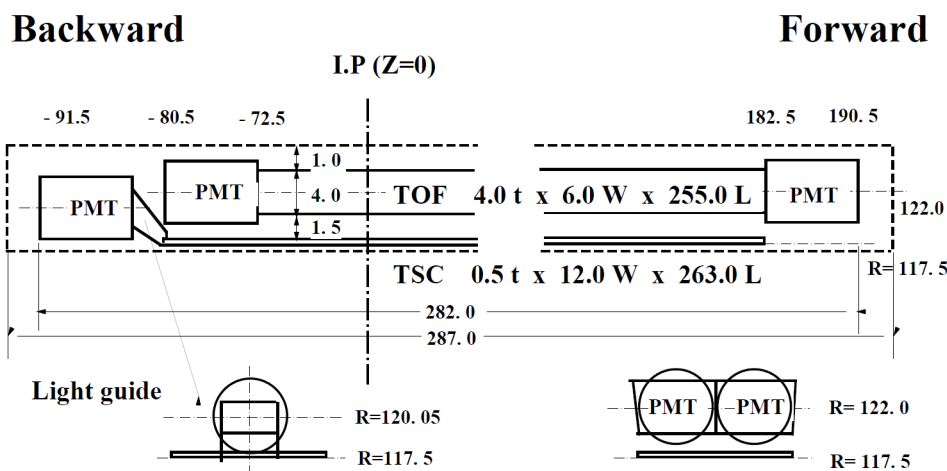


Figure 2.15: Illustration of a TOF/TSC module. The unit of length is in mm [23].

The resolution for the weighted average time is about 100 ps and is with a small z dependence. The mass for each track can be calculated using the equation

$$M^2 = \left(\frac{1}{\beta^2} - 1 \right) P^2 = \left(\frac{cT_{obs}}{L_{path}} - 1 \right) P^2, \quad (2.1)$$

where β is the particle's speed relative to light, T_{obs} is the observed time of flight (the time walk correction on measured PMT signal time), and $P(L_{path})$ is the momentum (path length) of the particle obtained by CDC tracking result assuming the muon mass. Figure 2.15 shows the mass distribution for charged particles with momenta below $1.2 \text{ GeV}/c$, in which clear separations between π^\pm , K^\pm and p^\pm peaks can be

seen.

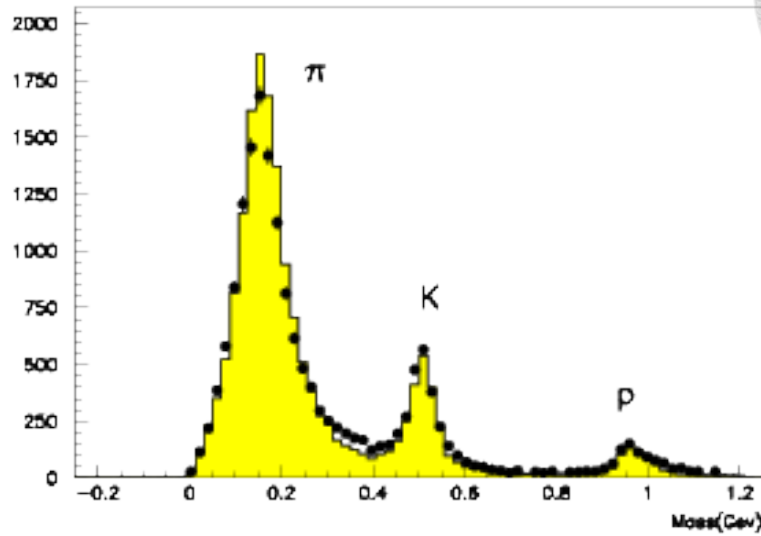


Figure 2.16: Mass distribution from TOF measurements for particle momenta below 1.2 GeV/c [23].

2.2.7 Electromagnetic Calorimeter (ECL)

ECL is an array of CsI(Tl) crystals, and is designed to detect photons from B meson decays with high efficiency and good resolutions in energy and position. Since most of the photons are end-product of decay cascades and are with relatively low momentum, good detection performance with photons below 500 MeV is necessary. Besides, good resolution up to 4 GeV is also essential for some two body decay modes such as $B \rightarrow K^*\gamma$ and $B^0 \rightarrow \pi^0\pi^0$. Electron identification relies on matching between CDC tracking and ECL clustering and the ratio E/P , where E is the energy deposits measured by ECL [27] and p is momentum measured by CDC. High momentum π^0 detection requires the separation of two nearby photons and a precise determination of their opening angle. Therefore, a fine-grained segmentation in ECL is required.

Figure 2.17 represents the overall configuration of ECL. It is composed of 8736 CsI(Tl) crystals with silicon photodiode readout installed inside the coil of solenoid magnet. 6624, 1152, and 960 crystals locate at the barrel, forward end-cap, and backward end-cap region, respectively. Each crystal has a tower-like shape and points toward IP with a small tilt angle ($1.3^\circ \sim 4^\circ$) to avoid photon leakage from the gaps between crystals. The geometrical configuration is summarized in Table 2.3.

The size of crystals also matters. Smaller size can provide better position resolution but also makes energy resolution worse due to the increase of gaps and inactive material between crystals. For the barrel region, a crystal has a typical dimension of $5.5 \times 5.5 \text{ cm}^2$ in the front face and of $6.5 \times 6.5 \text{ cm}^2$ in the rear face, while dimensions of the end-cap crystals have a large variation. The 30 cm length (corresponding to 16.2 radiation lengths) is chosen to avoid deterioration of the energy resolution at high energies due to the fluctuations of shower leakages out the rear of the counter. The small gaps between barrel and end-cap region cause about 3% loss of the total acceptance.

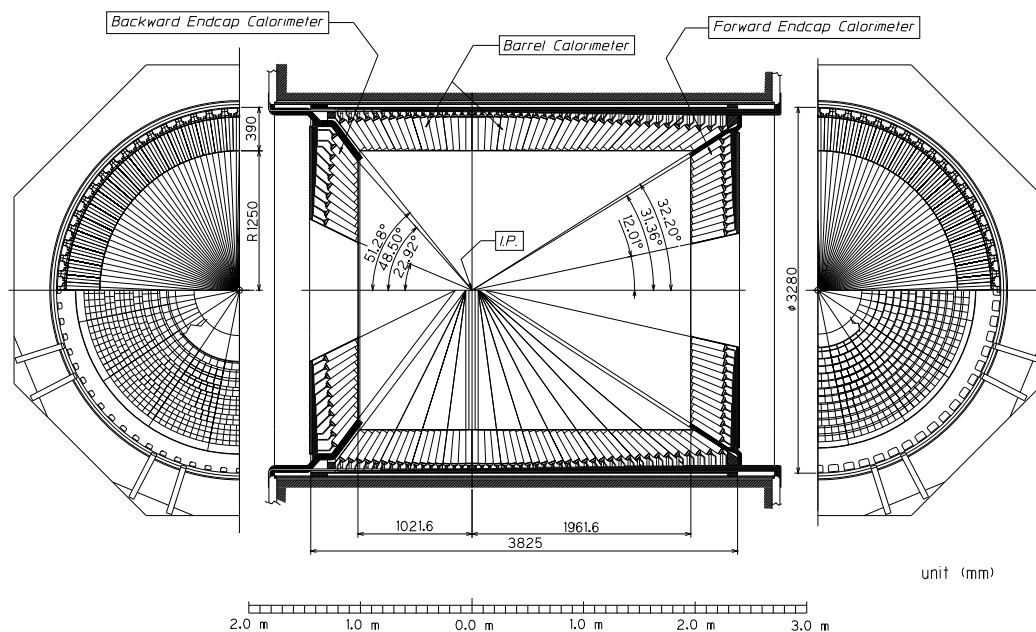


Figure 2.17: Overall configuration of ECL [23].

Item	θ coverage	θ seg.	ϕ seg.	No. of crystals
Forward end-cap	$12.4^\circ - 31.4^\circ$	13	48–144	1152
Barrel	$32.2^\circ - 128.7^\circ$	46	144	6624
Backward end-cap	$130.7^\circ - 155.1^\circ$	10	64–144	960

Table 2.3: Geometrical parameters of ECL [23].

After KEKB was commissioned in June 1999, the calibration on each counter is performed by a large amount of two photon and Bhabha events. The energy resolution reached 1.7%, 1.74% and 2.85% for the barrel ECL, forward ECL and backward ECL, respectively. For the first three years operation, mass resolutions of

the $\pi^0 \rightarrow \gamma\gamma$ and $\eta \rightarrow \gamma\gamma$ reconstruction were measured to be 4.8 and 12.1 MeV/c², respectively [28].



2.2.8 K_L and Muon Detection System (KLM)

The main purpose of the KLM detection system is high efficiency identification of K_L and muons [29] with momenta greater than 600 MeV/c. KLM has a polar angle coverage of $45^\circ \sim 125^\circ$ in barrel-shaped region around IP, and the forward and backward end-caps extend to range to $20^\circ \sim 155^\circ$. It consists of 15 (14) layers of glass-electrode-resistive plate counter (RPC) and 14 (14) layers of 4.7 cm-thick iron plates arranged alternatively in the octagonal barrel (forward and backward end-cap) region. The iron plates provide 3.9 cm interaction lengths of material. The schematic diagrams of two types of RPC modules in KLM are shown in Figure 2.18.

Each RPC module contains two parallel plate electrodes which provide high bulk resistivity ($\geq 10^{10}\Omega \cdot \text{cm}$) and are separated by a gas-filled gap. The interaction of hadrons with the iron plates and ECL would produce a shower of ionizing particles, which would fly through the RPC modules and induce streamers in the gas-filled gaps. The streamers result in a local discharges of the plates and induce signals on external pickup strips. The location of the showers provide the K_L momentum direction, while KLM doesn't have the capability of K_L energy measurement. The KLM hit associated charged tracks which is extrapolated from CDC tracks, will be identified as muons.

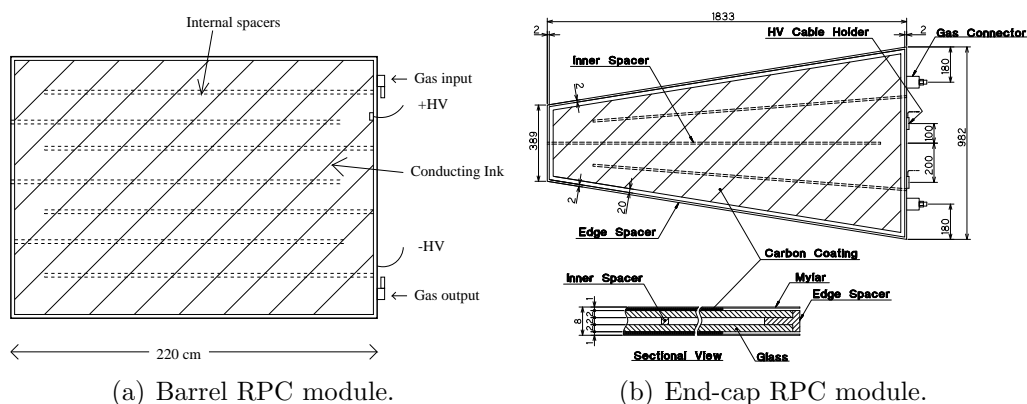


Figure 2.18: Schematic diagrams of the internal spacer arrangement of RPC [23].



Chapter 3

Search for $D^0 \rightarrow \nu\bar{\nu}$ Decay at Belle

3.1 Motivation

In the Standard Model (SM), heavy meson (D or B mesons) decay to $\nu\bar{\nu}$ is helicity suppressed [30] with an expectation of branching fraction of $\mathcal{B}(D^0 \rightarrow \nu\bar{\nu}) = 1.1 \times 10^{-30}^\dagger$, which is beyond reach of the current collider experiments. The SM decay diagrams of $D^0 \rightarrow \nu\bar{\nu}$ are shown in Figure 3.1. However, Ref. [30] estimates the production rates of D and B mesons to dark matter (DM) particles such as two-body decay, radiative decay, and with an additional light meson in the final states. Under different DM models, e.g. scalar DM, v quark of the hidden valley model [31], right-handed neutrino [32], or majorana fermion, the branching fraction of D^0 to invisible final states could be enhanced to $O(10^{-15})$.

The recent DM searches are mainly based on the direct detection of the nuclear recoil signal due to DM interaction, or γ ray production and $e^+e^-/p\bar{p}$ production due to the DM annihilation process. At the e^+e^- flavor factory, an indirect detection of DM candidates can be exploited, where two heavy flavor particles should be produced in the flavor-conjugate states. One of the D (B) can be tagged to produce a cleaner event sample and utilize the recoil information to search for the D (B) decay to invisible signal. There are large amount of $e^+e^- \rightarrow c\bar{c}$ continuum events, in which plenty of D mesons would be produced at the B factories. We use the charm tagger method to select an inclusive D^0 sample which allows to identify D^0 decays involving invisible particles. The similar method is used previously by Belle [33, 34, 35] and BaBar [36] to measure semileptonic and leptonic $D_{(s)}$ decays.

[†]Throughout this thesis, inclusion of charge-conjugate decay modes is always implied.

The process, $e^+e^- \rightarrow c\bar{c} \rightarrow D_{tag}^{(*)} X_{frag} \bar{D}_{sig}^{*-}$ with $\bar{D}_{sig}^{*-} \rightarrow \bar{D}_{sig}^0 \pi_s^-$ is fully reconstructed except for \bar{D}_{sig}^0 . Here, D_{tag} represents a charmed particle in tag-side: D^0 , D^+ , D_s^+ , and Λ_c^+ . Since the center-of-mass (c.m.) energy of KEKB is above the open charm threshold, the fragmentation system (X_{frag}) with a few light unflavored mesons would also be produced. Hence, this search for D^0 (B^0) \rightarrow invisible decay with flavor tagging methods at B factories provide an alternative way for DM search. Any clear signal would be an indication for new physics. Measurements on B^0 decays into invisible final state with hadronic and semileptonic B tagging were performed by Belle and BaBar, respectively [37, 38].

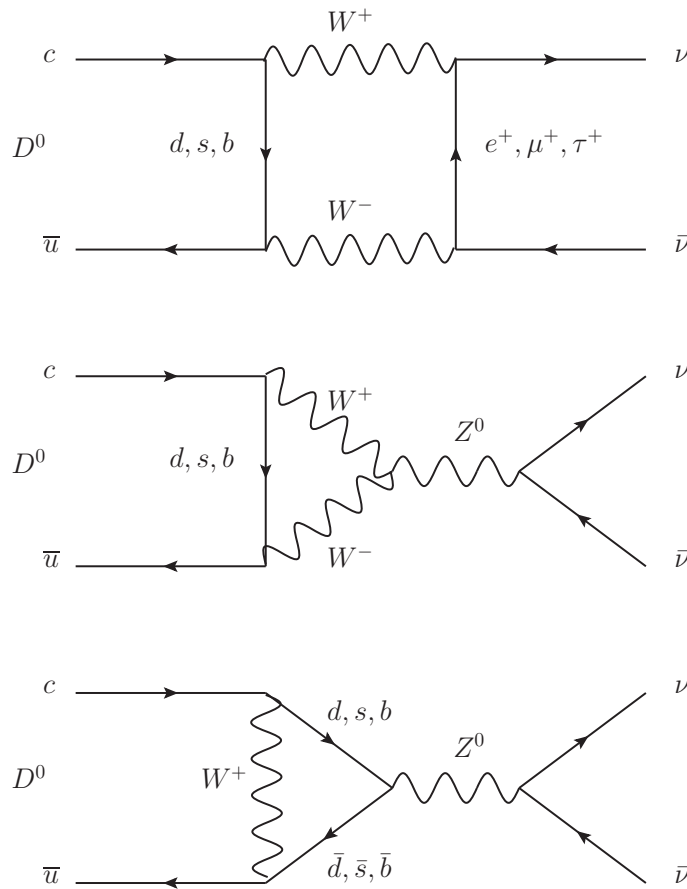
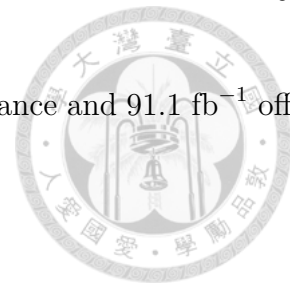


Figure 3.1: The decay diagrams of $D^0 \rightarrow \nu\bar{\nu}$.

3.2 Data Sample

This analysis is based on the data collected by the Belle detector at the KEKB asymmetric-energy e^+e^- collider at or near the $\Upsilon(4S)$ and $\Upsilon(5S)$ resonance, includ-

ing $711.0 \text{ fb}^{-1} \Upsilon(4S)$ on resonance, $121.4 \text{ fb}^{-1} \Upsilon(5S)$ on resonance and 91.1 fb^{-1} off resonance data sample.



3.2.1 Blind Analysis and Monte Carlo Samples

We study signal and backgrounds depending on a blind study with Monte Carlo (MC) simulation method. For the signal decays study, signal MC sample with $D^{*+} \rightarrow D^0 \pi^+$ with $D^0 \rightarrow \nu \bar{\nu}$ from $e^+ e^- \rightarrow c \bar{c}$ are generated with EvtGen [39] package and detector simulation is done with GEANT [40] package. The generic $c \bar{c}$ MC ($e^+ e^- \rightarrow c \bar{c}$) is essential for developing the charm tagger for inclusive D^0 study. Besides, the other continuum uds MC ($e^+ e^- \rightarrow q \bar{q}$, $q = u, d, s$), the generic $B \bar{B}$ ($e^+ e^- \rightarrow \Upsilon(4S) \rightarrow B \bar{B}$) MC, $B_s \bar{B}_s$ MC ($e^+ e^- \rightarrow \Upsilon(5S) \rightarrow$ final states with $B_s \bar{B}_s$) and non- $B_s \bar{B}_s$ MC ($e^+ e^- \rightarrow \Upsilon(5S) \rightarrow$ final states without $B_s \bar{B}_s$) are also considered for background study.

All of these MC and data are based on the new tracking algorithm, i.e., case B data in Belle environment setting.

3.3 Charm Tagger Method

3.3.1 Overview

The reconstruction method is based on a previous study by the Belle collaboration in leptonic D_s decay [35]. To obtain the inclusive D^0 sample with Belle data for absolute branching fraction measurement, the process followed by $e^+ e^- \rightarrow c \bar{c}$ which we are going to reconstruct is

$$e^+ e^- \rightarrow c \bar{c} \rightarrow D_{tag}^{(*)} X_{frag} \bar{D}_{sig}^{*-}, \bar{D}_{sig}^{*-} \rightarrow \bar{D}_{sig}^0 \pi_s^- . \quad (3.1)$$

Through this process, one of the c quark hadronizes into $D_{tag}^{(*)}$, which is going to be reconstructed as tag side. $D_{tag}^{(*)}$ includes four types of ground state D_{tag} (D^0 , D^+ , Λ_c^+ , and D_s^+) and three types of excited state D_{tag}^* (D^{*0} , D^{*+} , and D_s^{*+}). Since the beam energy is above the open charm threshold, for the $e^+ e^- \rightarrow c \bar{c}$ production, besides two hadrons with $c(\bar{c})$ flavor would be generated from the two jets with c and \bar{c} , a

few light unflavored mesons would also be generated from fragmentation, and they are denoted as X_{frag} . X_{frag} consists of any number of pions or γ , and even number of Kaons. The information of recoil \bar{D}_{sig}^{*-} is obtained by the missing momentum against the reconstructed $D_{tag}^{(*)}$ and X_{frag} . We use the inverse mass constrained fit to improve the resolution of recoil \bar{D}_{sig}^{*-} momentum. With tagging on an extra slow charged pion (π_s^-) decayed from recoil \bar{D}_{sig}^{*-} , we thus obtain the information of inclusive D^0 (\bar{D}_{sig}^0). The yield of inclusive D^0 is obtained by the fit on missing mass distribution recoiling against $D_{tag}^{(*)}$, X_{frag} , and π_s^- .

Measurement of absolute branching fraction of D^0 to an exclusive final state f is determined by this formula:

$$\mathcal{B} = \frac{N_{excl.}(D^0 \rightarrow f)}{N_{incl.}^{D^0} \cdot \epsilon(D^0 \rightarrow f|incl.D^0) \cdot C}, \quad (3.2)$$

where $N_{incl.}^{D^0}$ represents the total number of inclusive D^0 reconstructed by the charm tagger, $N_{excl.}(D^0 \rightarrow f)$ is the signal yield of exclusive $D^0 \rightarrow f$ decay, and the $\epsilon(D^0 \rightarrow f|incl.D^0)$ is the signal side selection efficiency of $D^0 \rightarrow f$ decay within an inclusive D^0 sample. The $\epsilon(D^0 \rightarrow f|incl.D^0)$ is calibrated by C due to different kinds of signal side selection. Basically, the most critical signal side selection is constraint on the remaining detector information which is only associated with \bar{D}_{sig}^0 . For instance, we will require there is no remaining detector information at signal side for $D^0 \rightarrow \nu\bar{\nu}$ study.

3.3.2 D_{tag} Reconstruction

The first step is to reconstruct the ground state D_{tag} . Four types of D_{tag} and 23 decay channels are considered and listed in Table 3.1.

Selection criterion of final state particles

- Impact parameter of charged tracks:
 - $|dr| < 0.5$ cm and $|dz| < 1.5$ cm. dr and dz are the deviations of a track from the IP position in the transverse (x-y) plane and in the z direction, respectively. where the z axis is opposite the position beam direction.
- Charged hadrons (π^+ , K^+ , and p):

D^0 decay	$\mathcal{B}(\%)$	D^+ decay	$\mathcal{B}(\%)$	Λ_c^+ decay	$\mathcal{B}(\%)$	D_s^+ decay	$\mathcal{B}(\%)$
$K^-\pi^+$	3.9	$K^-\pi^+\pi^+$	9.4	$pK^-\pi^+$	5.0	$K^+K^-\pi^+$	5.5
$K^-\pi^+\pi^0$	13.9	$K^-\pi^+\pi^+\pi^0$	6.1	$pK^-\pi^+\pi^0$	3.4	$K_S^0K^+$	1.5
$K^-\pi^+\pi^+\pi^-$	8.1	$K_S^0\pi^+$	1.5	pK_S^0	1.1	$K_S^0K_S^0\pi^+$	5.4
$K^-\pi^+\pi^+\pi^-\pi^0$	4.2	$K_S^0\pi^+\pi^0$	6.9	$\Lambda\pi^+$	1.1	$K^+K^-\pi^+\pi^0$	5.6
$K_S^0\pi^+\pi^-$	2.9	$K_S^0\pi^+\pi^+\pi^-$	3.1	$\Lambda\pi^+\pi^0$	3.6	$K_S^0K^+\pi^+\pi^+$	7.2
$K_S^0\pi^+\pi^-\pi^0$	5.4	$K^+K^-\pi^+$	1.0	$\Lambda\pi^+\pi^+\pi^-$	2.6		
Sum	38.4	Sum	28.0	Sum	16.8	Sum	25.2

Table 3.1: List of D_{tag} decay modes included in the charm tagger and the corresponding branching fraction.

- Charged hadron identification for this study is done with constraints on the likelihood values L_p , L_K , L_π , L_e , and L_μ , which are determined from the information provided by the hadron identification system.
- π^+ : $L_K/(L_K + L_\pi) < 0.9$
- K^+ : $L_K/(L_K + L_\pi) > 0.1$
- p : $L_K/(L_K + L_p) < 0.9$ and $L_\pi/(L_\pi + L_p) < 0.9$
- π^0 :
 - Obtained by Mdst_pi0 bank
 - $E_\gamma > 50$ MeV
 - $0.115 < M_{\gamma\gamma} < 0.150$ GeV/ c^2
 - Mass constrained fit is performed
- π^0 (strong):
 - We use the π^0 which passes this stronger selection criterion to reconstruct D_{tag} decay modes with complicated final state, as listed in Table 3.2.
 - Obtained by Mdst_pi0 bank
 - In addition to the criteria for π^0 listed above, we require $E_\gamma > 50$ MeV for barrel region and $E_\gamma > 100$ MeV for endcap region (Table 3.2). The π^0 mass distribution demonstration plots with the two selection criteria are shown in Figure 3.2.
- $K_S^0 \rightarrow \pi^+\pi^-$:
 - From Mdst_Vee2 bank
 - Loose goodKs selection [41]



- $0.468 < M_{\pi^+\pi^-} < 0.508 \text{ GeV}/c^2$
- Vertex fit is performed and the fit converges
- $\Lambda \rightarrow p\pi^+$ ($\bar{\Lambda} \rightarrow \bar{p}\pi^-$):
 - From Mdst_Vee2 bank [41]
 - $fl_{xy} > 0.1 \text{ cm}$, where fl_{xy} is the flight length in transverse plane.
 - $\cos(\Delta\theta) > 0.99$, where $\Delta\theta$ is the azimuthal angle between the momentum vector and the decay vertex vector.
 - $1.111 < M_{p\pi} < 1.121 \text{ GeV}/c^2$
 - Vertex fit is performed and the fit converges ($\chi^2 < 100$)

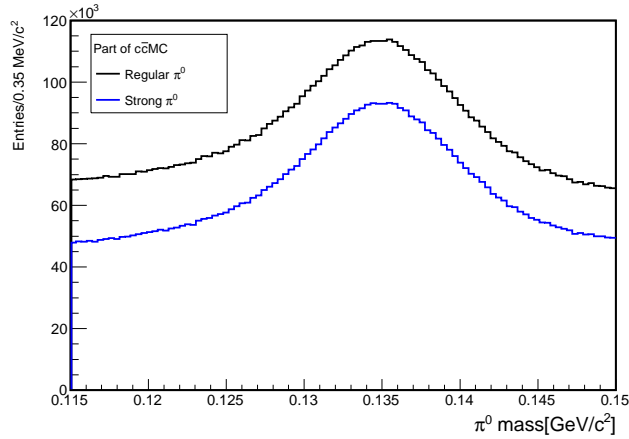
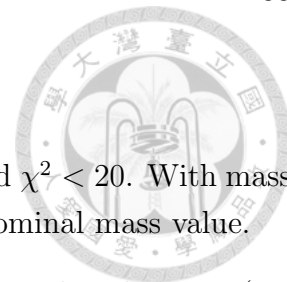


Figure 3.2: π^0 mass demonstration plot with direct π^0 reconstruction.

Selection criterion for D_{tag} candidate

- D_{tag} momentum in center of mass (CM) frame (p^*):
 - Besides from the $e^+e^+ \rightarrow c\bar{c}$ process, D_{tag} may also be decayed from B in Belle data. We require that p^* is greater than $2.3 \sim 2.5 \text{ GeV}/c$ to eliminate D_{tag} candidates from B decay and also reduce the combinatoric background. p^* selection of each mode is listed in Table 3.2. The p^* distribution demonstration plots for some cases are shown in Figure 3.3.
- Mass window:
 - In order to retain most of signal in the peaking structure of invariant mass distribution, selection on mass window is loose and is around 3σ or larger.



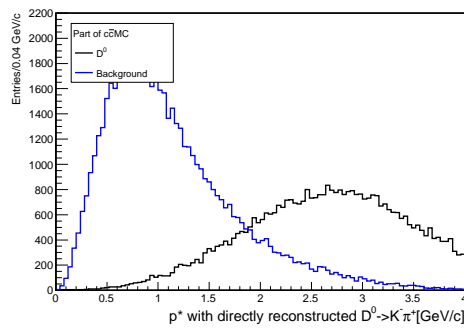
- Vertex fit and mass constrained fit:
 - The outcome of vertex fit is required to converge and $\chi^2 < 20$. With mass constrained fit, the invariant mass is fitted to its nominal mass value.
- In this stage, we keep all candidates which pass the selection listed above. (No best candidate selection is done.)

D^0 decay	p^* (GeV/c)	π^0 selection
$K^-\pi^+$	> 2.3	
$K^-\pi^+\pi^0$	> 2.5	regular π^0
$K^-\pi^-\pi^+\pi^+$	> 2.3	
$K^-\pi^-\pi^+\pi^+\pi^0$	> 2.5	strong π^0
$K_S^0\pi^+\pi^-$	> 2.3	
$K_S^0\pi^+\pi^-\pi^0$	> 2.5	strong π^0
<hr/>		
D^+ decay		
$K^-\pi^+\pi^+$	> 2.3	
$K^-\pi^+\pi^+\pi^0$	> 2.5	strong π^0
$K_S^0\pi^+$	> 2.3	
$K_S^0\pi^+\pi^0$	> 2.4	regular π^0
$K_S^0\pi^+\pi^+\pi^-$	> 2.4	
$K^+K^-\pi^+$	> 2.3	
<hr/>		
Λ_c^+ decay		
$pK^-\pi^+$	> 2.3	
$pK^-\pi^+\pi^0$	> 2.5	strong π^0
pK_S^0	> 2.3	
$\Lambda\pi^+$	> 2.3	
$\Lambda\pi^+\pi^0$	> 2.5	strong π^0
$\Lambda\pi^+\pi^+\pi^-$	> 2.3	
<hr/>		
D_s^+ decay		
$K^+K^-\pi^+$	> 2.3	
$K_S^0K^+$	> 2.3	
$K_S^0K_S^0\pi^+$	> 2.3	regular π^0
$K^+K^-\pi^+\pi^0$	> 2.5	strong π^0
$K_S^0K^-\pi^+\pi^+$	> 2.4	

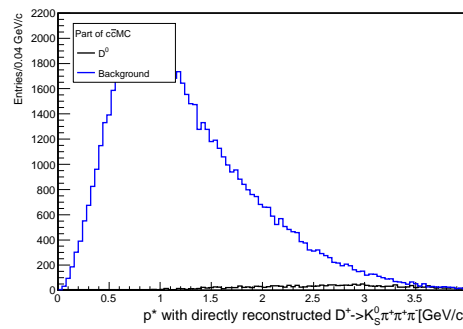
Table 3.2: p^* and π^0 selection for D_{tag} .

3.3.3 D_{tag}^* Reconstruction

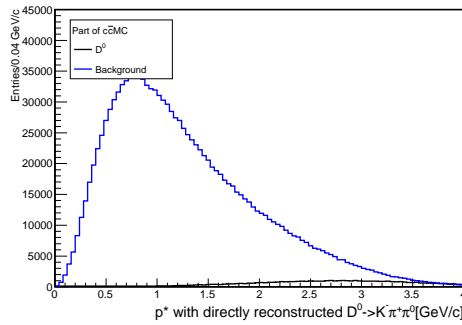
With reconstructed ground state D_{tag} candidates, we then further reconstruct the excited state D_{tag}^* with remaining particles. Three types of D_{tag} and five decay



(a) $D^0 \rightarrow K^- \pi^+$ (selection: $p^* > 2.3$ GeV/c).

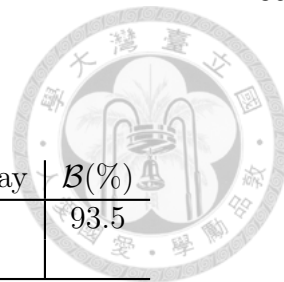


(b) $D^+ \rightarrow K_S^0 \pi^+ \pi^+ \pi^-$ (selection: $p^* > 2.4$ GeV/c).



(c) $D^0 \rightarrow K^- \pi^+ \pi^0$ (selection: $p^* > 2.5$ GeV/c).

Figure 3.3: p^* demonstration plots with direct D_{tag} reconstruction for some cases.



channels are considered and listed in Table 3.3.

D^{*+} decay	$\mathcal{B}(\%)$	D^{*0} decay	$\mathcal{B}(\%)$	D_s^{*+} decay	$\mathcal{B}(\%)$
$D^0\pi^+$	67.7	$D^0\pi^0$	61.9	$D_s^+\gamma$	93.5
$D^+\pi^0$	30.7	$D^0\gamma$	38.1		
Sum	98.4	Sum	100.0	Sum	93.5

Table 3.3: List of D_{tag}^{*+} decay modes included in the charm tagger and the corresponding branching fraction.

Selection criterion of final state particles

- π^+ and π^0 :
 - Same as the one used in D_{tag} . For π^0 , it follows the regular π^0 selection.
- γ :
 - Obtained by Mdst_Gamma bank
 - $E_\gamma > 0.12$ GeV
 - π^0 veto: For a γ , we combine it with other γ . If the two γ have invariant mass close to nominal π^0 mass within 0.01 GeV and the energy asymmetry ($|\frac{E_{\gamma 1} - E_{\gamma 2}}{E_{\gamma 1} + E_{\gamma 2}}|$) is less than 0.5, the γ will be vetoed.

Selection criterion for D_{tag}^* candidate

- Mass window and $\Delta M(M_{D_{tag}^*} - M_{D_{tag}})$:
 - Loose selection on mass window and ΔM to retain most of signal as listed in Table 3.4.
- Vertex fit:
 - The π^+ which is not decayed from D_{tag} but directly from D_{tag}^* will be refitted to the fitted D_{tag} vertex, and the fit is required to converge. π^0 's mass constrained fit information is used to adjust D_{tag}^* 's momentum.
- In this stage, no best candidate selection is done.

D_{tag}^* modes	Mass (GeV/ c^2)	ΔM (GeV/ c^2)
$D^{*+} \rightarrow D^0\pi^+$	1.975~2.045	0.144~0.147
$D^{*0} \rightarrow D^0\pi^0$	1.97~2.045	0.1375~0.1465
$D^{*0} \rightarrow D^0\gamma$	1.96~2.05	0.125~0.159
$D^{*+} \rightarrow D^+\pi^0$	1.97~2.045	0.1375~0.1465
$D_s^{*+} \rightarrow D_s^+\gamma$	2.07~2.15	0.125~0.17

Table 3.4: Mass window and ΔM selection of D_{tag}^* .

3.3.4 X_{frag} Reconstruction

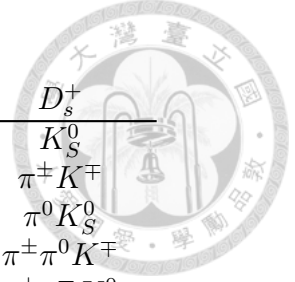
X_{frag} would be reconstructed with remaining π^+ , p , K^+ , K_S^0 and π^0 after $D_{tag}^{(*)}$ is reconstructed. Basically, the cases we consider are with up to three π and up to one π^0 . If D_{tag} is D^0 or D^+ , cases with K^+K^- is also considered in order to increase statistics. If D_{tag} is Λ_c^+ , a \bar{p} would be considered in X_{frag} for baryonic number conservation. If D_{tag} is D_s^+ , a Kaon would be considered in X_{frag} for s flavor conservation. Total charges of $D_{tag}^{(*)}$ and X_{frag} are required to be ± 1 . All the X_{frag} cases considered are listed in Table 3.5.

Selection criterion for X_{frag} candidate

- π^+ , p , π^0 and K_S^0 :
 - Same as the one used in D_{tag}
 - Additional requirement: $p > 0.1$ GeV/ c
- K^+ :
 - $p > 0.1$ GeV/ c
 - $L_K/(L_K + L_\pi) > 0.6$, $L_K/(L_K + L_p) > 0.1$ and $L_e < 0.99$
- In this stage, no best candidate selection is done.

3.3.5 Recoil Spectrum $\bar{D}_{sig}^{*-} \rightarrow \bar{D}_{sig}^0\pi_s^-$ (Inclusive D^0 Sample)

The momentum of recoil \bar{D}_{sig}^{*-} is obtained by the missing momentum against all combinations of reconstructed $D_{tag}^{(*)}$ and X_{frag} . With an additional π_s^- (with same



$D_{tag}^{(*)}$	D^0, D^+, D^{*0}, D^{*+}	Λ_c^+	D_s^+
X_{frag}	nothing	K^+K^-	K_S^0
	π^\pm	$\pi^\pm K^+K^-$	$\pi^\pm K^\mp$
	π^0	$\pi^0 K^+K^-$	$\pi^0 K_S^0$
	$\pi^\pm \pi^0$	$\pi^\pm \pi^0 K^+K^-$	$\pi^\pm \pi^0 K^\mp$
	$\pi^\pm \pi^\mp$	$\pi^\pm \pi^\mp K^+K^-$	$\pi^\pm \pi^\mp K_S^0$
	$\pi^\pm \pi^\pm \pi^\mp$	$\pi^\pm \pi^\pm \pi^\mp K^+K^-$	$\pi^\pm \pi^\pm \pi^\mp K^\mp$
	$\pi^\pm \pi^\mp \pi^0$	$\pi^\pm \pi^\mp \pi^0 K^+K^-$	$\pi^\pm \pi^\mp \pi^0 K_S^0$

Table 3.5: List of X_{frag} cases with corresponding $D_{tag}^{(*)}$.

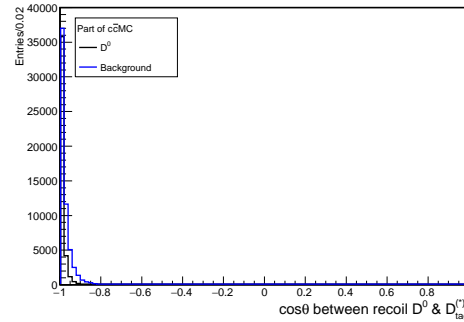
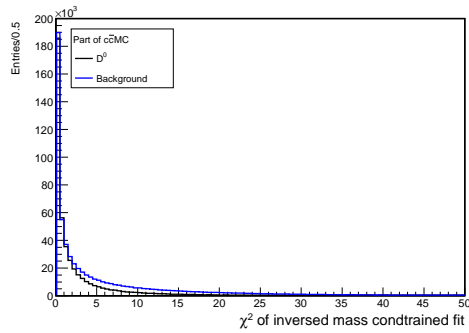
selection as the π^- in D_{tag}), we can obtain the information of recoil \bar{D}_{sig}^0 :

$$p_{\bar{D}_{sig}^{*-}}^{recoil} = p_{miss}(D_{tag}^{(*)}X_{frag}) \quad (3.3)$$

$$p_{\bar{D}_{sig}^0}^{recoil} = p_{miss}(D_{tag}^{(*)}X_{frag}\pi_s^-) \quad (3.4)$$

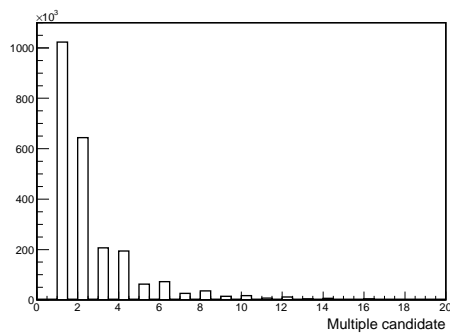
Selection criterion for the recoil spectrum $\bar{D}_{sig}^{*-} \rightarrow \bar{D}_{sig}^0 \pi_s^-$

- $1.86 \text{ GeV}/c^2 < M_{miss}(D_{tag}^{(*)}X_{frag}) < 2.16 \text{ GeV}/c^2$
- Momentum magnitude in C.M. frame: $p_{miss}^*(D_{tag}^{(*)}X_{frag}\pi_s^-) > 2.0 \text{ GeV}/c$
- In order to improve the resolution of $M_{miss}(D_{tag}^{(*)}X_{frag}\pi_s^-)$, inverse mass constrained fit is performed on the missing component against $D_{tag}^{(*)}X_{frag}$ with a condition: $M_{miss}(D_{tag}^{(*)}X_{frag}) = m_{D^{*-}}$ (nominal D^{*-} mass).
- Best candidate candidate selection:
 - The events have more than one \bar{D}_{sig}^{*-} candidates: Use the χ^2 from inverse mass constrained fit on the missing component against $D_{tag}^{(*)}X_{frag}$, whose distribution is shown in Figure 3.4(a). Choose the one with smaller χ^2 as the best \bar{D}_{sig}^{*-} .
 - The events have more than one \bar{D}_{sig}^0 candidates: Use the angle between \bar{D}_{sig}^0 and $D_{tag}^{(*)}$ in C.M. frame, whose distribution is shown in Figure 3.4(b). Choose the one with angle closer to 180° as the best \bar{D}_{sig}^0 .
 - For $c\bar{c}$ MC, the average multiplicity is about 2.72 and about 80.2% of true candidates can be selected. For data, the average multiplicity is about 2.68. The multiple candidate number distributions are shown in Figure 3.5

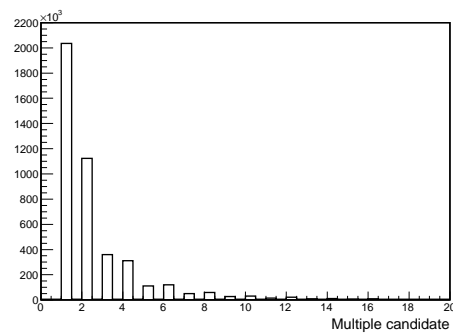


(a) χ^2 from inverse mass constrained fit on the missing component against $D_{tag}^{(*)} X_{frag}$. (b) Angle between recoil \bar{D}_{sig}^0 and $D_{tag}^{(*)}$.

Figure 3.4: The variables used in best candidate selection.

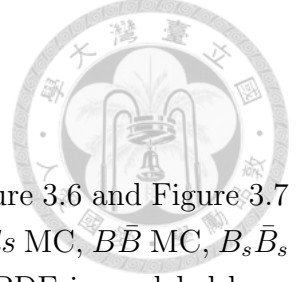


(a) $c\bar{c}MC$.



(b) data.

Figure 3.5: Multiple candidates number distribution.



Result on inclusive D^0

The charm tagger results on inclusive D^0 are shown in Figure 3.6 and Figure 3.7 for six times data size of generic MC (combination of $c\bar{c}$ MC, uds MC, $B\bar{B}$ MC, $B_s\bar{B}_s$ MC, and non- $B_s\bar{B}_s$ MC) and data, respectively. Signal D^0 PDF is modeled by a Breit-Wigner distribution, and it is with an additional Gaussian when fitting on six times data size of generic MC. Background PDF is modeled by a ARGUS distribution [42]. All shape parameters and numbers are floated. For the six times data size of MC result, the D^0 yield is $3294590^{+3016.33}_{-4219.81}$. For the data result including $\Upsilon(4S)$ on resonance, $\Upsilon(5S)$ on resonance, and off resonance, the D^0 yield is $694505^{+1029.99}_{-1472.24}$. The inclusive D^0 results under different $D_{tag}^{(*)}$ modes and X_{frag} modes, including D^0 yield and background yield, are listed in Appendix B.

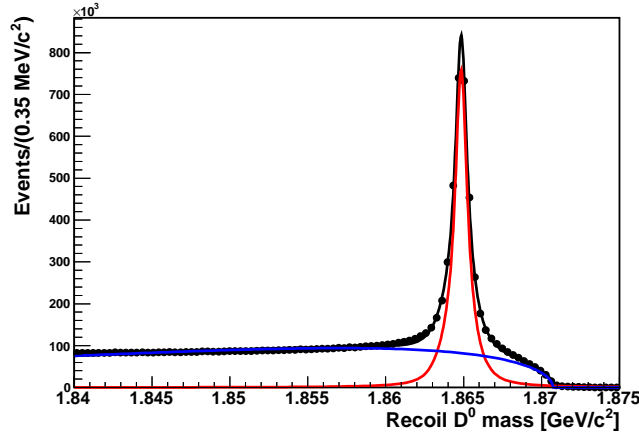


Figure 3.6: Inclusive D^0 fit result on six times data size generic MC.

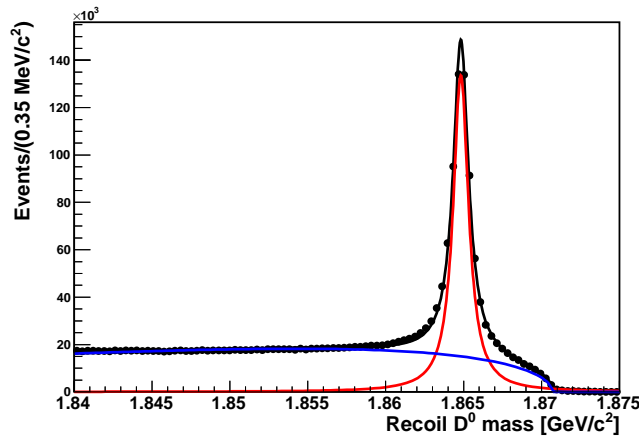


Figure 3.7: Inclusive D^0 fit result on data.



3.4 MC Study and Signal Extraction

3.4.1 Selection Criterion

$D^0 \rightarrow \nu\bar{\nu}$ is namely D^0 decay without visible final states. Therefore, the most critical selection criteria are constraints on remaining detector information at the signal side. E_{ECL} is the energy of remaining ECL clusters which are only associated with \bar{D}_{sig}^0 , which is also a useful variable for B/D meson decay with missing final state, e.g. neutrino.

- No remaining tracks, π^0 , K_S^0 , K_L^0 , and Λ ($\bar{\Lambda}$) at the signal side (only associated with \bar{D}_{sig}^0) after reconstruction of the charm tagger.
- $E_{ECL} < 2.1$ GeV (fitting region)
- Recoil $M_{D^0} > 1.84$ GeV/ c^2 (fitting region)

The overall efficiency is 56.72%.

3.4.2 Signal Extraction and Fitting Strategy

For the $D^0 \rightarrow \nu\bar{\nu}$ decay, there should be no detector information remained at the signal side after reconstruction of the the charm tagger. One distinctive variable can be used for signal extraction is energy of remaining clusters on ECL (E_{ECL}) and the method was also used in $B^+ \rightarrow \tau^+\nu_\tau$ measurement [43]. In order to remove the clusters made by beam background, there are constrains on cluster energy in different region of ECL:

- Energy > 0.05 GeV: barrel region
- Energy > 0.10 GeV: forward end-cap region
- Energy > 0.15 GeV: backward end-cap region

For the clusters which don't belong to the reconstructed component $D_{tag}^{(*)}X_{frag}\pi_s^+$, their energy is summed to calculate E_{ECL} .

We perform a fitter with two dimensional extended unbinned likelihood fit that maximizes the likelihood function

$$\mathbb{L} = \frac{e^{-\sum_j N_j}}{N!} \prod_{i=1}^N \left(\sum_j N_j P_j(M_{D^0}, E_{ECL}) \right) \quad (3.5)$$

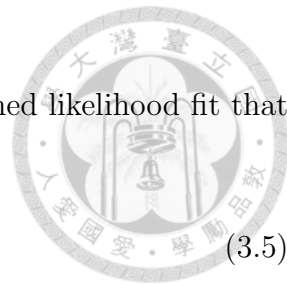
to estimate the signal in the region $M_{D^0} > 1.84 \text{ GeV}/c^2$ and $E_{ECL} < 2.1 \text{ GeV}$. Here N is the number of events in the fit, i denotes the i^{th} event, P_j denotes the probability density function (PDF) of signal and background components, which consists of a peaking background PDF and flat background PDF on M_{D^0} , and N_j denotes number of events corresponding to P_j .

Signal and the two background PDFs of E_{ECL} are determined by binned histogram function. Signal and peaking background PDF of M_{D^0} are modeled by a Breit-Wigner distribution. Flat background PDF of M_{D^0} is modeled by a ARGUS distribution [42]. The shape parameters of signal M_{D^0} PDF as the end-point of the ARGUS function is fixed. All N_j and other shape parameters are floated. PDF modeling for $D^0 \rightarrow \nu\bar{\nu}$ measurement is summarized in Table 3.19 and Figure 3.8. The relation between the two dimensions is shown in Figure 3.9 and Figure 3.10. The comparison between data and MC in the two dimensions' sideband region is shown in Figure 3.11 and the scale factor between MC and data is about 1.66 by the E_{ECL} sideband.

The definition of E_{ECL} is based upon counting on the remaining clusters. Thus, E_{ECL} would be exact 0 when there is no remaining cluster, and this makes a peak at 0 for the distribution. Table 3.6 shows the different source which contributes to the $E_{ECL} = 0$ peak from the background MC.

Source	Number of events
All background	459
D^0 decay	108
$D^0 \rightarrow K^0\pi^0$	53
$D^0 \rightarrow K^-\mu^+\nu_\mu$	12
$D^0 \rightarrow K_L^0 K_L^0$	8
$D^0 \rightarrow K^-e^+\nu_e$	6
$D^0 \rightarrow K^{*0}\pi^0$	2

Table 3.6: Contribution on $E_{ECL} = 0$ peak from six times data size of background MC.



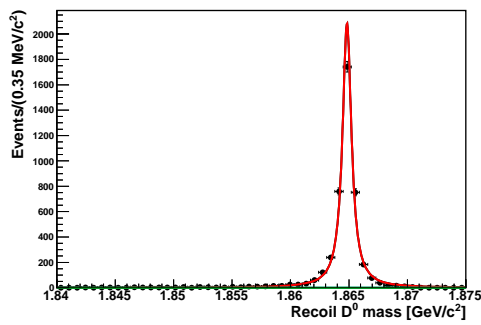
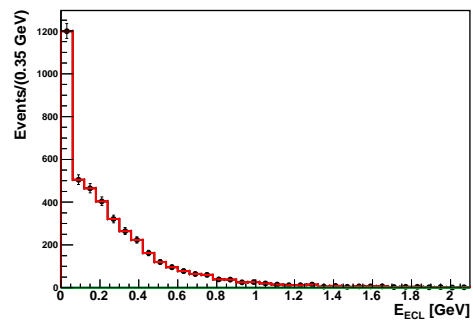
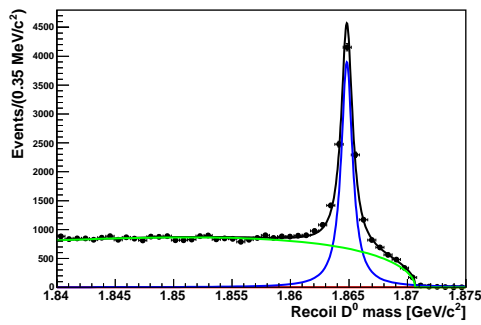
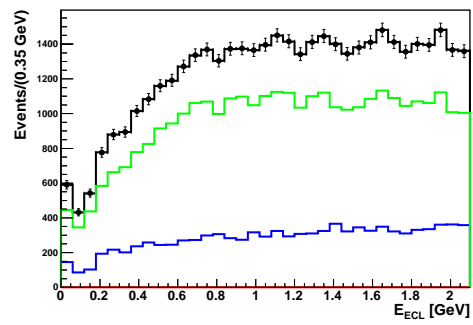
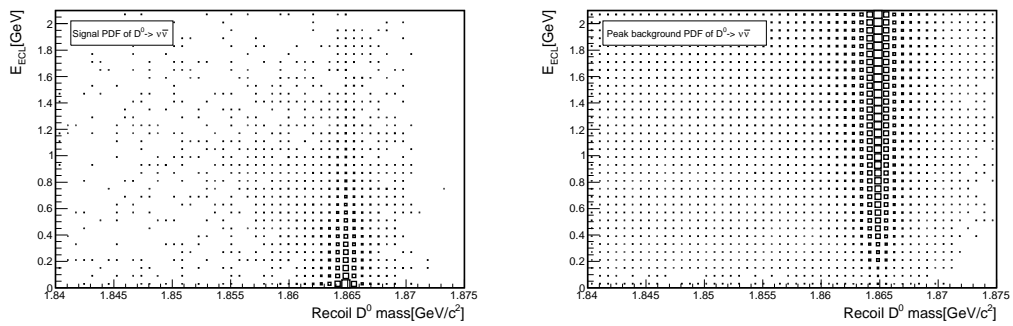
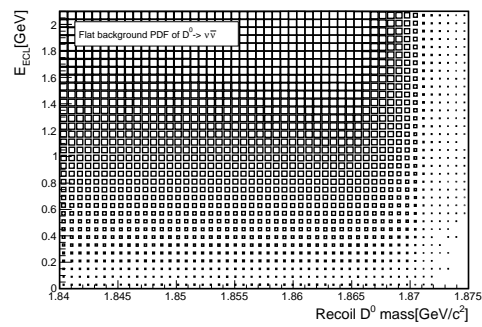
(a) Signal PDF of M_{D^0} .(b) Signal PDF of E_{ECL} .(c) Background PDFs of M_{D^0} .(d) Background PDFs of E_{ECL} .

Figure 3.8: PDF modeling in $D^0 \rightarrow \nu\bar{\nu}$ study with $E_{ECL} < 2.1$ GeV. Green solid line is flat background PDF. Blue solid line is peaking background PDF.



(a) Signal, correlation factor = -0.2939.

(b) Peak background, correlation factor = -0.054.



(c) Flat background, correlation factor = -0.0033.

Figure 3.9: Scattering plot of MC samples in $D^0 \rightarrow \nu\bar{\nu}$ study with $E_{ECL} < 2.1$ GeV.

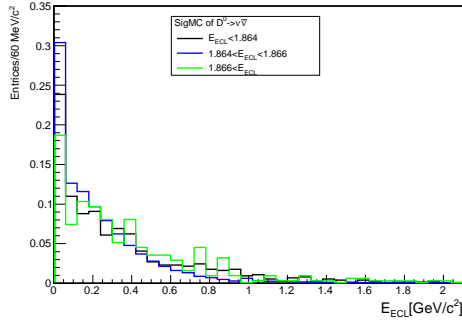
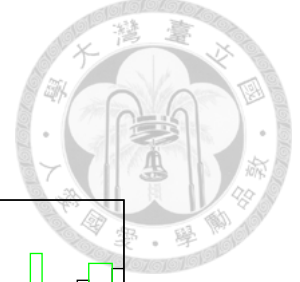
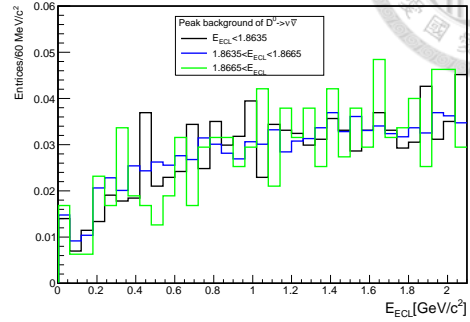
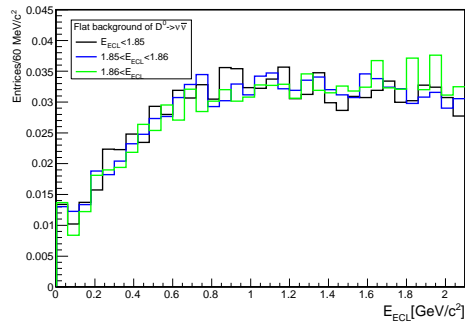
(a) Signal E_{ECL} .(b) Peak background E_{ECL} .(c) Flat background E_{ECL} .

Figure 3.10: E_{ECL} distribution of $D^0 \rightarrow \nu\bar{\nu}$ MC samples with projecting to different recoil M_{D^0} region.

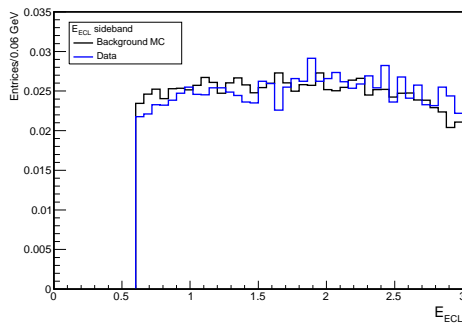
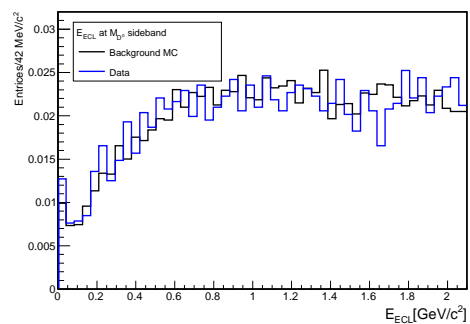
(a) E_{ECL} sideband.(b) E_{ECL} of recoil M_{D^0} sideband.

Figure 3.11: Comparison on sideband between data and MC. The histograms are normalized.



3.5 Ensemble Test

In order to check the validity of the fitter under different expected signal yield, we perform ensemble tests. For each set of fit, 3000 gsim/toyMC samples are generated. For each sample, Poisson-distributed random variables with expected values equal to N_{sig}^{input} , $N_{flatbck}^{input}$, and $N_{peakbck}^{input}$. N_{sig}^{input} varies from 0 to 50. $N_{flatbck}^{input}$ and $N_{peakbck}^{input}$ are obtained by background MC and then scaled by comparison on sideband E_{ECL} between data and MC. The result of the ensemble test including yield, fitting error and pull distribution. The yield means N_{sig} obtained by the fit, and fitting error presents the standard deviation of the fit. The fit bias is checked by the pull value which is defined as

$$\text{Pull} = \frac{\text{yield} - \text{expected yield}}{\text{fitting error}}. \quad (3.6)$$

Since there might be background rate difference between MC and data, we use the sideband region of E_{ECL} to check it, and use the ratio (1.66) to scale expected number of background. After scaling, $(N_{flatbck}^{input}, N_{peakbck}^{input}) = (9207.39, 2735.46)$ for $E_{ECL} < 2.1$ GeV, and $(10602.68, 3261.27)$ for $E_{ECL} < 2.4$ GeV.

3.5.1 Gsim Test

The gsim ensemble test results of the two cases ($E_{ECL} < 2.1$ GeV and $E_{ECL} < 2.4$ GeV) are shown in Figure 3.12 and Table 3.7, 3.8. The outcomes show good performance on fitter (N_{sig} , $Pull_{sig}$, and $Width_{sig}^{Pull}$ can cover their expected value within 3σ).

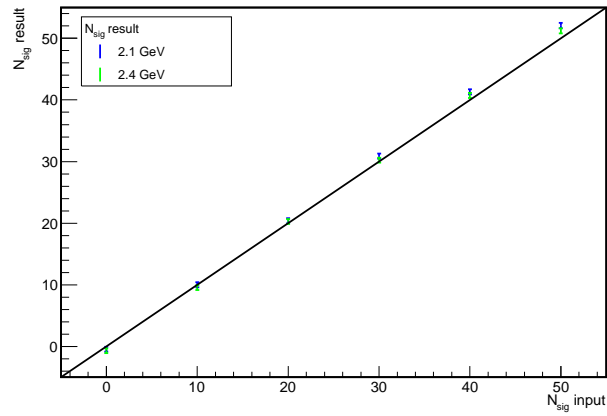
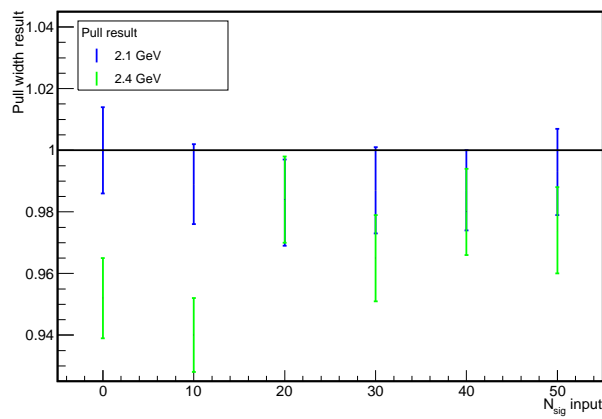
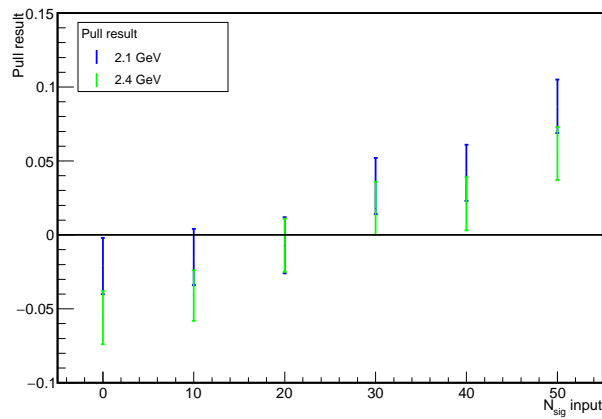
(a) N_{sig} .(b) $Pull_{sig}$ (c) $Width_{sig}^{Pull}$.

Figure 3.12: Gsim linearity test with different E_{ECL} range. ($N_{flatbck}^{input}$ and $N_{peakbck}^{input}$ are scaled by sideband data.)



N_{sig}^{input}	N_{sig}	Err_{sig}	$Pull_{sig}$	$Width_{sig}^{Pull}$
0	-0.462 ± 0.398	21.016 ± 0.014	-0.021 ± 0.019	1.000 ± 0.014
10	10.004 ± 0.398	21.523 ± 0.014	-0.015 ± 0.019	0.989 ± 0.013
20	20.382 ± 0.417	21.980 ± 0.014	-0.007 ± 0.019	0.983 ± 0.014
30	30.872 ± 0.426	22.432 ± 0.014	0.033 ± 0.019	0.987 ± 0.014
40	41.305 ± 0.420	22.844 ± 0.013	0.042 ± 0.019	0.987 ± 0.013
50	52.078 ± 0.431	23.281 ± 0.013	0.087 ± 0.018	0.993 ± 0.014
	$N_{peakbck}$	$Err_{peakbck}$	$Pull_{peakbck}$	$Width_{peakbck}^{Pull}$
0	2732.770 ± 1.599	87.700 ± 0.028	-0.038 ± 0.018	0.974 ± 0.013
10	2730.430 ± 1.585	87.800 ± 0.028	-0.043 ± 0.018	0.939 ± 0.013
20	2729.880 ± 1.653	87.854 ± 0.028	-0.052 ± 0.018	0.971 ± 0.013
30	2730.700 ± 1.626	87.959 ± 0.029	-0.041 ± 0.018	0.956 ± 0.013
40	2727.190 ± 1.558	88.024 ± 0.029	-0.055 ± 0.018	0.970 ± 0.014
50	2729.320 ± 1.627	88.062 ± 0.028	-0.061 ± 0.018	0.971 ± 0.014
	$N_{flatbck}$	$Err_{flatbck}$	$Pull_{flatbck}$	$Width_{flatbck}^{Pull}$
0	9213.650 ± 2.106	113.383 ± 1.038	0.074 ± 0.017	0.941 ± 0.013
10	9211.460 ± 2.106	110.614 ± 0.366	0.065 ± 0.018	0.943 ± 0.014
20	9211.750 ± 2.147	117.289 ± 0.230	0.071 ± 0.018	0.959 ± 0.014
30	9211.580 ± 2.116	107.541 ± 0.547	0.066 ± 0.018	0.934 ± 0.014
40	9209.370 ± 2.171	110.846 ± 0.469	0.053 ± 0.018	0.971 ± 0.014
50	9209.150 ± 2.109	117.325 ± 0.228	0.044 ± 0.018	0.936 ± 0.014

Table 3.7: Gsim linearity test detailed result with $E_{ECL} < 2.1$ GeV. ($N_{flatbck}^{input}$ and $N_{peakbck}^{input}$ are scaled by sideband data.)



N_{sig}^{input}	N_{sig}	Err_{sig}	$Pull_{sig}$	$Width_{sig}^{Pull}$
0	-0.702 ± 0.376	20.842 ± 0.014	-0.056 ± 0.018	0.952 ± 0.013
10	9.550 ± 0.384	21.338 ± 0.014	-0.041 ± 0.017	0.940 ± 0.012
20	20.275 ± 0.392	21.780 ± 0.014	-0.007 ± 0.018	0.984 ± 0.014
30	30.215 ± 0.400	22.227 ± 0.013	0.018 ± 0.018	0.965 ± 0.014
40	40.728 ± 0.415	22.655 ± 0.013	0.021 ± 0.018	0.980 ± 0.014
50	51.212 ± 0.422	23.068 ± 0.013	0.055 ± 0.018	0.974 ± 0.014
	$N_{peakbck}$	$Err_{peakbck}$	$Pull_{peakbck}$	$Width_{peakbck}^{Pull}$
0	3259.300 ± 1.701	94.934 ± 0.028	-0.012 ± 0.017	0.942 ± 0.013
10	3258.440 ± 1.657	94.962 ± 0.028	-0.011 ± 0.017	0.927 ± 0.013
20	3257.720 ± 1.658	95.043 ± 0.028	-0.019 ± 0.017	0.925 ± 0.013
30	3257.940 ± 1.670	95.117 ± 0.028	-0.022 ± 0.017	0.939 ± 0.014
40	3257.990 ± 1.690	95.150 ± 0.028	-0.034 ± 0.018	0.949 ± 0.013
50	3256.000 ± 1.677	95.209 ± 0.028	-0.045 ± 0.017	0.938 ± 0.014
	$N_{flatbck}$	$Err_{flatbck}$	$Pull_{flatbck}$	$Width_{flatbck}^{Pull}$
0	10607.300 ± 2.243	124.102 ± 0.258	0.051 ± 0.017	0.939 ± 0.013
10	10606.500 ± 2.252	126.162 ± 0.145	0.065 ± 0.018	0.943 ± 0.013
20	10604.500 ± 2.217	124.033 ± 0.616	0.036 ± 0.017	0.938 ± 0.013
30	10607.000 ± 2.206	123.180 ± 0.735	0.047 ± 0.017	0.917 ± 0.013
40	10603.200 ± 2.273	124.113 ± 0.238	0.042 ± 0.017	0.932 ± 0.013
50	10603.400 ± 2.213	126.141 ± 0.116	0.028 ± 0.017	0.925 ± 0.013

Table 3.8: Gsim linearity test detailed result with $E_{ECL} < 2.4$ GeV. ($N_{flatbck}^{input}$ and $N_{peakbck}^{input}$ are scaled by sideband data.)



3.5.2 ToyMC Test

As a cross check, the case with $E_{ECL} < 2.1$ GeV is re-tested with ToyMC samples, and the result is shown in Figure 3.13 and Table 3.9.

N_{sig}^{input}	N_{sig}	Err_{sig}	$Pull_{sig}$	$Width_{sig}^{Pull}$
0	0.370 ± 0.396	21.048 ± 0.015	0.001 ± 0.019	1.007 ± 0.013
10	9.219 ± 0.394	21.547 ± 0.014	-0.043 ± 0.018	0.988 ± 0.013
20	19.823 ± 0.402	22.016 ± 0.014	-0.035 ± 0.018	0.963 ± 0.013
30	29.834 ± 0.397	22.486 ± 0.014	-0.018 ± 0.018	0.951 ± 0.013
40	40.475 ± 0.422	22.909 ± 0.014	0.013 ± 0.018	0.975 ± 0.013
50	50.747 ± 0.441	23.352 ± 0.014	0.009 ± 0.018	0.979 ± 0.014
	$N_{peakbck}$	$Err_{peakbck}$	$Pull_{peakbck}$	$Width_{peakbck}^{Pull}$
0	2731.160 ± 1.580	86.406 ± 0.026	-0.029 ± 0.018	0.975 ± 0.014
10	2737.090 ± 1.616	86.483 ± 0.027	0.022 ± 0.019	0.996 ± 0.014
20	2735.440 ± 1.587	86.632 ± 0.031	0.008 ± 0.019	0.989 ± 0.014
30	2735.380 ± 1.598	86.718 ± 0.028	0.001 ± 0.018	0.971 ± 0.013
40	2732.320 ± 1.581	86.700 ± 0.029	-0.038 ± 0.018	0.961 ± 0.013
50	2734.400 ± 1.587	86.796 ± 0.029	-0.012 ± 0.019	0.987 ± 0.014
	$N_{flatbck}$	$Err_{flatbck}$	$Pull_{flatbck}$	$Width_{flatbck}^{Pull}$
0	9208.790 ± 2.118	114.130 ± 0.747	0.019 ± 0.018	0.962 ± 0.014
10	9207.610 ± 2.148	114.486 ± 0.942	0.002 ± 0.018	0.980 ± 0.013
20	9211.920 ± 2.189	114.781 ± 1.187	0.037 ± 0.019	0.989 ± 0.013
30	9208.290 ± 2.138	116.276 ± 0.032	0.011 ± 0.018	0.975 ± 0.014
40	9210.000 ± 2.069	116.316 ± 0.021	0.018 ± 0.018	0.950 ± 0.013
50	9208.760 ± 2.164	116.317 ± 0.030	0.023 ± 0.018	0.990 ± 0.013

Table 3.9: ToyMC linearity test detailed result with $E_{ECL} < 2.1$ GeV. ($N_{flatbck}^{input}$ and $N_{peakbck}^{input}$ are scaled by sideband data.)

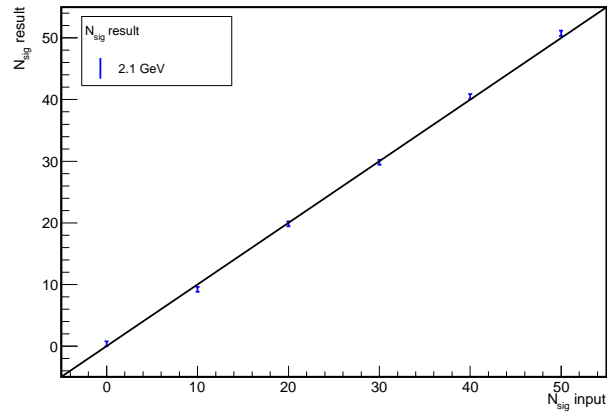
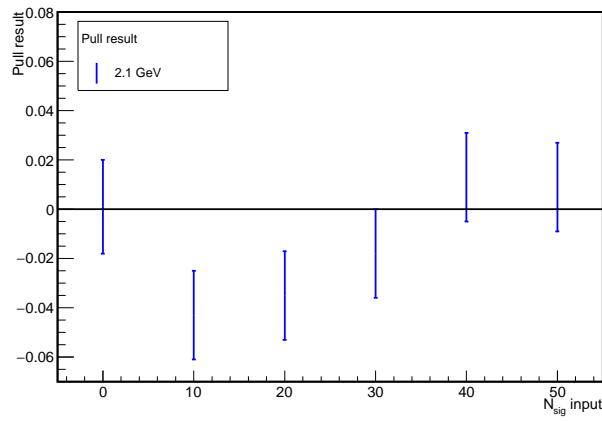
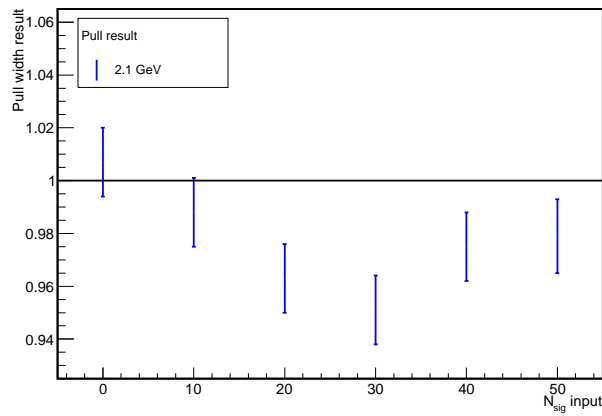
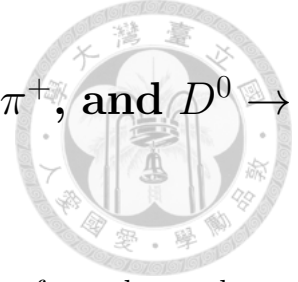
(a)
 N_{sig} (b) $Pull_{sig}$.(c) $Width_{sig}^{Pull}$.

Figure 3.13: ToyMC linearity test with $E_{ECL} < 2.1$ GeV. ($N_{flatbck}^{input}$ and $N_{peakbck}^{input}$ are scaled by sideband data.)

3.6 Control Sample Study: $D^0 \rightarrow K^-\pi^+$, and $D^0 \rightarrow h^-\ell^+\nu_\ell$



In order to check the validity of charm tagger, we also perform the study on $D^0 \rightarrow K^-\pi^+$, $D^0 \rightarrow K^-\mu^+\nu_\mu$, $D^0 \rightarrow K^-\nu_e$, $D^0 \rightarrow \pi^-\mu^+\nu_\mu$, and $D^0 \rightarrow \pi^-\nu_e$, which are with large branching fraction ($O(10^{-2}) \sim O(10^{-3})$) and clear final states. Most of the systematic uncertainties are also obtained by these measurements.

3.6.1 $D^0 \rightarrow K^-\pi^+$

Selection criterion

- Two remaining tracks, and no remaining π^0 , K_S^0 , K_L^0 , and Λ ($\bar{\Lambda}$) at the signal side after the tagger's reconstruction.
- For the two remaining tracks, one passes the selection for K and another passes selection for π .
 - K PID: $L_K/(L_K + L_\pi) > 0.6$, $L_e < 0.95$, $L_\mu < 0.95$
 - π PID: $L_K/(L_K + L_\pi) < 0.4$, $L_e < 0.95$, $L_\mu < 0.95$
- Missing energy ($\bar{D}_{sig}^0 - K^-\pi^+$) < 0.1 GeV: to reduce the semileptonic D^0 background.
- Recoil $M_{D^0} > 1.84$ GeV/ c^2 (fitting region)
- $E_{ECL} < 2.1$ GeV (fitting region)
- 1.80 GeV/ $c^2 < \text{Reconstructed } M_{D^0} < 1.92$ GeV/ c^2
- Vertex fit is performed and the fit converges
- Right-Sign (RS) selection: The flavor of D^0 (\bar{D}^0) should match the flavor of K^- (K^+).

The overall efficiency is 28.0%.



Signal extraction

Signal extraction of $D^0 \rightarrow K^-\pi^+$ is done with 2D fit on recoil M_{D^0} and E_{ECL} , and their distribution of six times data size of signal and all generic background MC are shown in Figure 3.14.

The three PDFs of E_{ECL} are all modeled by smoothed histogram from MC. Signal PDF and peak background PDF of recoil M_{D^0} are both modeled by a Breit-Wigner distribution. Flat Background PDF of recoil M_{D^0} is modeled by a smoothed histogram. PDF modeling with MC samples is shown in Figure 3.15.

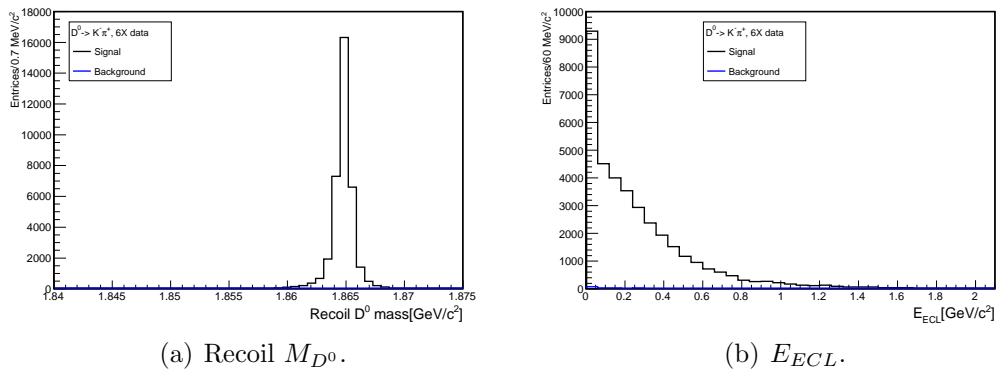


Figure 3.14: Recoil M_{D^0} and E_{ECL} distribution of six times data size of signal and all generic background MC in $D^0 \rightarrow K^-\pi^+$ study.

Measurement

In the data fit, the shape of signal PDF is floated and the shape of peak background PDF is fixed. The data fit result is shown in Figure 3.16 and the signal yield is $7890.5^{+124.50}_{-125.86}$ (Peak background yield is $-111.25^{+89.26}_{-83.82}$ and flat background yield is $144.74^{+18.40}_{-17.53}$). The branching fraction is measured to be $3.92^{+0.06}_{-0.06}\%$, where the error is statistical only and the eff. calibration factors due to charged PID and vetoes in Table 3.10 and Table 3.14 are all applied.

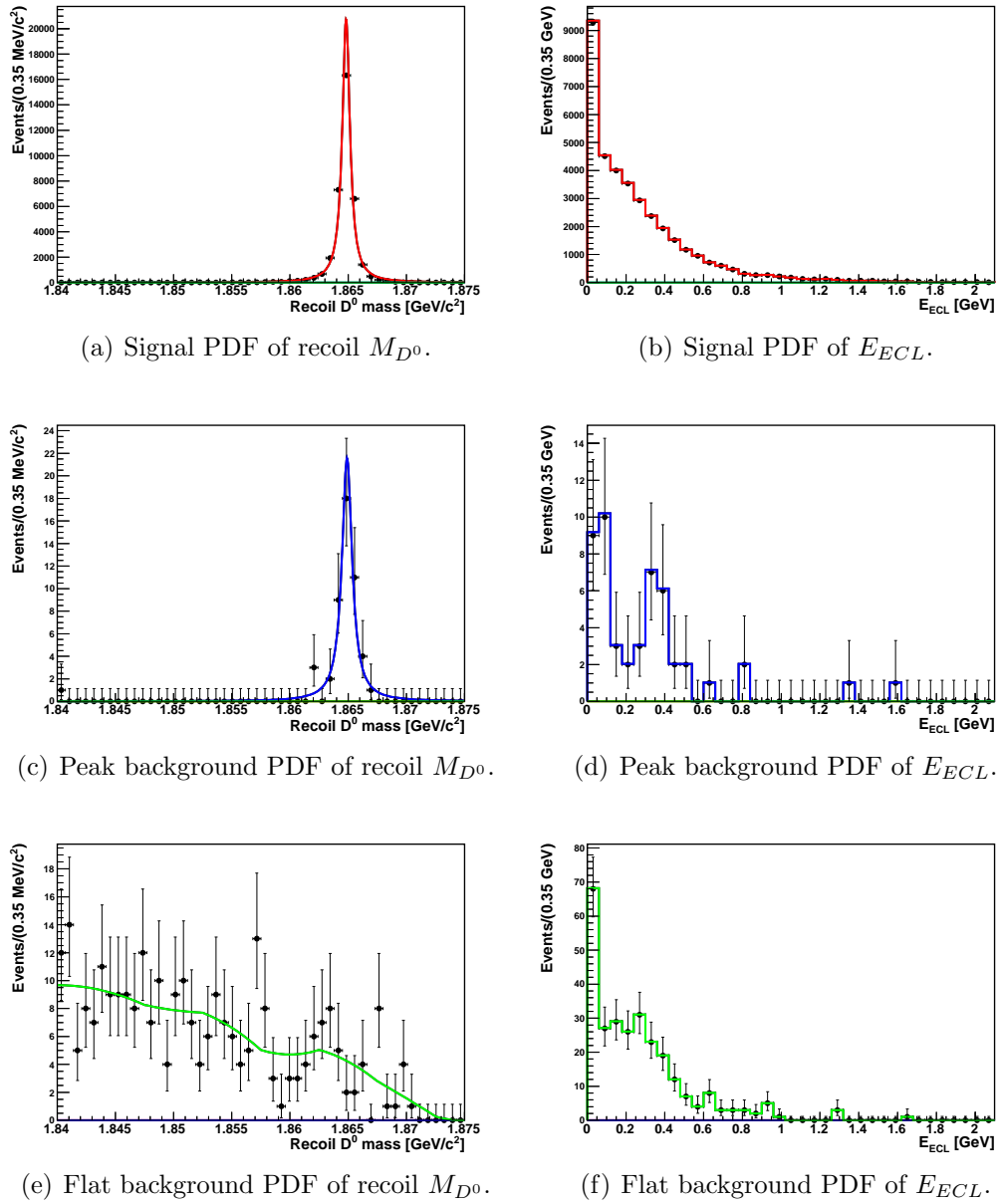


Figure 3.15: PDF modeling in $D^0 \rightarrow K^- \pi^+$ study.

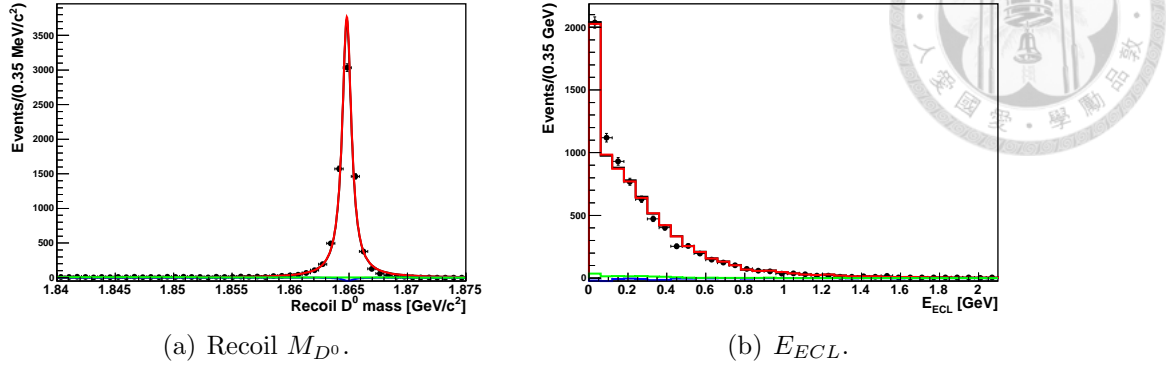


Figure 3.16: Data fit result of $D^0 \rightarrow K^- \pi^+$. Red solid line is signal PDF. Blue solid line is peak background PDF. Green solid line is flat background PDF.

3.6.2 $D^0 \rightarrow K^- \mu^+ \nu_\mu$

Selection criterion

- No remaining π^0 , and two remaining tracks at the signal side after the tagger's reconstruction.
- For the two remaining tracks, one passes the selection for K and another passes selection for μ .
 - K PID: $L_K / (L_K + L_\pi) > 0.6$
 - μ PID: $L_\mu > 0.9$
- $E_\nu > 0.5$ GeV: to reduce the hadronic D^0 background. e.g. $D^0 \rightarrow K^- \pi^+$
- $M_{D^0} > 1.86$ GeV/ c^2
- $|M_{miss}^2| < 0.2$ GeV $^2/c^4$ (fitting region)
- $E_{ECL} < 4$ GeV
- Vertex fit is performed and the fit converges
- RS selection

The overall efficiency is 22.5%.



Signal extraction

Signal extraction of $D^0 \rightarrow K^- \mu^+ \nu_\mu$ is done with 1D fit on M_{miss}^2 . The M_{miss}^2 distribution of six times data size of signal and all generic background MC are shown in Figure 3.17. Signal PDF is modeled by a Breit-Wigner distribution. The background contains a flat component and a peaking structure near $M_{miss}^2 = 0.05 \text{ GeV}^2/c^4$, which consists of a few harmonic decays such as $D^0 \rightarrow \rho^+ K^-$, $D^0 \rightarrow K^{*-} \pi^+$ and so on. The peaking and the flat background PDF are modeled by a Breit-Wigner distribution and a third order Chebyshev polynomial, respectively. PDF modeling with MC samples is shown in Figure 3.18.

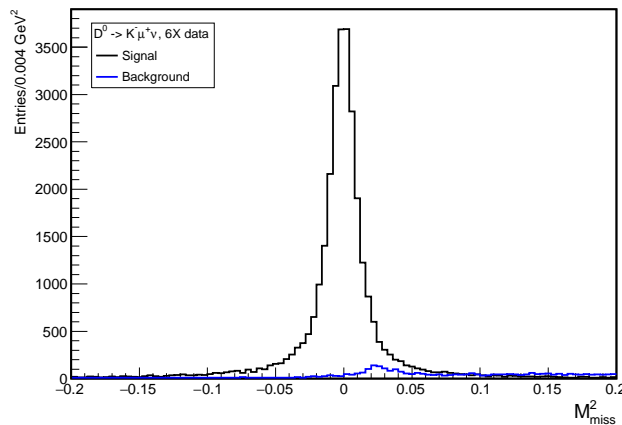
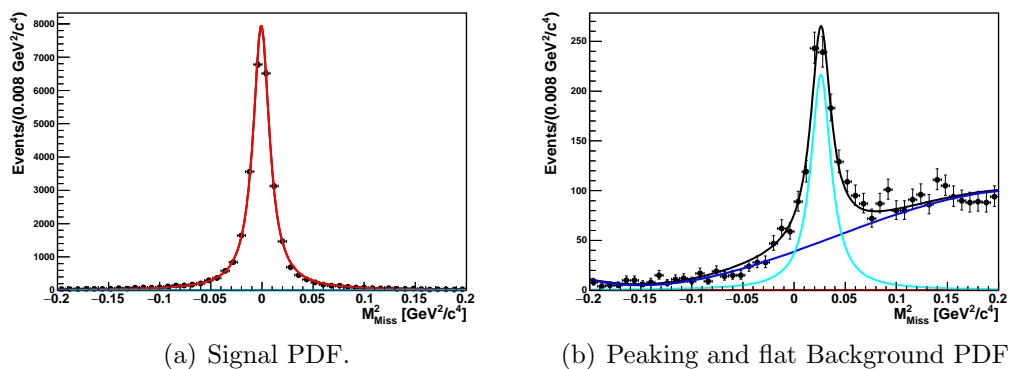


Figure 3.17: M_{miss}^2 distribution of six times data size of signal and all generic background MC in $D^0 \rightarrow K^- \mu^+ \nu_\mu$ study.



(a) Signal PDF.

(b) Peaking and flat Background PDF.

Figure 3.18: PDF modeling in $D^0 \rightarrow K^- \mu^+ \nu_\mu$ study.



Measurement

In the data fit, the shape of signal PDF and peaking background PDF are both fixed to avoid interference between these two yields. The data fit result is shown in Figure 3.19 and the signal yield is $5207.36^{+90.23}_{-89.77}$.

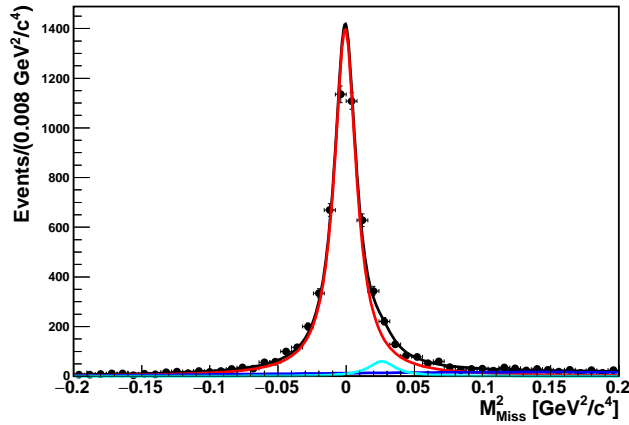


Figure 3.19: Data fit result of $D^0 \rightarrow K^- \mu^+ \nu_\mu$. Red solid line is signal PDF. Blue solid line is flat background PDF. Cyan solid line is peaking background PDF.

3.6.3 $D^0 \rightarrow K^- e^+ \nu_e$

Selection criterion

- At least two remaining tracks at the signal side after the tagger's reconstruction. For the two tracks, one passes the selection for K and another passes selection for e .
 - K PID: $L_K/(L_K + L_\pi) > 0.6$
 - e PID: $L_e > 0.9$
- $E_\nu > 0.1$ GeV
- $M_{D^0} > 1.86$ GeV/ c^2
- $|M_{miss}^2| < 0.5$ GeV²/ c^4 (fitting region)
- $E_{ECL} < 4$ GeV
- Vertex fit is performed and the fit converges



- RS selection

The overall efficiency is 54.74%.

Signal extraction

Signal extraction of $D^0 \rightarrow K^- e^+ \nu_e$ is done with 1D fit on M_{miss}^2 . The M_{miss}^2 distribution of six times data size of signal and all generic background MC are shown in Figure 3.20. Signal PDF is modeled by combination of a Breit-Wigner distribution and a Gaussian distribution. The background PDF is modeled by a smoothed histogram. PDF modeling with MC samples is shown in Figure 3.21.

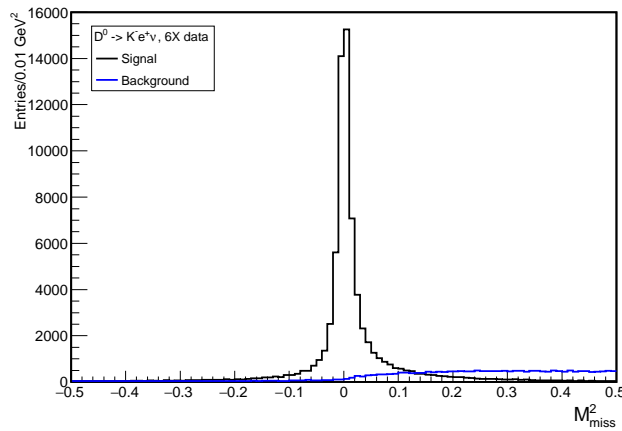
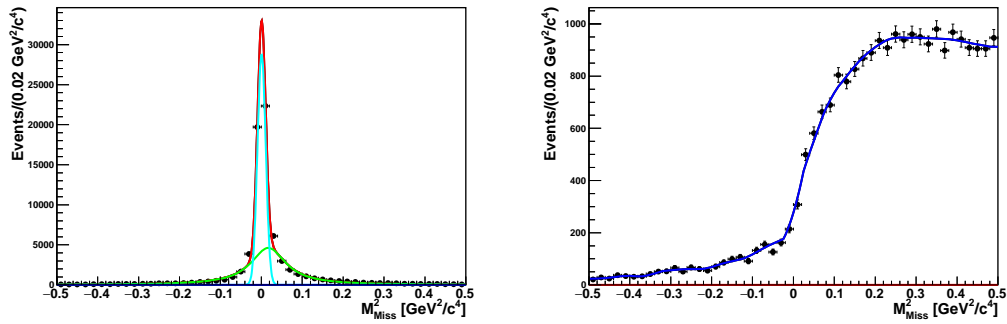


Figure 3.20: M_{miss}^2 distribution of six times data size of signal and all generic background MC in $D^0 \rightarrow K^- e^+ \nu_e$ study.

Measurement

In the data fit, the shape of signal PDF is floated. The data fit result is shown in Figure 3.22 and the signal yield is $13019.0^{+137.65}_{-136.74}$.



(a) Signal PDF. Green solid line is Breit-Wigner distribution. Cyan solid line is Gaussian distribution.

(b) Background PDF.

Figure 3.21: PDF modeling in $D^0 \rightarrow K^- e^+ \nu_e$ study.

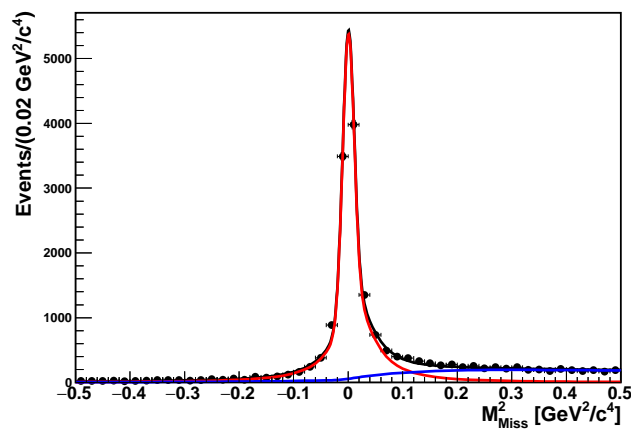


Figure 3.22: Data fit result of $D^0 \rightarrow K^- e^+ \nu_e$. Red solid line is signal PDF. Blue solid line is background PDF.



3.6.4 $D^0 \rightarrow \pi^-\mu^+\nu_\mu$

Selection criterion

- At least two remaining tracks at the signal side after the tagger's reconstruction. For the two tracks, one passes the selection for π and another passes selection for μ .
 - π PID: $L_K/(L_K + L_\pi) < 0.4$
 - μ PID: $L_\mu > 0.9$
- $E_\nu > 0.5$ GeV
- $M_{D^0} > 1.84$ GeV/ c^2
- $|M_{miss}^2| < 0.2$ GeV $^2/c^4$ (fitting region)
- $E_{ECL} < 4$ GeV
- Vertex fit is performed and the fit converges
- RS selection

The overall efficiency is 44.63%.

Signal extraction

Signal extraction of $D^0 \rightarrow \pi^-\mu^+\nu_\mu$ is done with 1D fit on M_{miss}^2 . The M_{miss}^2 distribution of six times data size of signal and all generic background MC are shown in Figure 3.23. For the $D^0 \rightarrow \pi^-\ell^+\nu_\ell$ measurement, the corresponding $D^0 \rightarrow K^-\ell^+\nu_\ell$ decay would be a non-negligible background due to the approximately ten times larger \mathcal{B} and K/π feed-across. Signal PDF is modeled by combination of a Breit-Wigner distribution and a Gaussian distribution. The $D^0 \rightarrow K^-\mu^+\nu_\mu$ background PDF is modeled by a smoothed histogram. The peaking background PDF is modeled by a Gaussian distribution. The flat background PDF is modeled by a second order Chebyshev polynomial. PDF modeling with MC samples is shown in Figure 3.24.

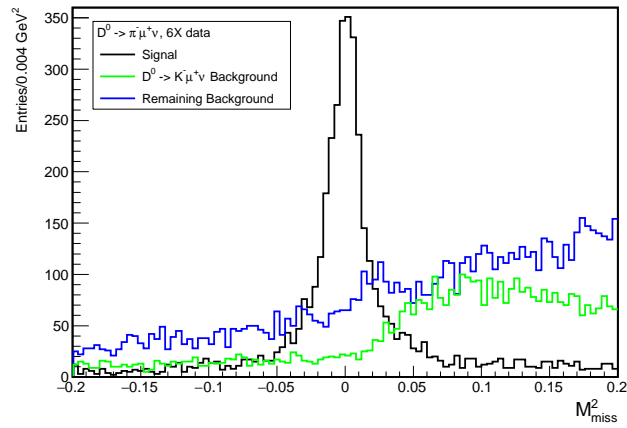
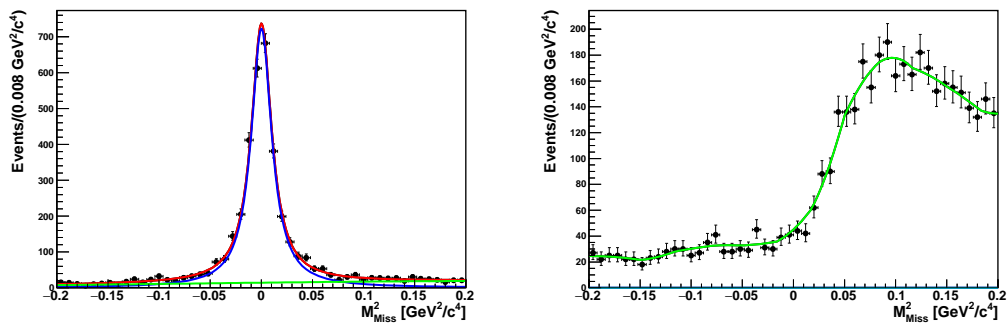
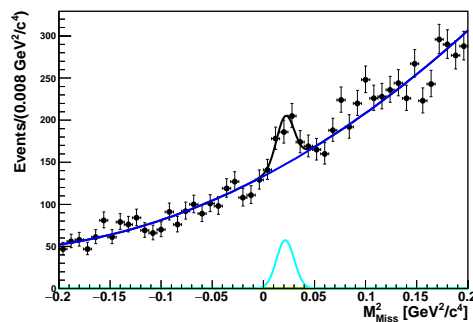


Figure 3.23: M_{miss}^2 distribution of six times data size of signal and all generic background MC in $D^0 \rightarrow \pi^- \mu^+ \nu_\mu$ study.



(a) Signal PDF. Blue solid line is Breit-Wigner distribution. Green solid line is Gaussian distribution.

(b) $D^0 \rightarrow K^- \mu^+ \nu_\mu$ background PDF.



(c) Peaking and flat background PDF.

Figure 3.24: PDF modeling in $D^0 \rightarrow \pi^- \mu^+ \nu_\mu$ study.



Measurement

In the data fit, the shape of signal PDF is fixed due to the complicated components, and the background shape is floated. The data fit result is shown in Figure 3.25 and the signal yield is $694.00^{+53.10}_{-50.92}$.

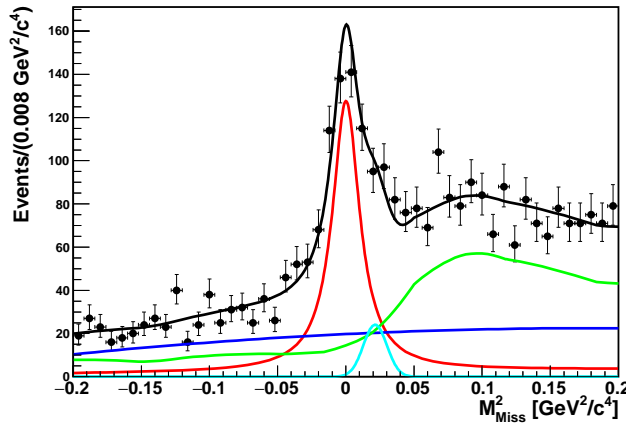


Figure 3.25: Data fit result of $D^0 \rightarrow \pi^- \mu^+ \nu_\mu$. Red solid line is signal PDF. Green solid line is $D^0 \rightarrow K^- \mu^+ \nu_\mu$ background PDF. Blue solid line is flat background PDF. Cyan solid line is peaking background PDF.

3.6.5 $D^0 \rightarrow \pi^- e^+ \nu_e$

Selection criterion

- No remaining π^0 , and two remaining tracks at the signal side after the tagger's reconstruction.
- For the two remaining tracks, one passes the selection for π and another passes selection for e .
 - π PID: $L_K/(L_K + L_\pi) < 0.4$
 - e PID: $L_\mu > 0.9$
- $E_\nu > 0.1$ GeV
- $M_{D^0} > 1.84$ GeV/ c^2
- $|M_{miss}^2| < 0.5$ GeV $^2/c^4$ (fitting region)



- $E_{ECL} < 4$ GeV
- Vertex fit is performed and the fit converges
- RS selection

The overall efficiency is 53.47%.

Signal extraction

Signal extraction of $D^0 \rightarrow \pi^- e^+ \nu_e$ is done with 1D fit on M_{miss}^2 . The M_{miss}^2 distribution of six times data size of signal and all generic background MC are shown in Figure 3.26. Signal PDF is modeled by combination of a Breit-Wigner distribution and a Crystal Ball distribution. The $D^0 \rightarrow K^- e^+ \nu_e$ background PDF is modeled by a smoothed histogram. The remaining background PDF is modeled by a second order Chebyshev polynomial. PDF modeling with MC samples is shown in Figure 3.27.

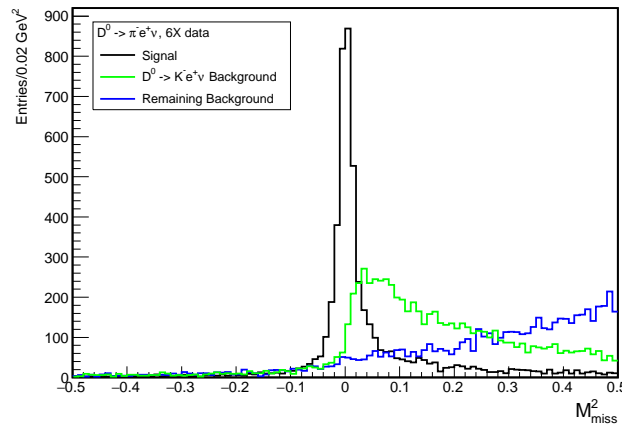


Figure 3.26: M_{miss}^2 distribution of six times data size of signal and all generic background MC in $D^0 \rightarrow \pi^- e^+ \nu_e$ study.

Measurement

In the data fit, the shape of signal PDF is fixed due to the complicated components, and the background shape is floated. The data fit result is shown in Figure 3.28 and the signal yield is $956.89^{+49.55}_{-48.74}$.

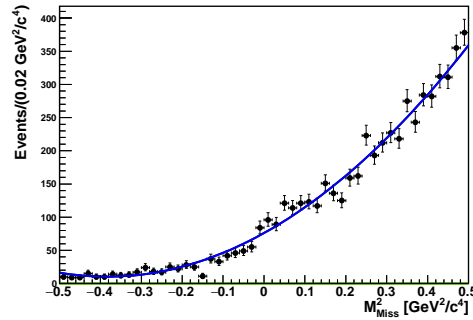
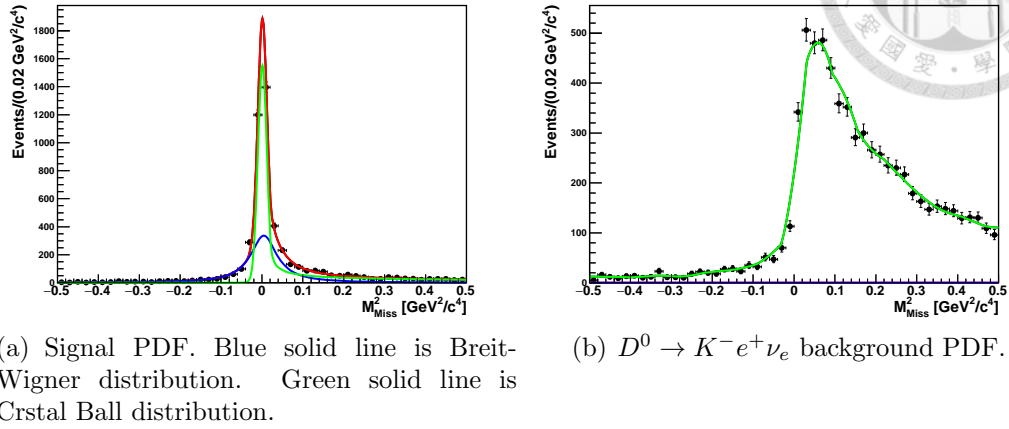
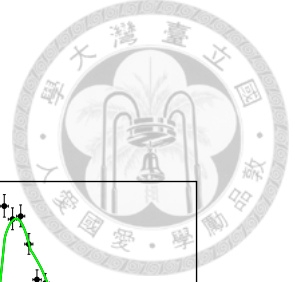


Figure 3.27: PDF modeling in $D^0 \rightarrow \pi^- e^+ \nu_e$ study.

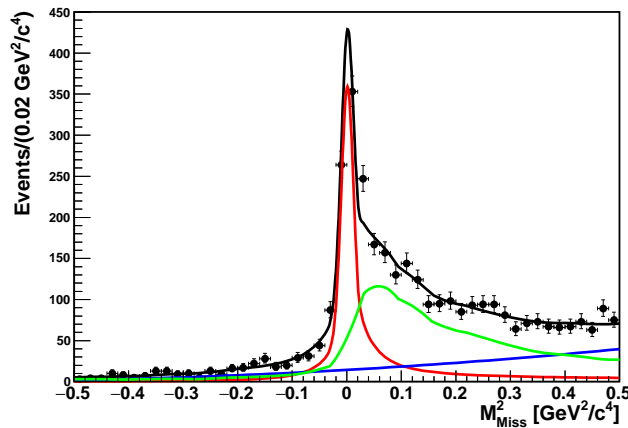


Figure 3.28: Data fit result of $D^0 \rightarrow \pi^- e^+ \nu_e$. Red solid line is signal PDF. Green solid line is $D^0 \rightarrow K^- e^+ \nu_e$ background PDF. Blue solid line is background PDF.



3.7 Systematic Uncertainties

Several systematic uncertainties are discussed in this section. The correlated errors are added linearly and the uncorrelated ones are added in quadrature. The summary of systematic uncertainties are shown in Table 3.18 and Table 3.20 for the four $D^0 \rightarrow h^-\ell^+\nu_\ell$ study, and $D^0 \rightarrow \nu\bar{\nu}$ study, respectively.

- Tracking uncertainty:

The systematic uncertainty due to charged-track reconstruction is studied using partially reconstructed $D^{*+} \rightarrow D^0\pi^+$ with $D^0 \rightarrow \pi^+\pi^-K_S^0$. For the tracks with $p_T > 200$ MeV/c, the systematic uncertainty of a charged track is estimated to be $(-0.13 \pm 0.30(\text{stat.}) \pm 0.10(\text{syst.}))\%$ per track. We apply the uncertainty to be 0.35% per track.

- Charged PID:

Since we use the selection on PID likelihood value for the charged Kaon, pion, muon and electron identification in the final state for $D^0 \rightarrow h^-\ell^+\nu_\ell$ and $D^0 \rightarrow K^-\pi^+$ study. The systematic uncertainties are estimated by using the package provided by the PID joint group [44, 45, 46, 47, 48] to calibrate the ratio between MC efficiency and data efficiency. The study is based upon various control samples such as $\Lambda \rightarrow p\pi^-$ and $D^{*+} \rightarrow D^0\pi^+$ with $D^0 \rightarrow K^-\pi^+$. The factors and uncertainties for the four modes are shown in Table 3.10.

mode	K/π ID	error	Lepton ID	error
$D^0 \rightarrow K^-\mu^+\nu$	0.9993	0.88%	0.9730	1.89%
$D^0 \rightarrow K^-e^+\nu$	0.9899	0.83%	0.9698	2.13%
$D^0 \rightarrow \pi^-\mu^+\nu$	0.9606	0.89%	0.9697	1.86%
$D^0 \rightarrow \pi^-e^+\nu$	0.9583	0.87%	0.9732	1.97%
mode	K ID	error	π ID	error
$D^0 \rightarrow K^-\pi^+$	0.9780	0.82%	0.9573	0.86%

Table 3.10: PID calibration factors and uncertainties in $D^0 \rightarrow h^-\ell^+\nu$ and $D^0 \rightarrow K^-\pi^+$ study.

- Number of inclusive D^0 :

Total number of inclusive D^0 reconstructed by the charm tagger is obtained by the fit on data. The yield is $694505^{+1029.99}_{-1472.24}$. Hence, the statistical uncertainty due to number of inclusive D^0 is $^{+0.15\%}_{-0.21\%}$.

For the systematic uncertainty due to signal D^0 PDF modeling, we perform

the data fit of $D^0 \rightarrow K^-\pi^+$ with a different signal shape function and take the variation of branching fraction of $D^0 \rightarrow K^-\pi^+$ control sample. We obtain $7890.5^{+124.50}_{-125.86}$ yield ($\mathcal{B} = 3.92 \pm 0.06$) from the nominal fit. For the case in which signal PDF is triple Gaussian, we obtain $7914.59^{+138.21}_{-139.20}$ yield ($\mathcal{B} = 3.93 \pm 0.07$). The systematic uncertainty is estimated to be $\pm 0.3\%$.

For the systematic uncertainty due to background PDF modeling, we perform the fit on inclusive D^0 sample with a different background shape function and take the variation of measured yield. We obtain $694505^{+1029.99}_{-1472.24}$ yield from the nominal fit. For the case in which flat background PDF is a smooth histogram, we obtain $660235^{+1076.44}_{-1076.40}$ yield. The systematic uncertainty is estimated to be $\pm 4.9\%$.

- Fit bias ($D^0 \rightarrow \nu\bar{\nu}$):

The uncertainty due to fit bias is examined by gsim ensemble test. We quote $+0.462$ (in terms of number) from the test result in Table 3.7.

- Signal PDF ($D^0 \rightarrow \nu\bar{\nu}$):

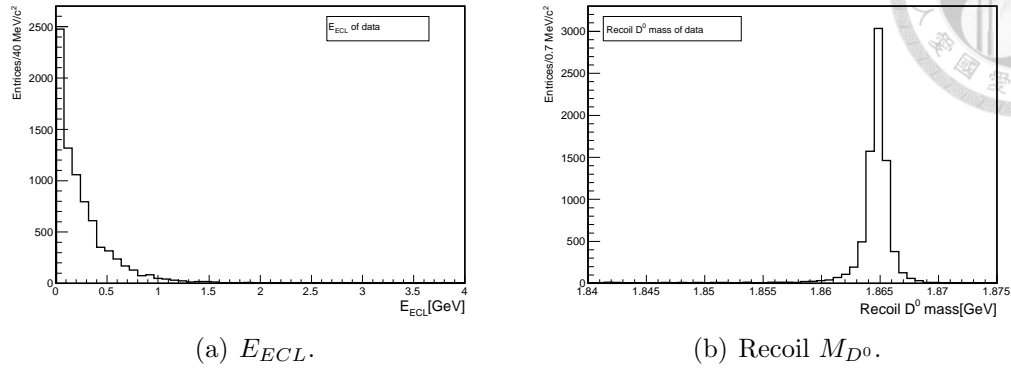
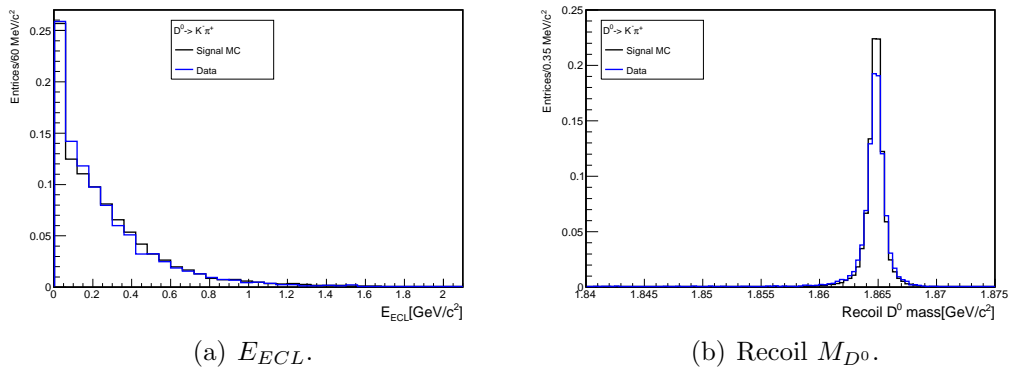
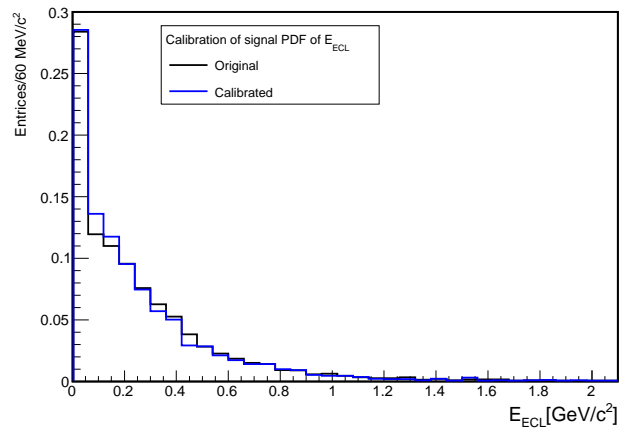
In order to calibrate the signal PDF used in $D^0 \rightarrow \nu\bar{\nu}$ measurement, we check $D^0 \rightarrow K^-\pi^+$ data distributions of E_{ECL} and recoil M_{D^0} , which are shown in Figure 3.29. The comparison between signal MC and data on these two dimensions is shown in Figure 3.30 and Table 3.11. E_{ECL} distribution of $D^0 \rightarrow \nu\bar{\nu}$ signal MC is also shown in Figure 3.30(a) for comparison.

For $D^0 \rightarrow \nu\bar{\nu}$ measurement, since the signal MC/data E_{ECL} distribution is quite similar as shown in Figure 3.30(a), we use the original PDF shape from signal MC in the nominal data fit. Besides, we also calibrate each bin content of the signal E_{ECL} PDF by Figure 3.30(a). The systematic uncertainty is obtained by fitting on data with the original and calibrated PDF, and check the signal yield deviation, which is estimated to be $+2.31$ in terms of number of yield. Figure 3.31 shows the original and calibrated signal E_{ECL} PDF.

For the signal recoil M_{D^0} PDF of $D^0 \rightarrow \nu\bar{\nu}$, it is calibrated by the fudge factors obtained by Table 3.11. The width is inflated in to 0.0011 with a factor of about 1.20, and the mean remains the same. The systematic uncertainty due to it is estimated by the yield deviation from data with tuning the fudge factors by $\pm 1\sigma$, which is estimated to be $^{+0.22}_{-0.10}$ in terms of number of yield.

	Mean	Width
Signal MC	$1.86482^{+0.00000308}_{-0.00000309}$	$0.000796^{+0.00000570}_{-0.00000563}$
Data	$1.86482^{+0.00000787}_{-0.00000792}$	$0.000952^{+0.0000149}_{-0.0000147}$

Table 3.11: Comparison between signal MC and data on recoil M_{D^0} PDF.

Figure 3.29: $D^0 \rightarrow K^-\pi^+$ data distribution of E_{ECL} and recoil M_{D^0} .Figure 3.30: $D^0 \rightarrow K^-\pi^+$ data and signal MC distribution of E_{ECL} and recoil M_{D^0} .Figure 3.31: The original and calibrated signal PDF of E_{ECL} .

- Flat background PDF ($D^0 \rightarrow \nu\bar{\nu}$):

Figure 3.11 is the data/background MC E_{ECL} distribution at recoil M_{D^0} side-band. We can obtain the calibration factors after binning on the two distributions and comparing between them, then we use the calibration factors to adjust each bin of the original flat background E_{ECL} PDF. Figure 3.32 shows the original and calibrated flat background PDF of E_{ECL} . The original PDF (from MC) is used in the nominal data fit. The systematic uncertainty is obtained by fitting on data with these two PDF and check the signal yield deviation, which is estimated to be -12.89 in terms of number of yield.

About the uncertainty due to fixed end-point (fixed value is from MC) in the ARGUS function, we first check the inclusive data sample with the fixed ARGUS end-point, and it causes about 0.045% on the D^0 yield, which is much smaller than the statistical uncertainty. For the systematic uncertainty, we check the yield deviation with a floated ARGUS end-point in the data fit, which is estimated to be +0.05 in terms of number of yield.

- Peak background PDF ($D^0 \rightarrow \nu\bar{\nu}$):

Table 3.6 shows various sources of $E_{ECL} = 0$ peak. For the peak background PDF (D^0 background), we change the content of $E_{ECL} = 0$ peak with $\pm 1\sigma$ of D^0 decay modes' measured branching fraction to check the signal yield deviation. The uncertainty is estimated to be $^{+2.42}_{-2.56}$ in terms of number of yield.

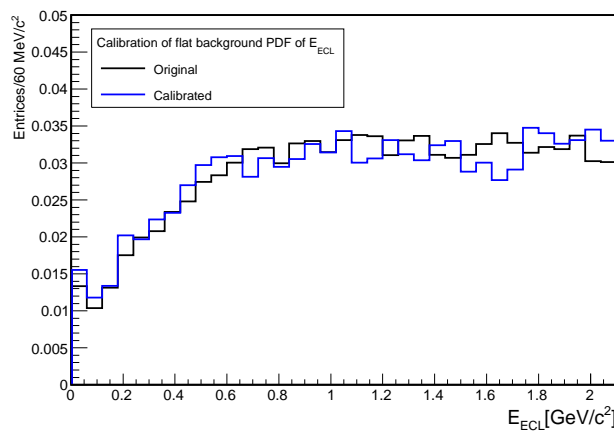


Figure 3.32: The original and calibrated flat background PDF of E_{ECL} .

- Signal PDF ($D^0 \rightarrow h^- \ell^+ \nu$):

The uncertainty due to shape-fixed signal PDF is studied by checking signal yield deviation between the fixed and floated signal PDF in $D^0 \rightarrow K^- e^+ \nu_e$.



The yields are 13167.8 and 13019.0 for fixed and floated signal PDF, respectively. The uncertainty is estimated to be -1.13%.

- Background PDF ($D^0 \rightarrow h^- \ell^+ \nu$):

The uncertainty due to shape-fixed background PDF is studied by checking signal yield deviation between the fixed and floated background PDF in $D^0 \rightarrow K^- \mu^+ \nu_\mu$. The yields are 5322.13 and 5207.36 for fixed and floated background PDF, respectively. The uncertainty is estimated to be -2.16%.

- Peak background PDF ($D^0 \rightarrow K^- \mu^+ \nu_\mu$ and $D^0 \rightarrow \pi^- \mu^+ \nu_\mu$):

For $D^0 \rightarrow K^- \mu^+ \nu_\mu$ and $D^0 \rightarrow \pi^- \mu^+ \nu_\mu$, the background contains a peaking structure near signal region, which is modeled as a PDF and is fixed in data fit. For the uncertainty due to shape-fixed peaking background PDF, we use two different functions (Breit-Wigner and Gaussian) to model the peaking background in $D^0 \rightarrow K^- \mu^+ \nu_\mu$, and check the signal yield deviation between these two cases. The yields are 5207.36 and 5229.26 for Breit-Wigner modeled and Gaussian modeled PDF, respectively. In the data fit of $D^0 \rightarrow K^- \mu^+ \nu_\mu$, the peaking background PDF is modeled as a Breit-Wigner function, so the uncertainty is estimated to be 0.42%. In the data fit of $D^0 \rightarrow \pi^- \mu^+ \nu_\mu$, the peaking background PDF is modeled as a Gaussian, so the uncertainty is estimated to be -0.42%.

- Reconstruction efficiency uncertainty:

The signal side selection efficiency of $D^0 \rightarrow f$ ($\epsilon(D^0 \rightarrow f|incl.D^0)$) is obtained by the ratio between the numbers of $D^0 \rightarrow f$ with and without all selection criteria, and all the numbers are obtained by fitting. We use the statistical uncertainty from fitting to estimate the reconstruction efficiency uncertainty. The summary is shown in Table 3.12.

mode	eff.	error
$D^0 \rightarrow K^- \pi^+$	$37053.1^{+192.74}_{-192.24} / 130156^{+451.47}_{-456.41}$	+0.64% -0.64%
$D^0 \rightarrow K^- \mu^+ \nu$	$29590^{+172.33}_{-171.71} / 131481^{+467.33}_{-466.42}$	+0.68% -0.68%
$D^0 \rightarrow K^- e^+ \nu$	$71607.1^{+267.86}_{-267.33} / 130817^{+459.33}_{-467.82}$	+0.51% -0.52%
$D^0 \rightarrow \pi^- \mu^+ \nu$	$4004.99^{+63.63}_{-62.94} / 8973.93^{+125.94}_{-127.01}$	+2.12% -2.12%
$D^0 \rightarrow \pi^- e^+ \nu$	$5020^{+71.18}_{-70.52} / 9387.84^{+130.46}_{-116.74}$	+1.99% -1.87%
$D^0 \rightarrow \nu\bar{\nu}$	$4224.01^{+63.32}_{-64.66} / 7447^{+85.63}_{-86.96}$	+1.89% -1.93%

Table 3.12: Summary of reconstruction efficiency uncertainties.

- Direct D^0 decay background:

For D^0 decay which is not decayed from $D^{*+} \rightarrow D^0 \pi^+$ but is decayed from

direct D^0 production, it peaks at the same region as signal in M_{miss}^2 and it is non-negligible for $D^0 \rightarrow K^-\pi^+$, $D^0 \rightarrow K^-\mu^+\nu_\mu$ and $D^0 \rightarrow K^-e^+\nu_e$ measurement. With tighter selection on recoil D^0 mass, the fraction can be reduced. Since it can not be distinguished from signal by fitting, we factor this into our signal. Therefore, both the efficiency and signal yield would be inflated by a factor $(1+r)$, and the branching fraction measurement won't be affected accordingly. To be conservative, we can directly use r as systematic uncertainty due to this kind of events. r value are 0.70% and 1.00% for $D^0 \rightarrow K^-\mu^+\nu_\mu$ and $D^0 \rightarrow K^-e^+\nu_e$, respectively.

- Veto on remaining detector information (track, π^0 , K_S^0 , K_L^0 , Λ , and $\bar{\Lambda}$):
For $D^0 \rightarrow \nu\bar{\nu}$ and some of $D^0 \rightarrow h^-\ell^+\nu_\ell$ study, the selection criteria include vetoes on the remaining detector information, e.g. tracks, π^0 , K_S^0 , K_L^0 , Λ and $\bar{\Lambda}$. The uncertainties due to them are obtained by using $D^0 \rightarrow K^-\pi^+$ to compare the ratio of MC events and ratio of signal yield from data under different vetoes. The comparison and uncertainties are shown in Table 3.13 and Table 3.14.

Veto	MC events	Signal yield	$Ratio_{MC}$	$Ratio_{data}$
None	$70309.7^{+265.80}_{-264.52}$	$13759^{+124.96}_{-125.67}$		
track	$69991.6^{+265.24}_{-263.88}$	$13692.3^{+124.61}_{-124.94}$	$0.9955^{+0.0053}_{-0.0053}$	$0.9952^{+0.0128}_{-0.0128}$
π^0	$53759.9^{+232.26}_{-231.47}$	$10091.1^{+107.09}_{-106.89}$	$0.7646^{+0.0044}_{-0.0044}$	$0.7334^{+0.0102}_{-0.0103}$
K_L^0	$49058.7^{+222.09}_{-220.90}$	$10875.8^{+111.61}_{-110.05}$	$0.6978^{+0.0041}_{-0.0041}$	$0.7904^{+0.0108}_{-0.0108}$
K_S^0 , Λ , and $\bar{\Lambda}$	$68768^{+263.57}_{-260.92}$	$13686.7^{+125.15}_{-124.72}$	$0.9781^{+0.0053}_{-0.0052}$	$0.9947^{+0.0128}_{-0.0128}$

Table 3.13: Comparison between MC and data under different vetoes.

Veto	$\frac{Ratio_{data}}{Ratio_{MC}}$	Uncertainty
track	$0.9997^{+0.0139}_{-0.0140}$	+1.39% -1.40%
π^0	$0.9592^{+0.0145}_{-0.0145}$	+1.51% -1.51%
K_L^0	$1.1329^{+0.0169}_{-0.0168}$	+1.49% -1.48%
K_S^0 , Λ , and $\bar{\Lambda}$	$1.0170^{+0.0142}_{-0.0142}$	+1.40% -1.40%

Table 3.14: Cabibration factors and uncertainties due to vetoes.

- Study of veto efficiency dependence on $D_{tag}^{(*)}/X_{frag}$ modes:
In order to check if there is dependence between signal side selection efficiency and $D_{tag}^{(*)}/X_{frag}$ modes, we check the ratio of MC events/signal yields with and without all vetoes (track, π^0 , K_S^0 , K_L^0 , Λ , and $\bar{\Lambda}$) are applied. The results are shown in Table 3.15 and Table 3.16, based on different $D_{tag}^{(*)}$ and X_{frag} cases, respectively.

For the systematic uncertainty of $D^0 \rightarrow \nu\bar{\nu}$ due to the vetoes, it is estimated to be $^{+4.73\%}_{-4.62\%}$ by weighted sum with the ratio of all $D_{tag}^{(*)}$ modes in signal MC and error corresponding to each modes in Table 3.15.





D_{tag}	D_{tag}^*	MC events before vetoes	after vetoes	$Ratio_{MC}$	Signal yields before vetoes	after vetoes	$Ratio_{data}$	$\frac{Ratio_{data}}{Ratio_{MC}}$	error
All	All	$70309.7^{+265.80}_{-264.52}$	$37053.1^{+192.74}_{-192.24}$	$0.5270^{+0.0034}_{-0.0034}$	$13759^{+124.96}_{-125.67}$	$7892.84^{+93.91}_{-94.31}$	$0.5736^{+0.0086}_{-0.0086}$	$1.0885^{+0.0177}_{-0.0178}$	$+1.63\%$ -1.63%
D^0		$21372^{+146.50}_{-145.88}$	$11250^{+106.42}_{-105.71}$	$0.5264^{+0.0061}_{-0.0061}$	$5612.12^{+75.13}_{-74.70}$	$3193.86^{+56.99}_{-56.05}$	$0.5691^{+0.0127}_{-0.0125}$	$1.0811^{+0.0272}_{-0.0269}$	$+2.52\%$ -2.49%
D^+		$13596.8^{+117.13}_{-116.08}$	$7162.9^{+85.07}_{-84.20}$	$0.5268^{+0.0077}_{-0.0077}$	$3001.11^{+55.01}_{-54.56}$	$1731^{+41.94}_{-41.28}$	$0.5768^{+0.0175}_{-0.0173}$	$1.0949^{+0.0369}_{-0.0365}$	$+3.37\%$ -3.33%
Λ_c^+		$4718.99^{+69.04}_{-68.35}$	$2249.07^{+47.69}_{-47.16}$	$0.4766^{+0.0123}_{-0.0121}$	$529.989^{+23.37}_{-22.68}$	$284^{+17.19}_{-16.52}$	$0.5359^{+0.0401}_{-0.0387}$	$1.1243^{+0.0890}_{-0.0861}$	$+7.92\%$ -7.66%
D_s^+		$3671^{+60.93}_{-60.26}$	$1863.01^{+43.48}_{-42.84}$	$0.5075^{+0.0145}_{-0.0143}$	$602.072^{+24.80}_{-24.28}$	$326.003^{+18.39}_{-17.73}$	$0.5415^{+0.0378}_{-0.0367}$	$1.0669^{+0.0805}_{-0.0783}$	$+7.34\%$ -7.34%
D^0	$D^{*+} \rightarrow D^0 \pi^+$	$8536.97^{+92.76}_{-92.03}$	$4565.01^{+67.89}_{-67.24}$	$0.5347^{+0.0098}_{-0.0098}$	$1388.03^{+37.57}_{-36.95}$	$792.001^{+28.48}_{-27.81}$	$0.5706^{+0.0257}_{-0.0251}$	$1.0671^{+0.0519}_{-0.0509}$	$+4.86\%$ -4.77%
D^0	$D^{*0} \rightarrow D^0 \pi^0$	$5940.92^{+77.50}_{-76.66}$	$3245.05^{+57.25}_{-56.68}$	$0.5462^{+0.0120}_{-0.0119}$	$942.023^{+31.00}_{-30.38}$	$566.069^{+24.06}_{-23.53}$	$0.6009^{+0.0323}_{-0.0316}$	$1.1001^{+0.0639}_{-0.0626}$	$+5.81\%$ -5.69%
D^0	$D^{*0} \rightarrow D^0 \gamma$	$7042.92^{+84.34}_{-83.51}$	$3842.06^{+62.26}_{-61.71}$	$0.5455^{+0.0110}_{-0.0109}$	$1200^{+34.97}_{-34.31}$	$697.977^{+26.78}_{-26.06}$	$0.5816^{+0.0280}_{-0.0274}$	$1.0662^{+0.0557}_{-0.0545}$	$+5.22\%$ -5.11%
D^+	$D^{*+} \rightarrow D^+ \pi^0$	$2217.03^{+47.39}_{-46.79}$	$1187.06^{+34.72}_{-34.19}$	$0.5354^{+0.0194}_{-0.0191}$	$297.003^{+17.57}_{-16.91}$	$175.008^{+13.56}_{-12.91}$	$0.5892^{+0.0574}_{-0.0549}$	$1.1005^{+0.1144}_{-0.1098}$	$+10.40\%$ -9.98%
D_s^+	$D_s^{*+} \rightarrow D_s^+ \gamma$	$3213.05^{+56.97}_{-56.40}$	$1689.03^{+41.40}_{-40.80}$	$0.5257^{+0.0159}_{-0.0157}$	$270.003^{+16.76}_{-16.10}$	$157.989^{+12.92}_{-12.23}$	$0.5851^{+0.0601}_{-0.0572}$	$1.1131^{+0.1191}_{-0.1137}$	$+10.70\%$ -10.22%

Table 3.15: MC and data veto eff. based on $D_{tag}^{(*)}$ modes.



X_{frag}	MC events		$Ratio_{MC}$	Signal yields		$Ratio_{data}$	$Ratio_{data}$ $Ratio_{MC}$	error
	before vetoes	after vetoes		before vetoes	after vetoes			
All	70309.7 ^{+265.80} _{-264.52}	37053.1 ^{+192.74} _{-192.24}	0.5270 ^{+0.0034} _{-0.0034}	13759.1 ^{+124.96} _{-125.67}	7892.84 ^{+93.91} _{-94.31}	0.5736 ^{+0.0086} _{-0.0086}	1.0885 ^{+0.0177} _{-0.0178}	+1.63%
Nothing	183.985 ^{+13.92} _{-13.22}	92.0042 ^{+9.92} _{-9.27}	0.5001 ^{+0.0659} _{-0.0619}	275.993 ^{+16.96} _{-16.28}	152 ^{+12.66} _{-12.00}	0.5507 ^{+0.0570} _{-0.0543}	1.1013 ^{+0.1845} _{-0.1742}	+16.75%
π^\pm	8589.78 ^{+93.23} _{-92.14}	4470 ^{+67.19} _{-66.52}	0.5204 ^{+0.0096} _{-0.0095}	2719.9 ^{+52.59} _{-51.72}	1534.02 ^{+39.48} _{-38.85}	0.5640 ^{+0.0182} _{-0.0179}	1.0838 ^{+0.0403} _{-0.0397}	+3.72%
π^0	1179.14 ^{+34.53} _{-34.14}	651.001 ^{+25.85} _{-25.18}	0.5521 ^{+0.0272} _{-0.0267}	473.939 ^{+22.17} _{-21.38}	277 ^{+16.98} _{-16.31}	0.5845 ^{+0.0451} _{-0.0434}	1.0586 ^{+0.0969} _{-0.0937}	+9.15%
$\pi^\pm\pi^0$	12829.9 ^{+113.67} _{-112.87}	6959.91 ^{+83.85} _{-83.00}	0.5425 ^{+0.0081} _{-0.0080}	2437.91 ^{+49.80} _{-48.96}	1399.87 ^{+37.88} _{-36.95}	0.5742 ^{+0.0195} _{-0.0190}	1.0585 ^{+0.0392} _{-0.0385}	+3.71%
$\pi^\pm\pi^\mp$	9642.77 ^{+98.76} _{-97.64}	4994.91 ^{+71.10} _{-70.26}	0.5180 ^{+0.0091} _{-0.0090}	1907.94 ^{+44.08} _{-43.29}	1100.98 ^{+33.54} _{-32.83}	0.5771 ^{+0.0221} _{-0.0216}	1.1140 ^{+0.0469} _{-0.0460}	+4.21%
$\pi^\pm\pi^\pm\pi^\mp$	19570 ^{+140.22} _{-139.56}	10202 ^{+101.36} _{-100.65}	0.5213 ^{+0.0064} _{-0.0063}	3259.28 ^{+57.14} _{-57.04}	1860.74 ^{+43.74} _{-42.54}	0.5709 ^{+0.0167} _{-0.0164}	1.0951 ^{+0.0348} _{-0.0342}	+3.18%
$\pi^\pm\pi^\pm\pi^0$	13640 ^{+117.12} _{-116.46}	7352.98 ^{+86.10} _{-85.40}	0.5391 ^{+0.0078} _{-0.0078}	2048.96 ^{+45.64} _{-44.89}	1182.85 ^{+34.89} _{-33.91}	0.5773 ^{+0.0213} _{-0.0208}	1.0709 ^{+0.0425} _{-0.0416}	+3.97%
With K^+K^-	4674.02 ^{+68.68} _{-68.05}	2330.02 ^{+48.59} _{-47.96}	0.4985 ^{+0.0127} _{-0.0126}	718.03 ^{+27.10} _{-26.49}	415.999 ^{+20.73} _{-20.06}	0.5794 ^{+0.0362} _{-0.0352}	1.1622 ^{+0.0785} _{-0.0764}	+6.75%

Table 3.16: MC and data veto eff. based on X_{frag} cases.



3.8 Physics Results

3.8.1 $D^0 \rightarrow h^- \ell^+ \nu_\ell$

For the four $D^0 \rightarrow h^- \ell^+ \nu_\ell$ decays, clear signal yields are observed. The calibration factors on efficiency are due to K/π ID, ℓ ID (e/μ) from Table 3.10, and constraints on remaining detector information (tracks, π^0) from Table 3.14. The summary of physics result, including signal side selection efficiency, signal yields, all calibration factors and measured \mathcal{B} , is shown in Table 3.17. The summary of systematic uncertainties for the four $D^0 \rightarrow h^- \ell^+ \nu_\ell$ decays is shown in Table 3.18.

Mode	$D^0 \rightarrow K^- \mu^+ \nu_\mu$	$D^0 \rightarrow K^- e^+ \nu_e$	$D^0 \rightarrow \pi^- \mu^+ \nu_\mu$	$D^0 \rightarrow \pi^- e^+ \nu_e$
eff.	22.5%	54.74%	44.63%	53.47%
Yield	$5207.36^{+90.23}_{-89.77}$	$13019.0^{+137.65}_{-136.74}$	$694.00^{+53.10}_{-50.92}$	$956.89^{+49.55}_{-48.74}$
$\mathcal{C}_{K/\pi\text{ID}}$	0.9993	0.9899	0.9606	0.9583
$\mathcal{C}_{\ell\text{ID}}$	0.9730	0.9698	0.9697	0.9732
$\mathcal{C}_{\text{track}}$	0.9997			0.9997
\mathcal{C}_{π^0}	0.9592			0.9592
Measured \mathcal{B} (10^{-3})	$35.7^{+0.6+2.1}_{-0.6-2.1}$	$35.7^{+0.4+2.0}_{-0.4-2.1}$	$2.40^{+0.18+0.14}_{-0.18-0.14}$	$2.88^{+0.15+0.18}_{-0.15-0.18}$
PDG fit (10^{-3})[8]	$33.0^{+1.3}_{-1.3}$	$35.7^{+0.6}_{-0.6}$	$2.38^{+0.24}_{-0.24}$	$2.89^{+0.08}_{-0.08}$
PDG average (10^{-3})[8]		$35.0^{+0.5}_{-0.5}$		$2.87^{+0.08}_{-0.08}$

Table 3.17: Summary of $D^0 \rightarrow h^- \ell^+ \nu_\ell$ measurement results. For the measured \mathcal{B} , the first uncertainties are statistical and the second are systematic. The calibration factors are obtained by Table 3.10 and Table 3.14.

3.8.2 $D^0 \rightarrow \nu \bar{\nu}$

The summary of fitting strategy of $D^0 \rightarrow \nu \bar{\nu}$ measurement is shown in Table 3.19. The signal M_{D^0} PDF shape is calibrated by the fudge factors from $D^0 \rightarrow K^- \pi^+$ control sample: (Mean, Width) = (1.86483, 0.00092199) \rightarrow (1.86483, 0.00110268). The width is inflated with a factor about 1.20, while the mean remains the same. The signal E_{ECL} PDF is from signal MC distribution, because the $D^0 \rightarrow K^- \pi^+$ data and MC have very similar shape, as shown in Figure 3.30.

The summary of systematic uncertainties for $D^0 \rightarrow \nu \bar{\nu}$ measurement is shown in Table 3.20.

The data fit result of $D^0 \rightarrow \nu \bar{\nu}$ is shown in Figure 3.33 and Table 3.21. The



	$D^0 \rightarrow K^- \mu^+ \nu$	$D^0 \rightarrow K^- e^+ \nu$	$D^0 \rightarrow \pi^- \mu^+ \nu$	$D^0 \rightarrow \pi^- e^+ \nu$
Tracking	$\pm 0.70\%$	$\pm 0.70\%$	$\pm 0.70\%$	$\pm 0.70\%$
Charged PID	$\pm 2.08\%$	$\pm 2.29\%$	$\pm 2.06\%$	$\pm 2.15\%$
$N_{incl}^{D^0}$	$\pm 4.9\%$	$\pm 4.9\%$	$\pm 4.9\%$	$\pm 4.9\%$
Signal PDF	-1.13%		-1.13%	-1.13%
Flat background PDF		-2.16%		
Peaking background PDF	$+0.42\%$		-0.42%	
Reconstruction eff.	$+0.68\%$	$+0.51\%$	$+2.12\%$	$+1.99\%$
Direct D^0 background	$\pm 0.70\%$	-0.52%	-2.12%	-1.87%
Track veto	$+1.39\%$	$\pm 1.00\%$		$+1.39\%$
π^0 veto	-1.40%			-1.40%
	$+1.51\%$			$+1.51\%$
	-1.51%			-1.51%
Total	$+5.85\%$ -5.94%	$+5.57\%$ -5.97%	$+5.77\%$ -5.89%	$+6.11\%$ -6.18%

Table 3.18: Summary of systematic uncertainties for $D^0 \rightarrow h^- \ell^+ \nu_\ell$ study.



	Template	PDF	parameters	note
Signal	M_{D^0}	Breit-Wigner	all fixed	Calibrated by $D^0 \rightarrow K^- \pi^+$ data/MC
Signal	E_{ECL}	Histogram	no	Validity is checked by $D^0 \rightarrow K^- \pi^+$
Peak bck	M_{D^0}	Breit-Wigner	all floated	
Peak bck	E_{ECL}	Histogram	no	Shape is from MC.
Flat bck	M_{D^0}	ARGUS	end-point fixed	End-point is fixed as MC
Flat bck	E_{ECL}	Histogram	no	Shape is from MC.

Table 3.19: Fitting strategy for $D^0 \rightarrow \nu \bar{\nu}$ measurement.

	in %
N_{D^0}	$\pm 0.2(\text{stat.}) \pm 4.9(\text{syst.})$
Reconstruction eff. (Table 3.12)	± 1.9
Vetoos eff. (Table 3.15)	+4.7 -4.6
Total	+7.1 -7.0
	in Number
Yield bias	+0.5
Signal PDF in E_{ECL}	+2.3
D^0 background PDF in E_{ECL}	+2.4 -2.6
Non- D^0 background PDF in E_{ECL}	-12.9
Signal PDF in M_{D^0}	+0.2 -0.1
Non- D^0 background PDF in M_{D^0}	+0.1
Total	+3.4 -13.2

Table 3.20: Summary of systematic uncertainties for $D^0 \rightarrow \nu \bar{\nu}$ study.



fitted signal yield is $-10.15_{-20.75}^{+22.10}$ which is consistent with zero.

Since the observed yield of $D^0 \rightarrow \nu\bar{\nu}$ decay is not significant, we evaluate the 90% confidence level (C.L.) Bayesian upper limits. The upper limit on signal yield N is obtained by integrating the likelihood function:

$$\int_0^N \mathcal{L}(n)dn = 0.9 \int_0^\infty \mathcal{L}(n)dn, \quad (3.7)$$

where $\mathcal{L}(n)$ denote the likelihood of fit result with condition that the number of signal yield is fixed at n .

The systematic uncertainties are taken into account by replacing $\mathcal{L}(n)$ with a smearing likelihood function:

$$\mathcal{L}_{smear}(n) = \int_0^\infty \mathcal{L}(n') \frac{e^{-\frac{(n-n')^2}{2\Delta n^2}}}{\sqrt{2\pi}\Delta n} dn' \quad (3.8)$$

The likelihood functions are shown in Figure 3.34.

The signal selection eff. is 56.7%. The calibration factor due to vetoes is estimated by the studies in Table 3.14: $C_{vetoes}(= C_{track} \times C_{\pi^0} \times C_{K_L^0} \times C_{K_S^0, \Lambda(\bar{\Lambda})}) = 1.1$. Therefore, the upper limit of branching fraction is determined to be $\mathcal{B}(D^0 \rightarrow \nu\bar{\nu}) < 8.8 \times 10^{-5}$ at the 90% C.L.

Floated variables	Fit result
N_{sig}	$-10.15_{-20.75}^{+22.10}$
$N_{peakbck}$	$2838.58_{-88.73}^{+91.62}$
$N_{flatbck}$	$8591.42_{-116.37}^{+115.55}$
$Mean_{peakbck}$	$1.86481_{-0.0000212085}^{+0.0000210809}$
$Width_{peakbck}$	$0.00130834_{-0.0000531234}^{+0.0000554981}$
Shape parameter of flat bck ARGUS	$-23.6599_{-1.6586}^{+1.70315}$

Table 3.21: Data fit result of $D^0 \rightarrow \nu\bar{\nu}$ measurement.

3.9 Summary

In conclusion, we have performed a search for D^0 decay to $\nu\bar{\nu}$ and $h^-\ell^+\nu_\ell$ ($h = K, \pi$, and $\ell = e, \mu$) using the data sample collected near the $\Upsilon(4S)$ and $\Upsilon(5S)$ with

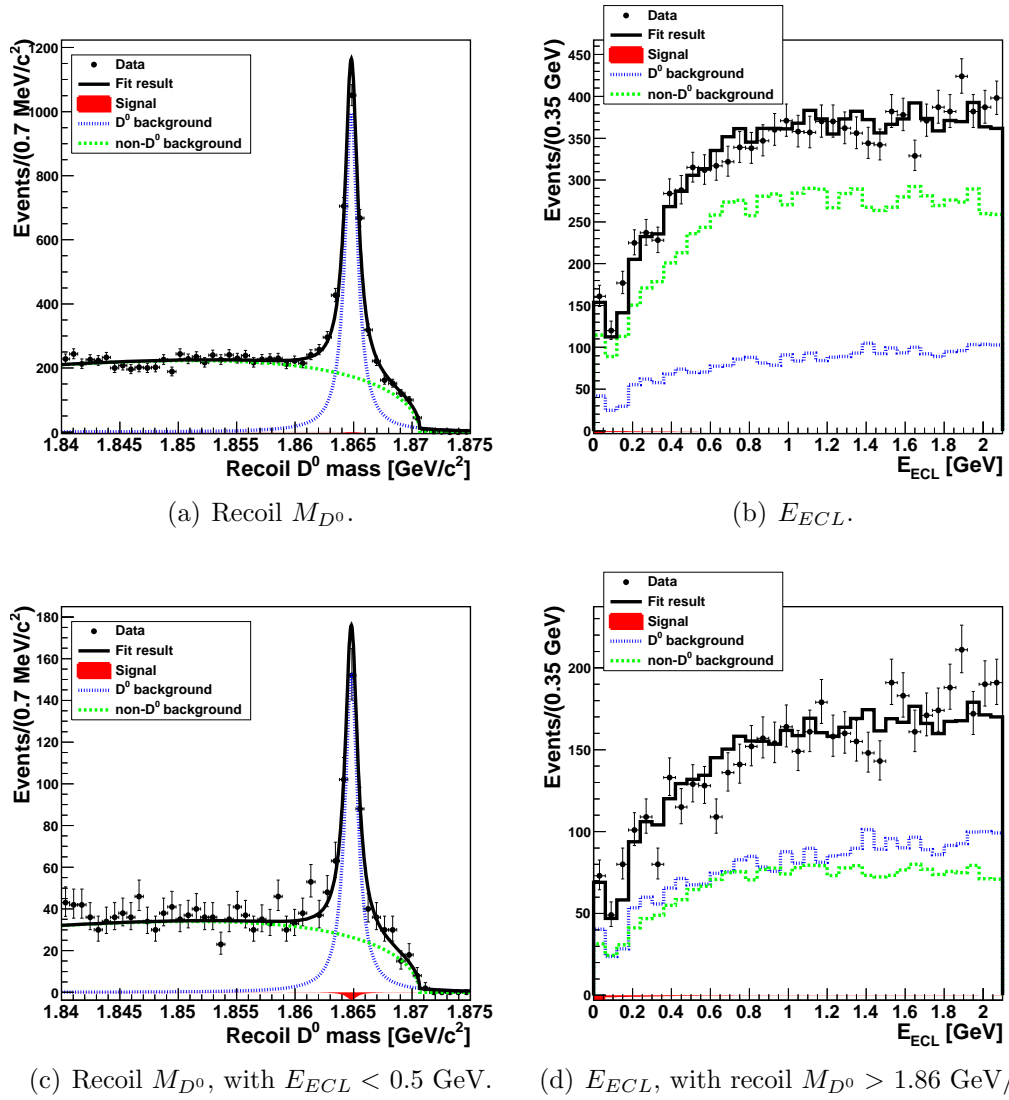


Figure 3.33: Data fit result of $D^0 \rightarrow \nu\bar{\nu}$ measurement.

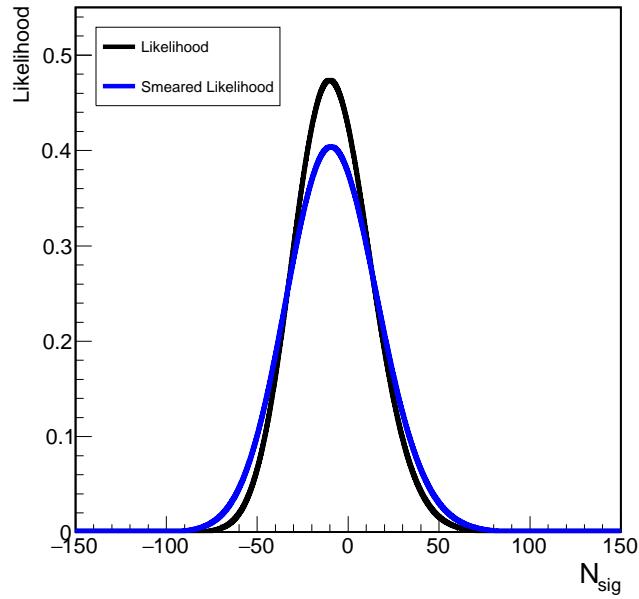


Figure 3.34: Likelihood distributions obtained by $D^0 \rightarrow \nu\bar{\nu}$ data fits.

Belle detector at the KEKB asymmetric energy e^+e^- collider. We develop a charm flavor tagging method in order to measure the absolute branching fraction of the D^0 decays with missing final state. Since no significant signal is found, we set an upper limit of 8.8×10^{-5} for the branching fraction of $D^0 \rightarrow \nu\bar{\nu}$ at the 90% confidence level. In addition, the measurement of $D^0 \rightarrow h^-\ell^+\nu_\ell$ is also performed and the measured branching fractions are consistent with the PDG world average.



Chapter 4

Search for $B^0 \rightarrow p\bar{\Lambda}\pi^-\gamma$ Decay at Belle

4.1 Motivation

In the Standard Model (SM), the heavy b quark can decay to an energetic s quark and a hard photon via the penguin loop diagram. The inclusive measurement of the branching fraction from B meson decays for the above process, $\mathcal{B}(B \rightarrow X_s\gamma)$, is very sensitive to physics beyond the SM since new heavy particles can contribute in the loop at the leading order. The up-to-date next-to-next-to-leading order SM calculation gives $\mathcal{B}(B \rightarrow X_s\gamma) = (3.15 \pm 0.23) \times 10^{-4}$ for $E_\gamma > 1.6$ GeV [49], which is consistent with the current world average of the experimental results, $\mathcal{B}(B \rightarrow X_s\gamma) = (3.40 \pm 0.21) \times 10^{-4}$ [8, 50, 51, 52].

In the Monte Carlo (MC) simulation of the $s \rightarrow X_s$ fragmentation and hadronization processes by JETSET [53], the X_s with a Λ in the final state contributes only at the 1% level. This is consistent with the known baryonic B decay rate, $\mathcal{B}(B^+ \rightarrow p\bar{\Lambda}\gamma) = (2.45_{-0.38}^{+0.44} \pm 0.22) \times 10^{-6}$ [8, 54]. There is an intriguing feature of this three-body decay: the mass of the $p\bar{\Lambda}$ system is peaked near threshold. A similar feature is seen in many other hadronic three-body B decay processes. In multi-body hadronic baryonic B decays, hierarchy in the branching fractions is also observed in different cases as following [8]:

- $b \rightarrow c$:



- $\mathcal{B}(B^+ \rightarrow p\bar{\Lambda}_c\pi^+\pi^0) = (1.81 \pm 0.29_{-0.50}^{+0.52}) \times 10^{-3}$
 - $\mathcal{B}(B^0 \rightarrow p\bar{\Lambda}_c\pi^+\pi^-) = (1.12 \pm 0.14 \pm 0.29) \times 10^{-3}$
 - $\mathcal{B}(B^+ \rightarrow p\bar{\Lambda}_c\pi^+) = (2.8 \pm 0.8) \times 10^{-4}$
 - $\mathcal{B}(B^0 \rightarrow p\bar{\Lambda}_c\pi^0) = (1.9 \pm 0.2 \pm 0.5) \times 10^{-4}$
 - $\mathcal{B}(B^0 \rightarrow p\bar{\Lambda}_c) = (2.0 \pm 0.4) \times 10^{-5}$
- $b \rightarrow s$:
 - $\mathcal{B}(B^+ \rightarrow p\bar{\Lambda}\pi^+\pi^-) = (5.92_{-0.84}^{+0.88} \pm 0.69) \times 10^{-6}$
 - $\mathcal{B}(B^0 \rightarrow p\bar{\Lambda}\pi^-) = (3.14 \pm 0.29) \times 10^{-6}$
 - $\mathcal{B}(B^+ \rightarrow p\bar{\Lambda}\pi^0) = (3.00_{-0.53}^{+0.61} \pm 0.33) \times 10^{-6}$
 - $\mathcal{B}(B^+ \rightarrow p\bar{\Lambda}) < 3.2 \times 10^{-7}$

These features motivate our interest in the search for $B^0 \rightarrow p\bar{\Lambda}\pi^-\gamma$. Figure 4.1 shows the lowest order SM decay diagram for $B^0 \rightarrow p\bar{\Lambda}\pi^-\gamma$. It proceeds via the radiative penguin process. The $p\bar{\Lambda}$ system in this decay will have a smaller maximum kinetic energy than in $B^+ \rightarrow p\bar{\Lambda}\gamma$ due to the extra pion in the X_s fragmentation process. This matches the threshold enhancement effect naturally and implies a higher decay rate [55]. The measured branching fraction of $B^0 \rightarrow p\bar{\Lambda}\pi^-\gamma$ can be useful to tune the parameters in JETSET and, in the case of a large enhancement of the branching fraction, the uncertainty on the measurement of $\mathcal{B}(B \rightarrow X_s\gamma)$ would be reduced using a sum of exclusive final states.

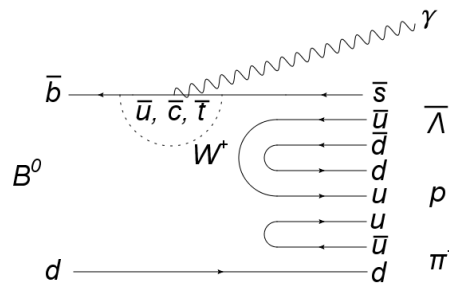


Figure 4.1: Decay diagram of $B^0 \rightarrow p\bar{\Lambda}\pi^-\gamma$.

4.2 Data Sample

This analysis is based on the data collected by the Belle detector at the KEKB asymmetric-energy e^+e^- collider at the $\Upsilon(4S)$ resonance. The total number of $B\bar{B}$



events for experiment 7 to 65 is 771.581 ± 10.566 million.

4.2.1 Blind Analysis and Monte Carlo Samples

We study signal and backgrounds depending on a blind study with Monte Carlo (MC) simulation method, which means using MC to simulate signal and background events for the optimization and finalizing the fitting procedure with an assumed branching fraction of 10^{-5} .

All the MC samples are generated with EvtGen [39] package and detector simulation is done with GEANT [40] package. These events are distributed into different experiment condition according to the proportion of each experiment. For the signal decays study, 771000 signal MC events are generated. For the background study, the continuum background MC ($e^+e^- \rightarrow q\bar{q}$, $q = u, d, s, c$) and the B generic background MC (B decay with $b \rightarrow c$ transition) are considered. Also, 50 times rare B decays (B decay with $b \rightarrow u, d, s$ transition) MC is taken into account.

All of these MC and data are based on the new tracking algorithm, i.e., case B data in Belle environment setting.

4.3 Signal MC Generation

According to the previous study on the baryonic B decay modes, such as $B^+ \rightarrow p\bar{\Lambda}\gamma$ [54, 8], we observe that the baryon-antibaryon mass distribution peaks near threshold. Besides, for B decay with $b \rightarrow s\gamma$, γ usually has an higher energy. Therefore, in our MC decay model, we assume that $p\bar{\Lambda}\pi^-$ is decayed from one particle X_s with mass to be $2.5 \text{ GeV}/c^2$ and the width to be $0.3 \text{ GeV}/c^2$ from B . $B^+ \rightarrow X_s + \gamma$ is a two-body decay, and $X_s \rightarrow p + \bar{\Lambda} + \pi^-$ is a three-body phase space decay. The X_s mass distribution from signal MC is a simple Breit-Wigner distribution, which is shown in Figure 4.3. The $p\bar{\Lambda}$ invariant mass distribution from signal MC is shown in Figure 4.2.

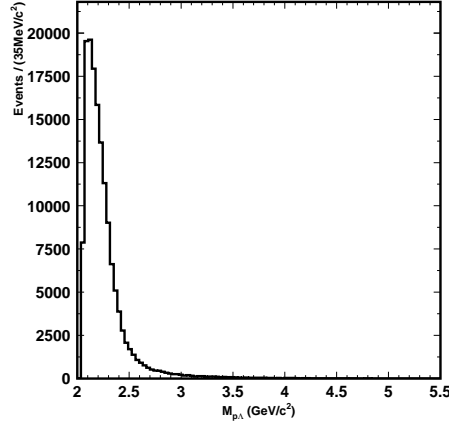


Figure 4.2: $p\bar{\Lambda}$ invariant mass distribution obtained by signal MC.

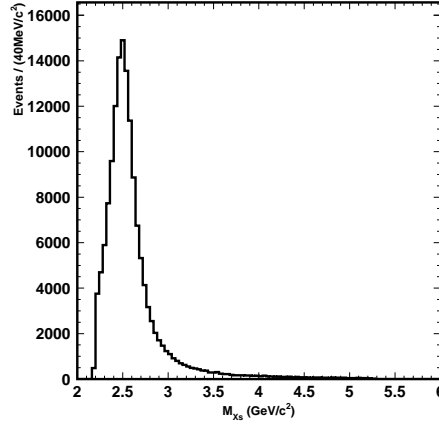


Figure 4.3: X_s mass distribution obtained by signal MC.

4.4 Event Selection and B Reconstruction

The event selection criteria are based on the information obtained by the tracking system (SVD and CDC) and the hadron identification system (CDC, ACC and TOF).

- Charged Proton, Pion Selection:

All the charged tracks except those from B decays are required to satisfy track quality criteria based on the track impact parameter relative to the interaction point (IP). The deviations from the IP position are required to be within ± 0.3 cm in the transverse (x-y) plane, and within ± 3 cm in the z direction, where the z axis is opposite the position beam direction. For the likelihood values L_p , L_K ,

L_π of each track, that is a proton, kaon, or pion, respectively, are determined from the information provided by the hadron identification system. The track is identified as a proton if $L_p/(L_p + L_K) > 0.6$ and $L_p/(L_p + L_\pi) > 0.6$, or as a pion if $L_\pi/(L_\pi + L_K) > 0.6$. The efficiency for identifying a pion is about 95%, depending on the momentum of the track, while the probability for a kaon to be misidentified as a pion is less than 10%. The efficiency for identifying a proton is about 95%, while the probability for a kaon or a pion to be misidentified as a proton is less than 10%. The efficiency and misidentification probability are averaged over the momentum of the particles in the final state.

- Λ Selection:

The Λ 's are obtained by Mdst_Vee2 bank. We apply good Λ selection [56] to reject combinatorial background. The invariant mass of Λ candidate ($m_{p\pi^-}$) is required to be within 1.111 GeV/ c^2 to 1.121 GeV/ c^2 , as shown on Figure 4.4. $L_p/(L_p + L_\pi)$ of Λ 's daughter proton is required to be greater than 0.6 in order to reject possible feed-across of K_S^0 and random combinations of off-IP pion tracks.

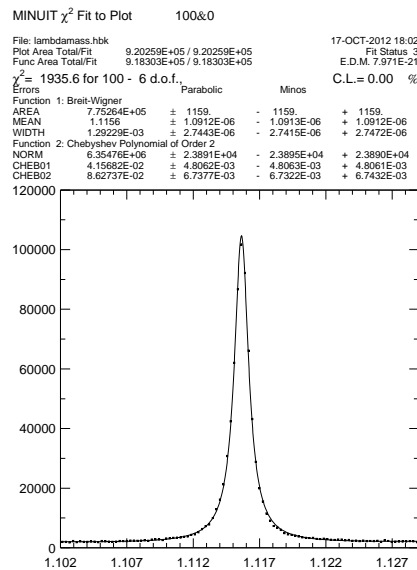


Figure 4.4: Λ mass ($M_{p\pi^-}$) distribution of signal MC.

- γ Selection:

The γ are obtained by Mdst_Gamma bank. We required that the γ 's energy in CM frame should be larger than 1.7 GeV, as shown in Figure 4.5.

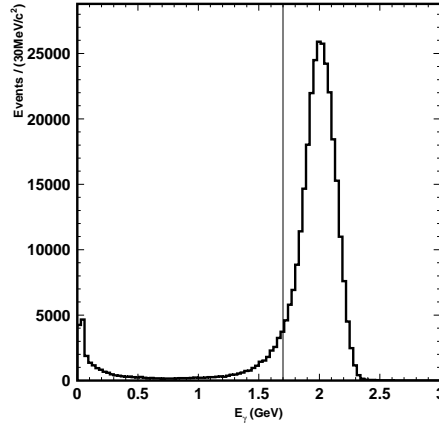


Figure 4.5: The γ energy distribution in CM frame of signal MC and the selected region.

- B vertex fit:

We use the tracks of p and π^- to determine the B vertex and the vertex fit is required to be successful.

- Best candidate selection:

If more than one reconstructed B candidate is found in a signal event, we choose the best candidate which is with the smaller sum of χ^2 of B vertex fit and χ^2 of Λ vertex fit. Multiple candidates are mainly due to the misreconstruction using a pion from the other B meson. The average multiplicity is 1.4 for signal MC and 2.2 for data.

- B reconstruction:

The B^0 candidates are reconstructed from the four momentum combination of proton, $\bar{\Lambda}$, π^- and γ . We use distributions of two kinetic variables in the CM frame to identify the reconstructed B meson candidates: the beam-energy-constrained mass M_{bc} , and the energy difference ΔE , which are defined as:

$$M_{bc} \equiv \sqrt{E_{beam}^2 - p_B^2} \quad (4.1)$$

$$\Delta E \equiv E_B - E_{beam}, \quad (4.2)$$

where E_{beam} is the beam energy, and p_B and E_B are the momentum and energy, respectively, of the reconstructed B^0 meson. The candidate region is defined as $-0.4 \text{ GeV} < \Delta E < 0.3 \text{ GeV}$ and $5.24 \text{ GeV}/c^2 < M_{bc} < 5.29 \text{ GeV}/c^2$. The signal box region is defined as $-0.05 \text{ GeV} < \Delta E < 0.05 \text{ GeV}$ and $5.27 \text{ GeV}/c^2 < M_{bc} < 5.29 \text{ GeV}/c^2$. The summary of selection criteria is shown in

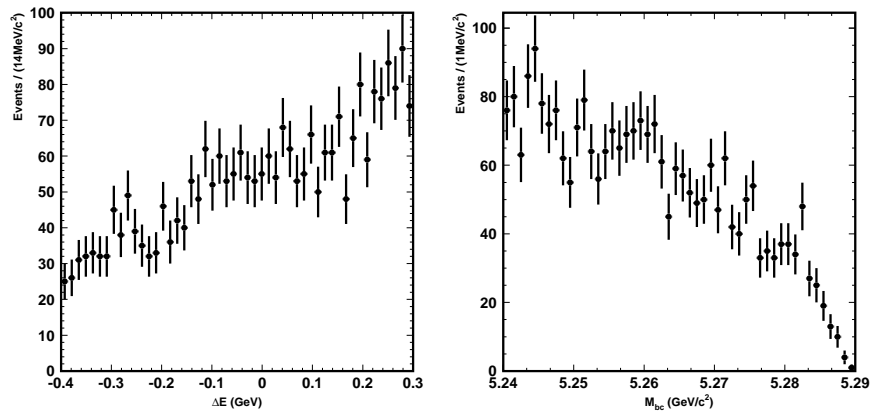


Table 4.3.

4.5 Background Suppression

4.5.1 Continuum Background

The main background is from the continuum $e^+e^- \rightarrow q\bar{q}$ ($q = u, d, s, c$) events. Continuum background MC ($q\bar{q}$ MC) is generated. The ΔE and M_{bc} distribution of the continuum background MC from all the experiments are shown in Figure 4.6.

Figure 4.6: The ΔE and M_{bc} distribution of the continuum background MC.



4.5.2 Continuum Background Suppression

The dominant background for this study is from the continuum processes. The difference between $B\bar{B}$ events and the continuum background is event topology ($B\bar{B}$ events: spherical distribution; continuum background: two jet-like distribution). The method of continuum background suppression is based upon such a topological difference and Fisher discriminant [57].

Kakuno Super Fox-Wolfram(KSFW)

KSFW is an improved version of the super-Fox-Wolfram method, which is a combination of six normalized Fox-Wolfram moments [58] and is first proposed by R. Enomoto. The variables of KSFW are defined as the following:

$$KSFW = \sum_{l=0}^4 R_l^{so} + \sum_{l=0}^4 R_l^{oo} + \gamma \sum_{l=0}^{N_t} |(P_t)_n| \quad (4.3)$$

whrer P_t means total transverse momentum, summing up the momenta of all particles (1 variables). And R_l^{so} is defined as:

$$R_l^{so} = \frac{\alpha_c(H_{charged})_l^{so} + \alpha_n(H_{neutral})_l^{so} + \alpha_m(H_{missing})_l^{so}}{E_{beam} - \Delta E} \quad (4.4)$$

as $l=1,3$ (2 variables)

$$(H_{charged})_l^{so} = \beta_l^{so} \sum_i \sum_{j_x} Q_i Q_{j_x} |p_i| |p_{j_x}| P_l(\cos\theta_{ij_x}) \quad (4.5)$$

$$(H_{neutral})_l^{so} = (H_{missing})_l^{so} \quad (4.6)$$

as $l=0,2,4$: (9 variables)

$$(H_x)_l^{so} = \sum_i \sum_{j_x} \beta_l^{so} |p_i| |p_{j_x}| P_l(\cos\theta_{ij_x}) \quad (4.7)$$

and i means the daughter of B_{sig} ; j means others. On the other hand, x means charged, neutral or missing; Q_x, Q_{j_x} are the electrical charged of particle i and j_x , respectively. P_l is the l -th Legendre polynomial; θ_{ij_x} is the angle particle i and particle j_x . And R_l^{oo} is defined as:

as $l=1,3$: (2 variables)

$$R_l^{oo} = \frac{\beta_l^{oo} \sum_j \sum_{k(\neq j)} Q_j Q_k |p_j| |p_k| P_l(\cos\theta_{jk})}{(E_{beam} - \Delta E)^2} \quad (4.8)$$

as $l=0,2,4$: (3 variables)

$$R_l^{oo} = \frac{\beta_l^{oo} \sum_j \sum_{k(\neq j)} |p_j| |p_k| P_l(\cos\theta_{jk})}{(E_{beam} - \Delta E)^2} \quad (4.9)$$

and j, k means others. Then the missing mass is defined as:

as $E_{\Upsilon(4S)} - \sum_{n=1}^{N_t} E_n > 0$:

$$MM^2 = (E_{\Upsilon(4S)} - \sum_{n=1}^{N_t} E_n)^2 - (\sum_{n=1}^{N_t} \vec{p}_n)^2 \quad (4.10)$$

as $E_{\Upsilon(4S)} - \sum_{n=1}^{N_t} E_n < 0$:

$$MM^2 = -((E_{\Upsilon(4S)} - \sum_{n=1}^{N_t} E_n)^2 - (\sum_{n=1}^{N_t} \vec{p}_n)^2) \quad (4.11)$$

Since the missing mass is related to the value of KSF \bar{W} , we divide the missing into seven regions, as shown in Table 4.1.

Region	1	2	3	4
$MM^2(GeV/c^2)$	< -0.5	$-0.5 \sim 0.3$	$0.3 \sim 1.0$	$1.0 \sim 2.0$
Region	5	6	7	
$MM^2(GeV/c^2)$	$2.0 \sim 3.5$	$3.5 \sim 6.0$	> 6.0	

Table 4.1: The regions of missing mass of KSF \bar{W} .

B flight direction

The θ_B is the angle between the B flight direction and the beam direction in the $\Upsilon(4S)$ rest frame. In the decay $\Upsilon(4S) \rightarrow B\bar{B}$, a vector particle (spin-1) decays to two scalar particles (spin-0). The angular distribution will obey $1 - \cos^2\theta_B$ formula based on the quantum physics, while the distribution is quite flat for $q\bar{q}$ backgrounds. The distributions of $\cos\theta_B$ are shown in Figure 4.7.



4.5.3 Likelihood Ratio

We pick 17 KSFW moments as the input variables for a Fisher discriminants [59]. The Fisher discriminator, \mathcal{F} , is a method that combines n-dimensional variables into one dimension by a linearly weight sum, with the coefficient for each variable is optimized to separate the signal and the background.

$$F = \vec{W} \cdot \vec{V} \quad (4.12)$$

where \vec{W} is a row vector consisting of the input variables. In addition to the Fisher discriminant, we also include $\cos\theta_B$ to determine a combined likelihood ratio (\mathcal{LR}) for continuum background suppression.

$$\mathcal{LR} = \frac{\mathcal{L}_S}{\mathcal{L}_S + \mathcal{L}_B}, \mathcal{L}_{S(B)} = P(\mathcal{F})_{S(B)} \times P(\cos\theta_B)_{S(B)} \quad (4.13)$$

where \mathcal{L}_S and \mathcal{L}_B are the event-by-event signal and background likelihoods, and $P(\mathcal{F})_{S(B)}$ and $P(\cos\theta_B)_{S(B)}$ are the PDFs of the Fisher discriminant and $\cos\theta_B$ from signal MC (continuum background MC), respectively. \mathcal{F} distribution is modeled by combined Gaussian distributions. $\cos\theta_B$ distributions of both signal and continuum background are modeled by second-ordered Legendre polynomial. The KSFW moments distributions are shown in Figure 4.8. Then the signal and background likelihoods are calculated by multiplying the probabilities of the functions. The normalized \mathcal{LR} distributions of signal MC and continuum MC are shown in Figure 4.9.

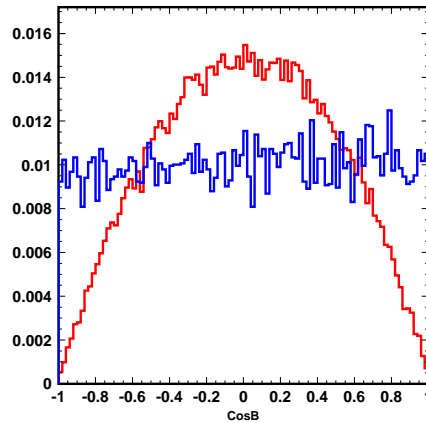


Figure 4.7: The normalized $\cos\theta_B$ distributions. Red: signal MC. Blue: continuum background.

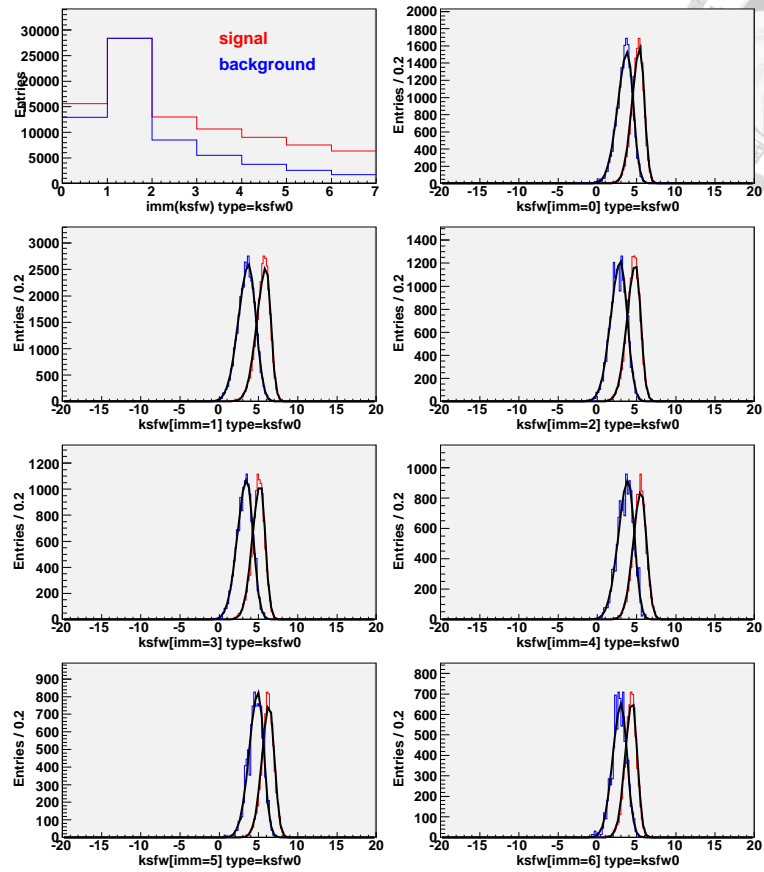
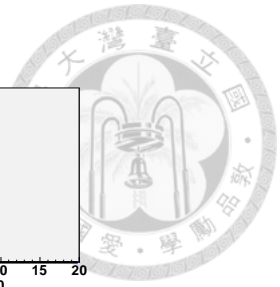


Figure 4.8: The KSFW moments distributions of the in seven missing mass regions. Red: signal MC. Blue: continuum background.

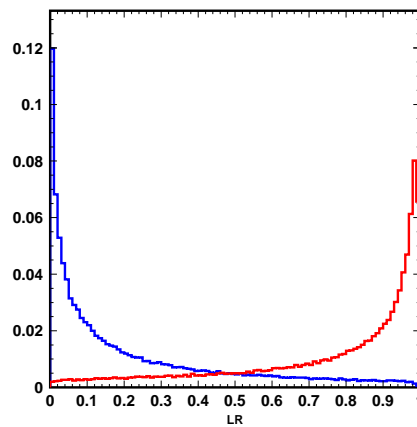


Figure 4.9: The normalized \mathcal{LR} distributions. Red: signal MC. Blue: continuum background.

Optimization of the \mathcal{LR} selection

The selection on \mathcal{LR} is determined by optimization of the figure of merit (F.O.M.):

$$F.O.M. = \frac{N_S}{\sqrt{N_S + N_B}},$$

where N_S and N_B denote the expected numbers of signal and background events in the signal box region, respectively. N_S is calculated by the assumed \mathcal{B} of 10^{-5} . The details of optimization are shown in Table 4.2 and Figure 4.10. \mathcal{LR} is required to be greater than 0.85 for continuum suppression.

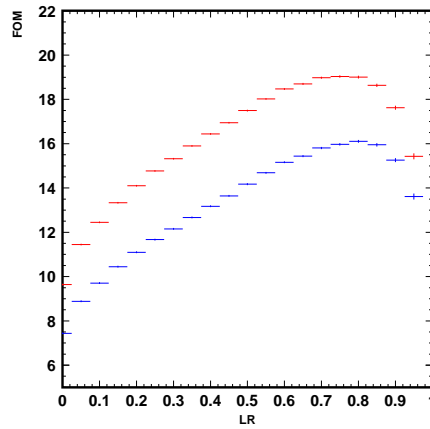



Figure 4.10: The F.O.M. distributions with different \mathcal{LR} selections, estimated by total number of signal (in red) and true signal (in blue).



\mathcal{LR}	N_b	$N_{s(tot)}$	F.O.M _{tot}	error _{tot}	$N_{s(true)}$	F.O.M _{true}	error _{true}
0	6855	845.96	9.64	0.034	643.96	7.43	0.039
0.05	4512	837.08	11.44	0.034	637.60	8.88	0.039
0.1	3590	827.26	12.44	0.034	630.56	9.70	0.039
0.15	2925	815.64	13.33	0.035	622.12	10.44	0.040
0.2	2442	803.45	14.10	0.035	613.33	11.09	0.040
0.25	2073	790.33	14.76	0.035	603.78	11.67	0.040
0.3	1794	776.71	15.31	0.035	593.77	12.15	0.041
0.35	1534	761.67	15.89	0.036	582.95	12.67	0.041
0.4	1309	745.16	16.44	0.036	571.24	13.17	0.041
0.45	1119	728.32	16.94	0.037	558.95	13.64	0.042
0.5	936	709.68	17.49	0.037	545.51	14.17	0.042
0.55	777	690.36	18.02	0.038	531.15	14.68	0.043
0.6	639	667.69	18.47	0.039	515.06	15.16	0.044
0.65	535	641.39	18.70	0.043	495.74	15.44	0.044
0.7	426	611.17	18.97	0.048	474.16	15.80	0.048
0.75	339	575.75	19.03	0.054	448.22	15.97	0.054
0.8	254	533.38	19.00	0.062	417.37	16.10	0.062
0.85	180	478.07	18.63	0.074	376.16	15.95	0.074
0.9	120	403.08	17.62	0.091	320.04	15.25	0.091
0.95	55	284.21	15.43	0.13	229.61	13.61	0.134

Table 4.2: Optimization of \mathcal{LR} selection with total number of signal (F.O.M_{tot}), and number of true signal (F.O.M_{true}). \mathcal{B} is assumed to be 10^{-5} .

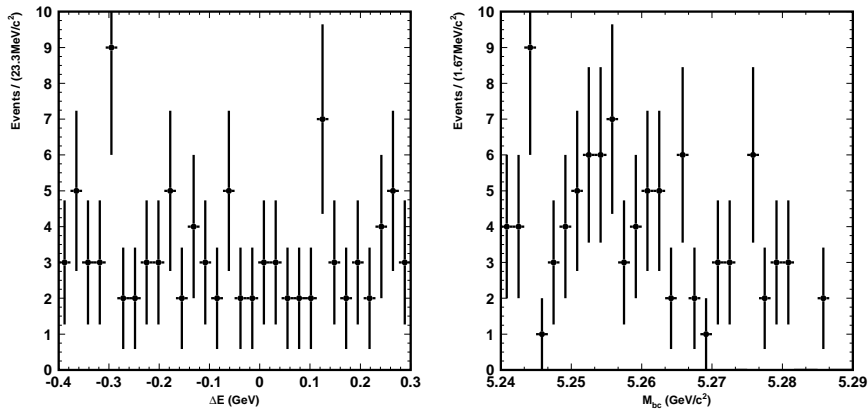
Proton identification	$\frac{L_p}{L_p+L_k} > 0.6$ and $\frac{L_p}{L_p+L_\pi} > 0.6$
Pion identification	$\frac{L_\pi}{L_\pi+L_k} > 0.6$
Λ selection	good Λ selection $1.111 \text{ GeV}/c^2 < M_{p\pi^-} < 1.121 \text{ GeV}/c^2$ $\frac{L_p}{L_p+L_k} > 0.6$ and $\frac{L_p}{L_p+L_\pi} > 0.6$ for the proton from Λ
Track impact parameters	$ dr < 0.3 \text{ cm}$ and $ dz < 3 \text{ cm}$
Photon selection	$E_\gamma > 1.7 \text{ GeV}$ in CM frame
B vertex fit	Successful vertex fit
Continuum suppression	$\mathcal{LR} > 0.85$
Candidate region	$-0.4 \text{ GeV} < \Delta E < 0.3 \text{ GeV}$, and $5.24 \text{ GeV}/c^2 < M_{bc} < 5.29 \text{ GeV}/c^2$
Best candidate selection	choose the candidate with the smallest $\chi_B^2 + \chi_\Lambda^2$

Table 4.3: Summary of the selection criteria.

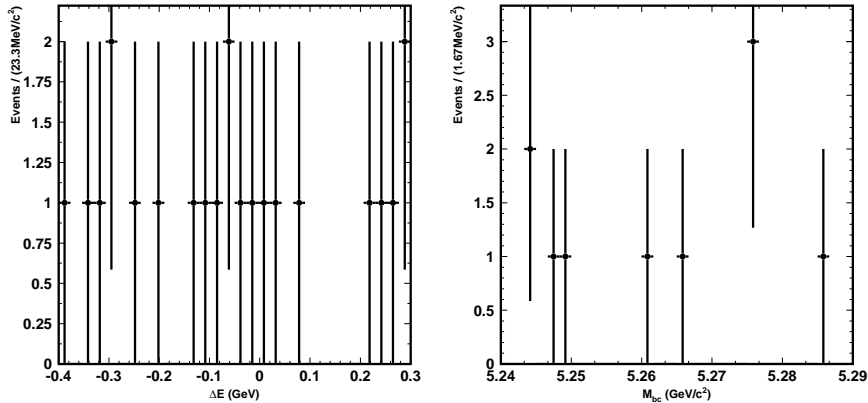


4.5.4 Generic B Background

We also consider the background from $B\bar{B}$ events. One kind of them is with the $b \rightarrow c$ transition, which usually has larger branching fraction (usually larger than 10^{-6}). Generic B MC is also generated to study this kind of background with one times of real data. The ΔE and M_{bc} distribution of the generic B MC are shown in Figure 4.11. Compared with continuum background, the remaining generic B background is few.



(a) In the candidate region.



(b) Each other's signal box region is selected.

Figure 4.11: The ΔE and M_{bc} distribution of the generic B MC.

4.5.5 Peaking Background in Rare B MC

Rare B events are $B\bar{B}$ events with charmless decay, and they usually have smaller branching fraction. The number of events of rare B MC is fifty times of real data.

There are seven modes which have peaking structure in ΔE and M_{bc} candidate region: $B^0 \rightarrow p\bar{\Lambda}\rho^-$, $B^0 \rightarrow p\bar{\Sigma}^0\rho^-$, $B^0 \rightarrow p\bar{\Lambda}\pi^-\eta$, $B^+ \rightarrow p\bar{\Lambda}\pi^0$, $B^+ \rightarrow p\bar{\Sigma}^0\pi^0$, $B^+ \rightarrow p\bar{\Lambda}\gamma$, and $B^+ \rightarrow p\bar{\Lambda}\eta$. Only two of these, $B^+ \rightarrow p\bar{\Lambda}\pi^0$ and $B^+ \rightarrow p\bar{\Lambda}\gamma$ [8, 54], have been measured experimentally. For these seven modes, we generate dedicated 771000 MC events to calculate their efficiency under all selection criteria.

4.5.6 Self-crossfeed Background

For signal MC, there are some events with the B reconstructed by some of the same final states particle from the other B , which is called self-crossfeed. In signal MC sample, there are 42% of self-crossfeed remained and cannot be removed without losing significant true signal. The ΔE and M_{bc} distributions of signal MC with all selection criteria are shown in Figure 4.12.

The efficiency of signal MC with selection criteria in the different region are listed in Table 4.6, and the number of remaining background MC are shown in Table 4.4 and Table 4.5. The comparison between background MC and data in the sideband region of ΔE and M_{bc} are shown in Figure 4.13. Sideband region is defined as $\Delta E < -0.05$ GeV or $\Delta E > 0.05$ GeV, and $M_{bc} < 5.27$ GeV/ c^2 .

	$q\bar{q}$	generic B
Candidate region	2648	99
Signal box region	110	4

Table 4.4: Number of remaining $q\bar{q}$ and generic B background MC events corresponding to one times data with all selection criteria.

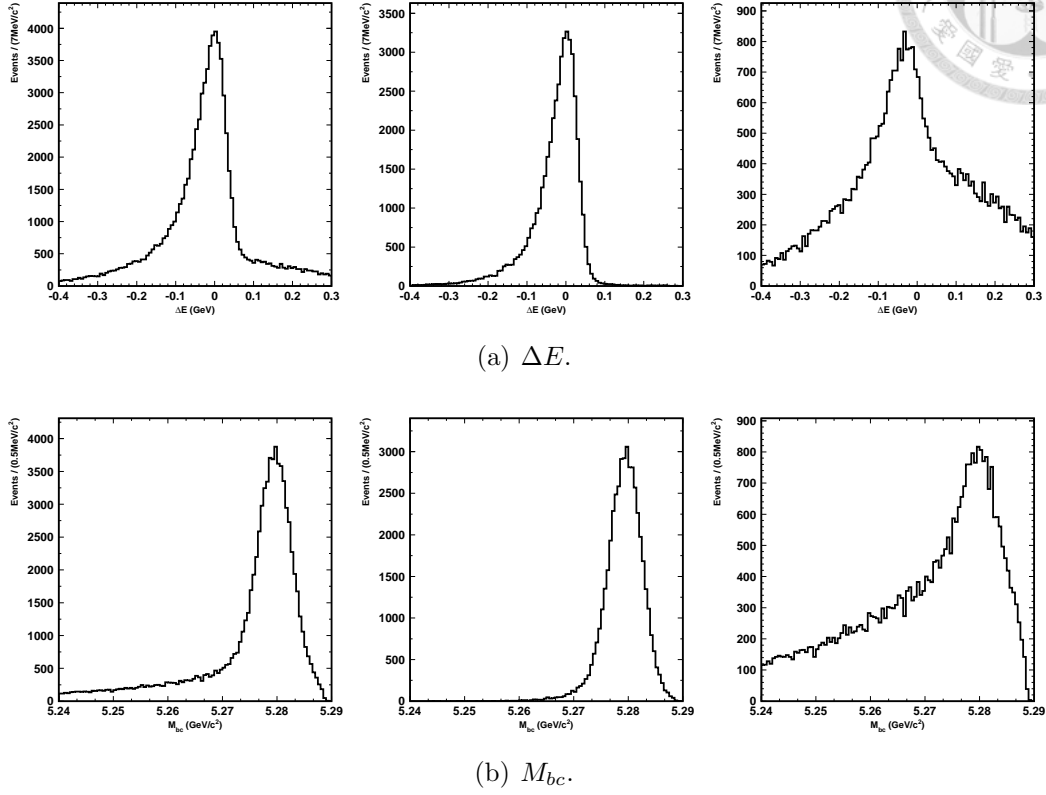


Figure 4.12: The ΔE and M_{bc} distributions of signal MC events with the selection criteria (left), true events (middle), and self-cross feed (right).

	$B^0 \rightarrow p\Lambda\rho$	$B^0 \rightarrow p\Sigma^0\rho$	$B^0 \rightarrow p\Lambda\pi^-\eta$
Candidate region	1.9	1.5	4.74
Signal box region	0.42	0.12	0.1

	$B^+ \rightarrow p\Lambda\pi^0$	$B^+ \rightarrow p\Sigma^0\pi^0$	$B^+ \rightarrow p\Lambda\gamma$	$B^+ \rightarrow p\Lambda\eta$
Candidate region	39.54	4.76	78.10	11.58
Signal box region	4.08	0.58	2.28	0.82

Table 4.5: Number of remaining rare B MC corresponding to one times data with all selection criteria. The red number is from the rare B MC result with assumed branching fraction, and the black number is scaled with measured branching fraction.

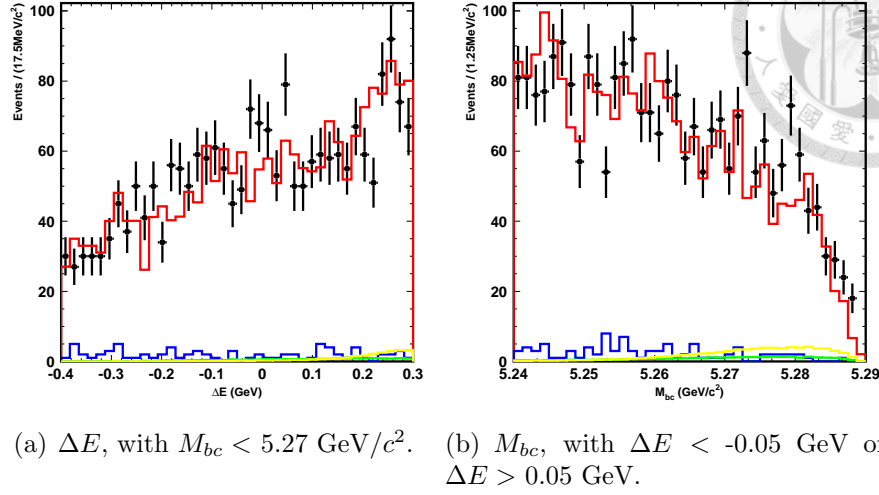


Figure 4.13: The comparison between background MC and data in the sideband region. Black error bar: data. Red: the combination of all background MC ($q\bar{q}$ MC, generic B MC, $B^+ \rightarrow p\bar{\Lambda}\pi^0$, and $B^+ \rightarrow p\bar{\Lambda}\gamma$). Blue: generic B MC. Green: $B^+ \rightarrow p\bar{\Lambda}\pi^0$. Yellow: $B^+ \rightarrow p\bar{\Lambda}\gamma$.

	Total signal		True signal	
	eff.	Numbers	eff.	Numbers
Candidate region	10.33%	79607	5.98%	46137
Signal box region	5.13%	39561	4.26%	32847

Table 4.6: Efficiency of Signal MC with all selection criteria.

4.6 Signal Extraction

4.6.1 Fitting Strategy

We perform a fitter with two dimensional extended unbinned likelihood fit that maximizes the likelihood function

$$\mathbf{L} = \frac{e^{-\sum_j N_j}}{N!} \prod_{i=1}^N \left(\sum_j N_j P_j(M_{bc}, \Delta E) \right) \quad (4.15)$$

to estimate the signal in the region $-0.4 \text{ GeV} < \Delta E < 0.3 \text{ GeV}$ and $5.24 \text{ GeV}/c^2 < M_{bc} < 5.29 \text{ GeV}/c^2$. Here N is the number of events in the fit, i denotes the i^{th} event, P_j denotes the PDF of signal and all background component, and N_j denotes number

of events corresponding to P_j . PDF and fitting parameters for all components will be discussed later and is shown in Table 4.7.



4.6.2 Probability Density Function

Due to the correlation between M_{bc} and ΔE two dimensions in signal MC, we use a 2D smoothed histogram to model the M_{bc} and ΔE distribution of true signal and self-crossfeed, which is shown in Figure 4.12. The smoothed histogram is based upon the distribution from signal MC. The scattering plot of M_{bc} and ΔE distribution of the true signal MC is shown in Figure 4.14. The ratio between signal and self-cross feed is fixed as 0.7254 from Table 4.6.

In order to model the background MC, we use the parameterization which is first used by the ARGUS collaboration [42]:

$$f(M_{bc}) \propto M_{bc} \sqrt{1-x^2} \exp[-\xi(1-x^2)], \quad (4.16)$$

to model the M_{bc} background, with x given by M_{bc}/E_{beam} and ξ as a fit parameter. The ΔE background shape is modeled by a normalized second order Chebyshev polynomial whose coefficients are fitting parameters.

In rare B background, there are two measured modes, $B^+ \rightarrow p\bar{\Lambda}\pi^0$ and $B^0 \rightarrow p\bar{\Lambda}\gamma$ will be included in the fit with fixed number of events, and the fixed numbers are scaled by measured branching fractions. We generate dedicated MC and use 2D smooth histogram to model them. For the other five unmeasured rare modes, we also generate MC and use 2D smooth function to model them, and their effect on measurement is studied by including one-by-one in the fit to check the signal yield deviation. The seven modes' distribution of MC result are shown in Figure 4.15 and Figure 4.16.

The fitting strategy for $B^0 \rightarrow p\bar{\Lambda}\pi^-\gamma$ measurement is summarized in Table 4.7.



P_j	PDF	fitting parameters
P_{sig} , true signal	2D smooth histogram	N_{sig} is floated
P_{scf} , self-crossfeed	2D smooth histogram	$N_{scf} = ratio \times N_{sig}$ ratio is fixed as 0.7254
P_{bck} , $q\bar{q}$ and generic B	2_{nd} order Chebyshev for ΔE ARGUS for M_{bc}	N_{bck} is floated Shape parameters are floated
$P_{p\bar{\Lambda}\pi^0}, B^+ \rightarrow p\bar{\Lambda}\pi^0$	2D smooth histogram	$N_{p\bar{\Lambda}\pi^0}$ is fixed as 39.54
$P_{p\bar{\Lambda}\gamma}, B^0 \rightarrow p\bar{\Lambda}\gamma$	2D smooth histogram	$N_{p\bar{\Lambda}\gamma}$ is fixed as 78.10
P_{rare} , other rare modes	2D smooth histogram	N_{rare} is floated, include one per fit

Table 4.7: PDF and fitting parameters in $B^0 \rightarrow p\bar{\Lambda}\pi^-\gamma$ study. Note that P_{rare} is not included in the nominal fit for measurement.

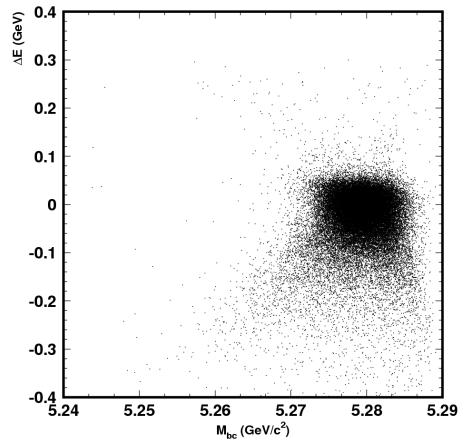


Figure 4.14: Scattering plot of M_{bc} and ΔE distribution of the true signal MC.

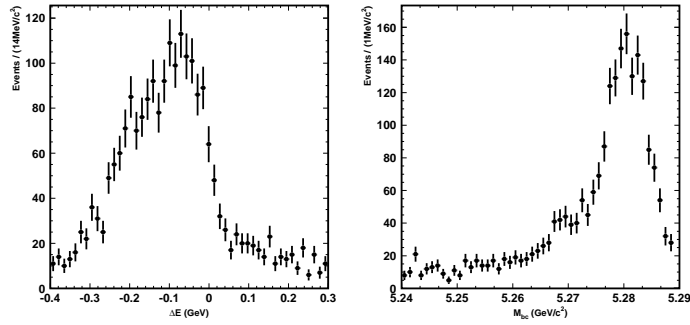
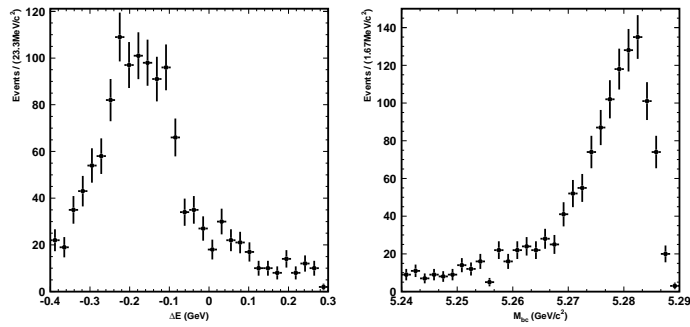
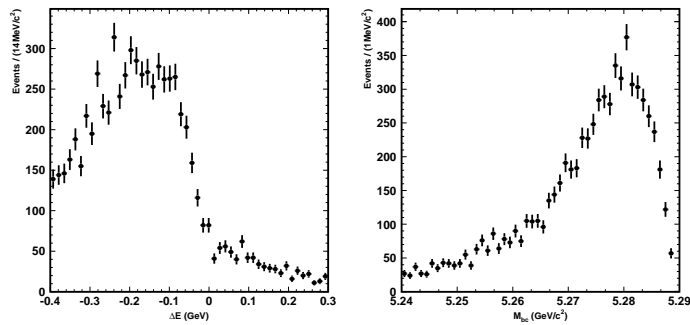
(a) $B^0 \rightarrow p\bar{\Lambda}\rho^-$.(b) $B^0 \rightarrow p\bar{\Sigma}^0\rho^-$.(c) $B^0 \rightarrow p\bar{\Lambda}\pi^-\eta$.

Figure 4.15: The ΔE and M_{bc} distribution of the rare B^0 peaking modes with all selection criteria.

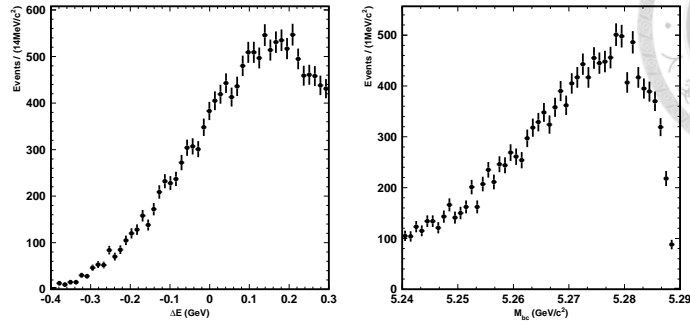
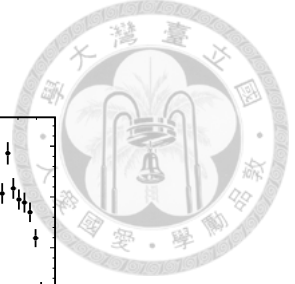
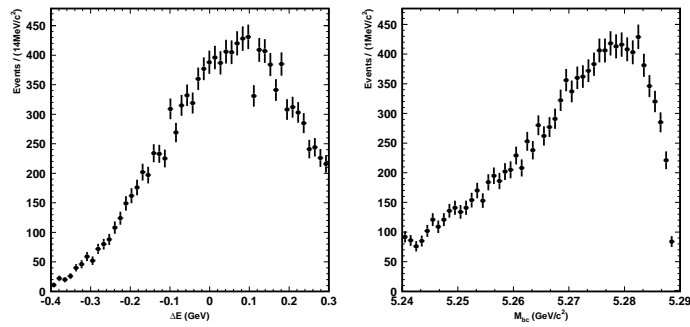
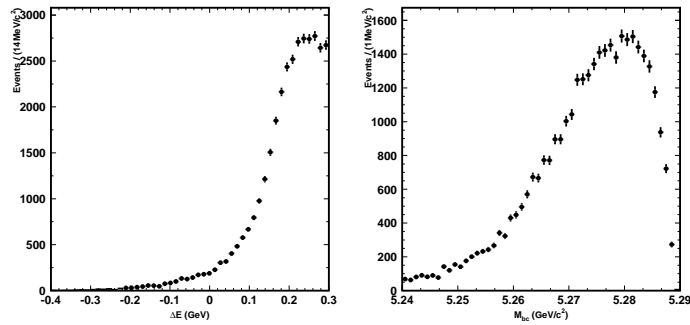
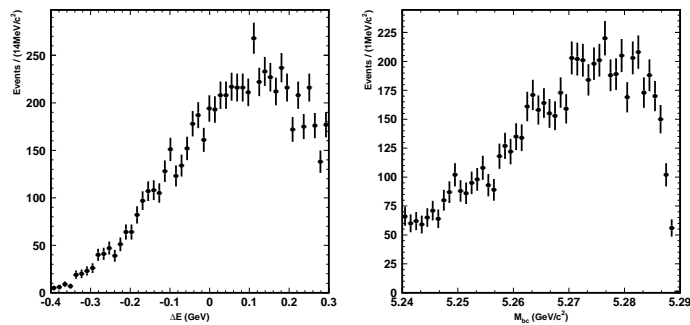
(a) $B^+ \rightarrow p\bar{\Lambda}\pi^0$.(b) $B^+ \rightarrow p\bar{\Sigma}^0\pi^0$.(c) $B^+ \rightarrow p\bar{\Lambda}\gamma$.(d) $B^+ \rightarrow p\bar{\Lambda}\eta$.

Figure 4.16: The ΔE and M_{bc} distribution of the rare B^+ peaking modes all selection criteria.



4.6.3 Measurements for the Branching Fraction

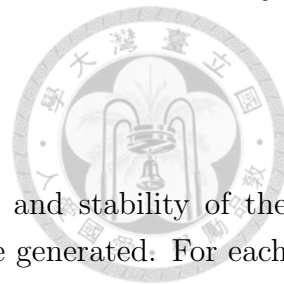
The formula which evaluate the branching fraction (\mathcal{B}) is

$$\mathcal{B} = \frac{\text{yield}}{N_{B\bar{B}} \times \epsilon_{MC} \times \mathcal{C}_{PID} \times \mathcal{C}_{\mathcal{LR}} \times \mathcal{C}_{fit}} \quad (4.17)$$

- Yield: Number of signal yield obtained by fitting on data.
- $N_{B\bar{B}}$: The number of $B\bar{B}$ events for experiment 7 to 65 is 771.581 ± 10.566 million.
- ϵ_{MC} : The signal MC efficiency which evaluated by counting the remaining events after all selection criteria. We generate 771000 events in signal MC, and 46137 true events left with all selections in Table 4.6, so $\epsilon_{MC} = 5.98\%$.
- \mathcal{C}_{PID} : The correction factors are due to the difference between the MC and data efficiencies while applying constraints on the charged particle likelihood. The correction factors is calculated by the package provided by PID joint group [44, 45, 46] and they are studied by various control samples with different particle types such as $\Lambda \rightarrow p\pi^-$ and $D^{*+} \rightarrow D^0\pi^+$ with $D^0 \rightarrow K^-\pi^+$. The factors are shown in Table 4.8 and the product of them is 0.928.
- $\mathcal{C}_{\mathcal{LR}}$: The correction factor is due to the difference between the MC and data efficiencies while applying the selection $\mathcal{LR} > 0.85$. The factor $\mathcal{C}_{\mathcal{LR}}$ is studied by $B^+ \rightarrow K^{*+}\gamma$ control sample, and it is estimated to be 0.973.
- \mathcal{C}_{fit} : The correction factor is due to the fit bias. We perform an ensemble test with toyMC samples. The factor \mathcal{C}_{fit} is 0.9758 by ensemble test result in Table 4.11.

Source	Factor	Uncertainty
Proton from B	0.9679	± 0.003
Proton from Λ	0.9667	± 0.003
Pion from B	0.9923	± 0.011
Total (Product)	0.928	± 0.011

Table 4.8: PID correction factors.



4.6.4 Ensemble Test

We perform ensemble test to verify the validity of fitter and stability of the fitting model. For each set of fitting, 1000 toyMC samples are generated. For each sample, Poisson-distributed random variables with expected values equal to N_{sig} , $N_{scf}(=ratio \times N_{sig})$, and N_{bck} and the distribution of toyMC is generated according to these three kinds of PDF model. The result of the ensemble test including yield, fitting error and pull distribution. The yield means N_{sig} from the fitting, and fitting error presents the standard deviation of the fitting. And we define the pull value as

$$\text{Pull} = \frac{\text{yield} - \text{expected value}}{\text{fitting error}}. \quad (4.18)$$

In the fit, N_{sig} and N_{bck} are floated, and the ratio of the number of self-crossfeed to N_{sig} is fixed as 0.7254. The results of ensemble test are summarized in Table 4.9. One of the yield, fitting error and pull distribution result with $N_{sig} = 4$ is shown in Figure 4.17.

In another ensemble test, $B^0 \rightarrow p\bar{\Lambda}\gamma$ and $B^0 \rightarrow p\bar{\Lambda}\pi^0$ components are considered additionally in toyMC generation. For these two modes, Poisson-distributed random variables with expected values equal to $N_{p\bar{\Lambda}\gamma} = 78.10$ and $N_{p\bar{\Lambda}\pi^0} = 39.54$. In the fit, $N_{p\bar{\Lambda}\gamma}$ is fixed as 78.10 and $N_{p\bar{\Lambda}\pi^0}$ is fixed as 39.54. The results for this case are summarized in Table 4.10. One of the yield, fitting error and pull distribution result for this case with $N_{sig} = 25$ is shown in Figure 4.18.

With the data measurement result, we also do another test with 3000 events, and the Poisson-distributed random variables and toyMC is generated by the fitting result of data. We use the result of this set to calculate the correction factor due to fit bias. By the result shown in Table 4.11 and Figure 4.19, the correction factor C_{fit} is $9.26/9.49 = 0.9758$.



N_{sig}	N_{scf}	N_{bck}	$Mean_{sig}$	$Error_{sig}$	$Pull_{sig}$
295	214	2648	293.56 ± 1.52	20.15 ± 0.060	-0.13 ± 0.064
265	192	2648	261.70 ± 1.24	19.36 ± 0.054	-0.10 ± 0.068
235	170	2648	232.30 ± 1.27	18.55 ± 0.052	-0.21 ± 0.067
205	149	2648	203.47 ± 1.27	17.69 ± 0.067	-0.13 ± 0.074
175	127	2648	173.35 ± 1.17	16.75 ± 0.067	-0.15 ± 0.065
145	105	2648	144.91 ± 1.20	15.72 ± 0.065	0.0013 ± 0.070
115	83	2648	114.36 ± 1.13	14.56 ± 0.078	-0.0040 ± 0.063
85	62	2648	84.41 ± 0.88	13.72 ± 0.099	-0.021 ± 0.063
55	40	2648	54.05 ± 0.39	12.16 ± 0.023	-0.073 ± 0.034
25	18	2648	24.81 ± 0.34	10.54 ± 0.022	-0.015 ± 0.032
11	8	2648	10.50 ± 0.33	9.55 ± 0.026	-0.10 ± 0.034
4	3	2648	3.62 ± 0.29	9.09 ± 0.025	-0.047 ± 0.032

N_{sig}	N_{scf}	N_{bck}	$Mean_{bck}$	$Error_{bck}$	$Pull_{bck}$
295	214	2648	2643.38 ± 4.45	57.87 ± 0.071	-0.046 ± 0.077
265	192	2648	2647.71 ± 4.20	57.71 ± 0.082	0.001 ± 0.075
235	170	2648	2658.88 ± 3.89	57.48 ± 0.081	0.136 ± 0.068
205	149	2648	2650.42 ± 4.51	56.85 ± 0.078	-0.093 ± 0.063
175	127	2648	2648.05 ± 3.96	56.34 ± 0.063	0.041 ± 0.068
145	105	2648	2645.01 ± 3.80	55.95 ± 0.059	-0.027 ± 0.069
115	83	2648	2652.69 ± 3.71	55.83 ± 0.086	0.028 ± 0.071
85	62	2648	2642.70 ± 4.42	55.33 ± 0.069	-0.059 ± 0.073
55	40	2648	2651.47 ± 1.72	54.68 ± 0.035	0.061 ± 0.032
25	18	2648	2646.81 ± 1.78	54.20 ± 0.027	-0.021 ± 0.032
11	8	2648	2651.24 ± 1.75	53.92 ± 0.029	0.067 ± 0.032
4	3	2648	2650.86 ± 1.74	53.80 ± 0.026	0.046 ± 0.032

Table 4.9: Results of ensemble test.

N_{sig}	N_{scf}	N_{bck}	$Mean_{sig}$	$Error_{sig}$	$Pull_{sig}$
295	214	2648	293.65 ± 0.71	20.39 ± 0.023	-0.055 ± 0.034
145	105	2648	143.57 ± 0.56	15.98 ± 0.021	-0.097 ± 0.035
25	18	2648	25.20 ± 0.36	10.75 ± 0.023	-0.0085 ± 0.033

N_{sig}	N_{scf}	N_{bck}	$Mean_{bck}$	$Error_{bck}$	$Pull_{bck}$
295	214	2648	2650.62 ± 1.94	59.10 ± 0.035	0.037 ± 0.033
145	105	2648	2649.49 ± 1.94	57.27 ± 0.034	0.224 ± 0.032
25	18	2648	2646.76 ± 1.76	55.39 ± 0.033	-0.023 ± 0.033

Table 4.10: Result of ensemble tests with considering $B^0 \rightarrow p\bar{\Lambda}\gamma$ and the $B^0 \rightarrow p\bar{\Lambda}\pi^0$ components.

N_{sig}	N_{scf}	N_{bck}	$Mean_{sig}$	$Error_{sig}$	$Pull_{sig}$
9.49	6.88	2898	9.26 ± 0.20	11.05 ± 0.013	-0.032 ± 0.018

N_{sig}	N_{scf}	N_{bck}	$Mean_{bck}$	$Error_{bck}$	$Pull_{bck}$
9.49	6.88	2898	2896.70 ± 1.05	58.05 ± 0.011	-0.030 ± 0.018

Table 4.11: Result of ensemble test by using data fit result as input.

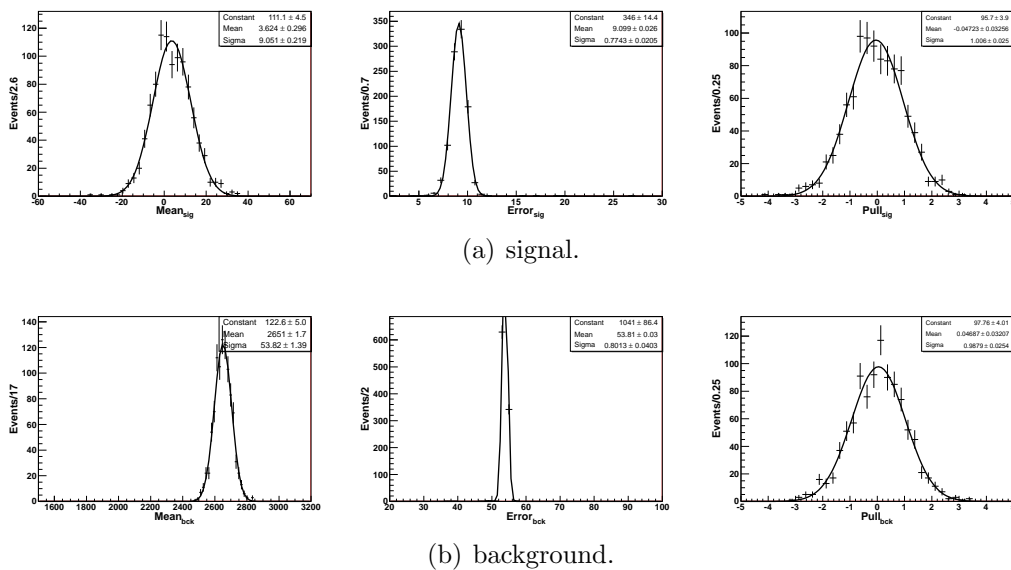


Figure 4.17: Ensemble test results (yield, fitting error and pull distribution) with $N_{sig} = 4$.

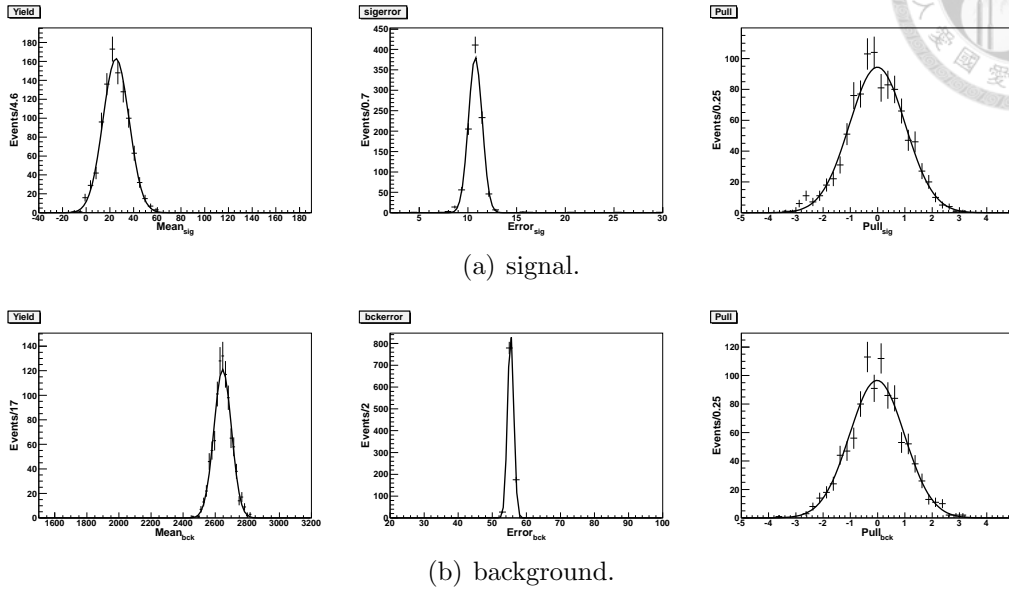
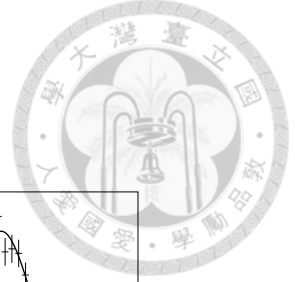


Figure 4.18: Ensemble test results (yield, fitting error and pull distribution) with considering $B^0 \rightarrow p\bar{\Lambda}\gamma$, $B^0 \rightarrow p\bar{\Lambda}\pi^0$ components, and $N_{sig} = 25$.

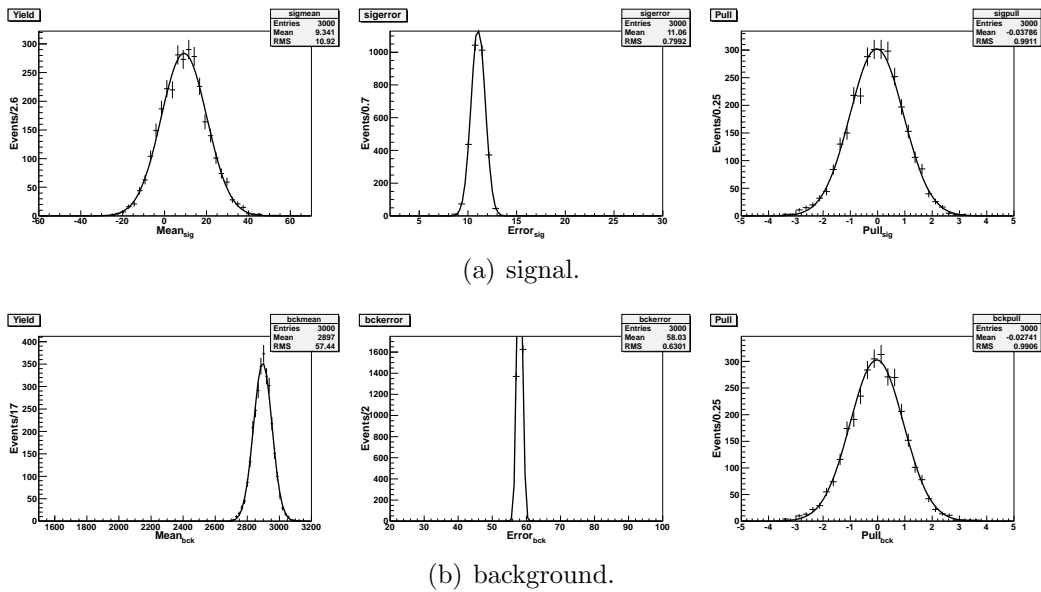


Figure 4.19: Ensemble test result (yield, fitting error and pull distribution) by using data fit result as input.



4.7 Control Sample Study: $B^+ \rightarrow K^{*+}\gamma$

4.7.1 Event selection and MC Study

The main purpose of the control sample study is calibration on signal PDF and systematic uncertainty study due to \mathcal{LR} selection. With all the selection criteria applied, the signal MC efficiency is 16.63% with about 7.0% of self-crossfeed events. The summary of the selection criteria for $B^+ \rightarrow K^{*+}\gamma$ study is shown in Table 4.12. The ΔE and M_{bc} distribution of signal MC, continuum background, and rare B MC are shown in Figure 4.20, 4.21, and 4.22, respectively.

Pion identification	$L_\pi/(L_\pi + L_k) > 0.6$ for the three pion in final states
K_S^0 selection	good K_S^0 selection $0.487 \text{ GeV}/c^2 < M_{K_S^0} < 0.507 \text{ GeV}/c^2$
K^{*+} selection	$0.817 \text{ GeV}/c^2 < M_{K^{*+}} < 0.967 \text{ GeV}/c^2$
Track impact parameters	$ dr < 0.3 \text{ cm}$ and $ dz < 3 \text{ cm}$, only for the pion from K^{*+} ,
Photon selection	$E_\gamma > 1.7 \text{ GeV}$ in CM frame π^0 and η veto
Continuum suppression	$\mathcal{LR} > 0.85$
Candidate region	$-0.4 < \Delta E < 0.3$ $5.24 < M_{bc} < 5.29$
Best candidate selection	choose the candidate with the smallest χ_B^2 from vertex fit

Table 4.12: Summary of the selection criteria for $B^+ \rightarrow K^{*+}\gamma$ study.

4.7.2 Signal Extraction

We use the same fitting strategy (two dimensional fit with M_{bc} and ΔE) as $B^0 \rightarrow p\bar{\Lambda}\pi^-\gamma$ measurement for $B^+ \rightarrow K^{*+}\gamma$ study. We use a 2D smoothed histogram to model the true signal M_{bc} and ΔE distribution due to the correlation between M_{bc} and ΔE in signal MC. The scattering plot of M_{bc} and ΔE distribution of the true signal MC of $B^+ \rightarrow K^{*+}\gamma$ is shown in Figure 4.23. Also, the self-crossfeed component from the signal MC and rare B component are modeled by 2D smoothed histograms. In the data fit, the ratio between signal and self-crossfeed is fixed as 0.0756. For continuum background, For the continuum background, we also use ARGUS for M_{bc} and second order Chebyshev polynomial for ΔE .

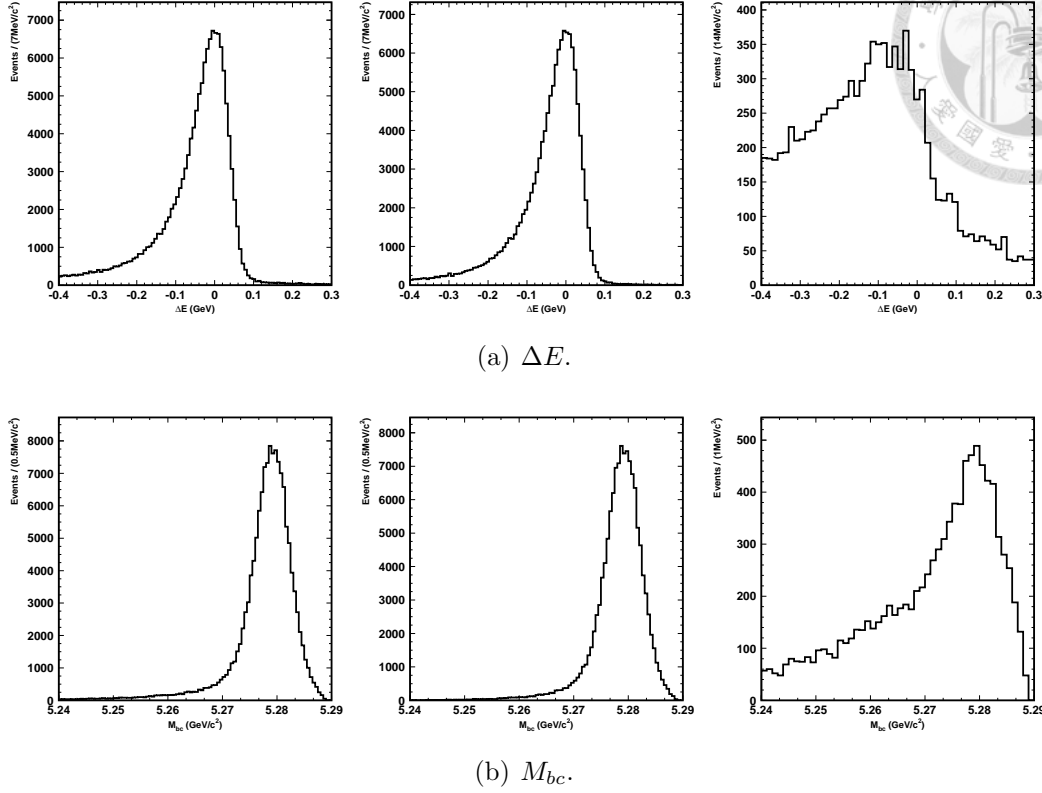


Figure 4.20: The ΔE and M_{bc} distributions of signal MC with all selection criteria (left), true signal (middle), and self-crossfeed (right) in $B^+ \rightarrow K^{*+}\gamma$ study.

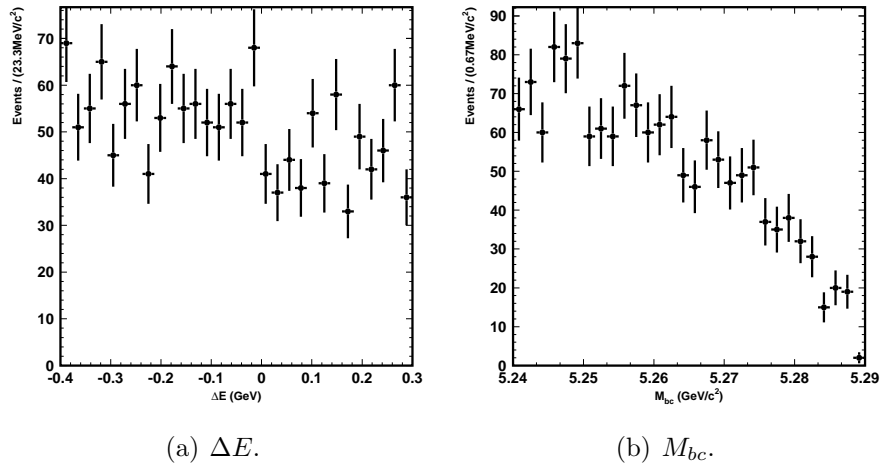
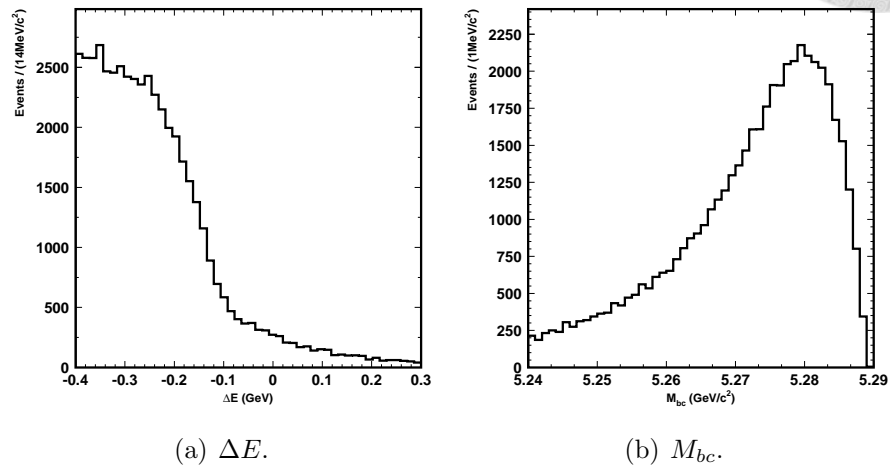
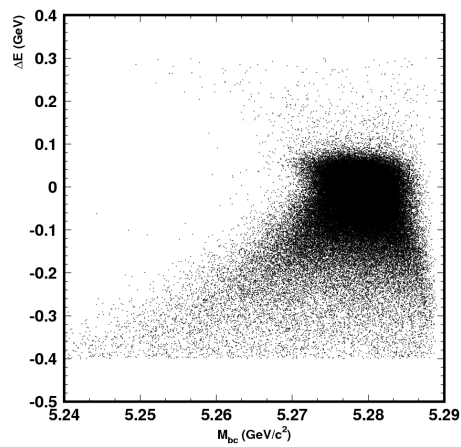


Figure 4.21: The ΔE and M_{bc} distribution of the continuum background in $B^+ \rightarrow K^{*+}\gamma$ study.

PDF calibration with smoothed histogram

In order to study the signal PDF shape difference (mean shift and width expansion) between signal MC and data by using the 2D smooth histogram. We design

Figure 4.22: ΔE and M_{bc} distribution of rare B MC in $B^+ \rightarrow K^{*+}\gamma$ study.Figure 4.23: Scattering plot of M_{bc} and ΔE distribution of the true signal MC in $B^+ \rightarrow K^{*+}\gamma$ study.

a PDF to include six additional shape parameters in the fixed-shape 2D smooth histogram. We look for the mean point (the maximum of the function) first to add two mean shift parameters in the PDF. For each dimension, give the function two width expansion parameters for each direction relative to the mean point (larger than the mean, and smaller than the mean). Therefore, we can get the fudge factor by using 2D smooth histogram with the six shape parameters. The illustration of this method is shown in Figure 4.24.

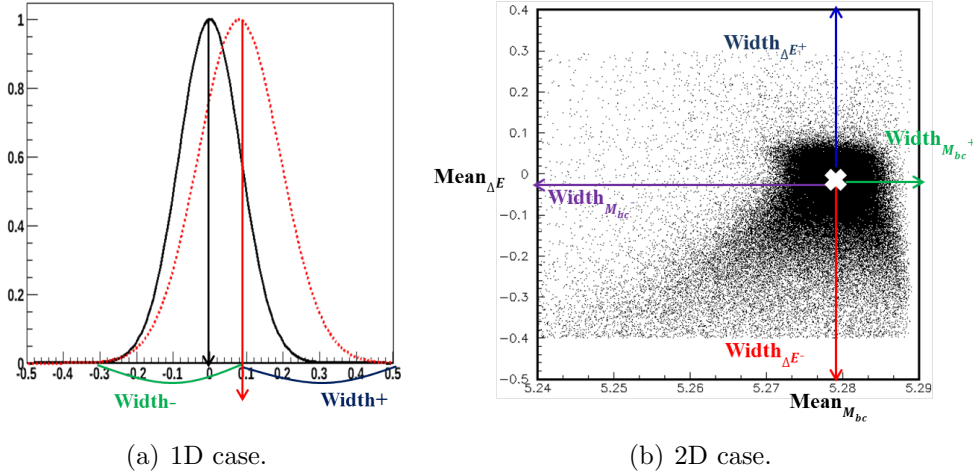


Figure 4.24: Illustration of smoothed histogram with additional shape parameters.

4.7.3 Result

We obtain $1094.60^{+41.81}_{-41.20}$ signal yield for the $B^+ \rightarrow K^{*+}\gamma$ decay and the projection of data fit result is shown in Figure 4.25. The obtained fudge factors in signal PDF with comparison between data and signal MC are shown in Table 4.13.

$\Delta\text{Mean}_{\Delta E}$	0.00488358	0.00607	-0.00658
$\Delta\text{Mean}_{M_{bc}}$	0.00044492	0.000265	-0.000258
$\Delta\text{Width}_{\Delta E+}$	1.227	0.147	-0.136
$\Delta\text{Width}_{\Delta E-}$	1.042	0.075	-0.089
$\Delta\text{Width}_{M_{bc}+}$	0.958	0.056	-0.056
$\Delta\text{Width}_{M_{bc}-}$	1.016	0.082	-0.077

Table 4.13: Fauge factors of signal PDF obtained by $B^+ \rightarrow K^{*+}\gamma$ data fit.

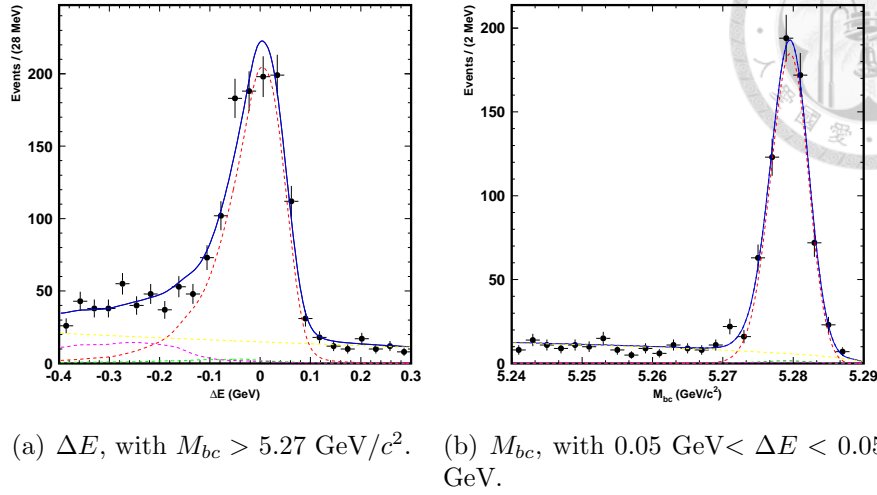


Figure 4.25: $B^+ \rightarrow K^{*+}\gamma$ data fit result. Black error bar: data. Blue: total PDF. Red: signal PDF. Green: self-crossfeed PDF. Yellow: continuum background PDF. Magenta: rare B PDF.

The measured branching fraction is obtained by this formula:

$$\mathcal{B} = \frac{\text{yield}}{N_{B\bar{B}} \times \epsilon_{MC} \times \mathcal{C}_{PID} \times \mathcal{C}_{\mathcal{LR}}}, \quad (4.19)$$

in which the branching fraction of each sub-decay [8] needs to be considered as following:

$$\mathcal{B}(K^{*+} \rightarrow K^0\pi^+) = \frac{2}{3} \quad (4.20)$$

$$\mathcal{B}(K^0 \rightarrow K_S^0) = \frac{1}{2} \quad (4.21)$$

$$\mathcal{B}(K_S^0 \rightarrow \pi^+\pi^-) = (69.20 \pm 0.05)\% \quad (4.22)$$

About the PID correction of three pions in the final state, the correction factor is shown in Table 4.14. The summary of systematic uncertainties is shown in Table 4.15.

1 st child of K_S^0	0.9628	± 0.0087
2 nd child of K_S^0	0.9630	± 0.0088
Pion from K^{*+}	0.9575	± 0.0084

Table 4.14: PID correction factors in $B^+ \rightarrow K^{*+}\gamma$ study.

Tracking uncertainty	1.05% (3 tracks)
Charged identification	2.69% (3 pions)
$N_{B\bar{B}}$	1.37%
Sub-decay	0.07%
Photon selection	2.2%
\mathcal{LR} selection	3.23%
Reconstruction eff. error	0.25%
total	5.05%



Table 4.15: Summary of the systematic uncertainties for $B^+ \rightarrow K^{*+}\gamma$ study.

The measured branching fraction is:

$$\mathcal{B}(B^+ \rightarrow K^{*+}\gamma) = (4.24 \pm 0.16(stat) \pm 0.21(syst)) \times 10^{-5}, \quad (4.23)$$

which is consistent with the PDG value:

$$\mathcal{B}(B^+ \rightarrow K^{*+}\gamma) = (4.21 \pm 0.18) \times 10^{-5}. \quad (4.24)$$

4.8 Physics Result

4.8.1 Fit Results

The projection of data fit result of $B^0 \rightarrow p\bar{\Lambda}\pi^-\gamma$ is shown in Figure 4.26. The fitted signal yield is $9.5^{+11.5}_{-10.7}$ with a statistical significance 0.9. The statistical significance is defined as $\sqrt{-2\ln(\mathcal{L}_0/\mathcal{L}_{\max})}$, where \mathcal{L}_0 and \mathcal{L}_{\max} are the likelihood values obtained by the fit with and without the signal yield fixed to zero, respectively.

4.8.2 Systematic Uncertainties

Several systematic uncertainties are discussed in this section. The correlated errors are added linearly and the uncorrelated ones are added in quadrature. The summary of systematic uncertainties is shown in Table 4.16.

- Tracking uncertainty:

The systematic uncertainty due to charged-track reconstruction is studied us-

ing partially reconstructed $D^{*+} \rightarrow D^0\pi^+$ with $D^0 \rightarrow \pi^+\pi^-K_S^0$. For the tracks with $p_T > 200$ MeV/ c , the systematic uncertainty of a charged track is estimated to be $(-0.13 \pm 0.30 \pm 0.10)\%$ per track. We apply the uncertainty to be 0.35% per track.

- Charged particles identification:

For the charged particles identification, we have constrains on likelihood values for protons and pions. The systematic uncertainties are estimated by using the package provided by the PID joint group [44, 45, 46] to do the correction of the ratio between MC efficiency and data efficiency. They are studied by various control samples with different particle types such as $\Lambda \rightarrow p\pi^-$ and $D^{*+} \rightarrow D^0\pi^+$ with $D^0 \rightarrow K^-\pi^+$. The systematic uncertainties is estimated to be both 0.3% for the 2 proton and 1.1% for the pion.

- Number of $B\bar{B}$:

The number of $B\bar{B}$ for experiment 7 to 65 is $771.581 \pm 10.566 \times 10^6$. Hence, the systematic uncertainty on $B\bar{B}$ is 1.4% [60].

- Secondary sub-decay:

The systematic due to sub-decay branching fraction are calculated by the ratio of error to the corresponding branching fraction in PDG: $\mathcal{B}(\Lambda \rightarrow p\pi^-) = (63.9 \pm 0.5)\%$. The sub-decay uncertainty is 0.8%.

- Λ selection:

The systematic uncertainty due to Λ reconstruction [56] is estimated by considering the uncertainty on efficiencies for the tracks displaced from the IP, which is determined by the difference between the proper time distribution of Λ for data and MC. There are also uncertainty from the Λ mass and vertex selection, which has different value in different Λ momentum regions. The uncertainty is estimated to be 3.3% for this study.

- γ selection:

The uncertainty due to the photon reconstruction is studied by a radiative Bhabha sample, and it is estimated to be 2.2%.

- \mathcal{LR} selection:

The systematic uncertainty due to \mathcal{LR} selection is estimated by the control sample study $B^+ \rightarrow K^{*+}\gamma$. Without \mathcal{LR} selection, there are 200210 true events in signal MC and $1756.07^{+68.72}_{-67.88}$ signal yield in data. As \mathcal{LR} selection is set to be 0.85, there are 128229 true events in signal MC and $1094.60^{+41.81}_{-41.20}$ signal yield in data. With $Ratio_{MC} = 0.6405 \pm 0.0011$ and $Ratio_{data} = 0.6233 \pm$



0.0116, the correction factor $\mathcal{C}_{\mathcal{LR}}$ is 0.9732 ± 0.0181 . The systematic uncertainty is 1.9%.

- Reconstruction efficiency (MC statistics):

We also use the ensembles test result in Table 4.11 and estimate the fit bias as: $0.2/9.26 = 2.2\%$.

- Signal decay Modeling:

For the uncertainty due to Signal decay modeling is considered by a set of toyMC with an alternative decay model: $B^0 \rightarrow X_s + \gamma$, $X_s \rightarrow X_{pl} + \pi^-$, and $X_{pl} \rightarrow p + \bar{\Lambda}$, where X_{pl} stands for the threshold peak in Ref. [54]. (In our analysis, the signal MC decay model is $X_s \rightarrow p + \bar{\Lambda} + \pi^-$, a three-body phase space decay). We fit the toyMC sample generated by the alternative decay model, and estimate the uncertainty by the deviation of branching fraction. The eff. of true events is 5.98%, and signal yield in data is 9.49. In another decay model, the eff. of true events is 5.42% and the toyMC fit result is 9.04. The uncertainty due to signal MC modeling is 5.1%.

- PDF shape:

The uncertainty due to signal PDF shape is done on control sample study $B^+ \rightarrow K^{*+}\gamma$, and is estimated by the signal yield deviation with and without fudge factors. Due to the presence of the self-crossfeed PDF in the fit, the uncertainty due to the signal PDF shape is inflated by a factor of $\sqrt{2}$. The uncertainty is 4.1%.

- Measured rare B backgrounds ($B^+ \rightarrow p\bar{\Lambda}\pi^0$ and $B^+ \rightarrow p\bar{\Lambda}\gamma$):

For $N_{p\bar{\Lambda}\pi^0}$ and $N_{p\bar{\Lambda}\gamma}$, the expected number is scaled with their branching fraction: $\mathcal{B}(B^+ \rightarrow p\bar{\Lambda}\pi^0) = (3.00_{-0.53}^{+0.61} \pm 0.33) \times 10^{-6}$, and $\mathcal{B}(B^+ \rightarrow p\bar{\Lambda}\gamma) = (2.45_{-0.38}^{+0.44} \pm 0.22)$ [8]. The uncertainties are estimated by varying each yield in the fit by $\pm 1\sigma$ of the measurement error on the branching fraction, and it is estimated to be 8.2%.

- Unmeasured rare B modes:

The uncertainty for the five unmeasured rare B modes ($B^0 \rightarrow p\bar{\Lambda}\rho^-$, $B^0 \rightarrow p\bar{\Sigma}^0\rho^-$, $B^0 \rightarrow p\bar{\Lambda}\pi^-\eta$, $B^+ \rightarrow p\bar{\Sigma}^0\pi^0$, and $B^+ \rightarrow p\bar{\Lambda}\eta$) is estimated by incorporating their PDFs in the fit and floating their yields. As the signal yield is reduced by this fit, we did not include this effect in the upper limit calculation



described below to get a conservative upper limit.

Tracking uncertainty	1.4% (4 tracks)
Charged identification	0.6% (2 protons) 1.1% (pion)
$N_{B\bar{B}}$	1.4%
Sub-decay	0.8%
Λ selection	3.3%
Photon selection	2.2%
\mathcal{LR} selection	1.9%
Reconstruction efficiency	2.2%
Signal decay model	5.1%
PDF shape	4.1%
Rare B decay	8.2%
Total	11.8%

Table 4.16: Summary of the systematic uncertainties for $B^0 \rightarrow p\bar{\Lambda}\pi^-\gamma$ study.

4.8.3 Upper Limit Estimation

Since the observed yield for $B^0 \rightarrow p\bar{\Lambda}\pi^-\gamma$ is not significant, we evaluate the 90% confidence-level Bayesian upper limit branching fraction. The upper limit is obtained by integrating the likelihood function:

$$\int_0^{\mathcal{B}_{UL}} \mathcal{L}(\mathcal{B}) d\mathcal{B} = 0.9 \int_0^1 \mathcal{L}(\mathcal{B}) d\mathcal{B}, \quad (4.25)$$

where $\mathcal{L}(\mathcal{B})$ denotes the likelihood value. The likelihood function is shown in Figure 4.27. The systematic uncertainties are taken into account by replacing $\mathcal{L}(\mathcal{B})$ with a smeared likelihood function.

We thus determine the upper limit on the branching fraction of $\mathcal{B}(B^0 \rightarrow p\bar{\Lambda}\pi^-\gamma)$ to be 6.5×10^{-7} at the 90% confidence level.

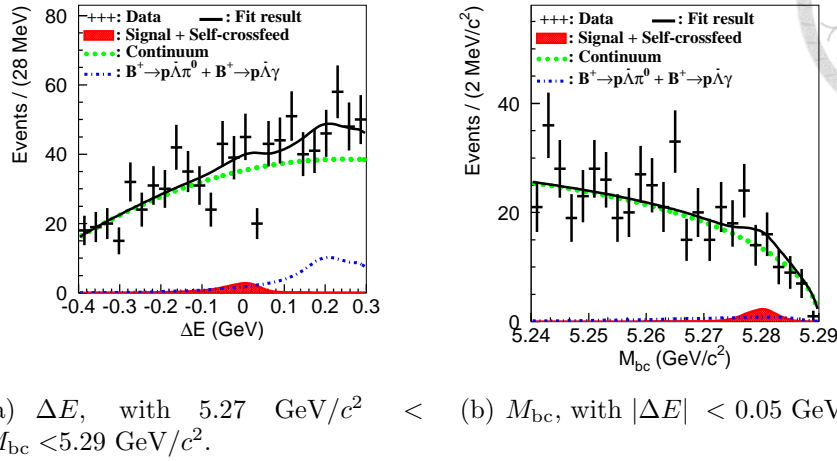


Figure 4.26: Data fit result of $B^0 \rightarrow p\bar{\Lambda}\pi^-\gamma$. The points with error bars are data; the solid line is the fit result; the green dotted line is continuum background; the blue dash-dotted line is the combination of $B^+ \rightarrow p\bar{\Lambda}\pi^0$ and $B^+ \rightarrow p\bar{\Lambda}\gamma$, and the red area is the combination of signal and self-crossfeed.

4.9 Summary

In conclusion, we have performed a search for $B^0 \rightarrow p\bar{\Lambda}\pi^-\gamma$, which proceeds via the $b \rightarrow s\gamma$ radiative penguin process, by using the full $\Upsilon(4S)$ data sample of $772 \times 10^6 B\bar{B}$ pairs collected by Belle. No significant signal yield is found and we set the upper limit on the branching fraction to be 6.5×10^{-7} at the 90% confidence level. We also conclude that the decay under study does not follow the expected hierarchy; instead, we find $\mathcal{B}(B^0 \rightarrow p\bar{\Lambda}\pi^-\gamma) < \mathcal{B}(B^+ \rightarrow p\bar{\Lambda}\gamma)$.

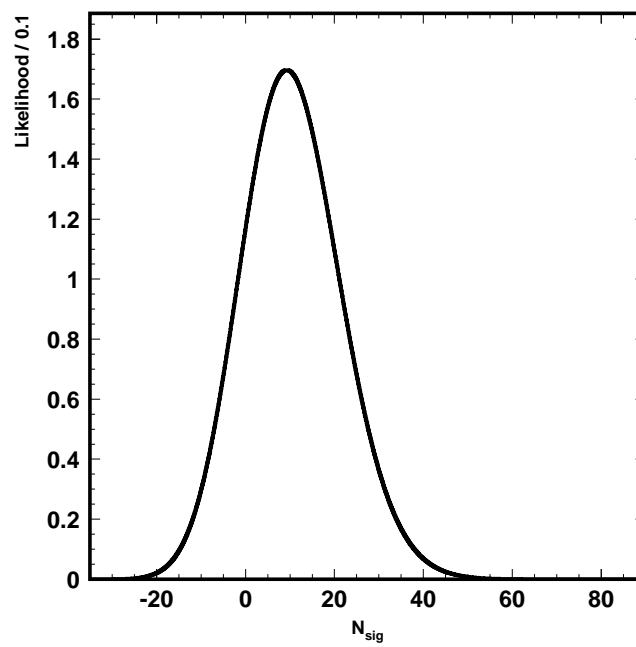


Figure 4.27: The likelihood function obtained by $B^0 \rightarrow p\bar{\Lambda}\pi^-\gamma$ data fit.





Chapter 5

Belle II Experiment and CDC Trigger System

5.1 Super KEK- B Factory (SuperKEKB)

SuperKEKB [21] is a Super B factory level upgrade of KEKB using the same tunnel. The whole design remains as a B factory which aims for the $B\bar{B}$ events from the $\Upsilon(4S)$ resonance and a much larger data sample is expected. Studies with SuperKEKB can provide source of new physics which is not covered by the recent hadron colliders. With much larger number of $B\bar{B}$ events, we are able to reach rare B decay and other new physics with higher sensitivity. Some of the basic parameters are different from the original KEKB. The half crossing angle is 41.5 mrad, which is about four times larger than that of the present KEKB. The beam energies have been changed from the present values of 3.5 and 8.0 GeV to 4.0 and 7.0 GeV. SuperKEKB is expected to have a 40 times larger instantaneous luminosity than the present KEKB. A schematic view of SuperKEKB is shown in Figure 5.1.

5.2 Belle II Detector

As an upgrade of Belle experiment, the Belle II collaboration was formed in December 2008. The main concern of Belle II detector is to maintain current performance of Belle in a new environment with probable higher background rate. Under the new design on the SuperKEKB with higher currents, smaller beam sizes and

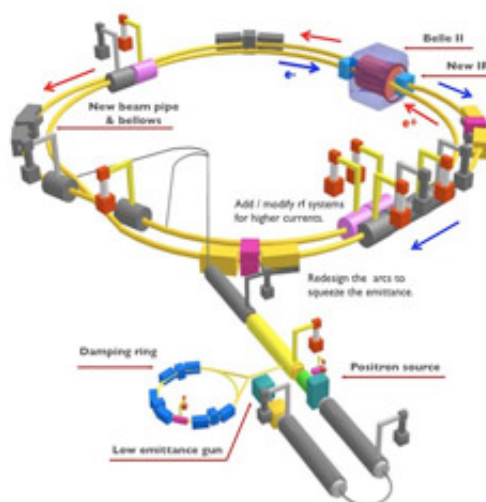


Figure 5.1: A schematic view of SuperKEKB [61].

modified interaction region, there is possible degradation of the performance in a higher background rate. It is assumed as a conservative factor of twenty increase in the background hit rate and the physics event rate will become about fifty times higher. It is important for Belle II detector to achieve better detection resolution.

Figure 5.2 shows the structure of Belle II detector and sub-detectors, and Figure 5.3 shows the comparison between Belle and Belle II detector in side view. With the similar structure as Belle detector, the sub-detectors of Belle II are either new-built or upgraded from the original one. New design and modifications on sub-detectors are briefly introduced as following:

- Pixel Detector (PXD):

As the inner most part, the silicon strip detector is replaced by a new two-layer silicon pixel detector based on the DEPLETED Field Effect Transistor (DEPFET) technology to improve the vertex resolution. Due to the large occupancy with higher luminosity, B vertex reconstruction with silicon strip becomes much more difficult. The solution is to use pixel sensors rather than strips for the innermost layers, which have a much larger number of channels and therefore a much smaller occupancy.

- Silicon Vertex Detector (SVD):

Because of the installation of new PXD, the silicon strip detector extends from just outside the pixel detector to a larger radius. SVD is a double sided silicon strip detector. Together with PXD, the main purpose of vertex detectors is to measure the two B decay vertices for the measurement of mixing-induced CP



asymmetry. SVD also provides precise vertex information of D meson and τ decay.

- Central Drift Chamber (CDC):

Belle II CDC is a newly-designed detector and is located just outside SVD. Compared with Belle CDC, chamber volume is larger and drift cells are smaller than Belle CDC. The details will be discussed later.

- Particle Identification (PID):

Belle II PID detector system is a completely new device. The main purpose is to improve the charged hadron ($p/K/\pi$) identification with the higher background environment. The original Belle PID system consists of time-of-flight detector using plastic scintillation counters and Aerogel Čherenkov Counter. In the barrel region of the spectrometer, the present TOF and ACC are replaced with a Time-Of-Propagation (TOP) counter, which measures the time of projection of the Čherenkov photons internally reflected inside a quartz radiator. In the forward endcap, the proximity-focusing Aerogel Ring-Imaging Čherenkov detector (ARICH) has been designed to separate kaons from pions over most of their momentum spectrum and to provide discrimination between pions, muons and electrons below 1 GeV/ c .

- Electromagnetic Calorimeter (ECL):

For the Belle II ECL, the modification on electronics is to shorten the shaping time with a newly developed shaper-digitizer module (Shaper-DSP). The replacement of endcap scintillator crystal (CsI(Tl)) with a faster and radiation tolerant version (e.g. pure CsI) is considered as an upgrade option.

- K_L^0 and μ detection (KLM):

The barrel part of KLM is still equipped with RPCs. In the endcaps, the background is worse because of the limited shielding of neutrons and other particles that are generated externally along the beam lines. In SuperKEKB, the background rate in the endcaps is expected to be a factor of twenty to forty higher, resulting in an RPC efficiency of below 50%. Therefore, the endcap part is replaced with scintillators instrumented with silicon photomultipliers.



Belle II Detector

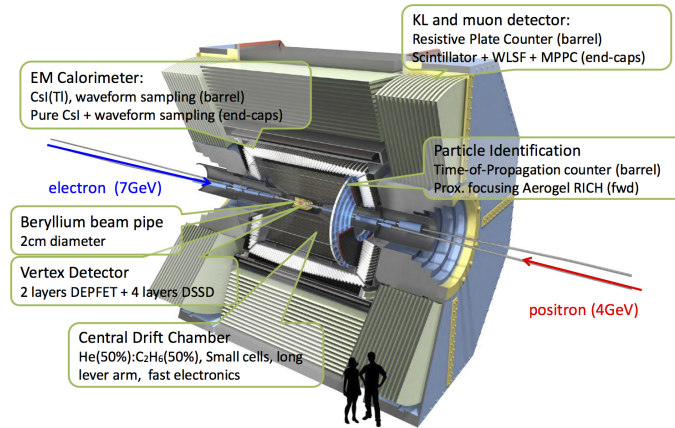


Figure 5.2: Cut view of BelleII detector [62].

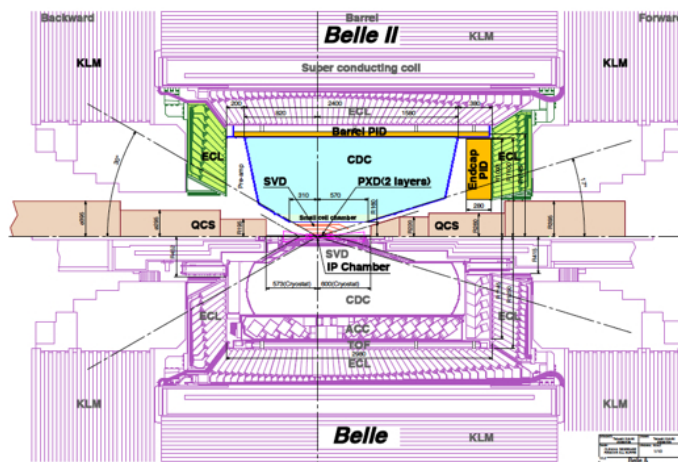


Figure 5.3: Side view of Belle and BelleII detector [63].

5.3 Belle II Central Drift Chamber (CDC)

The new design of Belle II CDC is similar to the original structure of Belle CDC. The main purpose is charged track reconstruction, momentum measurement, and dE/dx measurement. Belle II CDC has larger chamber volume, more sense and field wires, and less SuperLayers (SLs). The ionization gas is still the mixture of He and ethane. The comparison on main parameters between Belle and Belle II CDC is listed in Table 5.1. The overall structure of Belle II CDC is shown in Figure 5.4.

	Belle	Belle II
Radius of inner cylinder (mm)	77	160
Radius of outer cylinder (mm)	880	1130
Radius of innermost sense wire (mm)	88	168
Radius of outermost sense wire (mm)	863	1111.4
Number of sense wires	8400	14336
Number of wire layers	50	56
Number of SL	11	9
Gas	He and ethane	He and ethane
Diameter of sense wire (μm)	30	30

Table 5.1: Comparison on main parameters between Belle and Belle II CDC [64].

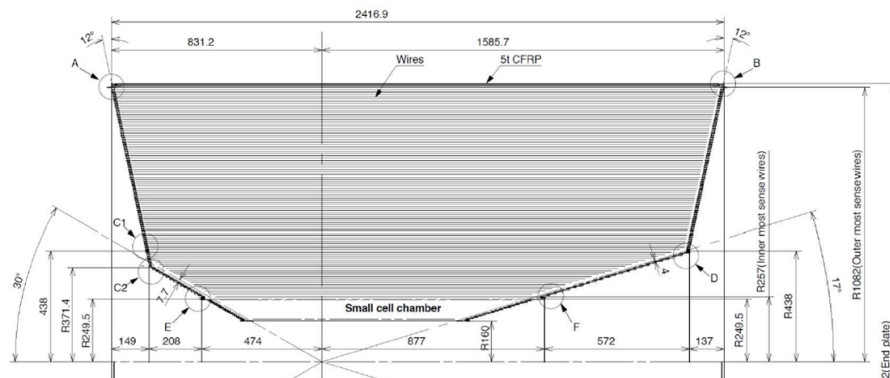


Figure 5.4: Overall structure of Belle II CDC [64].

5.3.1 Wire Configuration

In order to provide 3D tracking information, Belle II CDC an alternate sense wire configuration (AUVAUAVA), where A is axial SL parallel to z -axis, and U and V are stereo SL with two stereo angles. The detailed wire configuration is shown in Table 5.2. The SL ID of 9 SL in Table 5.2(Axial 0~Axial 8) is used in later chapter

about the CDCTR system. Sense wire configuration comparison between Belle and Belle II CDC is shown in Figure 5.5. Among the 8 wire layers in SL 0, only the outer 5 layers are used in Level-1 trigger system.

NTUHEP group also participated in the wire stringing of Belle II CDC. Figure 5.6 are photos taken during the wire stringing work in summers 2013.

SL type and ID	Number of layers	Signal cells per layer	radius (mm)	Stereo angle (mrad)
Axial 0	8	160	168.0 – 238.0	0.
Stereo U 1	6	160	257.0 – 348.0	45.4 – 45.8
Axial 2	6	192	365.2 – 455.7	0.
Stereo V 3	6	224	476.9 – 566.9	-55.3 – -64.3
Axial 4	6	256	584.1 – 674.1	0.
Stereo U 5	6	288	695.3 – 785.3	63.1 – 70.0
Axial 6	6	320	802.5 – 892.5	0.
Stereo V 7	6	352	913.7 – 1003.7	-68.5 – -74.0
Axial 8	6	384	1020.9 – 1111.4	0.

Table 5.2: Belle II CDC sense wire configuration. ID of 9 SL in is used in later chapter about the CDCTR system [64].

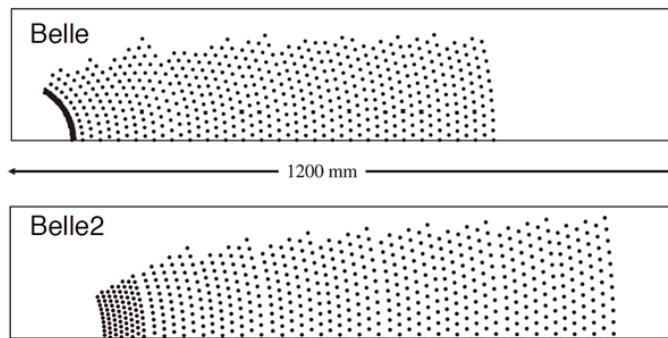


Figure 5.5: Sense wire configuration comparison between Belle and Belle II CDC [64].

5.4 Belle II Level-1 Trigger (TRG) System

During the operation of accelerator and detectors, detectors always keep outputting data. With the high luminosity of KEKB and SuperKEKB, throughput and storage are not enough to store all these data due to high event rate and short bunch spacing. The L1 trigger system (TRG) is an online hardware system that determines section with “data of interest”, physics event from continuous data flow,

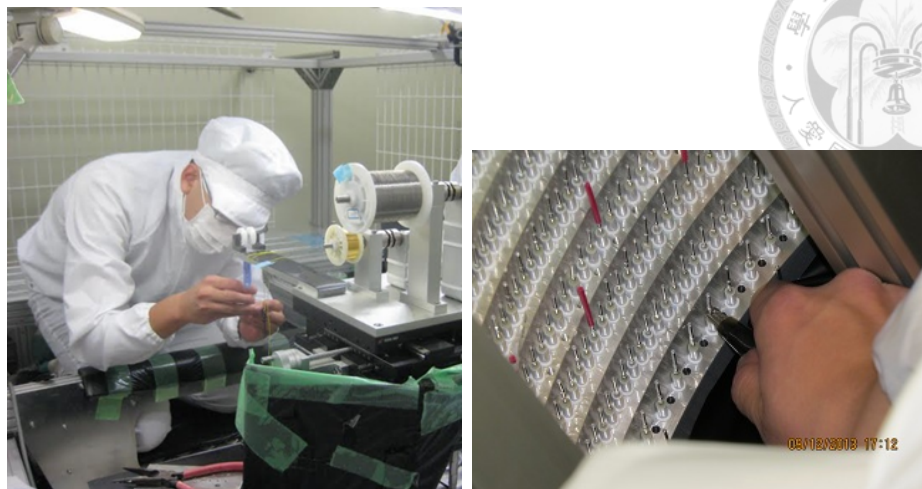


Figure 5.6: Photos taken during wire stringing work.

and issues L1 trigger signal to Data Acquisition system (DAQ). Then, DAQ will store the data in the triggered section for offline usage. The requirement of L1 trigger includes a fixed latency of $5 \mu\text{s}$, a maximum average trigger rate of 30 kHz due to the DAQ hardware limit, and ability to trigger different kind of physics events such as $\Upsilon(4S) \rightarrow B\bar{B}$ and hadronic $q\bar{q}$ with high efficiency. Since the Bhabha and $\gamma\gamma$ cross sections are very large compared with others, pre-scaling of these triggers is essential for L1.

Figure 5.7 is overview of the BelleII Level-1 trigger system. The sub-trigger system in Level-1 includes CDC, ECL, BPID (TOP) and KLM. The global trigger summarizes the information from sub-trigger system and issue the triggers for different physics events to DAQ. Due to the fixed $5 \mu\text{s}$ latency, each component is using Field Programmable Gate Array (FPGA) to process the logic flow with high clock rate. All the trigger algorithms are implemented as digitized FPGA firmware, and data are transmitted with high speed optical serial links. Each FPGA chip in the whole system is driven by a general 127 MHz clock source, which is called system clock (sysclk). The functions of each sub-trigger systems are listed as following:

- ECLTRG:

For the low-multiplicity physics events, ECLTRG can usually have clear clustering with higher energy and a significant back-to-back angular distribution of the found clusters. Hence, ECLTRG information is critical for trigger of low-multiplicity physics events (e.g. Bhabha, $\gamma\gamma$, $\mu\mu$, $\tau\tau$, and so on). In addition, the matching between ECL clusters and CDC tracks, and the E/P value are helpful for e and γ identification at L1.



- **CDCTRG:**
CDCTRG can provide the track information, including number of tracks and their track parameters. Basically, number of tracks in an event is an important condition for trigger of hadronic events.
- **TOPTRG:**
TOPTRG can provide timing information with a good resolution of under a ns.
- **KLMTRG:**
By matching with track information obtained by CDCTRG, KLMTRG can provide μ identification information.
- **GDLTRG:**
The global trigger system summarizes the sub-trigger information and make final trigger decision to DAQ.

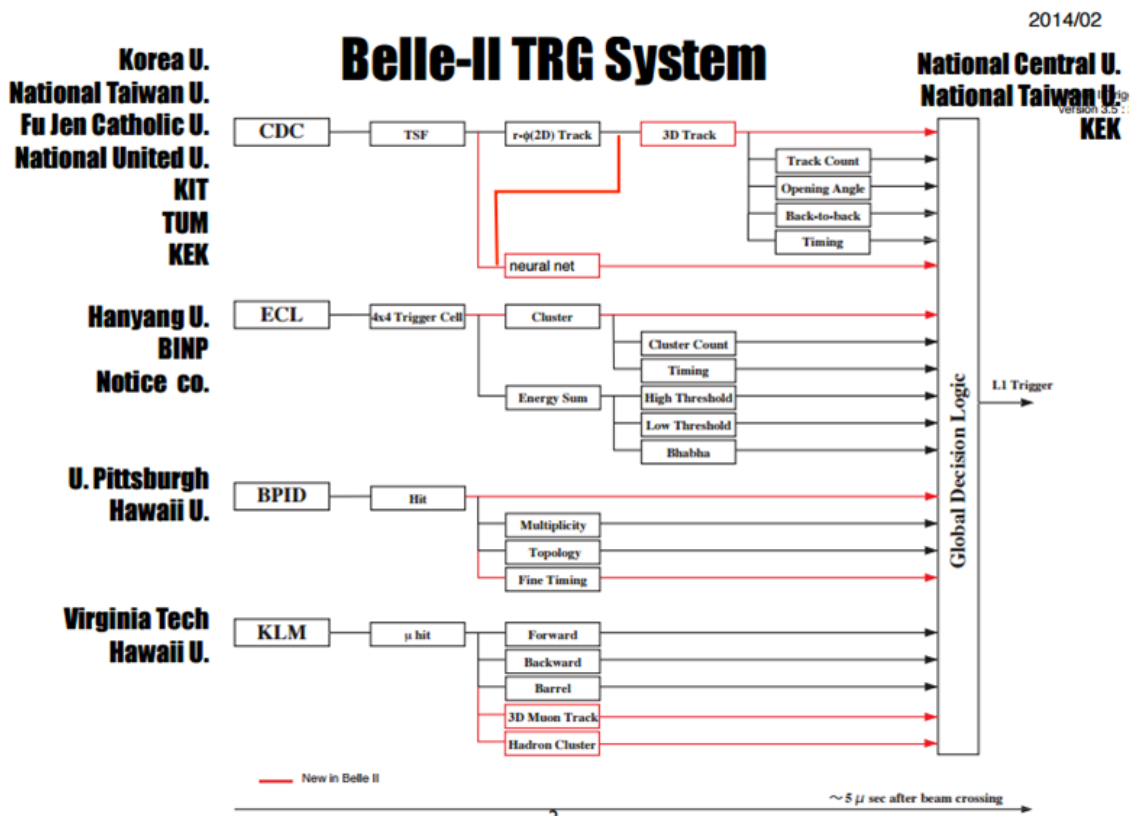


Figure 5.7: Signal flow of BelleII Level-1 trigger system.

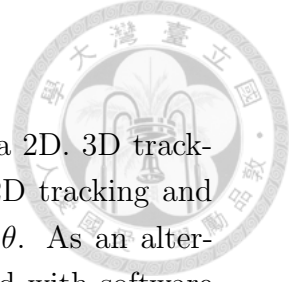


5.5 Belle II Central Drift Chamber Trigger (CDCTRГ)

CDCTRГ is designed to provide tracking information at L1 trigger by raw wire hit data from CDC and online tracking algorithms with FPGA chips. The output includes p_t (transverse momentum), ϕ (angle in transverse plane), d_z (longitudinal deviation between a track and IP at z -axis), θ (polar angle), and number of reconstructed tracks. The clock rate used in CDCTRГ to process the data is 31.75 MHz, which is called data clock (dataclk) and it is 1/4 the rate of sysclk.

Figure 5.8 is the data flow of CDCTRГ. The brief introduction to each stage in the system is as following:

- CDC Front-end (CDCFE):
There are 292 CDCFE boards used for L1 trigger purpose. CDCFE board is the readout system of CDC and each one is connected to 48 sense wires. The wire hit and timing information have a timing resolution of 1 ns, and they are summarized into partial track segment (PTS) information by the trigger algorithm in CDCFE. An example of PTS of sense wire cell is shown in Figure 5.9.
- Merger:
There are 73 Merger boards in CDCTRГ. Mergers simplify the data from CDCFE into track segment (TS) information. An example of TS of sense wire cell is shown in Figure 5.10.
- Track Segment Finder (TSF):
There are 9 TSF corresponding to 9 SL of CDC. TSF accumulates the wire hit patterns over time and uses lookup table (LUT) generated from simulation to determine the TS.
- Event Timing Finder (ETF):
There is 1 ETF board. ETF is used to calculate the event timing based on TS information from 9 TSF.
- 2D tracker (2D):
There are 4 2D trackers. Each 2D tracker utilize the TS from 5 axial SL and use Hough transformation for tracking. The output track information covers 1/4 of CDC. Illustration of the Hough transformation for 2D tracking is shown in Figure 5.11.



- 3D tracker (3D) and Neural Network z trigger (NN):

There are 4 3D trackers and 4 NN, and each corresponds to a 2D. 3D tracking in L1 trigger is new in Belle II. 3D trackers utilize the 2D tracking and 4 corresponding stereo TSF and do fitting to obtain d_z and θ . As an alternative approach, NN uses neural network which is pre-trained with software simulation.

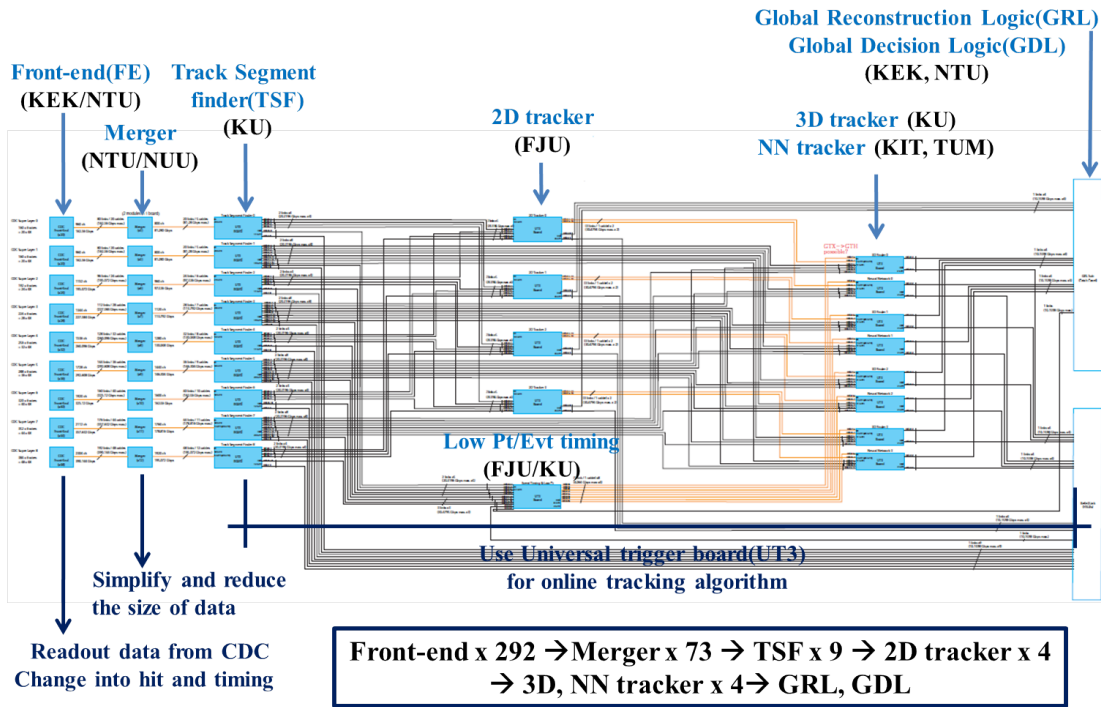


Figure 5.8: Belle II CDCTRG system.

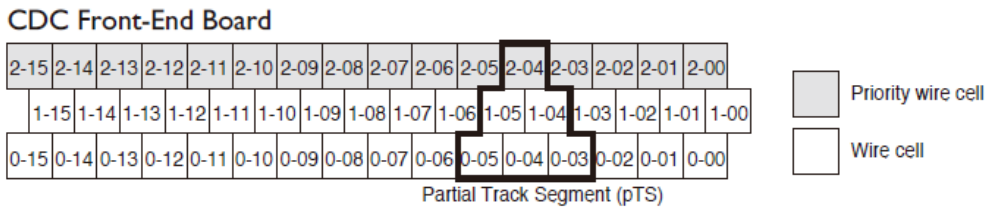


Figure 5.9: An example of PTS of sense wire cell. Each square corresponds to a wire cell in CDC.

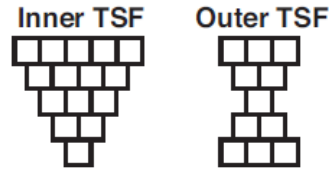


Figure 5.10: An example of TS of sense wire cell. Inner TSF is at SL0, and outer TSF is at SL 1~8. Each square corresponds to a wire cell in CDC [64].

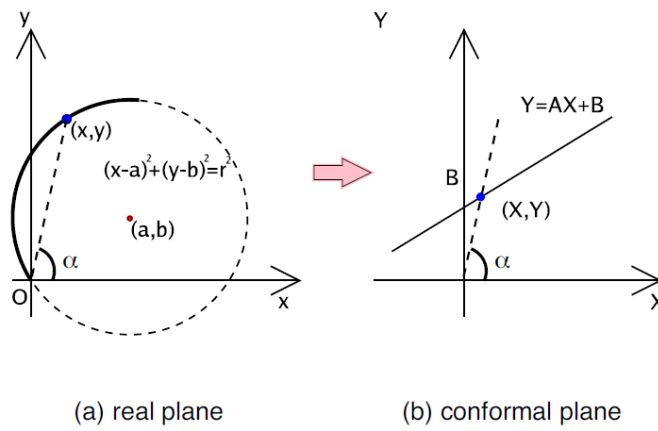


Figure 5.11: Schematic view of the conformal transformation: (a) in CDC transverse plane, (b) in the conformal plane [64].





Chapter 6

CDCTRG Merger Board

6.1 Introduction

Figure 6.1 is the Merger board v3.02 production type. 73 Merger boards are used in CDCTRG. The main function of Merger is to simplify the PTS data from CDCFE into TS information, and the output is sent to TSF. The hardware interface for different purposes are listed as following:

- 2 Altera Arria II FPGA [65, 66] (noted as U1FPGA and U2FPGA)
- Joint Test Action Group (JTAG) for firmware loading and monitoring with Altera logic analyzer software (Quartus II) [67]
- 4 AVAGO HFBR-7934WZ [68] connector, whose maximum line rate can live up to 3.125 Gbps (Giga bits/s) approximately.
- 1 AVAGO AFBR-79Q4Z [69] connector, whose maximum line rate can live up to 10 Gbps approximately.
- LEMO for clock input
- RJ45
- Dip switch as board ID
- VME interface for firmware loading and monitoring

The detailed usage of them will be discussed later.

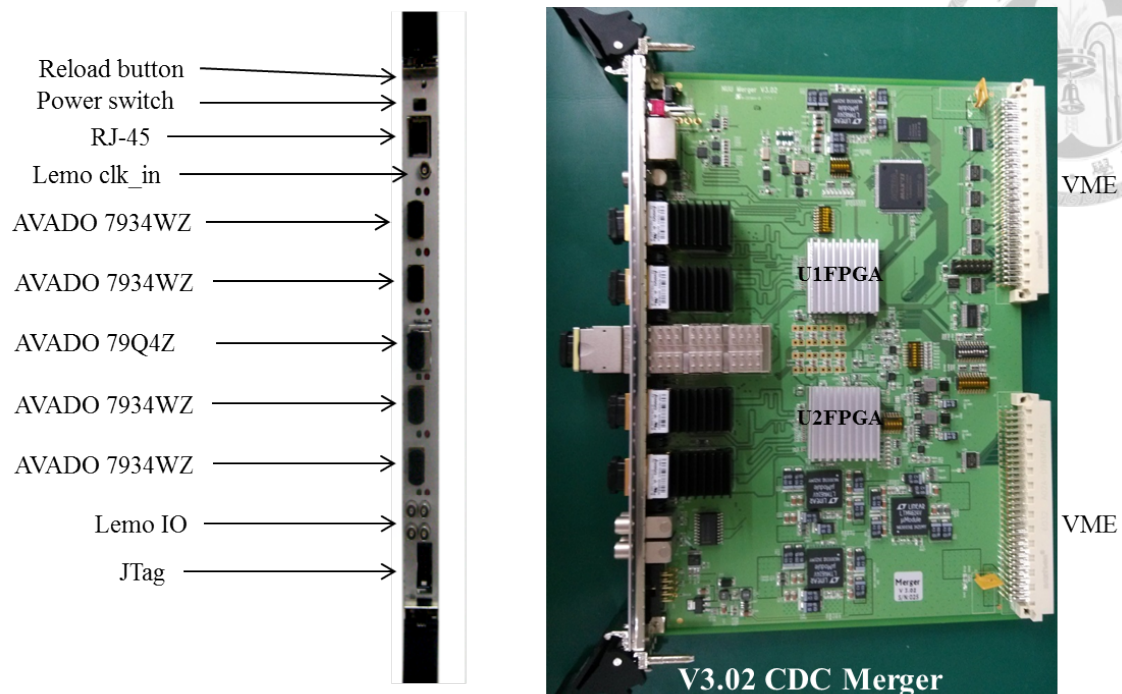


Figure 6.1: Merger board v3.02 production type.

6.2 Merger Firmware

Figure 6.2 and Figure 6.3 are the schematic view of Merger firmware's structure. A general 127 MHz clock source (sysclk) is used to drive all firmwares in TRG and DAQ, and the data rate of the whole CDCTRG is 31.75 MHz (dataclk).

The normal operation mode is the one with full functionalities and is used under regular operation. The data player mode is designed for debugging purpose. Details of these two operation modes and functions of all components are discussed in this section.

6.2.1 Normal Operation Mode

Under normal operation mode, Merger works with its full functionalities. All optical links (to CDCFE and TSF) should be connected and the Merger core logic will simplify the data from CDCFE then send to TSF.

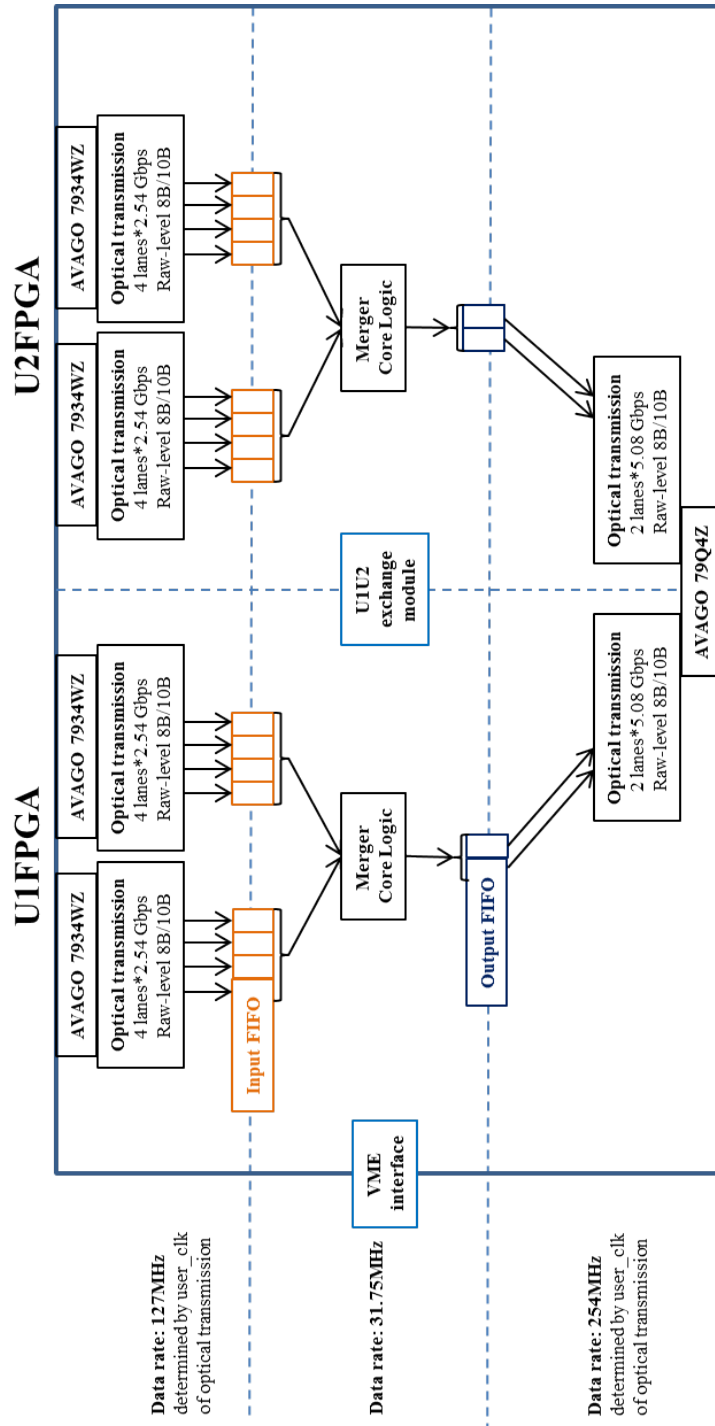


Figure 6.2: Schematic view of Merger firmware under normal operation mode.

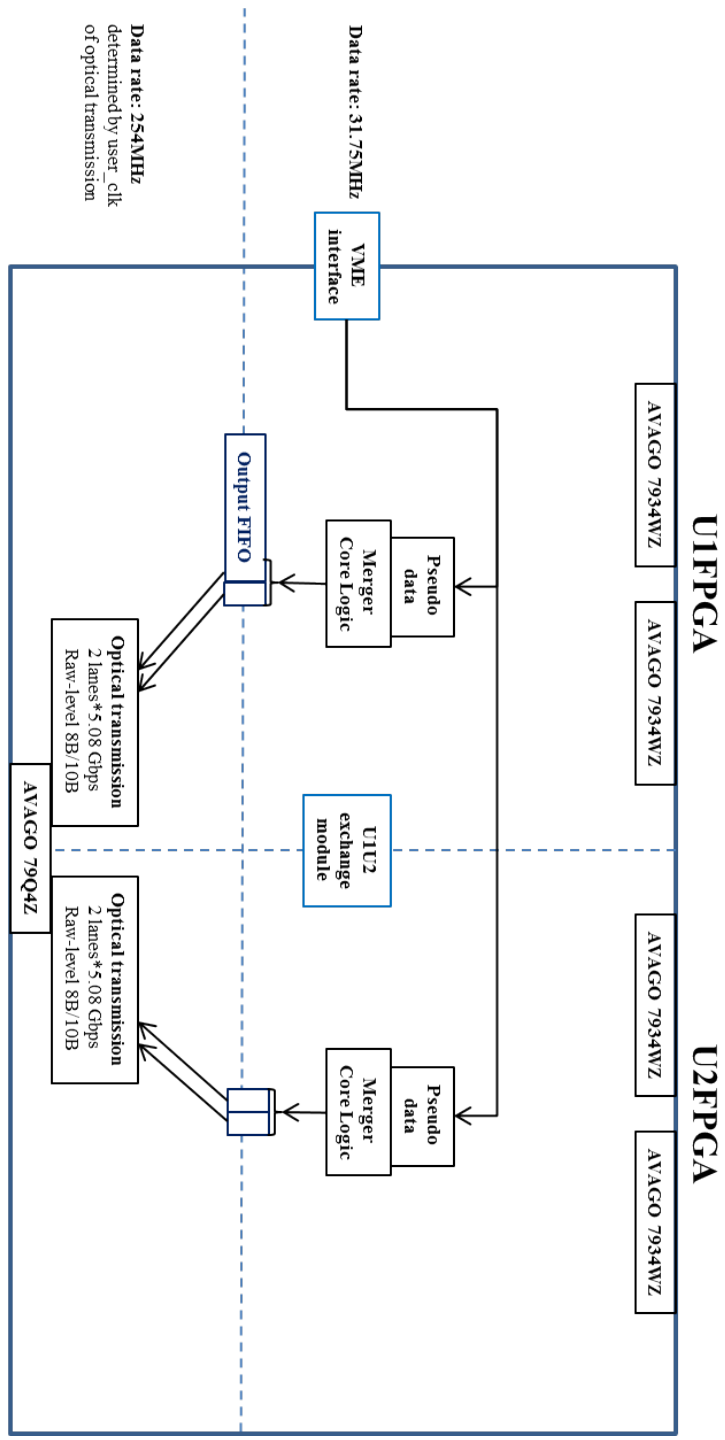


Figure 6.3: Schematic view of Merger firmware under data player mode.

6.2.2 Optical Transmission Module and First-In-First-Out (FIFO)



For data transmission, we use the raw-level 8B/10B protocol, which is designed by NTUHEP group and will be detailed in later chapter. For the input, each CDCFE - Merger connection includes 4 optical lanes (with 1 AVAGO 7934WZ). With transmission user clock is 127 MHz and data path width is 16 bits, the lane rate is 2.54 Gbps. For the output, each Merger unit - TSF connection includes 2 optical lanes (with half a AVAGO 79Q4Z). With transmission user clock is 254 MHz and data path width is 16 bits, the lane rate is 5.08 Gbps.

For the firmware structure, different sections of the data flow are driven by different clock rate. If there are multiple optical channels from different inputs, the incoming data won't arrive at the same time. Thus, we need First-In-First-Out (FIFO) to balance their data rate and synchronize the input data. About the FIFO to buffer CDCFE inputs, the input transmission module writes 16 bits to it with 127 MHz, and the Merger function reads the 64 bits data from it with 31.75 MHz. About the FIFO for output to TSF, the Merger function writes the 128 bits data to it with 31.75 MHz, and the output transmission module reads 16 bits from it with 254 MHz.

6.2.3 VME Interface

Through VME interface, we can download the firmware to flash memory, reload the firmware from flash memory, and monitor the operation. Although those functionalities can be also done through JTag cable and software, VME provides an alternative and faster way with Linux server and CPU server.

The signal we can read/write through VME every single time is 32 bits. Besides the simple 32 bits reading and writing function, there are many other functions are implemented with VME interface. For example, switching between different operation modes, inserting the pseudo data for Merger data player, monitoring the wire hit rate, and so on. All the Merger VME functionalities are summarized in Appendix A.

6.2.4 Data Exchange Module between U1 and U2

Due to the circuit design, we can only access U1 FPGA through VME interface. The design of data exchange module is based upon the 20 bi-directional pins between U1 and U2. With the exchange module, the data written to U1 through VME can be shared to U2, and the U2 information can also be sent to U1 to become readable by VME.

6.2.5 Data Player Mode

Under data player mode, only the optical links between Merger and TSF are necessary. Merger will directly generate dummy data patterns with clock counters and then send to TSF. User can insert pseudo data to Merger from CPU server by executing a VME function, and Merger will play the data into the running data flow. By preparing patterns from software simulation, we can test and debug the tracking algorithms of TSF and the other rear-end trackers with this scheme.

6.2.6 Transmission Test Mode

Transmission test mode is only used for Bit Error Rate Test (BERT) of optical modules, so other components in the firmware won't be activated. Under this mode, if the counterpart of an optical lane is also under transmission test mode, BERT will start automatically between two ends of this lane, and only dummy patterns for BERT will be transmitted/received.

6.2.7 Usage of LED on Front-Panel

LED on Merger's front-panel (Figure 6.4) are used to indicate the status of firmware operation as following:

- Two RJ45 LED:
 - Normal operation mode: the above LED (orange) will be on.
 - Data player mode: the below LED (green) will be on.



- Six green LED for AVAGO:
 - Normal operation mode: status of links (Links are healthy or not.)
 - Data player mode: status of links (Links are healthy or not.)
 - Transmission test mode: status of BERT (BERT is running or not.)
- Six red LED for AVAGO:
 - Normal operation mode: Data flow is off or not.
 - Data player mode: Data flow is off or not.
 - Transmission test mode: Bit error of transmission is found.

6.3 Core Logic of CDCFE and Merger

This section is about the trigger algorithms of CDCFE and Merger. The raw data of CDCFE readout includes wire hit (1 bit) and hit timing with 1 ns resolution (3 bits), with 127 MHz data rate. CDCFE core logic for TRG data summarizes the information of single wire into PTS information with 31.75 MHz dataclk, and the Merger core logic further simplifies the 2 PTS data (of inside and outside CDCFE) into TS information of a SL.

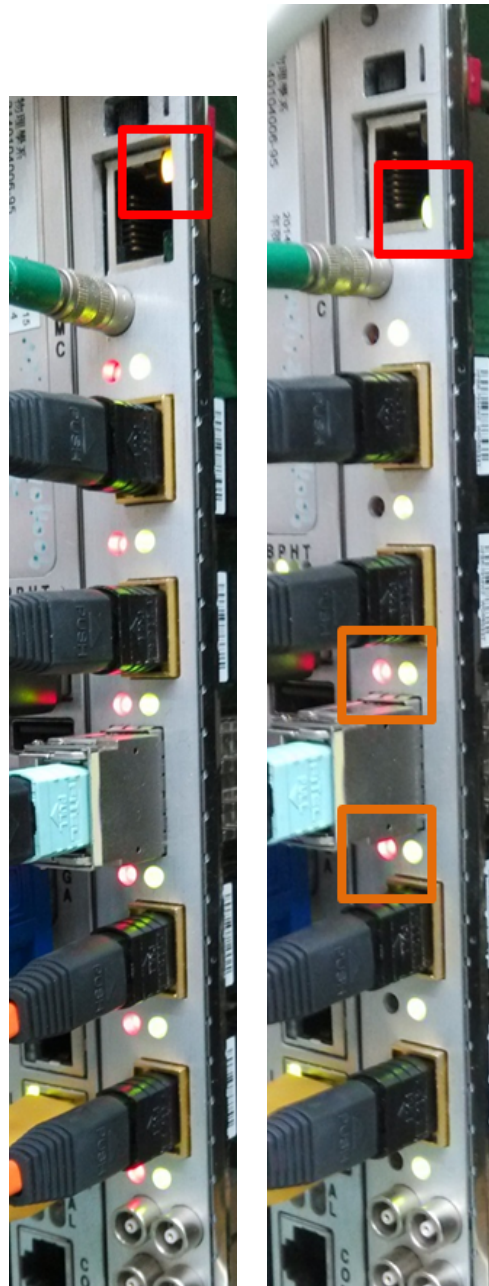
6.3.1 SL0 Inside CDCFE

Figure 6.5 is part of the CDC SL0 inside wire cell configuration corresponding to a CDCFE board. **First priority cells are cell 0~15. Secondary priority cells are cell 16~31.** A PTS in this case contains 3 cells, e.g. cell 10, 25, and 26 for PTS#10 in the thick frame of Figure 6.5.

Input: 1 bit wire hit and 3 bits hit timing in 127 MHz of 32 wires

Output:

- Hitmap of wire cells 0 ~ 31 (31~0, 32 bits)
- Priority cell timing (111~32, 5*16 bits)



(a) Normal operation mode. (b) Data player mode.

Figure 6.4: Merger's LED on front-panel.

	31	30	29	28	27	26	25	24	23	22	21	20	19	18	17	16	
	15	14	13	12	11	10	9	8	7	6	5	4	3	2	1	0	

Figure 6.5: Part of CDC SL0 inside wire cell configuration [70].

F3	Reserved														N/A	N/A	N/A	N/A	N/A	N/A	N/A	N/A	N/A	N/A	N/A	N/A	N/A	N/A	N/A	0xF0
	N/A	N/A	N/A	N/A	N/A	N/A	N/A	N/A	N/A	N/A	N/A	N/A	N/A	N/A	N/A	N/A	N/A	N/A	N/A	N/A	N/A	N/A	N/A	N/A	N/A	N/A	N/A	N/A	0xE0	
	N/A	N/A	cc										et00						0xD0											
	ft15					ft14					ft13					ft12	0xC0													
F2	ft12					ft11					ft10					ft09	0xB0													
	ft09				ft08				ft07				ft06			0xA0														
	ft06			ft05				ft04				ft03				0x90														
	ft03	ft02				ft01				ft00				0x80																
F1	sc15	sc14	sc13	sc12	sc11	sc10	sc09	sc08	sc07	sc06	sc05	sc04	sc03	sc02	sc01	sc00	0x70													
	pt15					pt14					pt13					pt12	0x60													
	pt12				pt11				pt10				pt09			0x50														
	pt09			pt08				pt07				pt06			0x40															
F0	pt06			pt05				pt04				pt03				0x30														
	pt03	pt02				pt01				pt00				0x20																
	h31	h30	h29	h28	h27	h26	h25	h24	h23	h22	h21	h20	h19	h18	h17	h16	0x10													
	h15	h14	h13	h12	h11	h10	h09	h08	h07	h06	h05	h04	h03	h02	h01	h00	0x00													

Figure 6.6: Bit map of CDC SL0 inside function output [70].


- Secondary priority cell hit position flag. It is '1' only when first priority cell is not hit and the left secondary one is hit. (127~112, 16 bits)
- Fastest hit timing among cells in each PTS (207~128, 5*16 bits)
- Edge information: hit timing of cell 31 (212~208, 5 bits)
- Time stamp (clock counter) (221~213, 9 bits)
- Check sum: XOR of all odd bits and event bits (255~254, 2 bits)

6.3.2 SL0 Outside CDCFE

			47	46	45	44	43	42	41	40	39	38	37	36	35	34	33	32		
			31	30	29	28	27	26	25	24	23	22	21	20	19	18	17	16		
			15	14	13	12	11	10	9	8	7	6	5	4	3	2	1	0		

Figure 6.7: Part of CDC SL0 outside wire cell configuration [70].

Figure 6.7 is part of the CDC SL0 outside wire cell configuration corresponding to a CDCFE board. A PTS in this case contains 12 cells, e.g. cell 7, 8, 9, 22, 23, 24, 25, 38, 39, 40, 41, and 42 for PTS#8 in the thick frame of Figure 6.7.



F3	Reserved				N/A	N/A	N/A	N/A	N/A	N/A	N/A	N/A	N/A	N/A	N/A	N/A	0xF0
	N/A	N/A	N/A	N/A	N/A	N/A	N/A	N/A	N/A	N/A	N/A	N/A	N/A	N/A	N/A	N/A	0xE0
	N/A	N/A	N/A	N/A	N/A	N/A	N/A	N/A	N/A	N/A	N/A	N/A	N/A	N/A	N/A	N/A	0xD0
	N/A	N/A	N/A	N/A	N/A	N/A	N/A	N/A	N/A	N/A	N/A	N/A	N/A	N/A	N/A	N/A	0xC0
F2	N/A	N/A	N/A	N/A	N/A	N/A	N/A	N/A	N/A	N/A	N/A	N/A	N/A	N/A	N/A	N/A	0xB0
	N/A	N/A	N/A	N/A	N/A	N/A	N/A	N/A	N/A	N/A	N/A	N/A	N/A	N/A	N/A	N/A	0xA0
	N/A	N/A	N/A	cc						et03						0x90	
	et03	et02				et01				et00				0x80			
F1	ft15				ft14				ft13				ft12	0x70			
	ft12			ft11				ft10				ft09	0x60				
	ft09		ft08				ft07				ft06	0x50					
	ft06	ft05				ft04				ft03	0x40						
F0	ft03	ft02				ft01				ft00				0x30			
	h47	h46	h45	h44	h43	h42	h41	h40	h39	h38	h37	h36	h35	h34	h33	h32	0x20
	h31	h30	h29	h28	h27	h26	h25	h24	h23	h22	h21	h20	h19	h18	h17	h16	0x10
	h15	h14	h13	h12	h11	h10	h09	h08	h07	h06	h05	h04	h03	h02	h01	h00	0x00

Figure 6.8: Bit map of CDC SL0 outside function output [70].

Input: 1 bit wire hit and 3 bits hit timing in 127 MHz of 48 wires

Output:

- Hitmap of wire cells 0 ~ 47 (47~0, 48 bits)
- Fastest hit timing among cells in each PTS (127~48, 5*16 bits)
- Edge information: hit timing of cell 32 (132~128, 5 bits)
- Edge information: fastest hit timing among cell 0, 16, 32, and 33 (137~133, 5 bits)
- Edge information: fastest hit timing among cell 15, 30, 31, 46, and 47 (142~138, 5 bits)
- Edge information: fastest hit timing among cell 31 and 47 (147~143, 5 bits)
- Time stamp (clock counter) (156~148, 9 bits)
- Check sum: XOR of all odd bits and event bits (255~254, 2 bits)



Figure 6.9: Part of CDC outer SL inside wire cell configuration [70].

6.3.3 Outer SL Inside CDCFE

Figure 6.9 is part of the CDC SL0 inside wire cell configuration corresponding to a CDCFE board. **First priority cells are cell 32~47.** A PTS in this case contains 6 cells, e.g. cell 1, 2, 3, 17, 18, and 34 for PTS#2 in the thick frame of Figure 6.9.

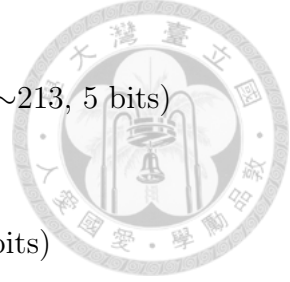
F3	Reserved												N/A	N/A	N/A	N/A	N/A	N/A	N/A	N/A	N/A	N/A	N/A	N/A	N/A	N/A	0xF0
	N/A	N/A	N/A	N/A	N/A	N/A	N/A	N/A	N/A	N/A	N/A	N/A	N/A	N/A	cc	0xE0											
	cc						et01						et00						0xD0								
	ft15						ft14						ft13						ft12	0xC0							
F2	ft12						ft11						ft10						ft09	0xB0							
	ft09						ft08						ft07						ft06	0xA0							
	ft06						ft05						ft04						ft03	0x90							
	ft03						ft02						ft01						ft00	0x80							
F1	pt15						pt14						pt13						pt12	0x70							
	pt12						pt11						pt10						pt09	0x60							
	pt09						pt08						pt07						pt06	0x50							
	pt06						pt05						pt04						pt03	0x40							
F0	pt03						pt02						pt01						pt00	0x30							
	h47	h46	h45	h44	h43	h42	h41	h40	h39	h38	h37	h36	h35	h34	h33	h32	0x20										
	h31	h30	h29	h28	h27	h26	h25	h24	h23	h22	h21	h20	h19	h18	h17	h16	0x10										
	h15	h14	h13	h12	h11	h10	h09	h08	h07	h06	h05	h04	h03	h02	h01	h00	0x00										

Figure 6.10: Bit map of CDC outer SL inside function output [70].

Input: 1 bit wire hit and 3 bits hit timing in 127 MHz of 48 wires

Output:

- Hitmap of wire cells 0 ~ 47 (47~0, 48 bits)
- First priority cell timing (127~48, 5*16 bits)
- Fastest hit timing among cells in each PTS (207~128, 5*16 bits)
- Edge information: hit timing of cell 0 (212~208, 5 bits)



- Edge information: fastest hit time among cell 15 and 31 (217~213, 5 bits)
- Time stamp (clock counter) (226~218, 9 bits)
- Check sum: XOR of all odd bits and event bits (255~254, 2 bits)

6.3.4 Outer SL Outside CDCFE



Figure 6.11: Part of CDC outer SL outside wire cell configuration [70].

Figure 6.11 is part of the CDC SL0 inside wire cell configuration corresponding to a CDCFE board. **Secondary priority cells are cell 0~15.** A PTS in this case contains 5 cells, e.g. cell 1, 2, 17, 18, and 19 for PTS#2 in the thick frame of Figure 6.11.

F3	Reserved				N/A	N/A	N/A	N/A	N/A	N/A	N/A	N/A	N/A	N/A	N/A	N/A	N/A	0xF0
	N/A	N/A	N/A	N/A	N/A	N/A	N/A	N/A	N/A	N/A	N/A	N/A	N/A	N/A	cc		0xE0	
	cc				et01				et00								0xD0	
	ft15				ft14				ft13				ft12				0xC0	
F2	ft12				ft11				ft10				ft09				0xB0	
	ft09		ft08				ft07				ft06				0xA0			
	ft06		ft05				ft04				ft03				0x90			
	ft03		ft02				ft01				ft00				0x80			
F1	st15				st14				st13				st12				0x70	
	st12				st11				st10				st09				0x60	
	st09		st08				st07				st06				0x50			
	st06		st05				st04				st03				0x40			
F0	st03		st02				st01				st00				0x30			
	h47	h46	h45	h44	h43	h42	h41	h40	h39	h38	h37	h36	h35	h34	h33	h32	0x20	
	h31	h30	h29	h28	h27	h26	h25	h24	h23	h22	h21	h20	h19	h18	h17	h16	0x10	
	h15	h14	h13	h12	h11	h10	h09	h08	h07	h06	h05	h04	h03	h02	h01	h00	0x00	

Figure 6.12: Bit map of CDC outer SL outside function output [70].

Input: 1 bit wire hit and 3 bits hit timing in 127 MHz of 48 wires

Output:



- Hitmap of wire cells 0 ~ 47 (47~0, 48 bits)
- Secondary priority cell timing (127~48, 5*16 bits)
- Fastest hit timing among cells in each PTS (207~128, 5*16 bits)
- Edge information: hit timing of cell 16 (212~208, 5 bits)
- Edge information: fastest hit timing among cell 15 and 31 (217~213, 5 bits)
- Time stamp (clock counter) (226~218, 9 bits)
- Check sum: XOR of all odd bits and event bits (255~254, 2 bits)

6.3.5 SL0 Merger




Figure 6.13: Part of CDC SL0 wire cell configuration [70].

Figure 6.13 is part of the CDC SL0 wire cell configuration corresponding to a Merger board. **First priority cells are cell 0~15.** **Secondary priority cells are cell 15~31.** A TS in this case contains 15 cells, e.g. cell 2, 17, 18, 33, 34, 35, 48, 49, 50, 51, 64, 65, 66, 67, and 68 for TS#2 in the thick frame of Figure 6.13.

Input: Data patterns from SL0 inside and SL0 outside CDCFE in 31.75 MHz (2*256 bits)

Output: 256 bits in 31.75 MHz (timing resolution is reduced to 2 ns.)

- Hitmap of wire cell 0 ~ 79 (79~0, 80 bits)
- Priority cell timing (143~80, 4*16 bits)
- Fastest hit timing among cells in each TS (207~144, 4*16 bits)
- Secondary priority cell hit position flag. It is '1' only when first priority cell is not hit and the left secondary one is hit. (223~208, 16 bits)



F7	Reserved				cc								et04				0xF0
	et3				et02				et01				et00				0xE0
F6	sc15	sc14	sc13	sc12	sc11	sc10	sc09	sc08	sc07	sc06	sc05	sc04	sc03	sc02	sc01	sc00	0xD0
	ft15				ft14				ft13				ft12				0xC0
F5	ft11				ft10				ft09				ft08				0xB0
	ft07				ft06				ft05				ft04				0xA0
F4	ft03				ft02				ft01				ft00				0x90
	pt15				pt14				pt13				pt12				0x80
F3	pt11				pt10				pt09				pt08				0x70
	pt07				pt06				pt05				pt04				0x60
F2	pt03				pt02				pt01				pt00				0x50
	h79	h78	h77	h76	h75	h74	h73	h72	h71	h70	h69	h68	h76	h66	h65	h64	0x40
F1	h63	h62	h61	h60	h59	h58	h57	h56	h55	h54	h53	h52	h51	h50	h49	h48	0x30
	h47	h46	h45	h44	h43	h42	h41	h40	h39	h38	h37	h36	h35	h34	h33	h32	0x20
F0	h31	h30	h29	h28	h27	h26	h25	h24	h23	h22	h21	h20	h19	h18	h17	h16	0x10
	h15	h14	h13	h12	h11	h10	h09	h08	h07	h06	h05	h04	h03	h02	h01	h00	0x00

Figure 6.14: Bit map of Merger SL0 function output [70].

- Edge information: hit timing of cell 31 (227~224, 4 bits)
- Edge information: hit timing of cell 64 (231~228, 4 bits)
- Edge information: fastest hit timing among cell 32, 48, 64 and 65 (235~232, 4 bits)
- Edge information: fastest hit timing among cell 31, 47, 62, 63, 78 and 79 (239~236, 4 bits)
- Edge information: fastest hit timing among cell 63 and 79 (243~240, 4 bits)
- Time stamp (clock counter) (252~244, 9 bits)
- Check sum: XOR of all odd bits and event bits (255~254, 2 bits)

6.3.6 Outer SL Merger

Figure 6.15 is part of the CDC outer SL wire cell configuration corresponding to a Merger board. **First priority cells are cell 32~47. Secondary priority cells are cell 48~63.** A TS in this case contains 11 cells, e.g. cell 1, 2, 3, 17, 18, 34, 49, 50, 65, 66, and 67 for TS#2 in the thick frame of Figure 6.15.



95	94	93	92	91	90	89	88	87	86	85	84	83	82	81	80	
	79	78	77	76	75	74	73	72	71	70	69	68	67	66	65	64
63	62	61	60	59	58	57	56	55	54	53	52	51	50	49	48	
	47	46	45	44	43	42	41	40	39	38	37	36	35	34	33	32
31	30	29	28	27	26	25	24	23	22	21	20	19	18	17	16	
	15	14	13	12	11	10	9	8	7	6	5	4	3	2	1	0

Figure 6.15: Part of CDC outer SL wire cell configuration [70].

F7	Reserved				N/A	N/A	N/A	N/A	N/A	N/A	N/A	cc				0xF0	
	cc				et02				et01				et00				0xE0
F6	sc15	sc14	sc13	sc12	sc11	sc10	sc09	sc08	sc07	sc06	sc05	sc04	sc03	sc02	sc01	sc00	0xD0
	ft15				ft14				ft13				ft12				0xC0
F5	ft11				ft10				ft09				ft08				0xB0
	ft07				ft06				ft05				ft04				0xA0
F4	ft03				ft02				ft01				ft00				0x90
	pt15				pt14				pt13				pt12				0x80
F3	pt11				pt10				pt09				pt08				0x70
	pt07				pt06				pt05				pt04				0x60
F2	pt03				pt02				pt01				pt00				0x50
	h79	h78	h77	h76	h75	h74	h73	h72	h71	h70	h69	h68	h76	h66	h65	h64	0x40
F1	h63	h62	h61	h60	h59	h58	h57	h56	h55	h54	h53	h52	h51	h50	h49	h48	0x30
	h47	h46	h45	h44	h43	h42	h41	h40	h39	h38	h37	h36	h35	h34	h33	h32	0x20
F0	h31	h30	h29	h28	h27	h26	h25	h24	h23	h22	h21	h20	h19	h18	h17	h16	0x10
	h15	h14	h13	h12	h11	h10	h09	h08	h07	h06	h05	h04	h03	h02	h01	h00	0x00

Figure 6.16: Bit map of Merger outer SL function output [70].



Input: Data patterns from outer SL inside and outer SL outside CDCFE in 31.75 MHz (2×256 bits)

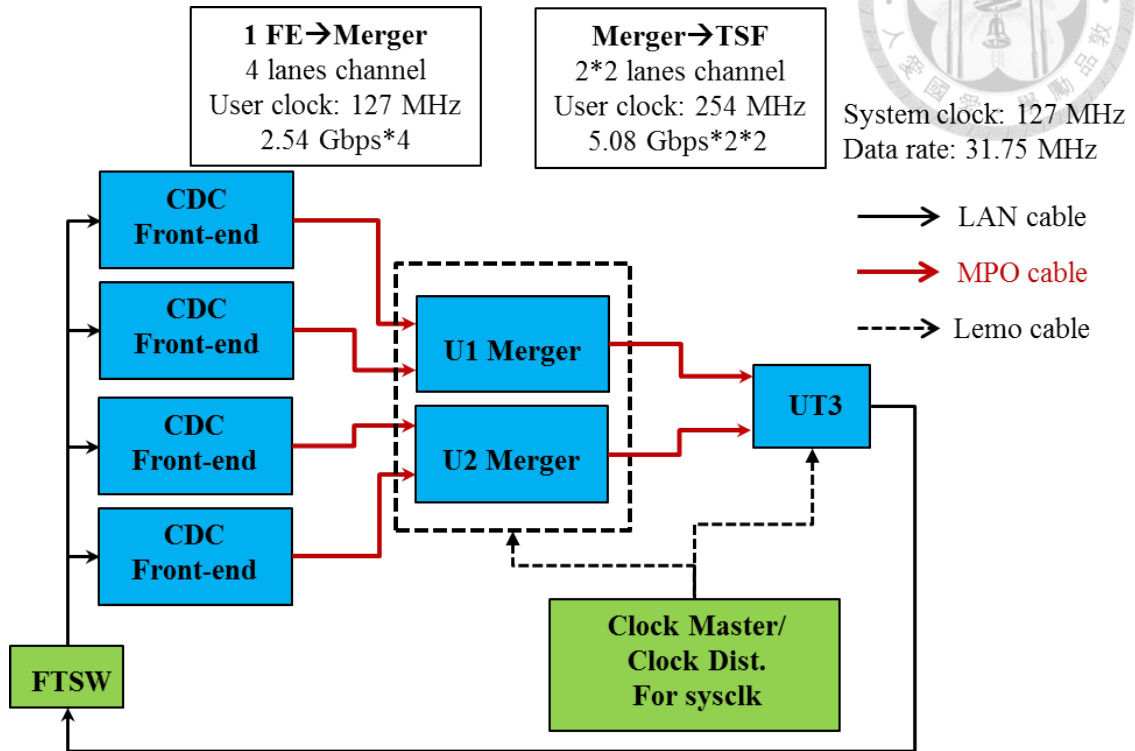
Output: 256 bits in 31.75 MHz (timing resolution is reduced to 2 ns.)

- Hitmap of wire cell 0 ~ 79 (79~0, 80 bits)
- Priority cell timing (143~80, 4×16 bits)
- Fastest hit timing among cells in each TS (207~144, 4×16 bits)
- Secondary priority cell hit position flag. It is '1' only when first priority cell is not hit and the left secondary one is hit. (223~208, 16 bits)
- Edge information: hit timing of cell 63 (227~224, 4 bits)
- Edge information: fastest hit timing among cell 0, and 64 (231~228, 4 bits)
- Edge information: fastest hit timing among cell 15, 31, 63, and 79 (235~232, 4 bits)
- Time stamp (clock counter) (244~236, 9 bits)
- Check sum: XOR of all odd bits and event bits (255~254, 2 bits)

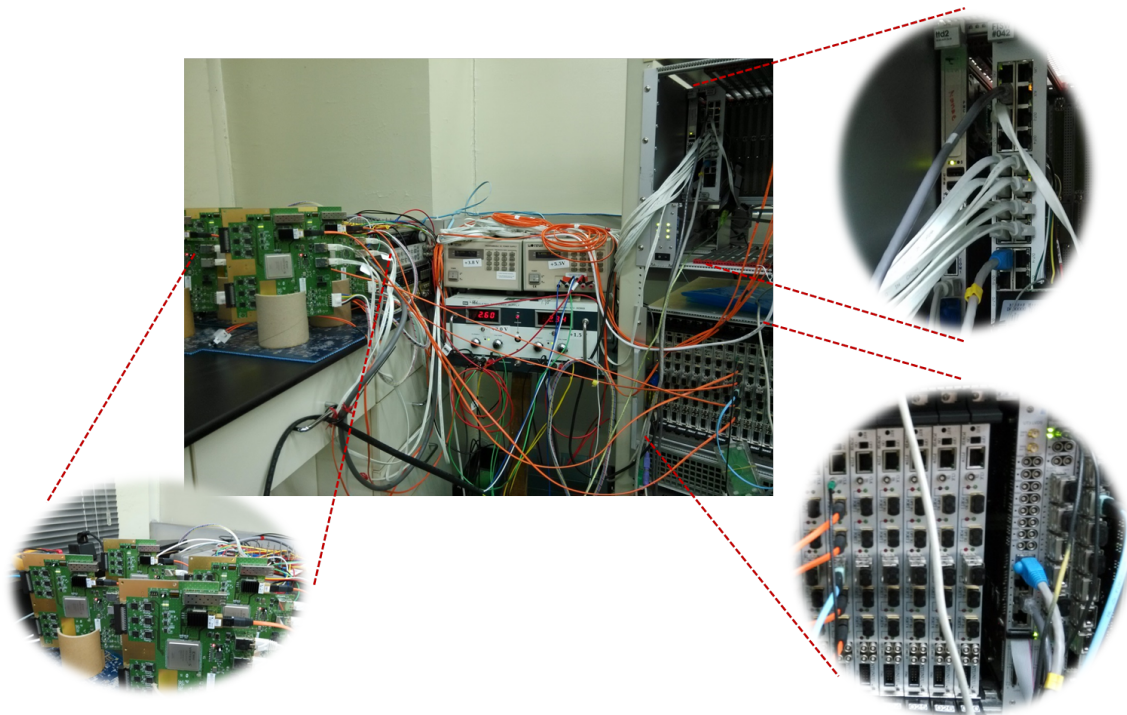
6.4 Operation Test

6.4.1 Setup

During mass production quality check in November 2014~January 2015, we built up a test bench in NTU to check the performance of Merger boards and the firmware design. The whole setup of the system is shown in Figure 6.17. A 6U VME crate is mounted with CPU server board, Merger boards, UT3, clock master and distributor. A 9U crate is mounted with a Frontend Timing Switch (FTSW) board. 4 CDCFE are powered by 4 standalone DC power supplies. The whole system is driven by a general 127 MHz sysclk source which is generated by clock master. Through the LEMO interface of clock distributor, clock is distributed to Mergers and UT3. FTSW is responsible for clock, trigger, timing, revolution signal and so on, of all CDCFE, and its interface is RJ45 (LAN cable). Therefore, UT3 needs to transform the LEMO clock into RJ45 interface for FTSW. The CPU server board is responsible for Merger's VME interface.



(a) Schematic view of data flow.



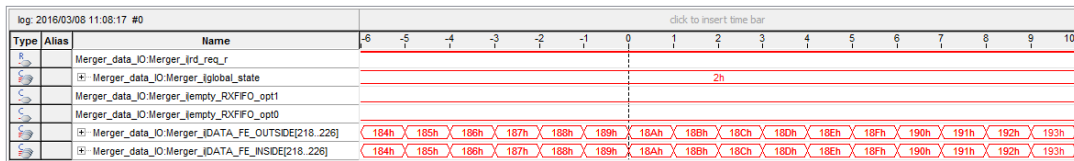
(b) Hardware setup.

Figure 6.17: Setup of the testbench for Merger operation test.

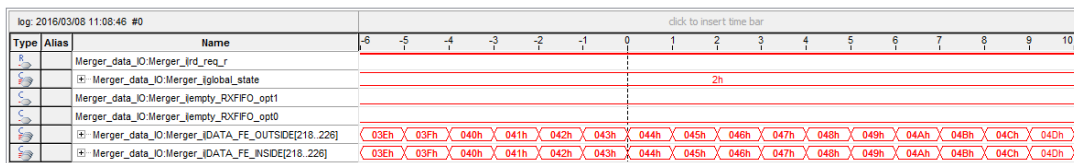


6.4.2 Test Result of Normal Operation Mode

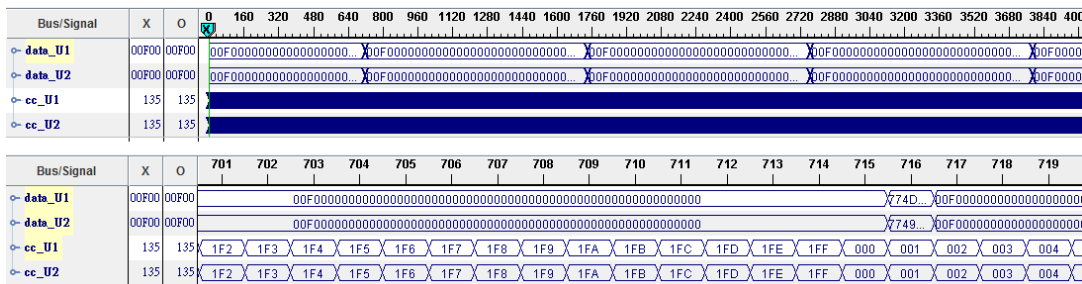
Under the normal operation mode, we can check if the LED on Merger behave like Figure 6.4(a) to know data flow status of the system. Six green LED represent the status of optical channels, and Six red LED represent the data flow status through the corresponding channel or not. During operation, the most important thing we need to check is the synchronization of clock counters, since it represents the data flow is running stably and is synchronized in this stage. In this system, we check the status of clock counters during operation and results at various stages (U1 Merger, U2 Merger, and UT3) of the system are in Figure 6.18 with the logic analyzer software of Xilinx [71] and Altera [72]. In order to check the core logics, CDCFE firmware is implemented with pseudo wire hit generator which will make all wires hit in every $10\mu s$. The wire hit patterns received by UT3 are shown in Figure 6.19.



(a) At U1 Merger.

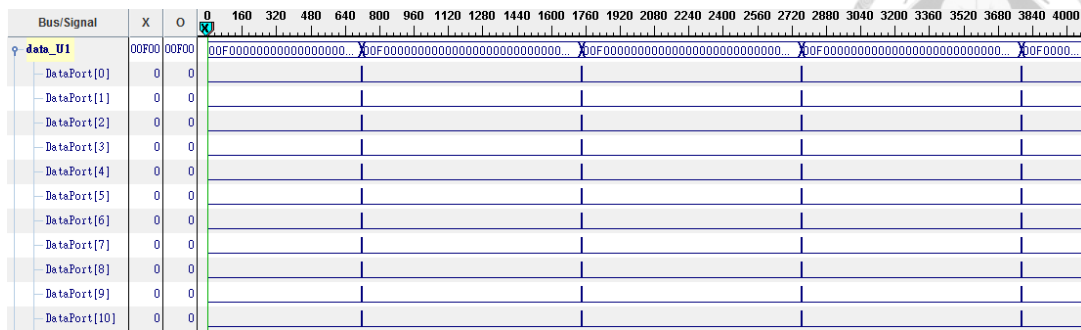
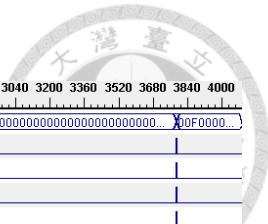


(b) At U2 Merger.

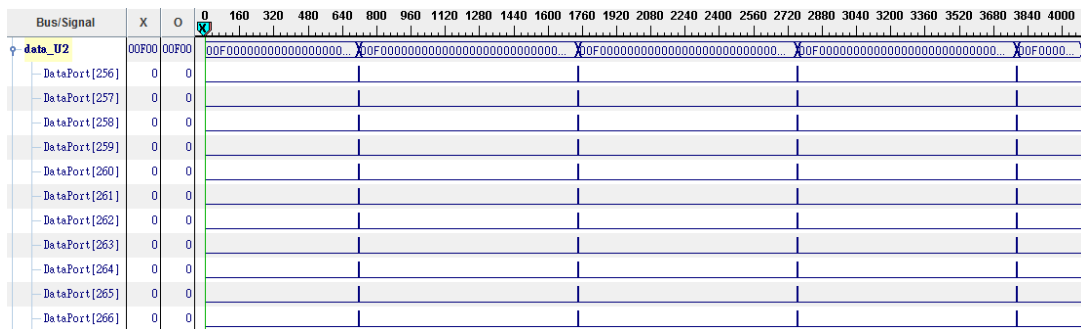


(c) At UT3.

Figure 6.18: Clock counters synchronization at two Merger units and UT3 under normal operation mode.



(a) From U1 Merger.



(b) From U2 Merger.

Figure 6.19: Wire hit patterns from two Merger units received by UT3.

6.4.3 Test Result of Data Player Mode

Switching between two operation modes is done by executing the VME function. Under data player mode, there is no data flow through the CDCFE - Merger channels. Figure 6.20 shows the clock counter synchronization at UT3. After the pseudo data patterns are inserted from VME to Merger, the patterns will be played periodically, as shown in Figure 6.21.

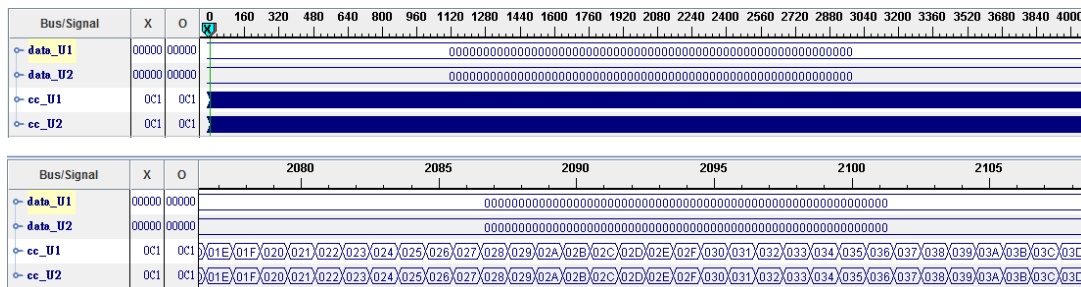


Figure 6.20: Clock counters synchronization at UT3 under data player mode.



Chapter 7

Data Transmission in CDCTRG

7.1 Introduction

Figure 5.8 is the data flow chart of CDCTRG. The whole system is a tree-diagram network with optical connections. For the optical data transmission in CDCTRG, we started from studying on open-sourced Aurora 8B/10B protocols and then designed user-defined protocols, which are called raw-level protocols including different encoding for different hardware components. Based upon the properties of hardware and protocols, we also designed a flow control and synchronization scheme for the whole system. The summary of all transmission-related hardware components in CDCTRG is in Table 7.1.

7.2 Introduction to Hardware Components

7.2.1 Embedded Optical Module (AVAGO connector)

AVAGO connector transforms the electric signal from the circuit to optical signal which is transmitted through optical fiber cable. There are two types AVAGO connector used in CDCTRG, including 7934WZ (Figure 7.1) and 79Q4Z (Figure 7.2).



AVAGO HFBR-7934WZ

HFBR-7934WZ [68] contains four optical lanes and its transmission rate supports from 1 to 3.125 Gbps per lane. 7934WZ is used in connections between CDCFE and Merger. Since CDCFE will be at the high radiation level region (directly mounted on Belle II CDC), we had a radiation hardness test with Co-60 source in Tokyo Institute of Technology. The radiation hardness was tested to be 350 ± 25 Gy, which corresponds about 15 years of Belle II operation.



Figure 7.1: AVAGO HFBR-7934WZ connector.

AVAGO AFBR-79Q4Z

AFBR-79Q4Z [69] contains four optical lanes and its transmission rate supports up to 10 Gbps per lane approximately. It is used in the connections from Merger to global trigger with higher transmission rate.



Figure 7.2: AVAGO AFBR-79Q4Z connector.



7.2.2 FPGA Chips and Transceivers in CDCTR

CDCFE

CDCFE (Figure 7.3) is based on a Xilinx Virtex-5 FPGA [73] and its RocketIO (high speed transceiver) is Virtex-5 GTP [74]. Virtex-5 GTP can support transmission rate from 0.1 to 3.7 Gbps per lane.

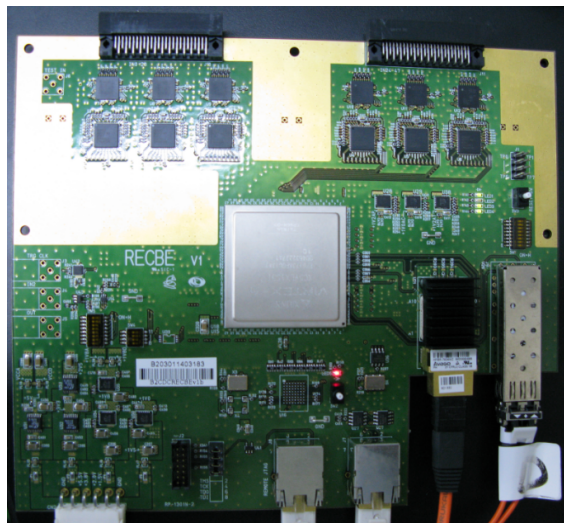


Figure 7.3: CDCFE board.

Merger

Merger (Figure 7.4) is based on two Altera Arria II FPGA [66] and its transceiver can support transmission rate from up to about 6.375 Gbps per lane [75]. In one Merger unit, Eight of the lanes are bounded with two 7934WZ and the other two of them are bounded with half a 79Q4Z.

Universal Trigger Board (UT3)

UT3 (Figure 7.5) is based on a Xilinx Virtex-6 FPGA [76] and its RocketIO includes Virtex-6 GTX [77] and GTH [78]. Virtex-6 GTX can support transmission rate from 0.6 to 6.6 Gbps per lane. Virtex-6 GTH can support transmission rate within the ranges 1.24~1.397 Gbps, 2.48~2.795 Gbps, 4.96~5.591 Gbps, and 9.92~11.182 Gbps per lane. 40 GTX in UT3 are bounded with ten 79Q4Z at daughter board and 24 GTX in UT3 are bounded with six 79Q4Z at main board.

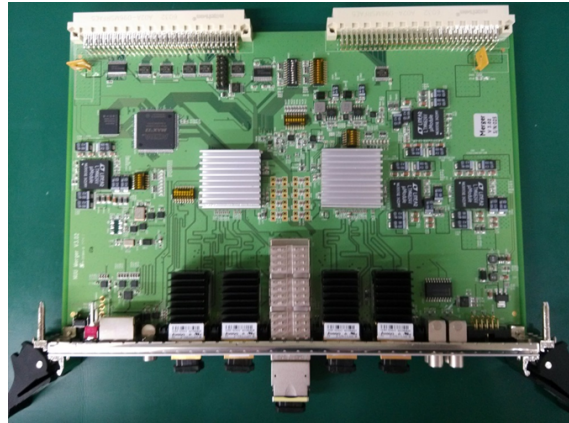


Figure 7.4: Merger board.



Figure 7.5: Universal Trigger board (UT3).

Type	Component	TRG board	Supported lane rate (Gbps)
Optical module	HFBR-7934WZ	CDCFE, Merger	1~3.125
Optical module	AFBR-79Q4Z	Merger, UT3	0~10
Transceiver	GTP	CDCFE	0.1~3.7
Transceiver	GTX	UT3	0.6~6.6
Transceiver	GTH	UT3	1.24~1.397, 2.48~2.795, 4.96~5.591, 9.92~11.182
Transceiver	Merger	Merger	0~6.375

Table 7.1: Summary of all hardware components used for CDCTRG optical transmission.



7.3 Aurora Protocols

At first, the open-sourced Aurora protocols [79] provided by Xilinx company are the solution of CDCTRG data transmission. The design of raw-level protocols are also based on our previous study on Aurora 8B/10B protocol with GTX. This chapter mentions the basic firmware structure, user interface, and properties of Aurora.

7.3.1 Firmware Structure

The basic Aurora firmware can be generated by the Core Generator tool [80] in Xilinx software ISE [81]. The schematic view of Aurora firmware structure is shown in Figure 7.6.

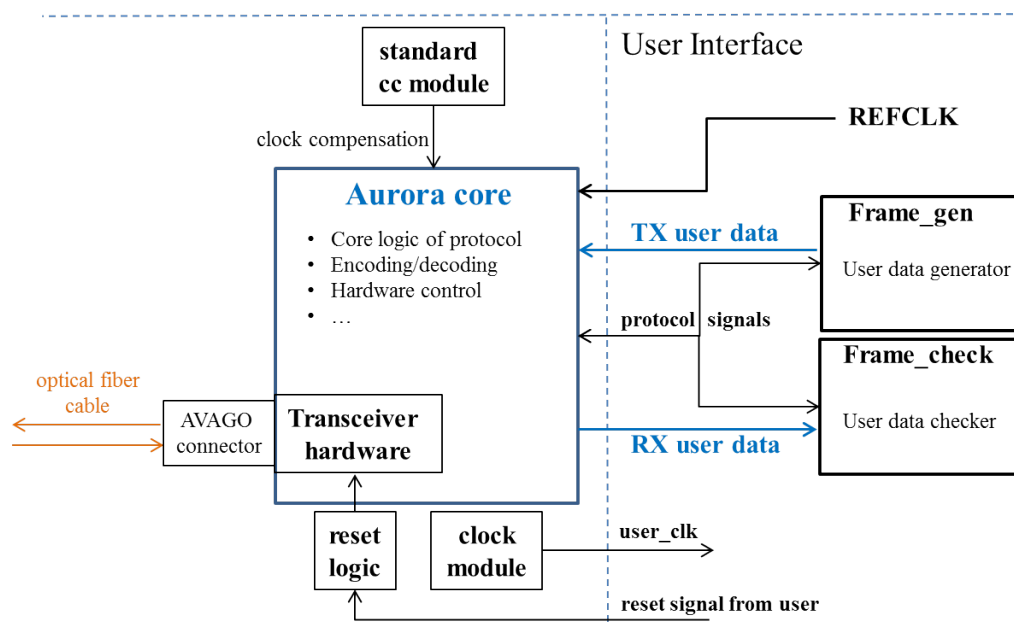


Figure 7.6: Schematic view of Aurora firmware structure.

Aurora core

Aurora core is the core logic of this protocol design. Its functions include encoding for transmitter side (TX), decoding for receiver side (RX), channel bonding, control on hardware side, user interface clock (*user_clk*) generation, provide protocol signals to user interface, and so on.

In the FPGA circuit design with RocketIO, the reference clock (REFCLK) is not a global pin but a local pin which is directly connected to the transceiver. Since high speed transmission requires a clock source with better quality, REFCLK is not free running in the rest part of firmware design. The RocketIO uses a Phase-locked Loop (PLL) and clocking module to generate user_clk, which is distributed to user interface. In user interface, data needs to be transmitted/received aligned to the edge of user_clk. The frequency ratio between REFCLK and user_clk is limited to be some specific rational number since clocking module is based upon a frequency multiplier/divider.

For stability, the data is usually encoded under the optical serial transmission. For instance, each 8 bits pattern would be encoded into a differential pair of 10 bits with 8B/10B encoding, and each 64 bits pattern would be encoded into a differential pair of 66 bits with 64B/66B encoding. Following are the transmission lane rate estimation with these two encoding cases:

- 8B/10B encoding:

$$\text{Lane rate} = \frac{10}{8} \times \text{user_clk} \times \text{data path width}, \quad (7.1)$$

where data path width is the user data size which is transmitted per lane per user_clk. The inflation factor $\frac{10}{8}$ is due to 8B/10B encoding. For 8B/10B encoding, data path width must be multiple of 8 bits. For instance, if we choose data path width = 16 bits and lane rate = 2.54 Gbps, user_clk would be 127 MHz.

- 64B/66B encoding:

$$\text{Lane rate} = \frac{66}{64} \times \text{user_clk} \times \text{data path width}. \quad (7.2)$$

The inflation factor $\frac{66}{64}$ is due to 64B/66B encoding. For 64B/66B encoding, data path width must be 64 bits. For instance, if we choose lane rate = 11.176 Gbps, user_clk would be 169.33 MHz.

User interface

Here are the protocol signals provided from Aurora core to user interface to control/detect:

- `user_clk`: All the transmission works in user interface need to be done aligned to the edge of `user_clk`.
- `channel_up` (`lane_up`): Flag signal. This signal indicates the status of hardware connection. If two ends of the connection are driven with same configuration (protocol, encoding, lane rate, REFCLK and so on) and the connection itself is healthy, `channel_up` would be 1.
- `TX_DST_RDY_N`: Flag signal. When `TX_DST_RDY_N = 0`, the Aurora core is ready for user to transmit user data.
- `TX_SRC_RDY_N`: User-controlled signal. After `TX_DST_RDY_N = 0`, user can switch `TX_SRC_RDY_N` to 0 and send to user data to Aurora core at the same time to start transmission.
- `RX_SRC_RDY_N`: Flag signal. When `RX_SRC_RDY_N = 0`, data from another end is available at this end and user should read it simultaneously.

In Figure 7.6, `Frame_gen` is the user TX module, in which the TX work is done by detecting `TX_DST_RDY_N` and control `TX_SRC_RDY_N`. `Frame_check` is the user RX module, in which the RX work is done by detecting `RX_DST_RDY_N` and receiving data passively. The behavior and control of protocol signals in user interface are shown in Figure 7.7~7.8.

Standard cc module

In regular cases of serial transmission, the configurations of two ends of a link are usually driven by the same REFCLK source and the same `user_clk`. Under a stable transmission, the buffers inside Aurora core should be written/read with a constant speed. If the clock sources are different, the tiny frequency difference would cause the buffers to be overflowed/empty. By checking the status of buffers, clock compensation signal will be generated to resolve this circumstance.

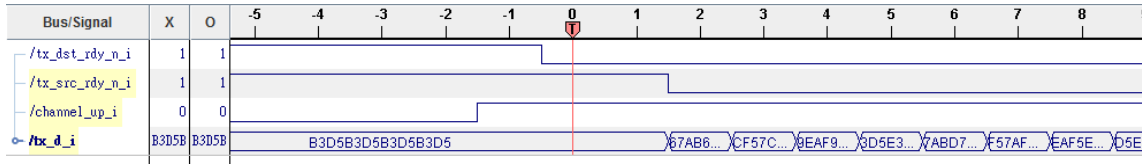
Reset logic

The reset logic module is connected to user interface. User can send a pulse signal to reset logic module to reset the firmware configuration of Aurora core and the transceiver hardware.

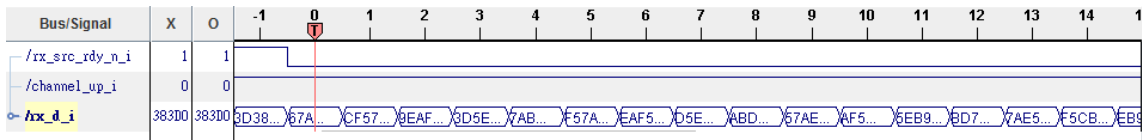


7.3.2 Firmware Test Results

The test result of firmware with Aurora 8B/10B protocol are shown in Figure 7.7~7.8 for UT3 and Merger, respectively.

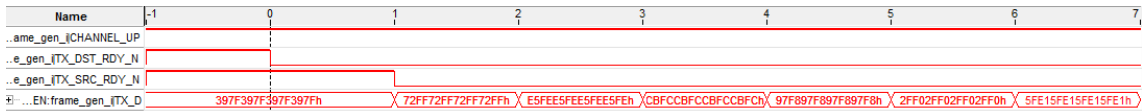


(a) TX result at frame_gen.

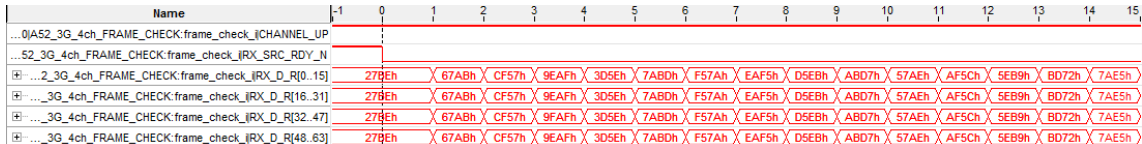


(b) RX result at frame_check.

Figure 7.7: Test result of firmware with Aurora 8B/10B protocol for UT3.



(a) TX result at frame_gen.

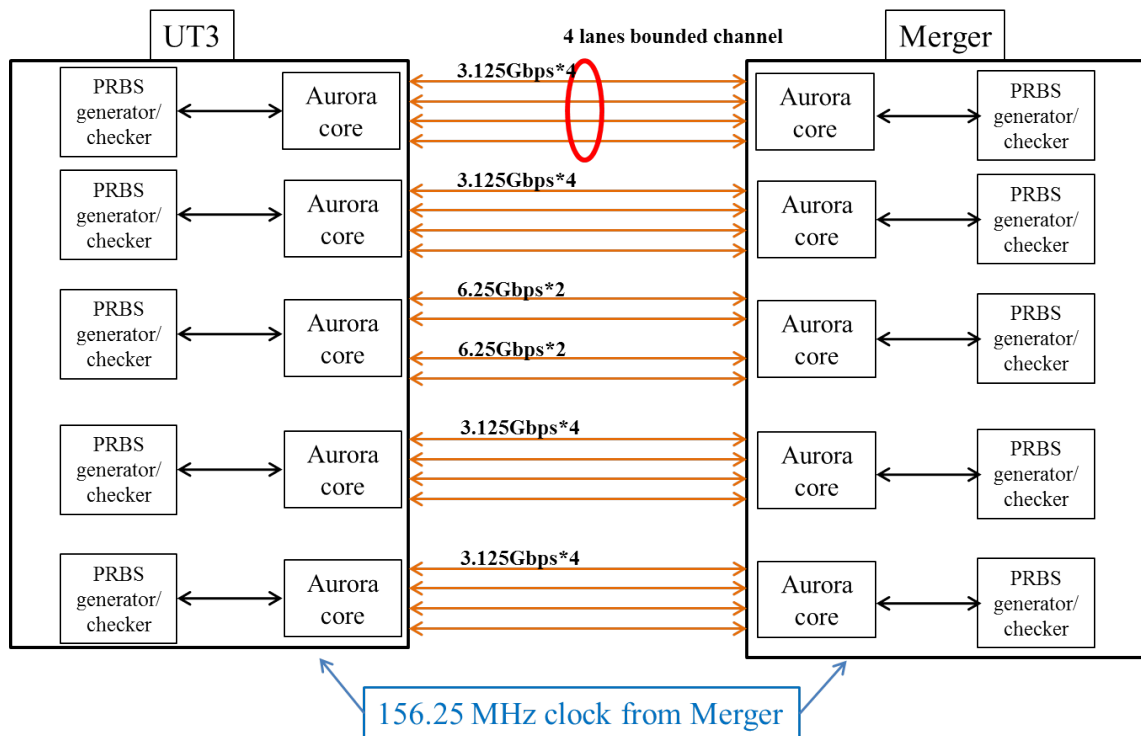


(b) RX result at frame_check.

Figure 7.8: Test result of firmware with Aurora 8B/10B protocol for Merger.

7.3.3 Long-Term BERT on Aurora 8B/10B Protocol

We built up a test bench with Merger and GTX in UT3 to test stability of Aurora 8B/10B protocol in NTU. The test bench is shown in Figure 7.9. GTX in UT3 and Merger are both driven with a general 156.25 MHz clock source. The middle two channels are both bounded with two lanes, which are configured with a lane rate of 6.25 Gbps. The remaining four channels are bounded with four lanes, which are configured with a lane rate of 3.125 Gbps. There is no bit error observed in 1 week and the combined bit error rate $< 1.56 \times 10^{-17}$.



(a) Schematic view.



(b) Hardware setup.

Figure 7.9: Long-term BERT on Aurora 8B/10B protocol with UT3 and Merger.



7.4 Raw-Level Protocols

Mainly due to the long latency, the open-sourced Aurora protocols can not fit our request in the CDCTRG data flow. Therefore, NTUHEP group designs an user-defined streaming protocol from scratch for optical transmission, which is called raw-level protocols, in order to resolve the latency issue.

7.4.1 Design of the Protocols

The firmware structure of raw-level protocols is shown in Figure 7.10. The interface to transceiver hardware (transceiver wizard) is generated from Xilinx Core Generator [80] and Altera MegaWizard Plug-In [82], and they provide the simplest interface to utilize the RocketIO hardware, including GTP [83], GTX [84], GTH [85], and Merger's transceiver [86]. The whole design of protocols is realized by the three additional manual modules (protocol core, lane connection, and reset logic), with which we control the transceiver hardware and provide protocol signals to user interface. There are two version of raw-level protocols with two types of encoding: 8B/10B and 64B/66B. The 8B/10B version can be applied with GTP, GTX, GTH and Merger. The 64B/66B version can be applied with GTH.

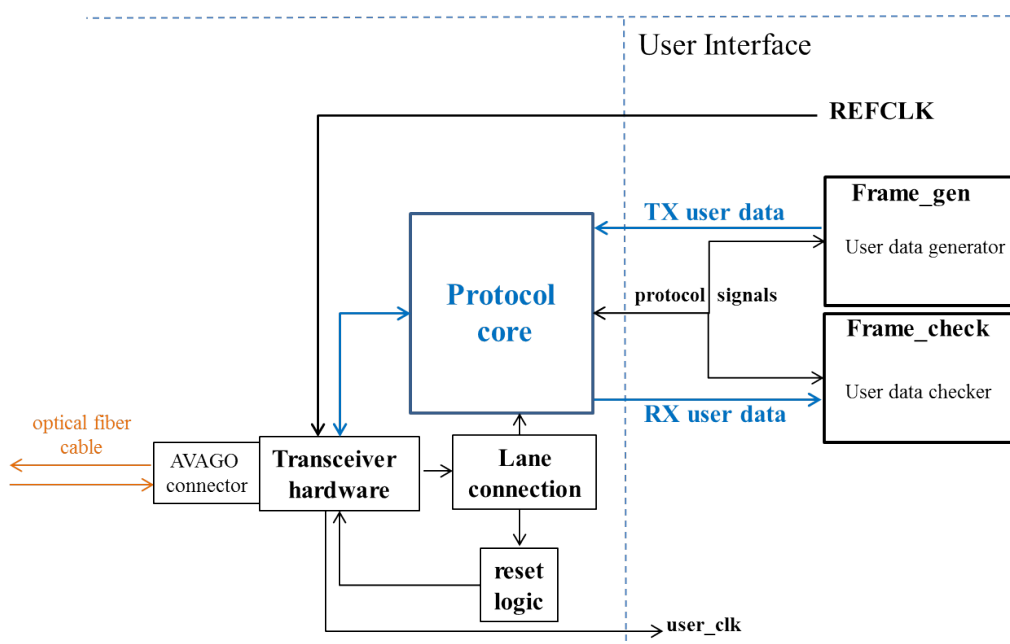
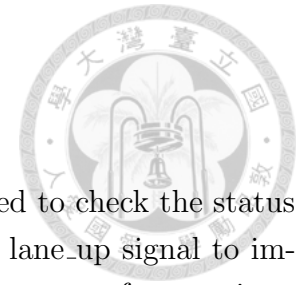


Figure 7.10: Schematic view of raw-level protocols firmware structure.



Lane connection module

Before starting the operation of protocol core logic, we need to check the status and health of the link. The lane connection module provides lane_up signal to immediately reflect the status of each optical lane. With different types of transceiver, different signals are utilized to construct lane_up. The following situations are used to define health of a lane:

- GTP with 8B/10B encoding:
 - In the 16 bits data, 2*8 bits patterns are swapped or not.
 - RXVALID: Reflected from transceiver. Indicates the RX data is available or not.
 - RXDISPERR: Indicates if RX data was received with a disparity error.
 - RXNOTINTABLE: Indicates if RX data is the result of an illegal 8B/10B code and is in error.
- GTX with 8B/10B encoding:
 - In the 16 bits data, 2*8 bits patterns are swapped or not.
 - RXVALID: Reflected from transceiver. Indicates the RX data is available or not.
 - RXDISPERR: Indicates if RX data was received with a disparity error.
 - RXNOTINTABLE: Indicates if RX data is the result of an illegal 8B/10B code and is in error.
- GTH with 8B/10B encoding:
 - In the 16 bits data, 2*8 bits patterns are swapped or not.
 - GTHINITDONE: Indicates the process of programming the bits from the configuration memory to the registers in the GTH primitive is completed.
 - RXVALID: Reflected from transceiver. Indicates the RX data is available or not.
 - RXDISPERR: Indicates if RX data was received with a disparity error.
 - RXCODEERR: Indicates if RX data is the result of an illegal 8B/10B code and is in error.
- GTH with 64B/66B encoding:



- For a unhealthy lane, the 64 bits RX pattern would keep showing X"5555555555555555" or X"FEFEFEFEFEFEFEFE" or X"0100009C0100009C".
 - GTHINITDONE: Indicates the process of programming the bits from the configuration memory to the registers in the GTH primitive is completed.
 - RXCODEERR: Indicates if RX data is the result of an illegal 8B/10B code and is in error.
- Merger with 8B/10B encoding:
 - In the 16 bits data, 2*8 bits patterns are swapped or not.
 - RX_FREQLOCKED: Indicates the receiver clock data recovery (CDR) lock state.
 - RX_DISPERR: Indicates if RX data was received with a disparity error.
 - RX_errdetect: Indicates if RX data is the result of an illegal 8B/10B code and is in error.

Figure 7.11 shows other protocol signals' reaction to lane_up's flip. In this case, we remove the optical fiber cable to make the transceiver unconnected intentionally. Then, the lane connection module detects the instability of link and turn down the lane_up signal. Hence, the protocol interface (TX_DST_RDY_N, TX_SRC_RDY_N, RX_SRC_RDY_N) goes back to the initial state and waits for resumption of connection.

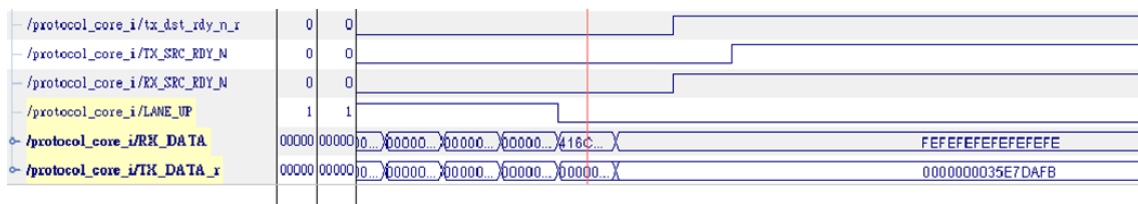


Figure 7.11: The lane_up signal provided by the lane connection module.

Reset logic module

The reset logic module is responsible for initialization and reset of hardware. It confirms the stability of link's health by monitoring on lane_up. After confirmation of stability, the core logic of protocol will start to work. Otherwise, the reset signal will be asserted to transceiver hardware interface for recovery. The work flow chart of reset logic is shown in Figure 7.12.

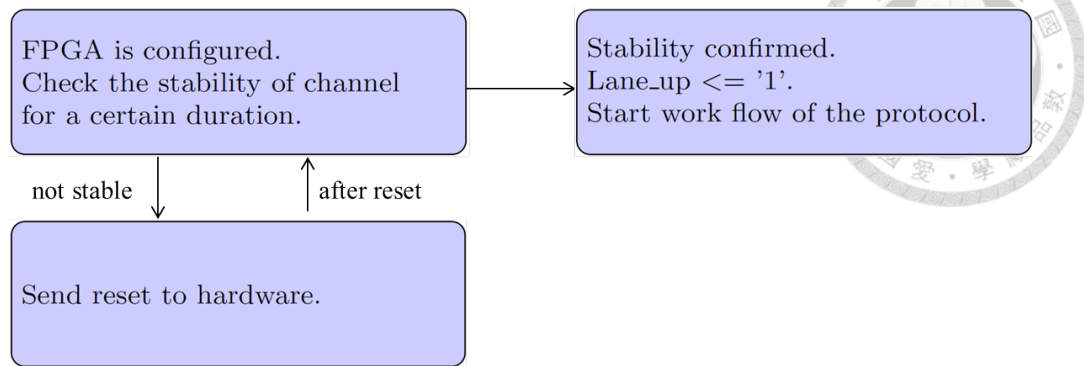


Figure 7.12: Work flow chart of reset logic module.

Protocol core

The protocol core module is core logic of the protocol design. After the lane is confirmed to be healthy, which means, reset logic module finishes initialization and lane_up signal is stable, the protocol core modules will start their own work flow. The basic concept of the design is utilizing the switch between pre-defined specific patterns to represent different states in the work flow state machine, and protocol core contains two parts of logics, which are TX and RX. The work flow chart of the protocol core logics are shown in Figure 7.14 and 7.15 for the 8B/10B version and 64B/66B version, respectively. With this design, we can provide the user interface whose usage is the same as Aurora's (TX_DST_RDY_N, TX_SRC_RDY_N, RX_SRC_RDY_N).

K character with 8B/10B encoding

The basic unit of pattern size with 8B/10B encoding is 8 bits and the available data path width includes 8 bits, 16 bits, and 32 bits. For instance, if data path width is 16 bits, 2*8 bits patterns are bounded and transmitted/received in 1 user_clk. To make sure the boundary of each 2*8 bits is not shifted, we utilize a property of 8B/10B encoding called comma alignment. Comma means a special 8bits pattern and it is called K character for 8B/10B encoding. For instance, K28.5 is X"BC". We also have to control tx_charisk to 1 to indicate the 8 bits X"BC" is not user data but K character. An example of K character utilization is shown in Figure 7.13.

In the beginning of 8B/10B transmission, transmitted data will be crashed and the boundary of patterns will be shifted without any K character transmitted. Therefore, the frequent appearance of K character in early stage is necessary for the qual-

ity of transmission. As shown in Figure 7.14, the pre-defined patterns in core logic (patternK0 and patternK1) are both with K character.

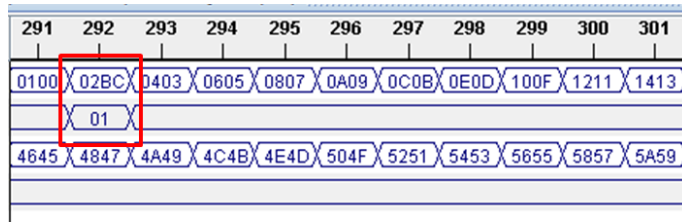


Figure 7.13: K character with 8B/10B encoding.

7.4.2 Test Mode

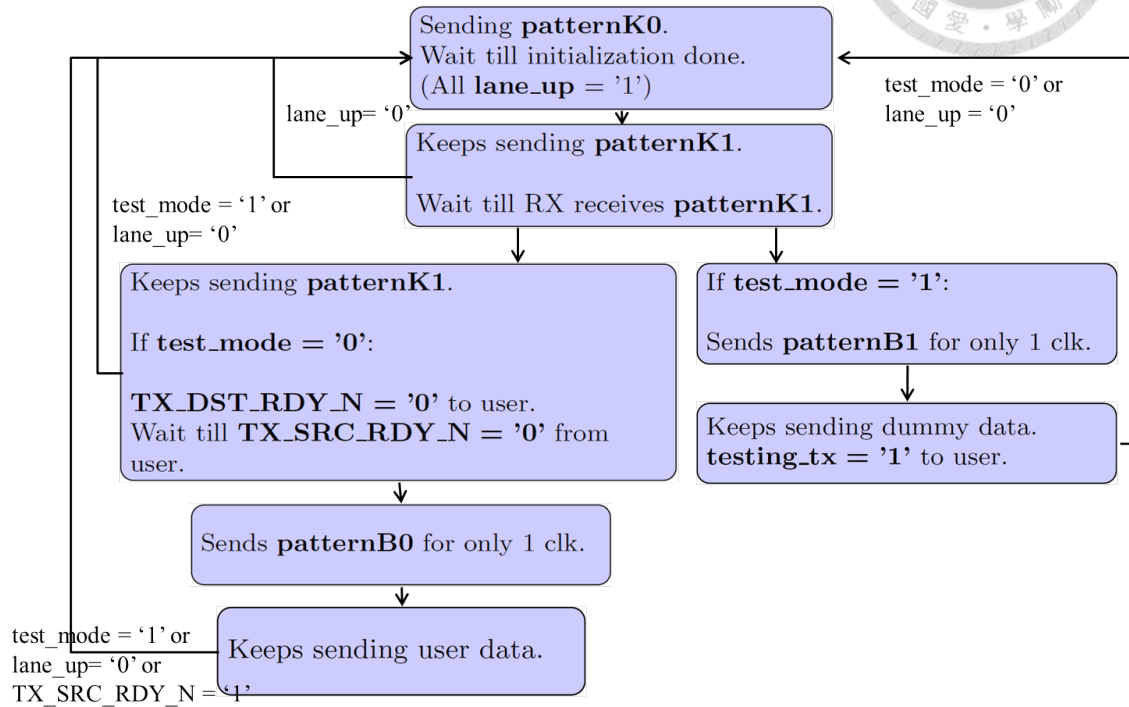
The transmission test mode provides a simpler interface for BERT with the raw-level protocols. Under the normal operation, user (Frame_gen and Frame_check in Figure 7.10) have to detect and control the protocol interface (TX_DST_RDY_N, TX_SRC_RDY_N, RX_SRC_RDY_N) to transmit/receive user data. Under test mode, there is only testing data flow inside the protocol for BERT, and user can check the status of BERT by the additional interface:

- test_mode: This signal is connected to VME interface and is used to switch between the normal operation and test mode for a transceiver which is implemented with the protocol.
- TX_testing: This signal indicates that TX of this end is sending testing data
- RX_testing: This signal indicates that RX of this end is receiving testing data
- err_count: The counter of bit error.

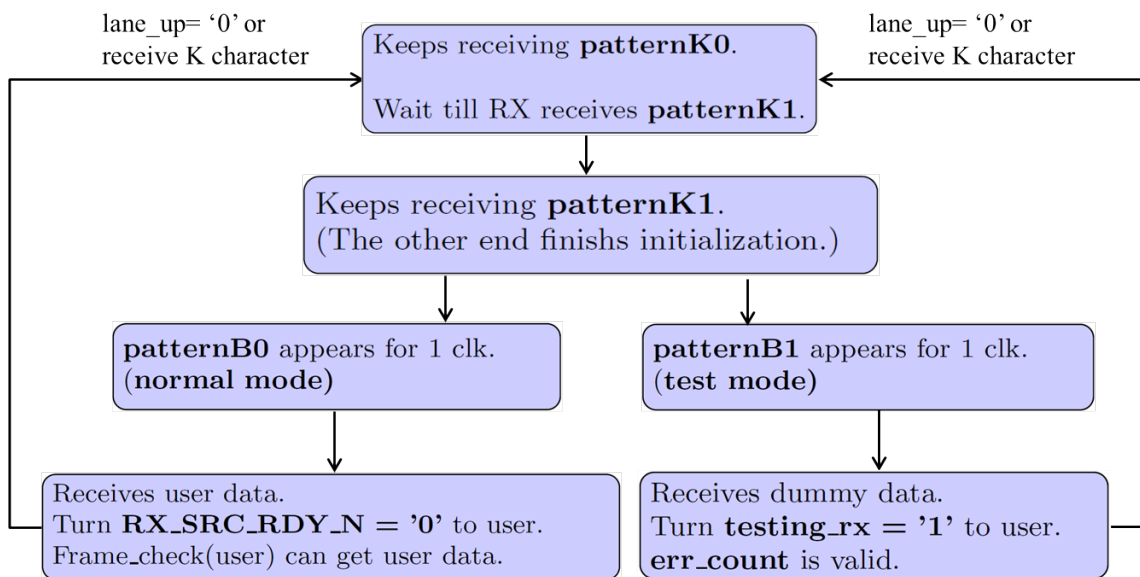
7.4.3 Test Result on Raw-Level Protocols

The test result of raw-level 8B/10B protocol core module is shown in Figure 7.16, which illustrates the core logic of the protocol design (patterns' switch: patternK1→patternB0→user data), and Figure 7.17 shows the test result at user side.

The patterns' switch design (patternA→patternB0→user data) of raw-level 64B/6B protocol core module is shown in Figure 7.18, and Figure 7.19 shows the test result

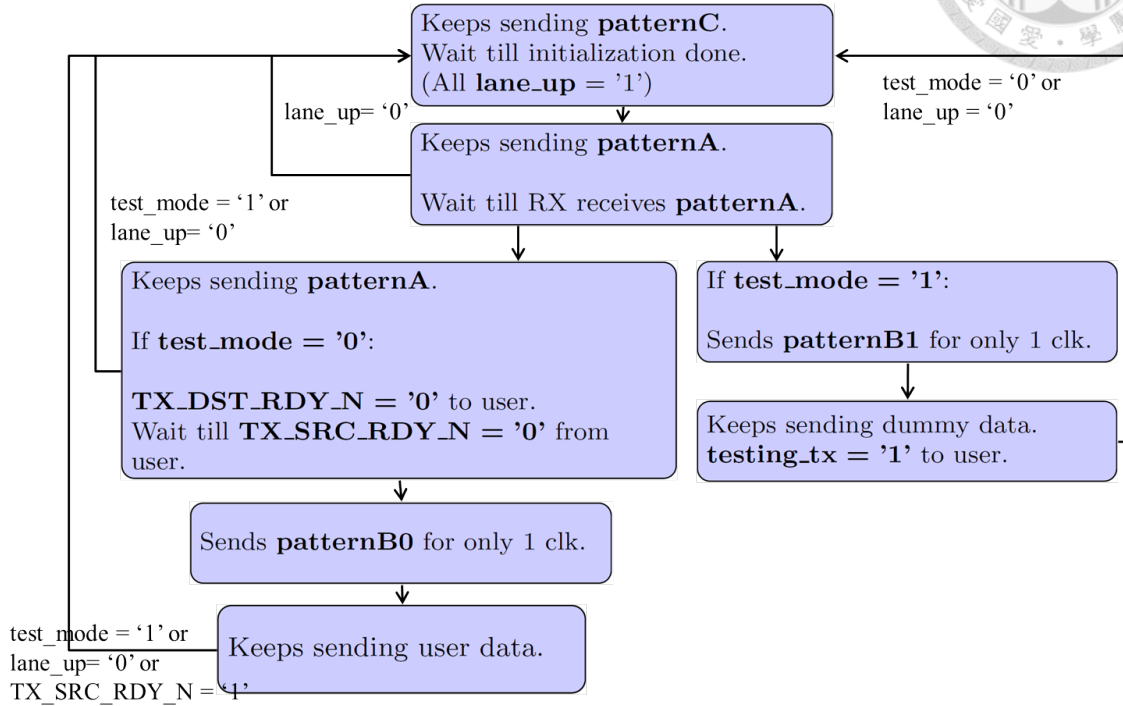


(a) TX work flow chart.

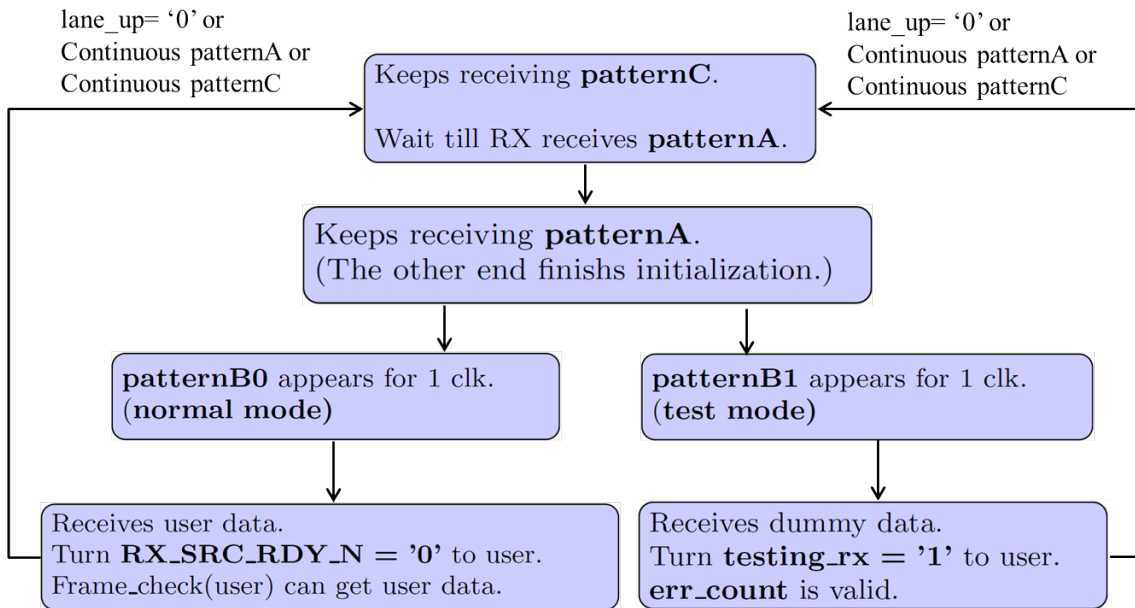


(b) RX work flow chart.

Figure 7.14: Work flow chart of the raw-level 8B/10B protocol core logic.



(a) TX work flow chart.



(b) RX work flow chart.

Figure 7.15: Work flow chart of the raw-level 64B/66B protocol core logic.

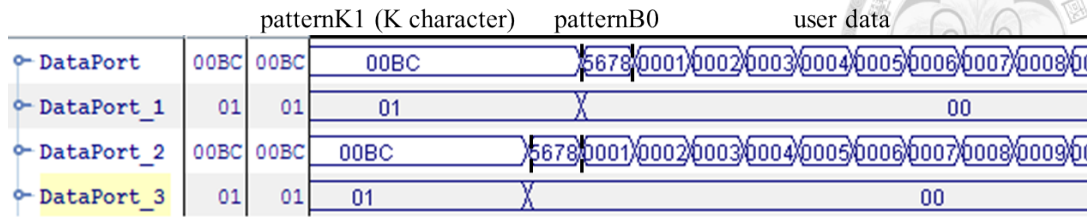
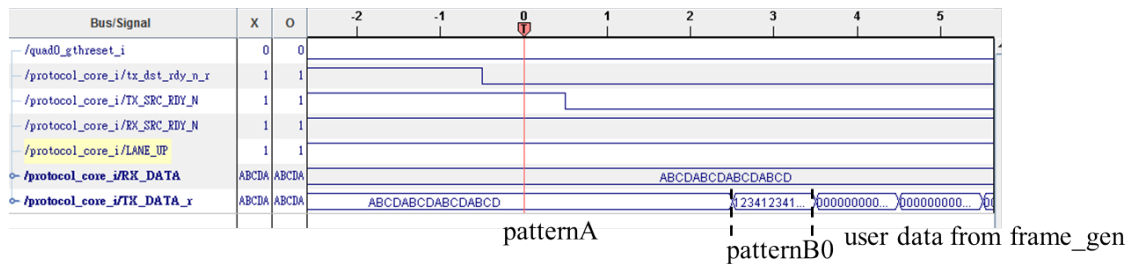


Figure 7.16: Test result of raw-level 8B/10B protocol core module.

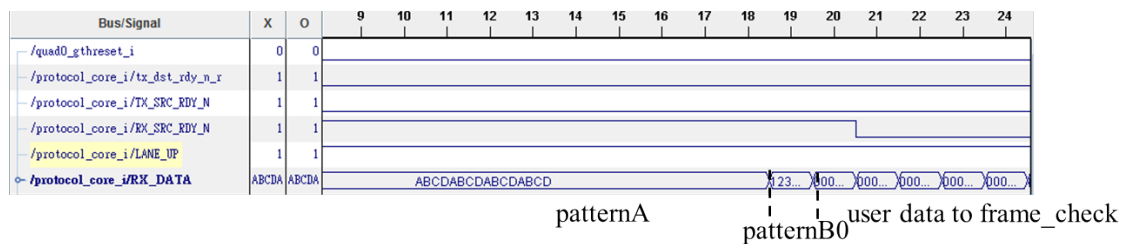
Bus/Signal	X	O	515	516	517	518	519	520	521	522	523	524	525	526	527	528	529	530
txdata	3043	3043	3246	3247	3248	3249	324A	324B	324C	324D	324E	324F	3250	3251	3252	3253	3254	3255
txcharisk	0	0	0															
rxdata	302D	302D	3230	3231	3232	3233	3234	3235	3236	3237	3238	3239	323A	323B	323C	323D	323E	323F
rxcharisk	0	0	0															
rx_ex	302D	302D	3230	3231	3232	3233	3234	3235	3236	3237	3238	3239	323A	323B	323C	323D	323E	323F
diff	0000	0000	0000															
err_count	00	00	00															

Figure 7.17: Test result of raw-level 8B/10B protocol at user side.

at user side.



(a) TX.



(b) RX.

Figure 7.18: Test result of raw-level 64B/66B protocol core module.

7.4.4 Long-Term BERT on Raw-Level Protocols

For the long-term BERT on raw-level 8B/10B, we use the four transceivers with 7934WZ among 73 Merger boards and connect them to each other. All the con-

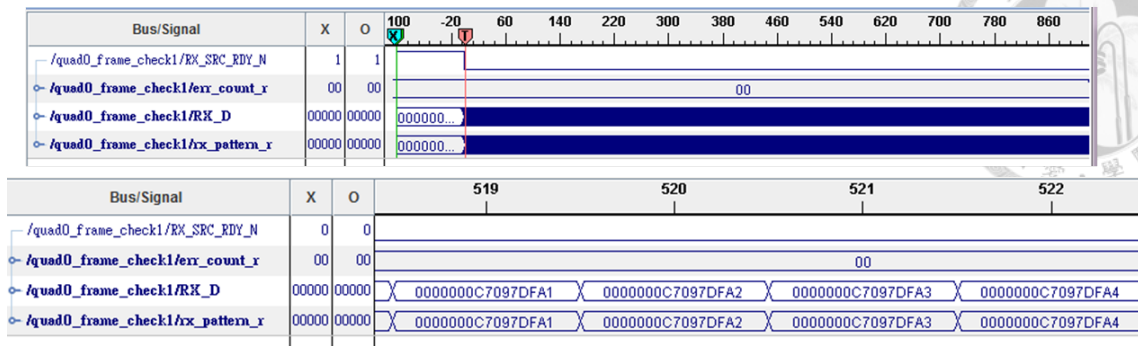


Figure 7.19: Test result of raw-level 64B/66B protocol at user side.

nections are implemented with raw-level 8B/10B and 2.54 Gbps lane rate. The total number of lanes is 1168. There is no nit error observed in two weeks and the combined error rate $< 2.95 \times 10^{-19}$.

For the long-term BERT on raw-level 64B/66B, we use three UT3 boards with the connections in Figure 7.20. 12 GTH are used and are implemented with raw-level 64B/66B and 11.176 Gbps lane rate. The total number of lanes is 24. In two weeks, one lane’s bit error count is 2, another is 4, and another one’s error count is overflowed, which is due to jitter and is ignored in bit error rate estimation. The combined error rate is 9.45×10^{-18} .

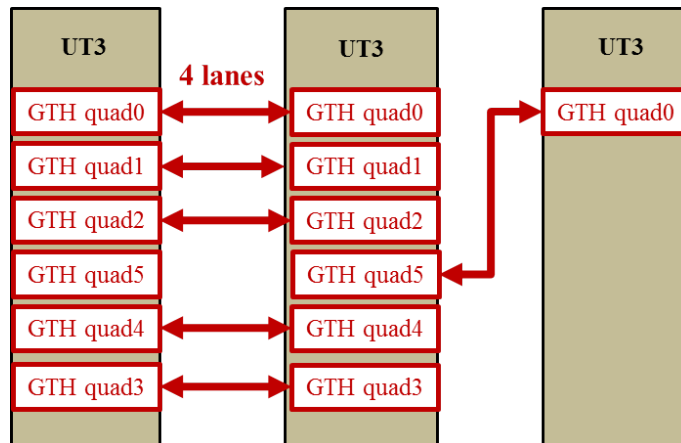


Figure 7.20: Hardware setup for BERT on raw-level 64B/66B protocol.

7.4.5 Summary of Functionalities

- 64B/66B encoding for GTH (higher speed)
- 8B/10B encoding for GTP, GTH, GTX, and Merger



- Detection of hardware setup (lane_up)
- Aurora-like user interface (TX_DST_RDY_N, TX_SRC_RDY_N, RX_SRC_RDY_N): application to flow control and synchronization
- Streaming transmission
- Smaller latency than Aurora: the comparison is shown in Table 7.2.
- Initialization and automatic reset for hardware resumption
- Channel bonding: done with FIFO (outside of the protocol, at user side)
- Test mode for BERT
- Stability: confirmed by long-term BERT

Protocol	Lane rate	user_clk	Link type	Latency (ns)
Aurora 8B/10B	5.08 Gbps	254 MHz	GTX-GTX	185~190
Raw-level 8B/10B	5.08 Gbps	254 MHz	GTX-GTX	132~136
	5.08 Gbps	254 MHz	GTH-GTX	132~136
	5.08 Gbps	254 MHz	GTH-GTH	91~95
	5.08 Gbps	254 MHz	GTX-GTH	91~95
Aurora 64B/66B	10.16 Gbps	158.75 MHz	GTH-GTH	296~302
Raw-level 64B/66B	11.176 Gbps	169.33 MHz	GTH-GTH	106~112

Table 7.2: Latency comparison between raw-level protocols and Aurora.

7.5 CDCTRG Data Flow

7.5.1 CDCTRG Data Flow

Figure 7.21 shows the data flow of CDCTRG system. All of the optical links are built with raw-level protocols. All the TRG boards and their optical transmission modules are driven with a general 127 MHz/254 MHz clock source. Table 7.3 classifies all the link types which are used in CDCTRG data flow with different raw-level protocols and hardware configurations.

The details of CDCTRG data flow in all sections are listed as following:

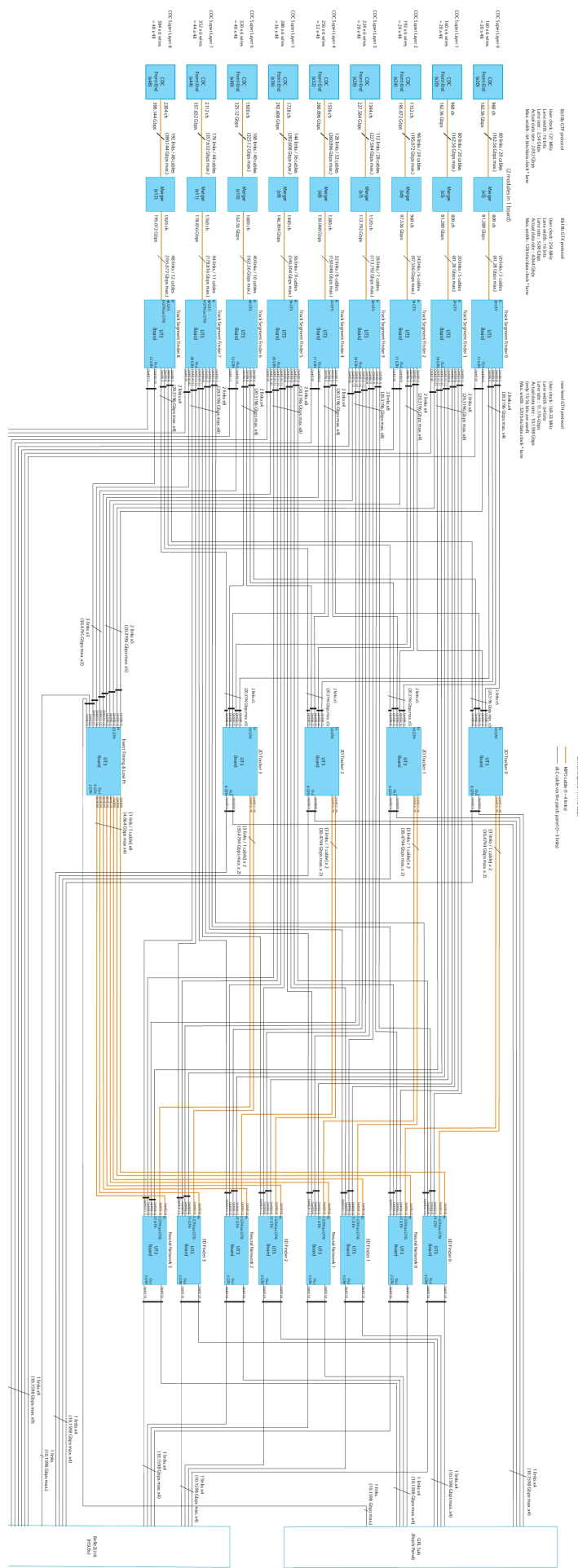


Figure 7.21: CDCTRG data flow.

Type	Encoding	lane rate	user_clk	data path width	hardware link
D			31.75 MHz		Inside TRG boards
1	8B/10B	2.54 Gbps	127 MHz	16 bits	GTP-Merger
2.1	8B/10B	5.08 Gbps	254 MHz	16 bits	Merger-GTX
2.2	8B/10B	5.08 Gbps	254 MHz	16 bits	Merger-GTH
2.3	8B/10B	5.08 Gbps	254 MHz	16 bits	GTH-GTX
3	64B/66B	11.176 Gbps	169.33 MHz	64 bits	GTH-GTH

Table 7.3: Type of links with different raw-level protocols and hardware configurations used in CDCTRG data flow.

- Type-D:

Type-D is the data flow inside each TRG board. For all the TRG algorithms, all the data patterns are processed under 31.75 MHz dataclk.

- CDCFE→Merger (Type-1):

The links between 292 CDCFE boards and 73 Merger boards are configured as Type-1. Each Merger board has four connections from four CDCFE boards. Each connection between a CDCFE and a Merger is configured with four lanes of Type-1. All the CDCFE→Merger links are summarized in Table 7.4. Total number of used lanes is $(292 \text{ CDCFE}) \times (4 \text{ lanes}) = 1168 \text{ lanes}$.

SL	# of CDCFE	# of Merger	# of lanes
0	20	5	20*4
1	20	5	20*4
2	24	6	24*4
3	28	7	28*4
4	32	8	32*4
5	36	9	36*4
6	40	10	40*4
7	44	11	44*4
8	48	12	48*4

Table 7.4: Summary of CDCFE→Merger links.

- Merger→TSF (Type-2.1 and Type-2.2):

The links between 73 Merger boards and nine TSF are configured as Type-2.1 and Type-2.2. Each Merger board has one connections to a TSF. Each connection between a Merger and a TSF is configured with four lanes of Type-2.1 or Type-2.2 (For SL7 and SL8 TSF, all the GTX are occupied, so they need to use additional GTH for this case.). All the Merger→TSF links are summarized in Table 7.5. Total number of used lanes is $(73 \text{ Mergers}) \times (4 \text{ lanes})$

= 534 lanes.

SL	Type	RX	# of Merger	# of lanes
0	2.1	GTX	5	5*4
1	2.1	GTX	5	5*4
2	2.1	GTX	6	6*4
3	2.1	GTX	7	7*4
4	2.1	GTX	8	8*4
5	2.1	GTX	9	9*4
6	2.1	GTX	10	10*4
7	2.1	GTX	10	10*4
	2.2	GTH	1	1*4
8	2.1	GTX	10	10*4
	2.2	GTH	2	2*4

Table 7.5: Summary of Merger→TSF links.

- Axial TSF→2D (Type-3):

The links between five axial TSF and four 2D trackers are configured as Type-3. Each 2D tracker has five connections from five axial TSF (SL 0, 2, 4, 6, 8). Each connection between an axial TSF and a 2D tracker is configured with two lanes of Type-3. Total number of used lanes is $(5 \text{ axial TSF}) * (4 \text{ 2D trackers}) * (2 \text{ lanes}) = 40 \text{ lanes}$.

- Stereo TSF→3D/NN (Type-3):

The links between four stereo TSF and four 3D trackers/four NN are configured as Type-3. Each 3D/NN has four connections from four axial TSF (SL 1, 3, 5, 7). Each connection between a stereo TSF and a 3D/NN is configured with two lanes of Type-3. Total number of used lanes is $(4 \text{ stereo TSF}) * (4 \text{ 3D} + 4 \text{ NN}) * (2 \text{ lanes}) = 64 \text{ lanes}$.

- TSF→ETF (Type-3):

The links between nine TSF and one ETF trackers are configured as Type-3. ETF has nine connections from nine TSF. Each connection between a TSF and ETF is configured with two lanes of Type-3 for SL0~4 and three lanes of Type-3 for SL5~8. Total number of used lanes is $(5 \text{ connections}) * (2 \text{ lanes}) + (4 \text{ connections}) * (3 \text{ lanes}) = 22 \text{ lanes}$.

- 2D→3D/NN (Type-3):

The links between four 2D trackers and four 3D trackers/four NN are configured as Type-3. Each 3D/NN has one connections from a 2D tracker. Each



connection between a 2D and a 3D/NN is configured with three lanes of Type-3. Total number of used lanes is (8 connections)*(3 lanes) = 24 lanes.

- ETF→3D/NN (Type-2.3):

The links between one ETF and four 3D trackers/four NN are configured as Type-2.3. Each 3D/NN has one connections from ETF. Each connection between ETF and a 3D/NN is configured with two lanes of Type-2.3 (GTX of ETF to GTH of 3D/NN). Total number of used lanes is (8 connections)*(2 lanes) = 16 lanes.

- 2D/3D/NN→GRL (Type-3):

The links between four 2D/four 3D/four NN and GRL are configured as Type-3. Each 2D/3D/NN has one connection to GRL. Each connection between a 2D/3D/NN and GRL is configured with one lanes of Type-3. Total number of used lanes is (12 connections)*(1 lanes) = 12 lanes.

7.5.2 Balance between Sections by First-In-First-Out (FIFO)

For the data flow system with different sections driven by different clock rates, the balance between them is essential in a long-term stable operation. Besides, a TRG board usually has multiple input from different links, we also need to buffer the latency difference between them. In order to do those, we use FIFO between Type-D section (data flow inside TRG boards) and others (optical transmission). FIFO module can be generated from Core Generator of Xilinx [80] and MegaWizard Plug-In of Altera [82]. The supported configuration is 1 - 2ⁿ(n = integer), which means the clock rate ratio between reading side and writing side. Table 7.6 lists the details of FIFO used in CDCTRG data flow.

R	W	FIFO type	R size	W size	R clock	W clock rate
D	1	1 - 4	64 bits	16 bits	31.75 MHz	127 MHz
1	D	4 - 1	16 bits	64 bits	127 MHz	31.75 MHz
D	2	1 - 8	128 bits	16 bits	31.75 MHz	254 MHz
2	D	8 - 1	16 bits	128 bits	254 MHz	31.75 MHz
D	3	3 - 16	320 bits	64 bits	31.75 MHz	169.33 MHz
3	D	16 - 3	64 bits	320 bits	169.33 MHz	31.75 MHz

Table 7.6: FIFO types used in CDCTRG data flow.



Regular type (take 1 - 4 FIFO as an example)

For instance, when the writing side is the Type-D with 31.75 MHz and reading side is Type-1 with 127 MHz, the FIFO type is 1 - 4 FIFO since the ratio of clock rate is 1/4. 1 clock of 31.75 MHz = 4 clocks of 127 MHz ~ 32 ns. In the period, writing side will write 64 bits into the FIFO with 1 clock of 31.75 MHz, and reading side will read out 4*16bits from the FIFO in 4 clocks of 127 MHz. The illustration of the regular 1 - 4 FIFO's operation is shown in Figure 7.22, and its test result is shown in Figure 7.23.

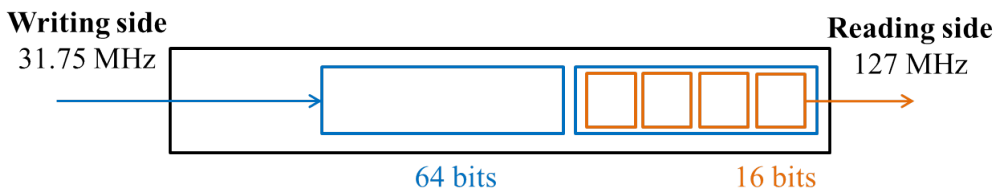


Figure 7.22: Illustration of a regular type 1 - 4 FIFO's operation.

Bus/Signal	x	O	519	520	521	522	523	524	525	526	527	528	529	530	531	532	533	534	535
/rd_req_r	1	1																	
/wr_req_r	1	1																	
/empty_r	0	0																	
/data_64b_in_r	00000	00000	0000B872A7E1F5	X	000000B872A7F306	X	000000B872A80417	X	000000B872A81528	X	000000								
/data_16b_out_	F0CF	F0CF	E54E8DB90000	X	1D00E54E43750000	X	1D00E54ECBFD0000	X	1D00E54E270B0000	X	1D00E5								

Figure 7.23: Test result of a regular type 1 - 4 FIFO.

3 - 16/16 - 3 FIFO

For the links configured with 64B/66B GTH (Type-3), the clock rate is 169.33 MHz, and the ratio between 169.33 and 31.75 is 16/3 (not 2ⁿ), so we can not use the regular type of FIFO for the situation. A special type FIFO, which is called 3 - 16/16 - 3 FIFO is designed to solve the buffering issue between 169.33 MHz and 31.75 MHz. The basic idea is shown in Figure 7.24: 3 clocks of 31.75 MHz = 16 clocks of 169.33 MHz ~ 95 ns. In this period, writing side can have 3*320 bits in 3 clock of 31.75 MHz. The 3 - 16 FIFO, which is driven by 169.33 MHz clock, will use 15 clocks to transmit 3*320 bits (into 15*64 bits), and a dummy 64 bits pattern will be transmitted in the remaining 1 clock. By sacrificing 15/16 of the bandwidth (= 1 clock of 169.33 MHz), it behaves like a 1 - 5 FIFO, and make the implementation simpler. For the test result, Figure 7.25(a) shows how 3*320 bits is divided into 15*64 bits, and Figure 7.25(b) shows how 3*320 bits is reconstructed from 15*64

bits. The reconstructed 320 bits data will come in each 5-5-6 clocks of 169.33 MHz, so we can still get 3*320 bits data in 3 clocks of 31.75 MHz averagely.

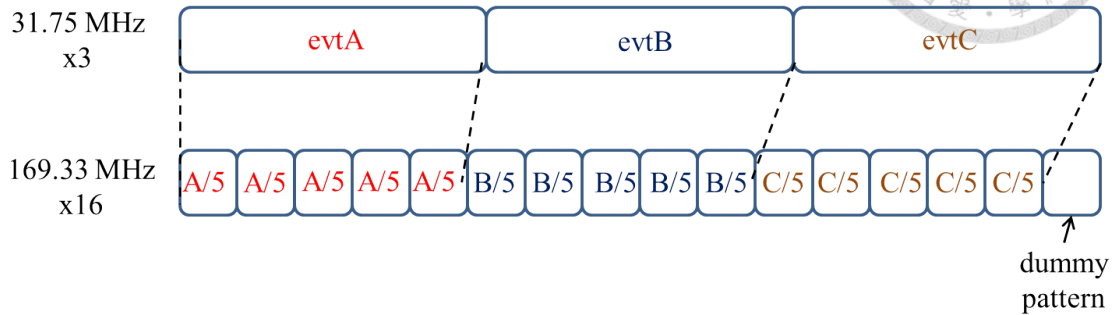
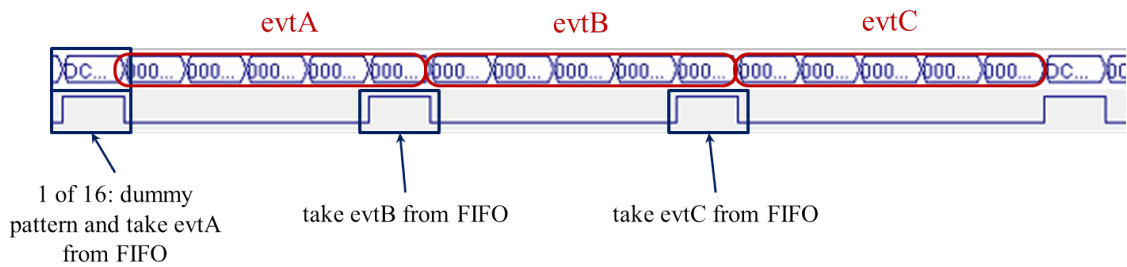
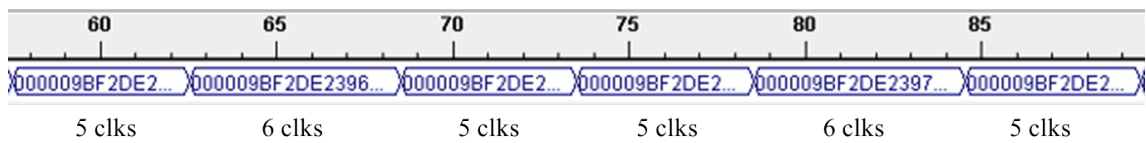


Figure 7.24: Design of the 3 - 16/16 - 3 FIFO.



(a) 3 - 16 FIFO ($3 \times 320 \rightarrow 15 \times 64$).

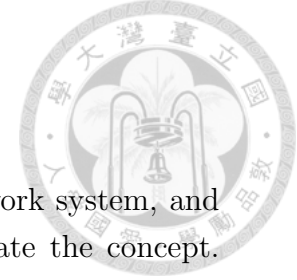


(b) 16 - 3 FIFO ($15 \times 64 \rightarrow 3 \times 320$).

Figure 7.25: Test results of the 3 - 16/16 - 3 FIFO.

7.5.3 TRG Data Flow Control and Synchronization

The whole CDCTRG data flow system is a complicated tree-diagram network. For each optical link, the time for it to be ready for transmission is different, and there is also latency difference between different links. In order to control the data flow and synchronize the timing for the whole system, we develop a scheme for data flow control and synchronization by utilizing bi-direction of all links.



Overview on the scheme

This scheme can be applied for any kinds of tree-diagram network system, and we use a system with four TRG boards as an example to illustrate the concept. The system is shown in Figure 7.26. In this case, two CDCFE are the front-most modules, Merger is the middle one, and TSF is the rear-most modules. The overview work flow chart is shown in Figure 7.27 and discussed as following:

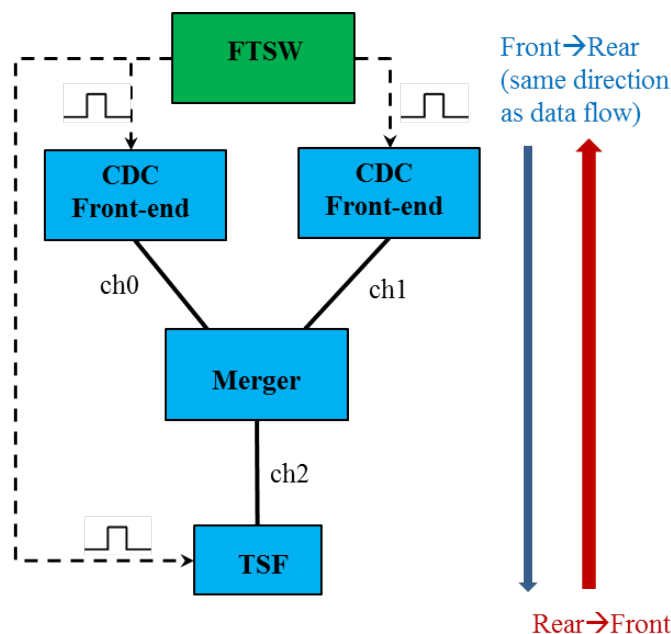


Figure 7.26: A simplified CDCTRG data flow.

- Step 1 (Front→Rear Scanning):

In the first step of flow control and synchronization, each module will keep checking the links are ready or not ($TX_DST_RDY_N = '0'$). For FEs, all the links are output. Once all links in CDCFE are ready stably, FE will turn $TX_SRC_RDY_N$ to '0' to Merger.

For Merger, it is a module at middle stage with both input and output links. Once all links in Merger are ready stably and it receives $RX_SRC_RDY_N = '0'$ from CDCFE, Merger will also turn $TX_SRC_RDY_N$ to '0' to TSF.

By doing so in all the other modules (checking if links are ready→send signal to its rear side), information of optical links will be accumulated. When the $RX_SRC_RDY_N = '0'$ reaches TSF (the rear-most module in the system), TSF will know that all links in the whole system are ready to start operation.

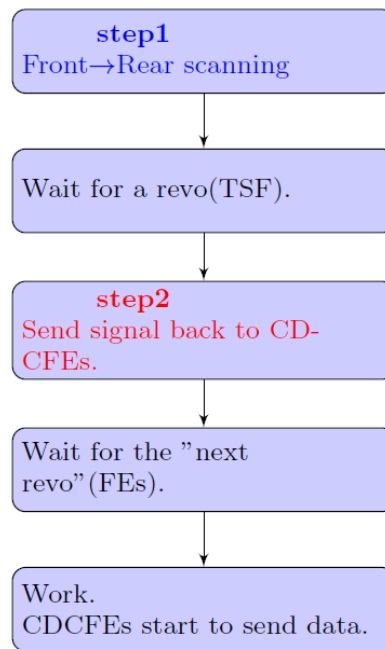


Figure 7.27: Overview work flow of the flow control and synchronization scheme.

- Wait for a revo (TSF):

The revolution signal is the accelerator revolution clock and distributed from FTSW, and it is the only standard of synchronized timing we can utilize in the setup. The timing of revolution signal to each module is synchronized and its revolution is $10 \mu\text{s}$, which is larger than the latency of the whole CDCTRG system.

After step 1 is done and TSF has all the accumulated information, TSF will wait for a revolution signal from FTSW, and then start to send $\text{TX_SRC_RDY_N} = '0'$ to all front modules.

- Step 2 (Send signal back to CDCFEs):

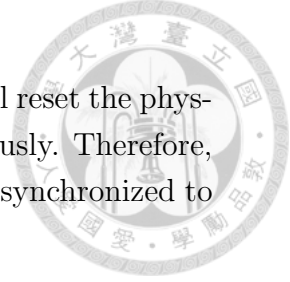
In step 2, once a module receives $\text{RX_SRC_RDY_N} = '0'$ from its rear side, it will directly respond to its front side, and then all the CDCFE will get the information.

- Wait for the "next revo" (CDCFEs):

After step 2 is done (All CDCFEs receive information from their rear side), all the modules know all links in the whole system are ready to start operation. Then, all CDCFE will wait for the "next" revolution signal. Since the latency of step 2 is less than $10 \mu\text{s}$, all CDCFE will align to exactly the same revolution signal which is the next one relative to the one TSF aligned to.

- Data flow starts:

When all CDCFE receive the "next" revolution signal, they will reset the physical timing information and also start the data flow simultaneously. Therefore, both the physical timing and data flow starting timing can be synchronized to the accelerator revolution clock.



Error recovery

During operation, if there is any one of links becomes unhealthy suddenly, the error recovery function will try to rebuild the data flow. Figure 7.28 is an example to illustrate the situation. when ch1 goes down, module B and C will detect it first, then B will stop the operation (turn TX_SRC_RDY_N to '1') of ch0 and C will also stop ch2. By doing so, when module detects problems from one link, other links' operation will be stopped. Finally, the whole data flow will be entirely stopped and all the modules will go back to their initial state of flow control. Then, flow control will restart and try to resume the data flow.

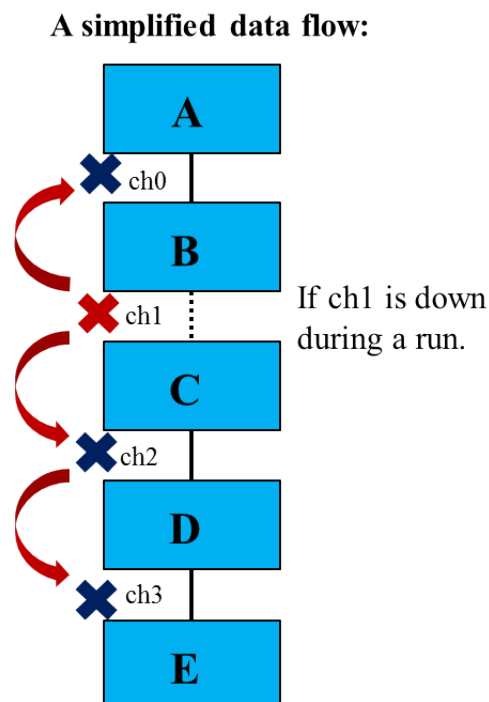


Figure 7.28: Illustration of error recovery function in flow control with a simplified data flow system.



Detailed view on each modules

Figure 7.29, 7.30, and 7.31 shows the detailed flow control firmware design of the front-most module, the middle module, and the rear-most module, respectively.

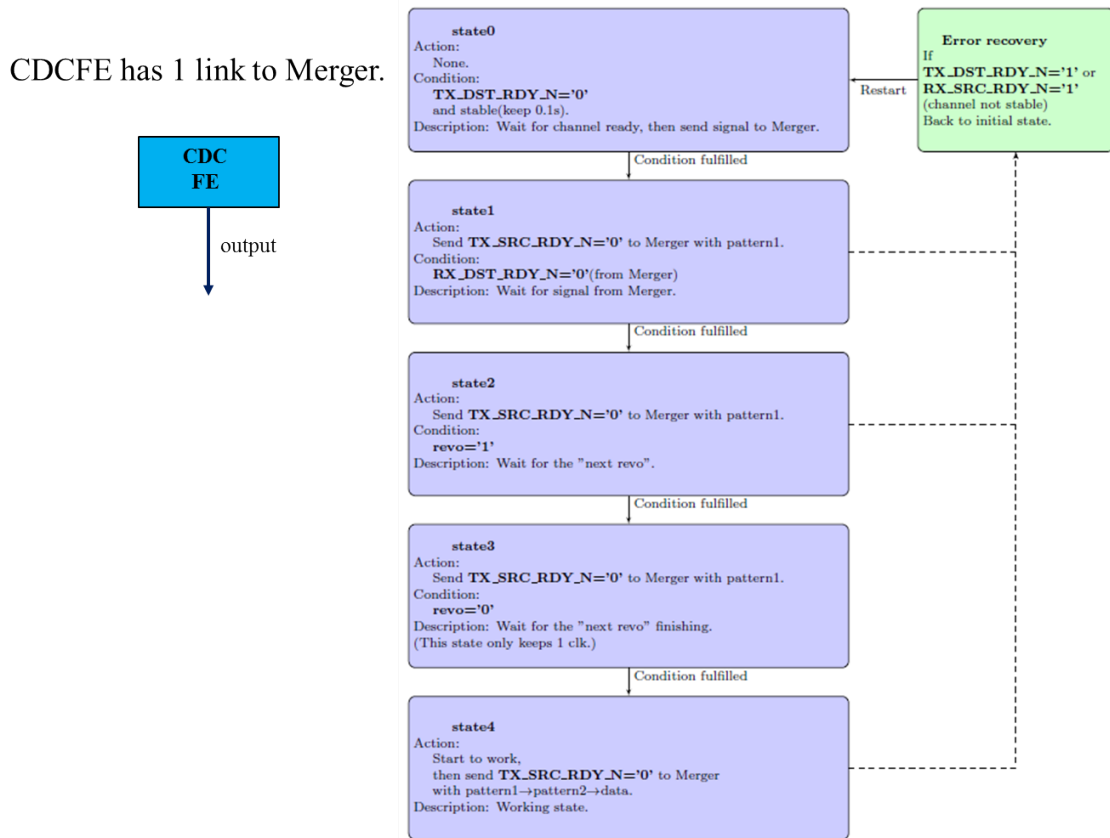
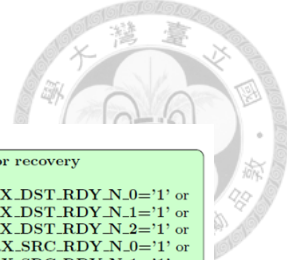


Figure 7.29: Detailed flow control firmware design of CDCFE (the front-most module).



Merger has 2 input and 1 output links.

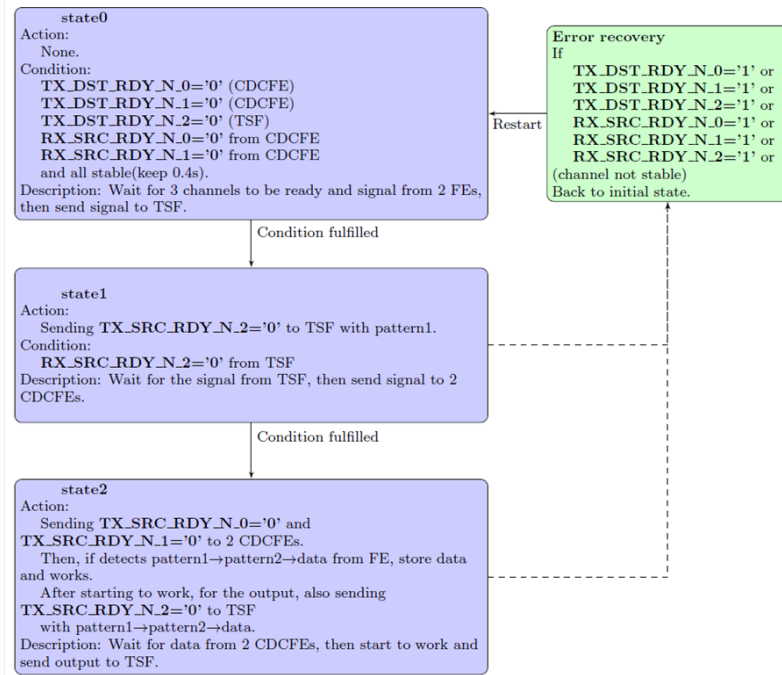
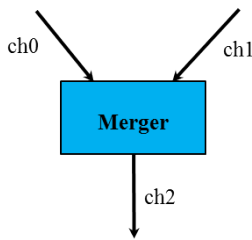


Figure 7.30: Detailed flow control firmware design of Merger (the middle module).

TSF has 1 link from Merger.

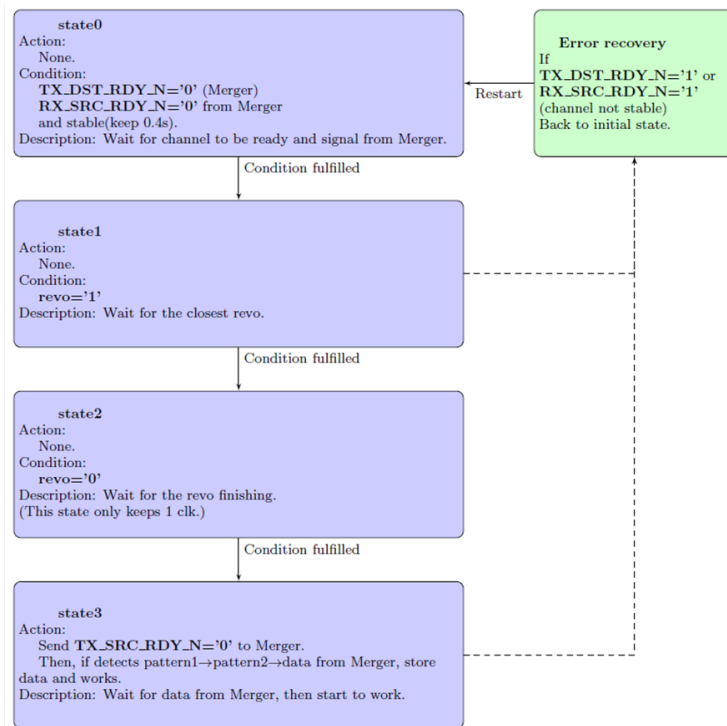
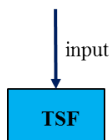
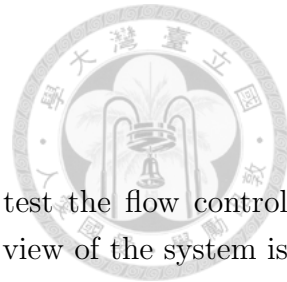


Figure 7.31: Detailed flow control firmware design of TSF (the rear-most module).



7.5.4 Operation Test

We use different kinds of simplified data flow system to test the flow control and synchronization scheme. For the first case, the schematic view of the system is shown in Figure 7.32. The system is with 6 CDCFE→3 Merger→3 TSF→1 2D. All the links in this system are built with the raw-level protocols.

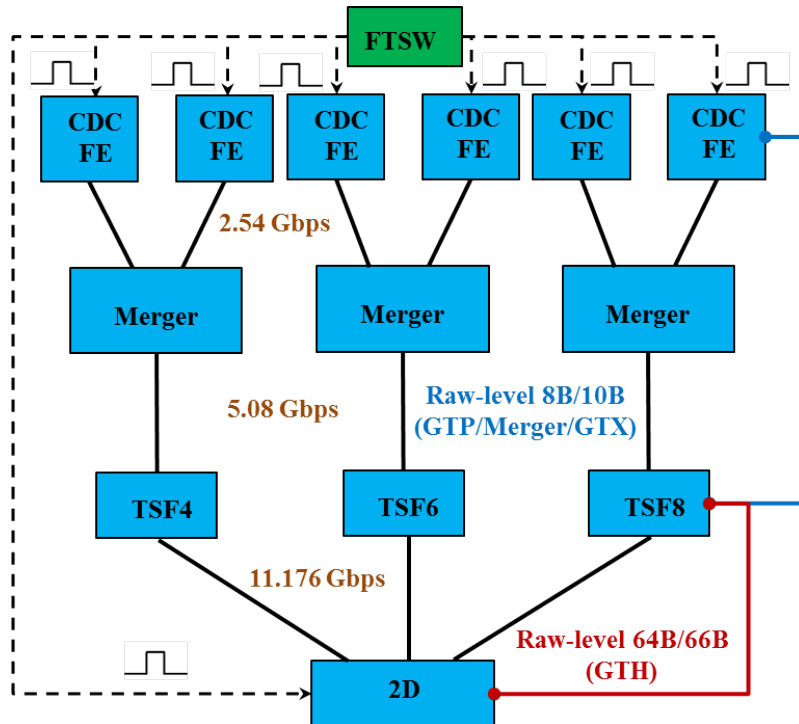


Figure 7.32: Schematic view of a simplified data flow system.

About the test result, the data flow is stable in a few days operation, which mean the protocols can co-work with the flow control and synchronization scheme well. At the 2D board, we also check the clock counters from 3 TSF are synchronized as Figure 7.33. The latency of the system is measured to be 1.28 μs (0.9 μs) for CDCFE→2D (CDCFE→TSF). Compared with the same system implemented with Aurora links, 0.5 μs is saved our our protocols.

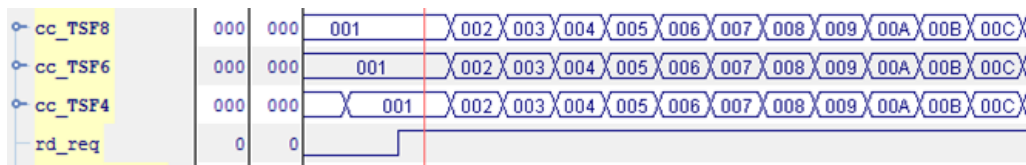


Figure 7.33: Clock counter synchronization at 2D of a simplified data flow system.

Another simplified system is also tested as shown in Figure 7.34. A 3D board and a Global Reconstruction Logic (GRL) board are included. It is closer to the



real setup as the number of serial stages is close to the real one. Since GRL also has multiple input links from 2D and 3D in this system, we also check the clock counters synchronization at GRL, as shown in Figure 7.35.

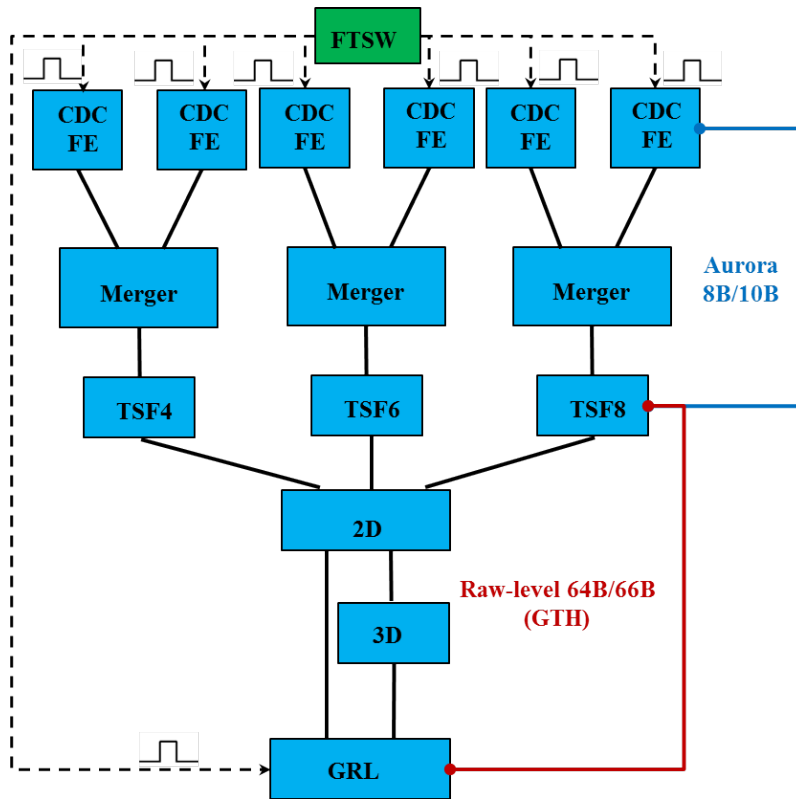


Figure 7.34: Schematic view of a simplified data flow system with additional 3D board and GRL board.

Bus/Signal	X	O	-1	0	1	2	3	4	5	6	7	8	9	10	11	12	13
cc_2D	107	107	001		002	003	004	005	006	007	008	009	00A	00B	00C	00D	
cc_3D	0BC	0BC		001	002	003	004	005	006	007	008	009	00A	00B	00C	00D	

Figure 7.35: Clock counter synchronization at GRL of a simplified data flow system.

7.6 Summary

NTUHEP designs raw-level protocols for optical data transmission in CDCTRG in order to solve the latency issue. The raw-level protocols can be applied on all the hardware transceivers and TRG boards in CDCTRG and the performance is proven to be robust by long-term BERT. We also develop a scheme to control and synchronize the data flow of all links to the accelerator revolution clock in the whole system. The scheme is tested to be working well under the interface of raw-level protocols.

At the E-Hut in KEK Tsukuba experimental hall, we complete the basic structure of CDCTRG data flow system with raw-level protocols, as shown in Figure 7.36. The data flow reaches the global trigger system (GRL) from CDCFE now.

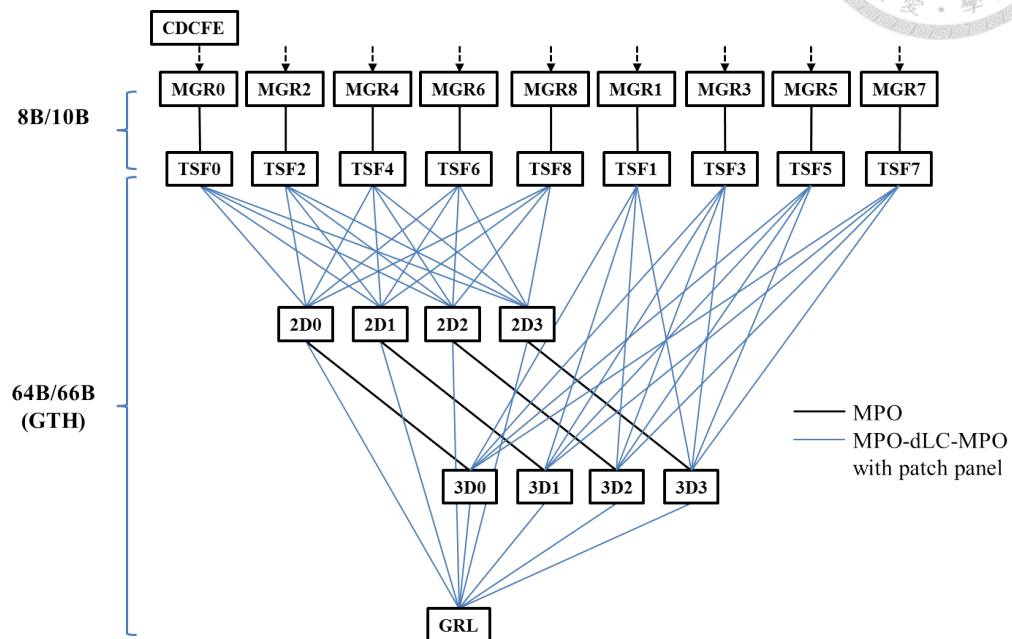


Figure 7.36: Status of CDCTRG data flow in KEK E-Hut.





Chapter 8

Conclusions

This thesis presents two physics analysis on D^0 and B^0 decays at Belle, and the FPGA firmware design for the Belle II CDCTRG system.

First, we have performed a search for D^0 decay to $\nu\bar{\nu}$ and $h^-\ell^+\nu_\ell$ ($h = K, \pi$, and $\ell = e, \mu$) using the data sample collected with Belle detector at the KEKB asymmetric energy e^+e^- collider. With charm flavor tagging method at the e^+e^- flavor factory, we can tag on one of the two D mesons and utilize the recoil information to search for the other D decaying to invisible signal, which provides an alternative way for Dark Matter search. We obtain 694505_{-1472}^{+1030} inclusive D^0 yield by the charm tagger. Since no significant signal is found, we set an upper limit of 8.8×10^{-5} for the branching fraction of $D^0 \rightarrow \nu\bar{\nu}$ at the 90% confidence level. In addition, the measurements of $D^0 \rightarrow h^-\ell^+\nu_\ell$ are also performed and the measured branching fractions are consistent with the PDG world averages.

The second topic is the search for $B^0 \rightarrow p\bar{\Lambda}\pi^-\gamma$. The decay proceeds via the $b \rightarrow s\gamma$ radiative penguin process. We use the full $\Upsilon(4S)$ data sample of $772 \times 10^6 B\bar{B}$ pairs collected by Belle. The study is basically motivated by the observed hierarchy of branching fractions in baryonic B decays modes. The result is also helpful to understand the fragmentation and hadronization in $B \rightarrow X_s\gamma$ and is useful to tune the parameters in JETSET. No significant signal yield is found and we set the upper limit on the branching fraction to be 6.5×10^{-7} at the 90% confidence level. We also conclude that the decay under study does not follow the expected hierarchy; instead, we find $\mathcal{B}(B^0 \rightarrow p\bar{\Lambda}\pi^-\gamma) < \mathcal{B}(B^+ \rightarrow p\bar{\Lambda}\gamma)$.

In the Belle II CDCTRG system, we participate in the FPGA firmware design

for CDCTRG Merger board and optical data transmission.

The CDCTRG Merger board is a data simplifier in CDCTRG. It receives the data from the front-end readout system and the output is transmitted to Track Segment Finder for further online tracking algorithm in rear-end of CDCTRG. Regarding the firmware design, all the necessary functionalities, including core logic of trigger algorithm, optical transmission, VME interface, and switching between operation modes are already completed and tested. All the necessary 73 boards are confirmed to be robust with different operation tests and are installed in the Electronic-hut in Tsukuba experimental hall in KEK in the beginning of 2015. Merger boards are ready for commissioning.

Regarding the data flow in CDCTRG, we use the optical fiber cables, embedded optical modules, and high speed transceivers of FPGA chips to realize data transmission. NTUHEP designs a user-defined protocol for optical data transmission in CDCTRG in order to solve the latency issue. With the new design, transmission latency can be reduced by a factor of 2~3 compared with the open-sourced Aurora protocols. The protocols can be applied on all the hardware transceivers and TRG boards in CDCTRG, and their performance is proven by long-term BERT. In addition, we also develop a scheme to control and synchronize the data flow of all links to the accelerator revolution clock in the whole system. The scheme is tested to be working well under the interface of user-defined protocol. At the E-Hut in KEK Tsukuba experimental hall, the whole data flow network from readout to global trigger is completed with our user-defined protocol implemented.





Appendix A

Merger VME Functions

For all the functionalities related to Merger VME interface, the programs are prepared in CPU server boards mounted on VME crate. Here are instructions about how to operate Merger boards with the functions.

- Dip switch:
Dip switch is used to recognize the specific Merger board which we would like to control through VME. As shown in Figure A.1, the LSB 4 bits(1~4) of SW403 are SL ID and 5~8 are local ID (In this case, SL ID = 0 and local ID = 0). The MSB 2 bits are reserved for the flash memory configuration, and they need to be always high.

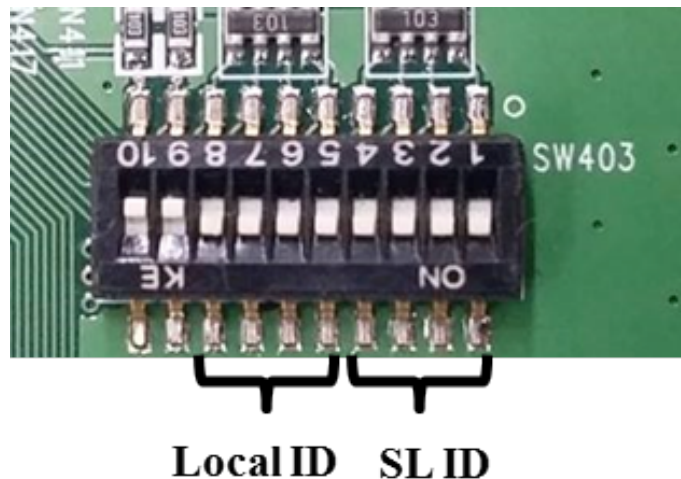


Figure A.1: Dip switch of Merger board.



- VME_IF:

This one includes all the basic functions shown in Figure A.2. The usage is:

```
./VME_IF [SL ID] [Local ID]
```

Then, the interface is shown in Figure A.2. Some functions which are related to Merger board are as following:

- 1) Read firmware variables: read the 32 bits signal corresponding to each address. An example is shown in Figure A.3. After we type the address (0x300), the board type, firmware version, and the 32 bits data will be shown.
- 2) Write one firmware variable: write 32 bits data to Merger
- 51) Multiple Unlock-Erase-Upload-Readback-Reboot for validation (for Merger): This function item will erase the flash memory, download firmware (mgr.pof at the same directory), and reboot the board. Therefore, the firmware in flash memory will be updated to a new one.
- 52) Reboot: reboot the Merger board. If there is firmware loaded in flash memory, reboot will make the board reload the firmware.

```
[belle2@localhost ~/new_exe_mgr]$ ./VME_IF 1 0
Calling gefVmeOpen
----- VME Access -----
 1) Read firmware variables
 2) Write one firmware variable
 3) Execute firmware uploading
 4) Readback CFG from Flash
11) Multiple Readback for validation
12) Multiple Unlock-Erase-Upload-Readback-Reboot for validation
----- Play&Record -----
 5) IO_saving   6) play_record  7) RAM_read    8) RAM_write   9) PR_reset
13) VAL_0 IO_saving   14) VAL_0 play_record
15) VAL_0 RAM_read   16) VAL_0 RAM_write   17) VAL_1-0 IO_saving & RAM_read
18) VAL_1-1 RAM_write(1),play_record,RAM_read,RAM_write(2),play_record,RAM_read
----- VME for MergerV3 -----
51) Multiple Unlock-Erase-Upload-Readback-Reboot for validation(for Merger)
52) Reboot
 0) Quit
Select master window action? █
```

Figure A.2: VME_IF.

- reload:

This is the function item 51) of VME_IF which is made as a standalone program. Before executing the function, the firmware (.pof) needs to be moved to the same folder and named as **mgr.pof**. The usage is:

```
./reload [SL ID] [Local ID]
```

```

Select master window action? 1
Enter internal address to read: 0x300
|-----|
| Version of Board      : Mgr3      |
| Firmware ID          : Merger|
| Firmware Version     : 00000240|
| Status               : 00000000|
| 0x00000300          : 00000000|
|-----|

```



Figure A.3: Read 32bits data by VME_IF.

To update firmware for all boards belonging to the same crate, use:

```
./reload_MGRX.csh
X = 0~5
```

- reboot:

This is the function item 52) of VME_IF which is made as a standalone program. The usage is:

```
./reboot [SL ID] [Local ID]
```

To reboot all boards belonging to the same crate, use:

```
./reboot_MGRX.csh
X = 0~5
```

- operation:

This function is used to switch the board to different operation modes

- Normal operation mode: execute

```
./operation [SL ID] [Local ID] 0
```

- Transmission test mode (for BERT): execute

```
./operation [SL ID] [Local ID] 1
```

- Data player mode: execute

```
./operation [SL ID] [Local ID] 2
```

To control the operation of all Mergers at the same crate, execute:



```
./switch_normal_MGRX.csh
./switch_test_MGRX.csh
./switch_dataplayer_MGRX.csh
X = 0~5
```

- insert:

This function is valid only under the data player mode. By executing

```
./insert [SL ID] [Local ID] X Y
X = 1 for U1
X = 2 for U2
Y is location of data file.(not necessary)
```

32*256 bits data patterns in the file test will be written to the board, then it will start to play the patterns in running data flow. The argument Y is used to indicate a specific data file, which is not necessary. If Y is not included when executing insert function, the default data file is under TSIM_data. For instance, if SL ID = 3, local ID =1, and FPGA is U2, the default data file is TSIM_data/3_1_u2.dat.

- hit_count:

This function is valid only under normal operation mode. After data flow of the system is on, by executing

```
./hit_count [SL ID] [Local ID]
```

the hit counters of all wires corresponding to the Merger will be read. The outcome is shown in Figure A.4.

```
[belle2@localhost ~/new_exe_mgr]$ ./hit_count 1 0
Calling geFvmeOpen
UIWire00 : a904010f, UIWire01 : a9040110, UIWire02 : a9040111, UIWire03 : a9040112, UIWire04 : a9040113, UIWire05 : a9040114, UIWire06 : a9040115, UIWire07 : a9040116,
UIWire08 : a9040117, UIWire09 : a9040118, UIWire10 : a9040119, UIWire11 : a904011a, UIWire12 : a904011b, UIWire13 : a904011c, UIWire14 : a904011d, UIWire15 : a904011e,
UIWire16 : a904011f, UIWire17 : a9040120, UIWire18 : a9040121, UIWire19 : a9040122, UIWire20 : a9040123, UIWire21 : a9040124, UIWire22 : a9040125, UIWire23 : a9040126,
UIWire24 : a9040127, UIWire25 : a9040128, UIWire26 : a9040129, UIWire27 : a904012a, UIWire28 : a904012b, UIWire29 : a904012c, UIWire30 : a904012c, UIWire31 : a904012d,
UIWire32 : a904012e, UIWire33 : a904012f, UIWire34 : a9040130, UIWire35 : a9040131, UIWire36 : a9040132, UIWire37 : a9040133, UIWire38 : a9040134, UIWire39 : a9040135,
UIWire40 : a9040136, UIWire41 : a9040137, UIWire42 : a9040138, UIWire43 : a9040139, UIWire44 : a904013a, UIWire45 : a904013c, UIWire46 : a904013c, UIWire47 : a904013d,
UIWire48 : a904013e, UIWire49 : a904013f, UIWire50 : a9040141, UIWire51 : a9040142, UIWire52 : a9040143, UIWire53 : a9040144, UIWire54 : a9040145, UIWire55 : a9040146,
```

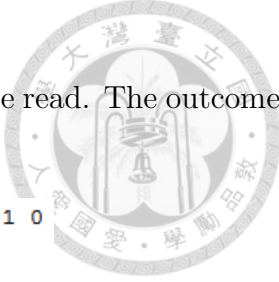
Figure A.4: Result of hit_count.

- hit_rate:

This function is valid only under normal operation mode. After data flow of the system is on, by executing

```
./hit_rate [SL ID] [Local ID]
```


the hit rate of all wires corresponding to the Merger will be read. The outcome is shown in Figure A.5.



```
[belle2@localhost ~/new_exe_mgr]$ ./hit_rate 1 0
Calling gefVmeOpen
U1Wire00 : 30519.791016 /sec,
U1Wire01 : 30519.791016 /sec,
U1Wire02 : 30519.791016 /sec,
U1Wire03 : 30519.791016 /sec,
U1Wire04 : 30519.791016 /sec,
U1Wire05 : 30519.791016 /sec,
U1Wire06 : 30519.791016 /sec,
U1Wire07 : 30519.791016 /sec,
U1Wire08 : 30519.791016 /sec,
U1Wire09 : 30519.791016 /sec,
U1Wire10 : 30519.791016 /sec,
U1Wire11 : 30519.791016 /sec,
U1Wire12 : 30519.791016 /sec,
```

Figure A.5: Result of hit_rate.

- reset_counter:

The wire hit rate is calculated with the hit scalars and time counter. Both the hit scalars and time counter can be reset to 0 by executing:

```
./reset_counter [SL ID] [Local ID]
```





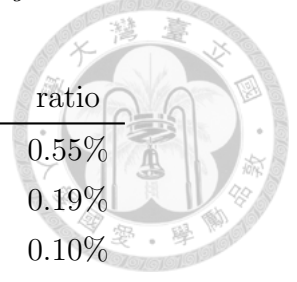
Appendix B

Inclusive D^0 under Different $D_{tag}^{(*)}/X_{frag}$ modes

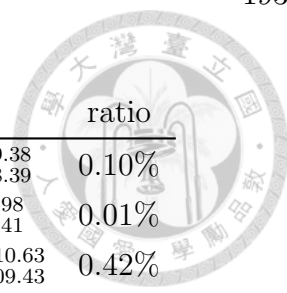
B.1 Inclusive D^0 under Different $D_{tag}^{(*)}$ Modes

The inclusive D^0 fit results of data and six times data size generic MC under different $D_{tag}^{(*)}$ modes are listed in Table B.1~B.4.

ID	D_{tag}	D_{tag}^*	N_{D^0}	ratio
1	$D^0 \rightarrow K^- \pi^+$		$62547.50^{+326.12}_{-343.76}$	9.01%
2	$D^0 \rightarrow K^- \pi^+ \pi^0$		$90360.20^{+963.41}_{-984.73}$	13.01%
3	$D^0 \rightarrow K^- \pi^+ \pi^+ \pi^-$		$87668.30^{+400.97}_{-362.32}$	12.62%
4	$D^0 \rightarrow K^- \pi^+ \pi^+ \pi^- \pi^0$		$21748.20^{+282.94}_{-280.18}$	3.13%
5	$D^0 \rightarrow K_S^0 \pi^+ \pi^-$		$11437.70^{+141.93}_{-141.96}$	1.65%
6	$D^0 \rightarrow K_S^0 \pi^+ \pi^- \pi^0$		$7643.34^{+137.75}_{-136.24}$	1.10%
21	$D^+ \rightarrow K^- \pi^+ \pi^+$		$81833.70^{+397.78}_{400.16}$	11.78%
22	$D^+ \rightarrow K^- \pi^+ \pi^+ \pi^0$		$30023.40^{+455.55}_{-439.20}$	4.32%
23	$D^+ \rightarrow K_S^0 \pi^+$		$4015.89^{+102.38}_{-89.62}$	0.58%
24	$D^+ \rightarrow K_S^0 \pi^+ \pi^0$		$8805.93^{+249.25}_{-241.24}$	1.27%
25	$D^+ \rightarrow K_S^0 \pi^+ \pi^+ \pi^-$		$6047.24^{+111.51}_{-111.31}$	0.87%
26	$D^+ \rightarrow K^+ K^- \pi^+$		$10125.30^{+169.20}_{-168.95}$	1.46%
31	$\Lambda_c^+ \rightarrow p K^- \pi^+$		$15613.50^{+166.01}_{-162.57}$	2.25%



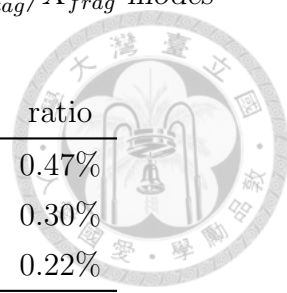
ID	D_{tag}	D_{tag}^*	N_{D^0}	ratio
32	$\Lambda_c^+ \rightarrow pK^-\pi^+\pi^0$		$3842.31^{+107.49}_{-106.01}$	0.55%
33	$\Lambda_c^+ \rightarrow pK_S^0$		$1328.87^{+48.08}_{-47.33}$	0.19%
34	$\Lambda_c^+ \rightarrow \Lambda\pi^+$		$687.33^{+33.55}_{-32.83}$	0.10%
35	$\Lambda_c^+ \rightarrow \Lambda\pi^+\pi^0$		$1339.59^{+57.67}_{-57.09}$	0.19%
36	$\Lambda_c^+ \rightarrow \Lambda\pi^+\pi^+\pi^-$		$1212.43^{+48.33}_{-47.50}$	0.17%
41	$D_s^+ \rightarrow K^+K^-\pi^+$		$16718.60^{+197.09}_{-196.09}$	2.41%
42	$D_s^+ \rightarrow K_S^0K^+$		$1220.61^{+54.20}_{-53.14}$	0.18%
43	$D_s^+ \rightarrow K_S^0K_S^0\pi^+$		$177.72^{+18.91}_{-18.26}$	0.03%
44	$D_s^+ \rightarrow K^+K^-\pi^+\pi^0$		$9895.03^{+280.69}_{-275.94}$	1.42%
45	$D_s^+ \rightarrow K_S^0K^+\pi^+\pi^+$		$1161.40^{+51.18}_{-50.31}$	0.17%
101	$D^0 \rightarrow K^-\pi^+$	$D^{*+} \rightarrow D^0\pi^+$	$26061.20^{+224.89}_{-223.97}$	3.75%
102	$D^0 \rightarrow K^-\pi^+\pi^0$	$D^{*+} \rightarrow D^0\pi^+$	$32400.70^{+272.84}_{-272.23}$	4.67%
103	$D^0 \rightarrow K^-\pi^+\pi^+\pi^-$	$D^{*+} \rightarrow D^0\pi^+$	$30881.70^{+245.06}_{-243.63}$	4.45%
104	$D^0 \rightarrow K^-\pi^+\pi^+\pi^-\pi^0$	$D^{*+} \rightarrow D^0\pi^+$	$4998.26^{+359.61}_{-341.83}$	0.72%
105	$D^0 \rightarrow K_S^0\pi^+\pi^-$	$D^{*+} \rightarrow D^0\pi^+$	$4466.70^{+93.69}_{-92.67}$	0.64%
106	$D^0 \rightarrow K_S^0\pi^+\pi^-\pi^0$	$D^{*+} \rightarrow D^0\pi^+$	$2515.05^{+76.49}_{-75.01}$	0.36%
201	$D^0 \rightarrow K^-\pi^+$	$D^{*0} \rightarrow D^0\pi^0$	$10916.50^{+140.90}_{-142.66}$	1.57%
202	$D^0 \rightarrow K^-\pi^+\pi^0$	$D^{*0} \rightarrow D^0\pi^0$	$14542.60^{+185.27}_{-184.27}$	2.09%
203	$D^0 \rightarrow K^-\pi^+\pi^+\pi^-$	$D^{*0} \rightarrow D^0\pi^0$	$12687.90^{+158.91}_{-154.46}$	1.83%
204	$D^0 \rightarrow K^-\pi^+\pi^+\pi^-\pi^0$	$D^{*0} \rightarrow D^0\pi^0$	$2426.82^{+89.42}_{-88.23}$	0.35%
205	$D^0 \rightarrow K_S^0\pi^+\pi^-$	$D^{*0} \rightarrow D^0\pi^0$	$1929.21^{+81.61}_{-69.21}$	0.28%
206	$D^0 \rightarrow K_S^0\pi^+\pi^-\pi^0$	$D^{*0} \rightarrow D^0\pi^0$	$1076.20^{+50.37}_{-49.35}$	0.15%
301	$D^0 \rightarrow K^-\pi^+$	$D^{*0} \rightarrow D^0\gamma$	$13170.30^{+169.77}_{-167.70}$	1.90%
302	$D^0 \rightarrow K^-\pi^+\pi^0$	$D^{*0} \rightarrow D^0\gamma$	$16714.30^{+228.39}_{-225.81}$	2.41%
303	$D^0 \rightarrow K^-\pi^+\pi^+\pi^-$	$D^{*0} \rightarrow D^0\gamma$	$16929.60^{+202.80}_{-201.12}$	2.44%
304	$D^0 \rightarrow K^-\pi^+\pi^+\pi^-\pi^0$	$D^{*0} \rightarrow D^0\gamma$	$4652.66^{+188.59}_{-185.23}$	0.67%
305	$D^0 \rightarrow K_S^0\pi^+\pi^-$	$D^{*0} \rightarrow D^0\gamma$	$2306.33^{+82.27}_{-81.91}$	0.33%
306	$D^0 \rightarrow K_S^0\pi^+\pi^-\pi^0$	$D^{*0} \rightarrow D^0\gamma$	$1325.55^{+66.32}_{-64.63}$	0.19%
121	$D^+ \rightarrow K^-\pi^+\pi^+$	$D^{*+} \rightarrow D^+\pi^0$	$8361.37^{+133.95}_{-132.30}$	1.20%
122	$D^+ \rightarrow K^-\pi^+\pi^+\pi^0$	$D^{*+} \rightarrow D^+\pi^0$	$2212.64^{+94.40}_{-90.87}$	0.32%
123	$D^+ \rightarrow K_S^0\pi^+$	$D^{*+} \rightarrow D^+\pi^0$	$441.98^{+31.03}_{-29.78}$	0.06%
124	$D^+ \rightarrow K_S^0\pi^+\pi^0$	$D^{*+} \rightarrow D^+\pi^0$	$805.25^{+48.87}_{-47.43}$	0.12%
125	$D^+ \rightarrow K_S^0\pi^+\pi^+\pi^-$	$D^{*+} \rightarrow D^+\pi^0$	$649.16^{+35.88}_{-35.00}$	0.09%
126	$D^+ \rightarrow K^+K^-\pi^+$	$D^{*+} \rightarrow D^+\pi^0$	$887.26^{+51.63}_{-50.18}$	0.13%
441	$D_s^+ \rightarrow K^+K^-\pi^+$	$D_s^{*+} \rightarrow D_s^+\gamma$	$8424.65^{+133.16}_{-133.15}$	1.21%



ID	D_{tag}	D_{tag}^{*}	N_{D^0}	ratio
442	$D_s^+ \rightarrow K_S^0 K^+$	$D_s^{*+} \rightarrow D_s^+ \gamma$	$714.68^{+39.38}_{-38.39}$	0.10%
443	$D_s^+ \rightarrow K_S^0 K_S^0 \pi^+$	$D_s^{*+} \rightarrow D_s^+ \gamma$	$85.38^{+15.98}_{-13.41}$	0.01%
444	$D_s^+ \rightarrow K^+ K^- \pi^+ \pi^0$	$D_s^{*+} \rightarrow D_s^+ \gamma$	$2942.80^{+110.63}_{-109.43}$	0.42%
445	$D_s^+ \rightarrow K_S^0 K^+ \pi^+ \pi^+$	$D_s^{*+} \rightarrow D_s^+ \gamma$	$541.19^{+34.48}_{-33.37}$	0.08%

Table B.1: Inclusive D^0 data fit results (N_{D^0}) under different $D_{tag}^{(*)}$ modes.

ID	D_{tag}	D_{tag}^{*}	N_{bck}	ratio
1	$D^0 \rightarrow K^- \pi^+$		$76813.6^{+356.23}_{-344.84}$	5.43%
2	$D^0 \rightarrow K^- \pi^+ \pi^0$		$279737^{+1107.48}_{-979.72}$	19.78%
3	$D^0 \rightarrow K^- \pi^+ \pi^+ \pi^-$		$135785^{+415.94}_{-461.86}$	9.60%
4	$D^0 \rightarrow K^- \pi^+ \pi^+ \pi^- \pi^0$		$101763^{+409.95}_{-414.65}$	7.20%
5	$D^0 \rightarrow K_S^0 \pi^+ \pi^-$		$13011.3^{+148.21}_{-146.58}$	0.92%
6	$D^0 \rightarrow K_S^0 \pi^+ \pi^- \pi^0$		$17716.4^{+169.25}_{-170.47}$	1.25%
21	$D^+ \rightarrow K^- \pi^+ \pi^+$		$104295^{+427.77}_{-424.62}$	7.38%
22	$D^+ \rightarrow K^- \pi^+ \pi^+ \pi^0$		$113372^{+520.29}_{-542.25}$	8.02%
23	$D^+ \rightarrow K_S^0 \pi^+$		$5256.14^{+111.85}_{-108.93}$	0.37%
24	$D^+ \rightarrow K_S^0 \pi^+ \pi^0$		$21699.9^{+267.12}_{-272.87}$	1.53%
25	$D^+ \rightarrow K_S^0 \pi^+ \pi^+ \pi^-$		$8684.11^{+123.07}_{-122.32}$	0.61%
26	$D^+ \rightarrow K^+ K^- \pi^+$		$35405.2^{+232.40}_{-231.77}$	2.50%
31	$\Lambda_c^+ \rightarrow p K^- \pi^+$		$14291.6^{+158.24}_{-162.23}$	1.01%
32	$\Lambda_c^+ \rightarrow p K^- \pi^+ \pi^0$		$13756.7^{+146.22}_{-145.74}$	0.97%
33	$\Lambda_c^+ \rightarrow p K_S^0$		$1007.09^{+44.69}_{-43.72}$	0.07%
34	$\Lambda_c^+ \rightarrow \Lambda \pi^+$		$582.699^{+31.99}_{-31.16}$	0.04%
35	$\Lambda_c^+ \rightarrow \Lambda \pi^+ \pi^0$		$2449.54^{+66.80}_{-65.91}$	0.17%
36	$\Lambda_c^+ \rightarrow \Lambda \pi^+ \pi^+ \pi^-$		$1166.57^{+47.84}_{-47.02}$	0.08%
41	$D_s^+ \rightarrow K^+ K^- \pi^+$		$29678.4^{+227.55}_{-226.80}$	2.10%
42	$D_s^+ \rightarrow K_S^0 K^+$		$1796.44^{+59.08}_{-58.50}$	0.13%
43	$D_s^+ \rightarrow K_S^0 K_S^0 \pi^+$		$231.323^{+20.41}_{-19.54}$	0.02%
44	$D_s^+ \rightarrow K^+ K^- \pi^+ \pi^0$		$47947.1^{+338.17}_{-341.81}$	3.39%
45	$D_s^+ \rightarrow K_S^0 K^+ \pi^+ \pi^+$		$2019.62^{+58.98}_{-58.21}$	0.14%
101	$D^0 \rightarrow K^- \pi^+$	$D^{*+} \rightarrow D^0 \pi^+$	$25667.8^{+223.90}_{-223.20}$	1.82%
102	$D^0 \rightarrow K^- \pi^+ \pi^0$	$D^{*+} \rightarrow D^0 \pi^+$	$41264.5^{+288.71}_{-287.96}$	2.92%
103	$D^0 \rightarrow K^- \pi^+ \pi^+ \pi^-$	$D^{*+} \rightarrow D^0 \pi^+$	$29726.3^{+242.04}_{-241.71}$	2.10%

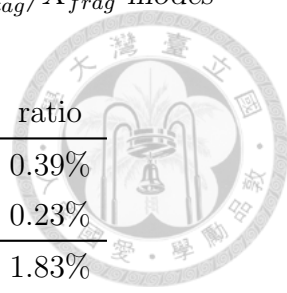


ID	D_{tag}	D_{tag}^*	N_{bck}	ratio
104	$D^0 \rightarrow K^- \pi^+ \pi^+ \pi^- \pi^0$	$D^{*+} \rightarrow D^0 \pi^+$	$6681.64^{+531.75}_{-376.33}$	0.47%
105	$D^0 \rightarrow K_S^0 \pi^+ \pi^-$	$D^{*+} \rightarrow D^0 \pi^+$	$4217.47^{+91.99}_{-91.67}$	0.30%
106	$D^0 \rightarrow K_S^0 \pi^+ \pi^- \pi^0$	$D^{*+} \rightarrow D^0 \pi^+$	$3048.93^{+79.32}_{-79.07}$	0.22%
201	$D^0 \rightarrow K^- \pi^+$	$D^{*0} \rightarrow D^0 \pi^0$	$12087.6^{+147.99}_{-144.56}$	0.85%
202	$D^0 \rightarrow K^- \pi^+ \pi^0$	$D^{*0} \rightarrow D^0 \pi^0$	$25975.4^{+213.84}_{-213.12}$	1.84%
203	$D^0 \rightarrow K^- \pi^+ \pi^+ \pi^-$	$D^{*0} \rightarrow D^0 \pi^0$	$15479^{+166.35}_{-163.06}$	1.09%
204	$D^0 \rightarrow K^- \pi^+ \pi^+ \pi^- \pi^0$	$D^{*0} \rightarrow D^0 \pi^0$	$8564.23^{+118.84}_{-118.04}$	0.61%
205	$D^0 \rightarrow K_S^0 \pi^+ \pi^-$	$D^{*0} \rightarrow D^0 \pi^0$	$1904.61^{+80.01}_{-70.26}$	0.13%
206	$D^0 \rightarrow K_S^0 \pi^+ \pi^- \pi^0$	$D^{*0} \rightarrow D^0 \pi^0$	$2040.75^{+59.15}_{-58.34}$	0.14%
301	$D^0 \rightarrow K^- \pi^+$	$D^{*0} \rightarrow D^0 \gamma$	$20972.1^{+190.03}_{-191.06}$	1.48%
302	$D^0 \rightarrow K^- \pi^+ \pi^0$	$D^{*0} \rightarrow D^0 \gamma$	$58001.2^{+309.82}_{-302.11}$	4.10%
303	$D^0 \rightarrow K^- \pi^+ \pi^+ \pi^-$	$D^{*0} \rightarrow D^0 \gamma$	$37660.7^{+247.80}_{-247.40}$	2.66%
304	$D^0 \rightarrow K^- \pi^+ \pi^+ \pi^- \pi^0$	$D^{*0} \rightarrow D^0 \gamma$	$23381.3^{+231.30}_{-232.21}$	1.65%
305	$D^0 \rightarrow K_S^0 \pi^+ \pi^-$	$D^{*0} \rightarrow D^0 \gamma$	$4044.45^{+105.58}_{-81.52}$	0.29%
306	$D^0 \rightarrow K_S^0 \pi^+ \pi^- \pi^0$	$D^{*0} \rightarrow D^0 \gamma$	$4530.62^{+86.57}_{-86.55}$	0.32%
121	$D^+ \rightarrow K^- \pi^+ \pi^+$	$D^{*+} \rightarrow D^+ \pi^0$	$10630.2^{+141.87}_{-140.88}$	0.75%
122	$D^+ \rightarrow K^- \pi^+ \pi^+ \pi^0$	$D^{*+} \rightarrow D^+ \pi^0$	$8966.69^{+122.88}_{-124.79}$	0.63%
123	$D^+ \rightarrow K_S^0 \pi^+$	$D^{*+} \rightarrow D^+ \pi^0$	$603.066^{+33.11}_{-32.77}$	0.04%
124	$D^+ \rightarrow K_S^0 \pi^+ \pi^0$	$D^{*+} \rightarrow D^+ \pi^0$	$1724.89^{+56.97}_{-56.84}$	0.12%
125	$D^+ \rightarrow K_S^0 \pi^+ \pi^+ \pi^-$	$D^{*+} \rightarrow D^+ \pi^0$	$838.833^{+38.42}_{-37.63}$	0.06%
126	$D^+ \rightarrow K^+ K^- \pi^+$	$D^{*+} \rightarrow D^+ \pi^0$	$2107.85^{+61.88}_{-61.61}$	0.15%
441	$D_s^+ \rightarrow K^+ K^- \pi^+$	$D_s^{*+} \rightarrow D_s^+ \gamma$	$11919.3^{+145.64}_{-145.79}$	0.84%
442	$D_s^+ \rightarrow K_S^0 K^+$	$D_s^{*+} \rightarrow D_s^+ \gamma$	$834.316^{+40.74}_{-40.05}$	0.06%
443	$D_s^+ \rightarrow K_S^0 K_S^0 \pi^+$	$D_s^{*+} \rightarrow D_s^+ \gamma$	$102.663^{+14.92}_{-15.69}$	0.01%
444	$D_s^+ \rightarrow K^+ K^- \pi^+ \pi^0$	$D_s^{*+} \rightarrow D_s^+ \gamma$	$14526.4^{+154.27}_{-153.64}$	1.03%
445	$D_s^+ \rightarrow K_S^0 K^+ \pi^+ \pi^+$	$D_s^{*+} \rightarrow D_s^+ \gamma$	$918.731^{+39.47}_{-38.73}$	0.06%

Table B.2: Inclusive D^0 data fit results (N_{bck}) under different $D_{tag}^{(*)}$ modes.

ID	D_{tag}	D_{tag}^*	N_{D^0}	ratio
1	$D^0 \rightarrow K^- \pi^+$		$237981^{+638.86}_{-641.18}$	7.22%
2	$D^0 \rightarrow K^- \pi^+ \pi^0$		$323918^{+871.91}_{-921.84}$	9.83%
3	$D^0 \rightarrow K^- \pi^+ \pi^+ \pi^-$		$321392^{+934.63}_{-695.01}$	9.76%
4	$D^0 \rightarrow K^- \pi^+ \pi^+ \pi^- \pi^0$		$114832^{+913.38}_{-910.27}$	3.49%

ID	D_{tag}	D_{tag}^*	N_{D^0}	ratio
5	$D^0 \rightarrow K_S^0 \pi^+ \pi^-$		$41581.9^{+272.46}_{-268.47}$	1.26%
6	$D^0 \rightarrow K_S^0 \pi^+ \pi^- \pi^0$		$30170.3^{+404.87}_{-283.18}$	0.92%
21	$D^+ \rightarrow K^- \pi^+ \pi^+$		$361274^{+798.36}_{-787.96}$	10.97%
22	$D^+ \rightarrow K^- \pi^+ \pi^+ \pi^0$		$148495^{+988.85}_{-959.19}$	4.51%
23	$D^+ \rightarrow K_S^0 \pi^+$		$15674.4^{+168.01}_{-167.59}$	0.48%
24	$D^+ \rightarrow K_S^0 \pi^+ \pi^0$		$35362.8^{+443.94}_{-440.73}$	1.07%
25	$D^+ \rightarrow K_S^0 \pi^+ \pi^+ \pi^-$		$29354.8^{+237.58}_{-236.09}$	0.89%
26	$D^+ \rightarrow K^+ K^- \pi^+$		$37435.6^{+312.00}_{-318.49}$	1.14%
31	$\Lambda_c^+ \rightarrow p K^- \pi^+$		$122098^{+415.80}_{-460.79}$	3.71%
32	$\Lambda_c^+ \rightarrow p K^- \pi^+ \pi^0$		$30628.9^{+276.35}_{-277.82}$	0.93%
33	$\Lambda_c^+ \rightarrow p K_S^0$		$8800.7^{+117.41}_{-117.36}$	0.27%
34	$\Lambda_c^+ \rightarrow \Lambda \pi^+$		$5051.15^{+89.93}_{-89.13}$	0.15%
35	$\Lambda_c^+ \rightarrow \Lambda \pi^+ \pi^0$		$7645.38^{+132.63}_{-127.85}$	0.23%
36	$\Lambda_c^+ \rightarrow \Lambda \pi^+ \pi^+ \pi^-$		$18852.7^{+172.12}_{-171.37}$	0.57%
41	$D_s^+ \rightarrow K^+ K^- \pi^+$		$81942.8^{+423.27}_{-419.18}$	2.49%
42	$D_s^+ \rightarrow K_S^0 K^+$		$9045.13^{+136.97}_{-135.34}$	0.27%
43	$D_s^+ \rightarrow K_S^0 K_S^0 \pi^+$		$1429.03^{+54.55}_{-53.74}$	0.04%
44	$D_s^+ \rightarrow K^+ K^- \pi^+ \pi^0$		$63216.7^{+686.76}_{-684.82}$	1.92%
45	$D_s^+ \rightarrow K_S^0 K^+ \pi^+ \pi^+$		$10381.9^{+165.21}_{-137.46}$	0.32%
101	$D^0 \rightarrow K^- \pi^+$	$D^{*+} \rightarrow D^0 \pi^+$	$165057^{+534.21}_{-584.13}$	5.01%
102	$D^0 \rightarrow K^- \pi^+ \pi^0$	$D^{*+} \rightarrow D^0 \pi^+$	$196959^{+650.49}_{-651.43}$	5.98%
103	$D^0 \rightarrow K^- \pi^+ \pi^+ \pi^-$	$D^{*+} \rightarrow D^0 \pi^+$	$186943^{+610.05}_{-582.13}$	5.67%
104	$D^0 \rightarrow K^- \pi^+ \pi^+ \pi^- \pi^0$	$D^{*+} \rightarrow D^0 \pi^+$	$29334.5^{+287.09}_{-257.80}$	0.89%
105	$D^0 \rightarrow K_S^0 \pi^+ \pi^-$	$D^{*+} \rightarrow D^0 \pi^+$	$26697.4^{+225.46}_{-227.09}$	0.81%
106	$D^0 \rightarrow K_S^0 \pi^+ \pi^- \pi^0$	$D^{*+} \rightarrow D^0 \pi^+$	$16044.7^{+255.42}_{-257.64}$	0.49%
201	$D^0 \rightarrow K^- \pi^+$	$D^{*0} \rightarrow D^0 \pi^0$	$69702.6^{+367.99}_{-331.14}$	2.12%
202	$D^0 \rightarrow K^- \pi^+ \pi^0$	$D^{*0} \rightarrow D^0 \pi^0$	$83038.5^{+410.20}_{-460.83}$	2.52%
203	$D^0 \rightarrow K^- \pi^+ \pi^+ \pi^-$	$D^{*0} \rightarrow D^0 \pi^0$	$72012.2^{+358.11}_{-362.50}$	2.19%
204	$D^0 \rightarrow K^- \pi^+ \pi^+ \pi^- \pi^0$	$D^{*0} \rightarrow D^0 \pi^0$	$13946.9^{+203.61}_{-205.43}$	0.42%
205	$D^0 \rightarrow K_S^0 \pi^+ \pi^-$	$D^{*0} \rightarrow D^0 \pi^0$	$10806.2^{+137.95}_{-137.65}$	0.33%
206	$D^0 \rightarrow K_S^0 \pi^+ \pi^- \pi^0$	$D^{*0} \rightarrow D^0 \pi^0$	$6761.14^{+123.97}_{-122.82}$	0.21%
301	$D^0 \rightarrow K^- \pi^+$	$D^{*0} \rightarrow D^0 \gamma$	$74772.4^{+382.40}_{-381.68}$	2.27%
302	$D^0 \rightarrow K^- \pi^+ \pi^0$	$D^{*0} \rightarrow D^0 \gamma$	$90066.3^{+480.81}_{-496.40}$	2.73%
303	$D^0 \rightarrow K^- \pi^+ \pi^+ \pi^-$	$D^{*0} \rightarrow D^0 \gamma$	$94042.3^{+447.36}_{-465.19}$	2.85%
304	$D^0 \rightarrow K^- \pi^+ \pi^+ \pi^- \pi^0$	$D^{*0} \rightarrow D^0 \gamma$	$21741.5^{+435.69}_{-415.21}$	0.66%



ID	D_{tag}	D_{tag}^*	N_{D^0}	ratio
305	$D^0 \rightarrow K_S^0 \pi^+ \pi^-$	$D^{*0} \rightarrow D^0 \gamma$	$12725.7^{+163.20}_{-162.92}$	0.39%
306	$D^0 \rightarrow K_S^0 \pi^+ \pi^- \pi^0$	$D^{*0} \rightarrow D^0 \gamma$	$7605.11^{+155.45}_{-154.07}$	0.23%
121	$D^+ \rightarrow K^- \pi^+ \pi^+$	$D^{*+} \rightarrow D^+ \pi^0$	$60218.8^{+343.02}_{-342.01}$	1.83%
122	$D^+ \rightarrow K^- \pi^+ \pi^+ \pi^0$	$D^{*+} \rightarrow D^+ \pi^0$	$16889.1^{+236.29}_{-234.97}$	0.51%
123	$D^+ \rightarrow K_S^0 \pi^+$	$D^{*+} \rightarrow D^+ \pi^0$	$2943.37^{+100.68}_{-101.44}$	0.09%
124	$D^+ \rightarrow K_S^0 \pi^+ \pi^0$	$D^{*+} \rightarrow D^+ \pi^0$	$4929.38^{+113.51}_{-112.10}$	0.15%
125	$D^+ \rightarrow K_S^0 \pi^+ \pi^+ \pi^-$	$D^{*+} \rightarrow D^+ \pi^0$	$4415.97^{+97.30}_{-96.81}$	0.13%
126	$D^+ \rightarrow K^+ K^- \pi^+$	$D^{*+} \rightarrow D^+ \pi^0$	$5700.05^{+115.84}_{-114.70}$	0.17%
441	$D_s^+ \rightarrow K^+ K^- \pi^+$	$D_s^{*+} \rightarrow D_s^+ \gamma$	$78229.2^{+379.28}_{-379.83}$	2.37%
442	$D_s^+ \rightarrow K_S^0 K^+$	$D_s^{*+} \rightarrow D_s^+ \gamma$	$9428.46^{+130.40}_{-129.32}$	0.29%
443	$D_s^+ \rightarrow K_S^0 K_S^0 \pi^+$	$D_s^{*+} \rightarrow D_s^+ \gamma$	$1379.69^{+51.11}_{-50.33}$	0.04%
444	$D_s^+ \rightarrow K^+ K^- \pi^+ \pi^0$	$D_s^{*+} \rightarrow D_s^+ \gamma$	$35857.2^{+459.02}_{-407.38}$	1.09%
445	$D_s^+ \rightarrow K_S^0 K^+ \pi^+ \pi^+$	$D_s^{*+} \rightarrow D_s^+ \gamma$	$8703.93^{+130.24}_{-129.21}$	0.26%

Table B.3: Inclusive D^0 six times data size MC fit results (N_{D^0}) under different $D_{tag}^{(*)}$ modes.

ID	D_{tag}	D_{tag}^*	N_{bck}	ratio
1	$D^0 \rightarrow K^- \pi^+$		$299409^{+659.25}_{-673.58}$	4.13%
2	$D^0 \rightarrow K^- \pi^+ \pi^0$		$1109460^{+1283.41}_{-1242.08}$	15.30%
3	$D^0 \rightarrow K^- \pi^+ \pi^+ \pi^-$		$634780^{+1070.10}_{-858.67}$	8.75%
4	$D^0 \rightarrow K^- \pi^+ \pi^+ \pi^- \pi^0$		$549874^{+1123.83}_{-1126.00}$	7.58%
5	$D^0 \rightarrow K_S^0 \pi^+ \pi^-$		$61460.4^{+304.95}_{-308.94}$	0.85%
6	$D^0 \rightarrow K_S^0 \pi^+ \pi^- \pi^0$		$103256^{+548.37}_{-368.55}$	1.42%
21	$D^+ \rightarrow K^- \pi^+ \pi^+$		$431707^{+826.31}_{-836.41}$	5.95%
22	$D^+ \rightarrow K^- \pi^+ \pi^+ \pi^0$		$584069^{+1159.18}_{-1194.56}$	8.05%
23	$D^+ \rightarrow K_S^0 \pi^+$		$19081.6^{+178.23}_{-177.19}$	0.26%
24	$D^+ \rightarrow K_S^0 \pi^+ \pi^0$		$92506.7^{+504.90}_{-501.95}$	1.28%
25	$D^+ \rightarrow K_S^0 \pi^+ \pi^+ \pi^-$		$48480.4^{+275.15}_{-273.57}$	0.67%
26	$D^+ \rightarrow K^+ K^- \pi^+$		$148018^{+453.58}_{-462.91}$	2.04%
31	$\Lambda_c^+ \rightarrow p K^- \pi^+$		$91595.4^{+408.35}_{-398.38}$	1.26%
32	$\Lambda_c^+ \rightarrow p K^- \pi^+ \pi^0$		$88998.8^{+368.46}_{-366.63}$	1.23%
33	$\Lambda_c^+ \rightarrow p K_S^0$		$5987.25^{+105.55}_{-103.90}$	0.08%
34	$\Lambda_c^+ \rightarrow \Lambda \pi^+$		$3571.79^{+81.32}_{-80.38}$	0.05%

ID	D_{tag}	D_{tag}^{*}	N_{bck}	ratio
35	$\Lambda_c^+ \rightarrow \Lambda \pi^+ \pi^0$		$14788.6^{+154.03}_{-153.33}$	0.20%
36	$\Lambda_c^+ \rightarrow \Lambda \pi^+ \pi^+ \pi^-$		$13152.3^{+154.69}_{-153.83}$	0.18%
41	$D_s^+ \rightarrow K^+ K^- \pi^+$		$143816^{+489.04}_{-489.31}$	1.98%
42	$D_s^+ \rightarrow K_S^0 K^+$		$11479.8^{+144.96}_{-144.68}$	0.16%
43	$D_s^+ \rightarrow K_S^0 K_S^0 \pi^+$		$2187.06^{+61.08}_{-60.41}$	0.03%
44	$D_s^+ \rightarrow K^+ K^- \pi^+ \pi^0$		$263902^{+182.97}_{-822.52}$	3.64%
45	$D_s^+ \rightarrow K_S^0 K^+ \pi^+ \pi^+$		$17193.2^{+167.97}_{-173.15}$	0.24%
101	$D^0 \rightarrow K^- \pi^+$	$D^{*+} \rightarrow D^0 \pi^+$	$172594^{+564.04}_{-525.41}$	2.38%
102	$D^0 \rightarrow K^- \pi^+ \pi^0$	$D^{*+} \rightarrow D^0 \pi^+$	$264179^{+638.48}_{-704.42}$	3.64%
103	$D^0 \rightarrow K^- \pi^+ \pi^+ \pi^-$	$D^{*+} \rightarrow D^0 \pi^+$	$199662^{+603.85}_{-585.07}$	2.75%
104	$D^0 \rightarrow K^- \pi^+ \pi^+ \pi^- \pi^0$	$D^{*+} \rightarrow D^0 \pi^+$	$46642.1^{+325.40}_{-290.40}$	0.64%
105	$D^0 \rightarrow K_S^0 \pi^+ \pi^-$	$D^{*+} \rightarrow D^0 \pi^+$	$29239.2^{+232.82}_{-230.82}$	0.40%
106	$D^0 \rightarrow K_S^0 \pi^+ \pi^- \pi^0$	$D^{*+} \rightarrow D^0 \pi^+$	$22251.3^{+280.35}_{-275.18}$	0.31%
201	$D^0 \rightarrow K^- \pi^+$	$D^{*0} \rightarrow D^0 \pi^0$	$76247.9^{+333.04}_{-330.58}$	1.05%
202	$D^0 \rightarrow K^- \pi^+ \pi^0$	$D^{*0} \rightarrow D^0 \pi^0$	$144153^{+617.13}_{-211.78}$	1.99%
203	$D^0 \rightarrow K^- \pi^+ \pi^+ \pi^-$	$D^{*0} \rightarrow D^0 \pi^0$	$94835.8^{+351.24}_{-387.74}$	1.31%
204	$D^0 \rightarrow K^- \pi^+ \pi^+ \pi^- \pi^0$	$D^{*0} \rightarrow D^0 \pi^0$	$51647.7^{+283.42}_{-280.64}$	0.71%
205	$D^0 \rightarrow K_S^0 \pi^+ \pi^-$	$D^{*0} \rightarrow D^0 \pi^0$	$12274.2^{+143.21}_{-142.89}$	0.17%
206	$D^0 \rightarrow K_S^0 \pi^+ \pi^- \pi^0$	$D^{*0} \rightarrow D^0 \pi^0$	$13402.9^{+148.24}_{-147.62}$	0.18%
301	$D^0 \rightarrow K^- \pi^+$	$D^{*0} \rightarrow D^0 \gamma$	$117915^{+435.37}_{-434.22}$	1.63%
302	$D^0 \rightarrow K^- \pi^+ \pi^0$	$D^{*0} \rightarrow D^0 \gamma$	$289114^{+675.66}_{-654.55}$	3.99%
303	$D^0 \rightarrow K^- \pi^+ \pi^+ \pi^-$	$D^{*0} \rightarrow D^0 \gamma$	$222094^{+588.69}_{-571.02}$	3.06%
304	$D^0 \rightarrow K^- \pi^+ \pi^+ \pi^- \pi^0$	$D^{*0} \rightarrow D^0 \gamma$	$153495^{+526.21}_{-563.85}$	2.12%
305	$D^0 \rightarrow K_S^0 \pi^+ \pi^-$	$D^{*0} \rightarrow D^0 \gamma$	$24521.4^{+195.60}_{-196.29}$	0.34%
306	$D^0 \rightarrow K_S^0 \pi^+ \pi^- \pi^0$	$D^{*0} \rightarrow D^0 \gamma$	$30084.6^{+216.16}_{-214.83}$	0.41%
121	$D^+ \rightarrow K^- \pi^+ \pi^+$	$D^{*+} \rightarrow D^+ \pi^0$	$75324.3^{+364.21}_{-363.59}$	1.04%
122	$D^+ \rightarrow K^- \pi^+ \pi^+ \pi^0$	$D^{*+} \rightarrow D^+ \pi^0$	$56215.9^{+309.46}_{-306.58}$	0.78%
123	$D^+ \rightarrow K_S^0 \pi^+$	$D^{*+} \rightarrow D^+ \pi^0$	$3406.87^{+107.78}_{-103.38}$	0.05%
124	$D^+ \rightarrow K_S^0 \pi^+ \pi^0$	$D^{*+} \rightarrow D^+ \pi^0$	$10434.5^{+135.32}_{-134.74}$	0.14%
125	$D^+ \rightarrow K_S^0 \pi^+ \pi^+ \pi^-$	$D^{*+} \rightarrow D^+ \pi^0$	$6802.22^{+109.08}_{-108.24}$	0.09%
126	$D^+ \rightarrow K^+ K^- \pi^+$	$D^{*+} \rightarrow D^+ \pi^0$	$11661.9^{+139.13}_{-138.41}$	0.16%
441	$D_s^+ \rightarrow K^+ K^- \pi^+$	$D_s^{*+} \rightarrow D_s^+ \gamma$	$92213.8^{+397.47}_{-389.38}$	1.27%
442	$D_s^+ \rightarrow K_S^0 K^+$	$D_s^{*+} \rightarrow D_s^+ \gamma$	$9354.56^{+129.95}_{-129.32}$	0.13%
443	$D_s^+ \rightarrow K_S^0 K_S^0 \pi^+$	$D_s^{*+} \rightarrow D_s^+ \gamma$	$1441.1^{+51.97}_{-50.69}$	0.02%
444	$D_s^+ \rightarrow K^+ K^- \pi^+ \pi^0$	$D_s^{*+} \rightarrow D_s^+ \gamma$	$102533^{+480.41}_{-563.28}$	1.41%

ID	D_{tag}	D_{tag}^*	N_{bck}	ratio
445	$D_s^+ \rightarrow K_S^0 K^+ \pi^+ \pi^+$	$D_s^{*+} \rightarrow D_s^+ \gamma$	$11576.8^{+139.96}_{-140.73}$	0.16%

Table B.4: Inclusive D^0 six times data size MC fit results (N_{bck}) under different $D_{tag}^{(*)}$ modes.



B.2 Inclusive D^0 under Different X_{frag} cases

The inclusive D^0 fit results of data and six times data size generic MC under different X_{frag} cases are listed in Table B.5~B.8.

ID	X_{frag}	N_{D^0}	ratio
0	nothing	$16170.6^{+129.76}_{-129.64}$	2.33%
1	π^\pm	$115837^{+364.80}_{-364.14}$	16.68%
2	π^0	$22420.5^{+205.27}_{-203.71}$	3.23%
3	$\pi^\pm\pi^0$	$121279^{+497.22}_{-526.74}$	17.46%
4	$\pi^\pm\pi^\mp$	$94087.4^{+374.17}_{-378.35}$	13.55%
5	$\pi^\pm\pi^\pm\pi^\mp$	$172419^{+713.89}_{-616.93}$	24.83%
6	$\pi^\pm\pi^\pm\pi^0$	$129050^{+880.86}_{-893.82}$	18.58%
10	with K^+K^-	$41182.7^{+628.82}_{-603.52}$	5.93%

Table B.5: Inclusive D^0 data fit results (N_{D^0}) under different X_{frag} cases.

ID	X_{frag}	N_{bck}	ratio
0	nothing	$1146.64^{+42.82}_{-41.97}$	0.08%
1	π^\pm	$49494.3^{+258.27}_{-257.47}$	3.50%
2	π^0	$18282.5^{+195.12}_{-194.18}$	1.29%
3	$\pi^\pm\pi^0$	$248278^{+636.65}_{-610.15}$	17.56%
4	$\pi^\pm\pi^\mp$	$65049.8^{+338.11}_{-332.80}$	4.60%
5	$\pi^\pm\pi^\pm\pi^\mp$	$446345^{+829.12}_{-923.42}$	31.57%
6	$\pi^\pm\pi^\pm\pi^0$	$308119^{+1015.40}_{-952.32}$	21.79%
10	with K^+K^-	$259209^{+758.90}_{-785.36}$	18.33%

Table B.6: Inclusive D^0 data fit results (N_{bck}) under different X_{frag} cases.



ID	X_{frag}	N_{D^0}	ratio
0	nothing	$8124.45^{+104.56}_{-104.09}$	0.25%
1	π^\pm	$339760^{+676.62}_{-662.54}$	10.31%
2	π^0	$55146.5^{+310.01}_{-316.54}$	1.67%
3	$\pi^\pm\pi^0$	$592632^{+1694.96}_{-1668.09}$	17.99%
4	$\pi^\pm\pi^\mp$	$497909^{+805.63}_{-707.35}$	15.11%
5	$\pi^\pm\pi^\pm\pi^\mp$	$957673^{+1411.50}_{-1442.64}$	29.07%
6	$\pi^\pm\pi^\pm\pi^0$	$828568^{+2150.06}_{-1874.53}$	25.15%
10	with K^+K^-	$228247^{+914.37}_{-978.16}$	6.93%

Table B.7: Inclusive D^0 six times data size MC fit results (N_{D^0}) under different X_{frag} cases.

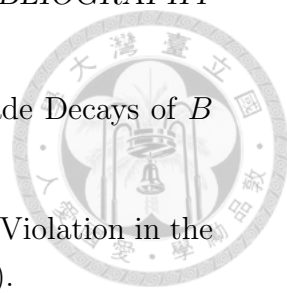
ID	X_{frag}	N_{bck}	ratio
0	nothing	$3830^{+81.70}_{-81.95}$	0.05%
1	π^\pm	$186619^{+514.31}_{-574.07}$	2.57%
2	π^0	$59577.3^{+323.64}_{-326.08}$	0.82%
3	$\pi^\pm\pi^0$	$1089640^{+1830.39}_{-1828.04}$	15.02%
4	$\pi^\pm\pi^\mp$	$286795^{+592.60}_{-670.11}$	3.95%
5	$\pi^\pm\pi^\pm\pi^\mp$	$2222600^{+1857.30}_{-1789.69}$	30.64%
6	$\pi^\pm\pi^\pm\pi^0$	$1697440^{+2092.30}_{-2339.19}$	23.40%
10	with K^+K^-	$1493380^{+1425.27}_{-1498.94}$	20.59%

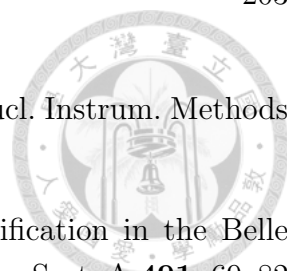
Table B.8: Inclusive D^0 six times data size MC fit results (N_{bck}) under different X_{frag} cases.

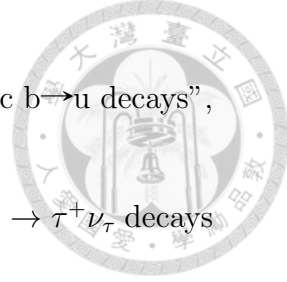


Bibliography

- [1] M. Herrero, “The Standard Model”, arXiv:hep-ph/9812242.
- [2] “Standard Model of Elementary Particles” (Wikipedia), http://en.wikipedia.org/wiki/File:Standard_Model_of_Elementary_Particles.svg.
- [3] “Elementary Particle Interactions” (Wikipedia), http://en.wikipedia.org/wiki/File:Elementary_particle_interactions.svg.
- [4] N. Cabibbo, “Unitary Symmetry and Leptonic Decays”, *Phys. Rev. Lett.* **10**, 531–533 (1963).
- [5] M. Kobayashi and T. Maskawa, “*CP*-Violation in the Renormalizable Theory of Weak Interaction”, *Progress of Theoretical Physics* **49**, **2**, 652–657 (1973).
- [6] L. L. Chau and W. Y. Keung, “Comments on the Parametrization of the Kobayashi-Maskawa Matrix”, *Phys. Rev. Lett.* **53**, 1802–1805 (1984).
- [7] L. Wolfenstein, “Parametrization of the Kobayashi-Maskawa Matrix”, *Phys. Rev. Lett.* **51**, 1945–1947 (1983).
- [8] J. Beringer *et al.* (Particle Data Group), “Review of Particle Physics”, *Phys. Rev. D* **86**, 010001 (2012).
- [9] T. D. Lee and C. N. Yang, “Question of Parity Conservation in Weak Interactions”, *Phys. Rev.* **104**, 254–258 (1956).
- [10] C. S. Wu, E. Ambler, R. W. Hayward, D. D. Hoppes, and R. P. Hudson, “Experimental Test of Parity Conservation in Beta Decay”, *Phys. Rev.* **105**, 1413–1415 (1957).
- [11] J. H. Christenson, J. W. Cronin, V. L. Fitch, and R. Turlay, “Evidence for the 2π Decay of the K_2^0 Meson”, *Phys. Rev. Lett.* **13**, 138–140 (1964).


- 
- [12] A. B. Carter and A. I. Sanda, “ CP Nonconservation in Cascade Decays of B Mesons”, *Phys. Rev. Lett.* **45**, 952–954 (1980).
- [13] K. Abe *et al.* (Belle Collaboration), “Observation of Large CP Violation in the Neutral B Meson System”, *Phys. Rev. Lett.* **87**, 091802 (2001).
- [14] S. W. Herb *et al.*, “Observation of a Dimuon Resonance at 9.5 GeV in 400-GeV Proton-Nucleus Collisions”, *Phys. Rev. Lett.* **39**, 252–255 (1977).
- [15] T. E. Browder and K. Honscheid, “ B Mesons”, *Prog. Part. Nucl. Phys.* **35**, **0**, 81–219 (1995).
- [16] “The Upsilon System” (Cornell’s Laboratory for Elementary-Particle Physics), <http://www.lns.cornell.edu/public/lab-info/upsilon.html>.
- [17] “High Energy Accelerator Research Organization (KEK)”, <http://accl.kek.jp/introKEKB/>.
- [18] S. Kurokawa and E. Kikutani, “Overview of the KEKB Accelerators” and other papers included in the same Volume, *Nucl. Instrum. Methods Phys. Res. Sect. A* **499**, **1**, 1–7 (2003).
- [19] T. Abe *et al.*, “Achievements of KEKB” and following articles up to 03A011., *Prog. Theor. Exp. Phys.* **2013**, **3** (2013).
- [20] “Crab Cavity”, https://en.wikipedia.org/wiki/Crab_cavity/.
- [21] “Super KEKB”, <http://www-acc.kek.jp/KEKB/>.
- [22] “Belle II Collaboration”, <http://belle2.kek.jp/>.
- [23] A. Abashian *et al.* (Belle Collaboration), “The Belle Detector”, *Nucl. Instrum. Methods Phys. Res. Sect. A* **479**, **1**, 117–232 (2002).
- [24] J. Brodzicka *et al.* (Belle Collaboration), “Physics Achievements from the Belle Experiment”, *Prog. Theor. Exp. Phys.* **2012**, **1** (2012).
- [25] Z. Natkaniec *et al.* (Belle SVD2 Group), “Belle SVD2 Vertex Detector”, *Nucl. Instrum. Methods Phys. Res. Sect. A* **568**, **1**, 269–273 (2006).
- [26] M. Z. Wang *et al.* (Belle Collaboration), “Review of EFC options” (*Belle internal*), Belle Note 164 (1996).
- [27] K. Hanagaki *et al.* (Belle Collaboration), “Electron Identification in Belle”, *Nucl. Instrum. Methods Phys. Res. Sect. A* **485**, **3**, 490–503 (2002).

- 
- [28] K. Miyabayashi, “Belle Electromagnetic Calorimeter”, Nucl. Instrum. Methods Phys. Res. Sect. A **494**, 1-3, 298 – 302 (2002).
- [29] A. Abashian *et al.* (Belle Collaboration), “Muon Identification in the Belle Experiment at KEKB”, Nucl. Instrum. Methods Phys. Res. Sect. A **491**, 69–82 (2002).
- [30] A. Badin and A. A. Petrov, “Searching for light dark matter in heavy meson decays”, Phys. Rev. D **82**, 034005 (2010).
- [31] M. J. Strassler and K. M. Zurek, “Echoes of a hidden valley at hadron colliders”, Physics Letters B **651**, 374 (2007).
- [32] H. E. Haber and G. L. Kane, “The search for supersymmetry: Probing physics beyond the standard model”, Physics Reports **117**, 75 (1985).
- [33] L. Widhalm *et al.* (Belle collaboration), “Measurement of $D^0 \rightarrow \pi l \nu (K l \nu)$ Form Factors and Absolute Branching Fractions”, Phys. Rev. Lett. **97**, 061804 (2006).
- [34] L. Widhalm *et al.* (Belle collaboration), “Measurement of $B(D_s^+ \rightarrow \mu^+ \nu_\mu)$ ”, Phys. Rev. Lett. **100**, 241801 (2008).
- [35] A. Zupanc *et al.* (Belle collaboration), “Measurements of branching fractions of leptonic and hadronic D_s^+ meson decays and extraction of the D_s^+ meson decay constant”, Journal of High Energy Physics **09**, 139 (2013).
- [36] P. del Amo Sanchez *et al.* (BABAR Collaboration), “Measurement of the absolute branching fractions for $D_s^- \rightarrow \ell^- \bar{\nu}_\ell$ and extraction of the decay constant $f_{D_s^-}$ ”, Phys. Rev. D **82**, 091103 (2010).
- [37] C. L. Hsu *et al.* (Belle Collaboration), “Search for B^0 decays to invisible final states at Belle”, Phys. Rev. D **86**, 032002 (2012).
- [38] J. P. Lees *et al.* (BABAR Collaboration), “Improved limits on B^0 decays to invisible ($+\gamma$) final states”, Phys. Rev. D **86**, 051105 (2012).
- [39] D. J. Lange, “The EvtGen Particle Decay Simulation Package”, Nucl. Instrum. Methods Phys. Res. Sect. A **462**, 1-2, 152–155 (2001).
- [40] R. Brun *et al.*, “GEANT 3.21”, CERN Report DD/EE/84-1 (1984).
- [41] F. Fanf (Belle Collaboration), “Study of $K_s \rightarrow \pi^+ \pi^-$ Selection” (*Belle internal*), Belle Note 323 (2000).

- 
- [42] H. Albrecht *et al.* (ARGUS collaboration), “Search for hadronic $b \rightarrow u$ decays”, Physics Letters B **241**, 2, 278 – 282 (1990), ISSN 0370-2693.
- [43] B. Kronenbitter, “Measurement of the branching fraction of $B^+ \rightarrow \tau^+ \nu_\tau$ decays with the semileptonic tagging method”, arXiv:1503.05613.
- [44] “PID Joint Group” (*Belle internal*), http://belle.kek.jp/group/pid_joint/.
- [45] G. Majumder (Belle Collaboration), “Proton identification efficiency and fake rates from K/π ” (*Belle internal*), Belle Note 670 (2003).
- [46] S. Nishida (Belle Collaboration), “Study of kaon and pion identification using inclusive D^* sample” (*Belle internal*), Belle Note 779 (2005).
- [47] L. Hinz, C. Jacoby, and J. Wicht (Belle Collaboration), “Lepton efficiency and systematic error for experiments 21 to 27” (*Belle internal*), Belle Note 777 (2004).
- [48] L. Hinz (Belle Collaboration), “Lepton ID efficiency correction and systematic error” (*Belle internal*), Belle Note 954 (2006).
- [49] M. Misiak *et al.*, “Estimate of $\mathcal{B}(\bar{B} \rightarrow X_s \gamma)$ at $O(\alpha_s^2)$ ”, Phys. Rev. Lett. **98**, 022002 (2007).
- [50] J. P. Lees *et al.* (BABAR Collaboration), “Exclusive measurements of $b \rightarrow s \gamma$ transition rate and photon energy spectrum”, Phys. Rev. D **86**, 052012 (2012).
- [51] A. Limosani *et al.* (Belle Collaboration), “Measurement of Inclusive Radiative B -Meson Decays with a Photon Energy Threshold of 1.7 GeV”, Phys. Rev. Lett. **103**, 241801 (2009).
- [52] S. Chen *et al.* (CLEO Collaboration), Phys. Rev. Lett. **87**, 51807 (2001).
- [53] T. Sjöstrand, “PYTHIA 5.7 and JETSET 7.4 Physics and Manual”, hep-ph/9508391.
- [54] M. Z. Wang *et al.* (Belle Collaboration), “Study of $B^+ \rightarrow p \bar{\Lambda} \gamma$, $p \bar{\Lambda} \pi^0$ and $B^0 \rightarrow p \bar{\Lambda} \pi^-$ ”, Phys. Rev. D **76**, 052004 (2007).
- [55] W. S. Hou and A. Soni, “Pathways to Rare Baryonic B Decays”, Phys. Rev. Lett. **86**, 4247–4250 (2001).
- [56] Y. J. Lee *et al.* (Belle Collaboration), “Lambda selection at Belle” (*Belle internal*), Belle Note 684 (2004).

- 
- [57] S. H. Lee *et al.* (Belle Collaboration), “Evidence for $B^0 \rightarrow \pi^0\pi^0$ ”, Phys. Rev. Lett. **91**, 261801 (2003).
- [58] G. C. Fox and S. Wolfram, “Observables for the Analysis of Event Shapes in e^+e^- Annihilation and Other Processes”, Phys. Rev. Lett. **41**, 1581–1585 (1978).
- [59] R. A. Fisher, “The Use of Multiple Measurements in Taxonomic Problems”, Annals of Eugenics **7**, 7, 179–188 (1936).
- [60] “Number of B Events in HadronB(J)” (*Belle internal*), <http://belle.kek.jp/secured/nbb/nbb.html>.
- [61] “SuperKEKB making headway toward higher luminosity”, <http://www2.kek.jp/proffice/archives/feature/2009/SuperKEKB.html>.
- [62] “The BelleII experiment”, <http://www.phy.olemiss.edu/HEP/belle2/index.html>.
- [63] “Belle II’s new logo and new beginning”, <http://www2.kek.jp/proffice/archives/feature/2009/BelleII4th.html>.
- [64] T. Abe *et al.* (Belle collaboration), “Belle II Technical Design Report”, arXiv:1011.0352.
- [65] “FPGA, SoC and CPLD from Altera”, <https://www.altera.com/>.
- [66] “Device Interfaces and Integration for the Arria II Device”, https://www.altera.com/en_US/pdfs/literature/hb/arria-ii-gx/arria-ii-gx_handbook.pdf.
- [67] “Introduction to the Quartus II Software - Altera”, https://www.altera.com/content/dam/altera-www/global/en_US/pdfs/literature/manual/intro_to_quartus2.pdf.
- [68] “Embedded Optical Modules”, <http://www.avagotech.com/products/fiber-optics/embedded-optical-module/>.
- [69] “AFBR-79Q4Z(-D) - Avago Technologies”, <http://www.avagotech.com/docs/AV02-2162EN>.
- [70] “Data bit map for CDC Trigger” (*Belle II internal*), https://belle2.cc.kek.jp/~twiki/pub/Detector/Trigger/JingGeSlides/data_bit_map.pdf.

- 
- [71] “ChipScope Pro 11.4 Software and Cores”, http://www.xilinx.com/support/documentation/sw_manuals/xilinx11/chipscope_pro_sw_cores_ug029.pdf.
- [72] “SignalTap II Logic Analyzer - Altera”, https://www.altera.com/en_US/pdfs/literature/hb/qts/qts_qii53009.pdf.
- [73] “Virtex-5 Family Overview”, http://www.xilinx.com/support/documentation/data_sheets/ds100.pdf.
- [74] “Virtex-5 FPGA RocketIO GTP Transceiver”, http://www.xilinx.com/support/documentation/user_guides/ug196.pdf.
- [75] “Transceiver Architecture in Arria II Devices”, https://www.altera.com/en_US/pdfs/literature/hb/arria-ii-gx/aiigx_52001.pdf.
- [76] “Virtex-6 Family Overview”, http://www.xilinx.com/support/documentation/data_sheets/ds150.pdf.
- [77] “Virtex-6 FPGA GTX Transceivers”, http://www.xilinx.com/support/documentation/user_guides/ug366.pdf.
- [78] “Virtex-6 FPGA GTH Transceivers”, http://www.xilinx.com/support/documentation/user_guides/ug371.pdf.
- [79] “LogiCORE™ IP Aurora 8B/10B v5.3”, http://www.xilinx.com/support/documentation/ip_documentation/aurora_8b10b_ug353.pdf.
- [80] “Xilinx Core Generator”, <http://www.xilinx.com/ise/products/coregen/overview.pdf>.
- [81] “ISE Design Suite”, <http://www.xilinx.com/products/design-tools/ise-design-suite.html>.
- [82] “MegaWizard Plug-Ins”, <https://www.altera.com/products/intellectual-property/megawizard.html>.
- [83] “LogiCORE™ IP Virtex-5 FPGA RocketIO™ GTP Transceiver Wizard v2.1”, http://www.xilinx.com/support/documentation/ip_documentation/v5_gtpwizard_gsg188.pdf.
- [84] “LogiCORE IP Virtex-6 FPGA GTX Transceiver Wizard v1.12”, http://www.xilinx.com/support/documentation/ip_documentation/v6_gtxwizard/v1_12/ug516_v6_gtxwizard.pdf.

- 
- [85] “LogiCORE IP Virtex-6 FPGA GTH Transceiver Wizard v1.11”, http://www.xilinx.com/support/documentation/ip_documentation/v6_gthwizard/v1_11/ug691_v6_gthwizard.pdf.
- [86] “ALTGX Transceiver Setup Guide for Stratix IV Devices”, https://www.altera.com/content/dam/altera-www/global/en_US/pdfs/literature/hb/stratix-iv/stx4_siv53001.pdf.